Università degli Studi di Milano-Bicocca

DIPARTIMENTO DI SCIENZA DEI MATERIALI
Corso di Dottorato in Scienza e Nanotecnologia dei Materiali
XXXI ciclo

Tesi di Dottorato

Nanomechanics of DNA and DNA-ligand interactions: focus on structural polymorphism and DNA condensation

Candidato:
Matteo Cristofalo
735404

Tutor:
Dott. Domenico Salerno

Coordinatore:
Prof. Marco Bernasconi

Anno accademico 2017/2018

CONTENTS

INTRODUCTION

In the last few decades, the constant development of novel microscopy techniques have created the basis for a new paradigm in the field of biophysics, which is an interdisciplinary subject involving different scientific areas, such as physics, biology, chemistry and the engineering of micro-/nano-technologies. Single-molecule techniques enabled to carry out experiments providing new information: the nanomanipulation of individual biomolecules revealed unknown insights into the elasticity and mechanics of molecules, improving the understanding of the fundamental relation between structural properties and biological functions. For instance, the double-helical structure of DNA prevents a too easy access by external molecules to the genetic content, and biological processes such as the protein folding mechanism, or DNA replication and DNA transcription, depend on the twisting or melting of specific regulatory sequences of DNA. Parameters which are impossible or very hard to monitor by means of conventional biophysical methods. Quantitative information about the interactions of proteins, such as enzymes, or drugs, with nucleic acids were also provided by using these techniques. The above mentioned mechanisms inside DNA structure turned out to be dependent on a combination of mechanical and enzymatic effects.

Therefore, several single-molecule nanomanipulation methods have been developed, including Atomic Force Microscopy (AFM), Optical Tweezers (OT), Magnetic Tweezers (MT), Acoustic Force Spectroscopy (AFS), and micro-needle manipulation, where the first three are the most widespread techniques. In particular, an AFM and mostly a MT setup were used during this thesis work, both located in the biomedical and biophysics laboratory of Prof. Francesco Mantegazza, at the University of Milano-Bicocca.

On the other hand, similar issues were encountered at the cellular level, because bulk experiments of conventional microscopy techniques provide information on average only, without taking into account the intrinsic biological heterogeneity. This heterogeneity concerns different aspects of the cell life, such as gene expression, mutation rates, or cell growth and division. Traditional methods are not capable of properly measuring these stochastic processes, consequently new single-cell microscopy methods were developed. At the beginning, the most common approach for time-lapse imaging of bacteria was to grow cells on agar pads and monitor micro-colonies over time. However there were several limitations, including short time series and difficulty in tracking cell lineages, low statistics and the conse-

quent high heterogeneity. Very recent developments in microfluidics enabled to follow individual cells over a long time and under controlled conditions. During the last part of this thesis project I used one of these microfluidic devices to perform time-lapse microscopy experiments at the single-cell level. These experiments were carried out during a visiting period of seven months in Prof. Pietro Cicuta's laboratory, in Cavendish laboratory at University of Cambridge.

In the first part of this thesis I give a general overview of the experimental and theoretical framework of the research projects I worked on during the Ph.D. program. Specifically, in chapter 1 I describe the main biophysical properties of DNA, in terms of the structural polymorphism and the topological properties, reporting how it is possible to quantitatively measure DNA supercoiling and the formation of plectonemes.

In the second chapter I introduce one of the main topic of my PhD thesis, the DNA condensation. Particularly I deal with the bacterial nucleoid structure and the role of Nucleoid Associated Proteins (NAPs). After a brief description of the main proteins involved in the nucleoid organization, I focus on the dual role of the Histone-like Nucleoid-Structuring protein (H-NS), the protein I investigated during my PhD project. I studied this protein at the single-molecule level by the MT setup, in order to analyse the nanomechanics of the binding inducing DNA bridging, and at the single-cell level by time-lapse microscopy, to understand the other biological function of this protein: its regulatory role involved in gene expression (section 2.2.1). The last section of the chapter presents an overview about macromolecular crowding effects on DNA condensation.

In chapter 3 I explain the theoretical background behind the experiments of this thesis work. I introduce the polymer physics theory models necessary to analyse the experimental findings. I start from the simplest elasticity model, the FJC model, and then I describe the WLC model adopted to quantify some mechanical properties of DNA. Finally I present the models necessary to describe the supercoiling behaviour of DNA, both plectonemes formation (section 3.4) and mechanical denaturation (section 3.5).

In part II the experimental setups used for this research activity are described: firstly the magnetic tweezers setup, from the operation principles to the calibration procedures necessary to perform the typical measurements. After that, the AFM technique is briefly described as well, particularly the imaging mode used during the DNA analogue studies (see section 6.2) and to collect images of DNA in a crowded environment (paragraph 9.2.1). Finally, the experimental setup used in Cambridge for the single cell-experiments is illustrated, including details about the fluorescence microscope and the imaging

analysis tools, as well as the microfluidic system adopted to grow bacterial cells.

In the second chapter of the materials and methods part I describe the details about the investigated biological samples, from the DNA fragments and DNA ligands, as drugs or proteins, used for MT and AFM experiments, to the bacterial strains for single-cell experiments.

In the following part I present the main results obtained during my PhD. In a first chapter I discuss the nanomechanical characterization of a DNA analogue, namely DAP DNA, see chapter 6. A systematic comparison between a wild-type DNA and DAP DNA is performed, in terms of thermal stability and nanomechanical properties, measured at low and high forces. At low forces the DNA extension and bending rigidity were investigated, by using both MT and AFM, while at high forces the overstretching transition behavior was explored.

Chapter 7 shows the project concerning the study of the supercoiling behavior of DNA. High supercoiling regimes are examined to unravel the overall behaviour of DNA during some structural transitions, induced by high torsions and specific values of the force. More precisely, for negative supercoiling a left-handed form of DNA, called L-DNA, was studied, while for positive turns DNA adopts a Pauling-like structure, a lesser known form called P-DNA. A sequence dependence of the B-L-DNA transition was also explored, by studying three DNA sequences with different GC content.

The third project of this thesis concerns the interactions between anticancer drugs and DNA, see chapter 8. Particularly, three platinum-based compounds used for the cancer treatment are investigated. The analysis focuses on the mechanical modifications of DNA structure produced by these drugs interacting with DNA, how the formation of plectonemes is influenced, as well as how the extension and the bending stiffness change after the drug binding. The most interesting result is achieved from the study of the stability of DNA structure, studied both by combining conventional methods (thermal melting), and nanomanipulation techniques (MT).

The last project, presented in chapter 9, is the more extensive one and deals with the analysis of the structural role of a specific NAP, the H-NS protein. I investigate the nanomechanics of the binding mechanism between DNA and H-NS, in the bridging binding mode. I present the features of the folding process of DNA, including the hysteresis and the kinetics of this event, which reveals a step-wise process characterised by some concentration-dependent features. I run experiments in the presence of a crowding agent as well, namely PEG, in order to have a situation more similar to the crowded cellular environment. A cooperative effect between the activity of the

H-NS protein and the depletion force created by PEG is suggested by preliminary data (section 9.3).

Finally, complementary data for the H-NS role related project are presented in chapter 10, where the experiments carried out during the visiting period in the University of Cambridge are described. The aim of these experiments is to study the second biological function of H-NS: the regulatory role which seems to be mainly occurring during the DNA coating binding mode. *E. Coli* cells are monitored at the single-cell level, specifically, cell growth and gene expression are measured over several hours as response to a nutrient upshift. Gene expression is measured by the activity of a specific H-NS-regulated promoter containing a fluorescent reporter.

In part IV the presented results are discussed, by dividing them into three chapters according to the main research topics of this thesis:

- ***DNA structural polymorphism***
- ***nanomechanics of DNA-ligand interactions***
- ***the dual role of H-NS protein: DNA condensation and gene regulation***

The study of the conformational changes of DNA, namely the property of *structural polymorphism*, is addressed during the projects about the nanomechanics of a DNA analogue and the behavior of DNA at high supercoiling. The study of a DNA analogue enables to observe how a chemical modification of nucleotides can induce structural rearrangements of the double-helix, biasing towards an A-like-form of DNA. The regimes of high supercoiling, both positive and negative supercoiling, show instead how an applied torsion at a certain forces can promote the formation of plectonemes or denaturation bubbles, which are conditions that favor particular structural transitions.

The second major theme concerns the analysis of the *nanomechanics of DNA-ligand complexes*, particularly the interactions of DNA with the anticancer drugs presented in chaper 8 or with the H-NS protein and the crowding agent PEG of chapter 9. The project about the interactions between DNA and drugs clearly shows how the mechanical properties and the stability of DNA change due to the binding with compounds commonly used in clinics to treat tumors. On the other hand, the H-NS protein forms relatively stable DNA loops and influences the stability of the double helix, as well as the crowding agent. The protein binding mechanism has a preference for some DNA sequences and an unexpected concentration-dependent behavior.

The analysis of the the DNA-H-NS interactions also enables, particularly in crowding conditions, to better understand the mechanism of *DNA condensation* inside the cell, one of the biological roles of H-NS. The second important function of this NAP is the *gene regulation* studied in chapter 10. To investigate the dual role of H-NS in great detail

two complementary techniques have been combined. The nanomanipulation technique is employed to observe the structural role of H-NS and its combined activity with a crowding agent leading to a clear and abrupt compaction of DNA. Time-lapse fluorescence microscopy is instead used to study the regulatory role of the protein, more precisely the gene silencing mechanism, at the single-cell level. This activity has also a strong influence in the cell physiology, by significantly changing the growth rate of bacteria.

Part I

STATE OF THE ART

1

BIOPHYSICS OF DNA

1.1 DNA STRUCTURAL POLYMORPHISM

The double helical structure of DNA was discovered in 1953 by Watson and Crick and it was a milestone for the beginning of modern molecular biology, when researchers started to focus on the understanding of the genetic code. The discovered structure was the so called B-form, which is the most common and important DNA form, other DNA structures were identified only later. In figure 1.1(a) the structure of B-DNA double helix is shown.

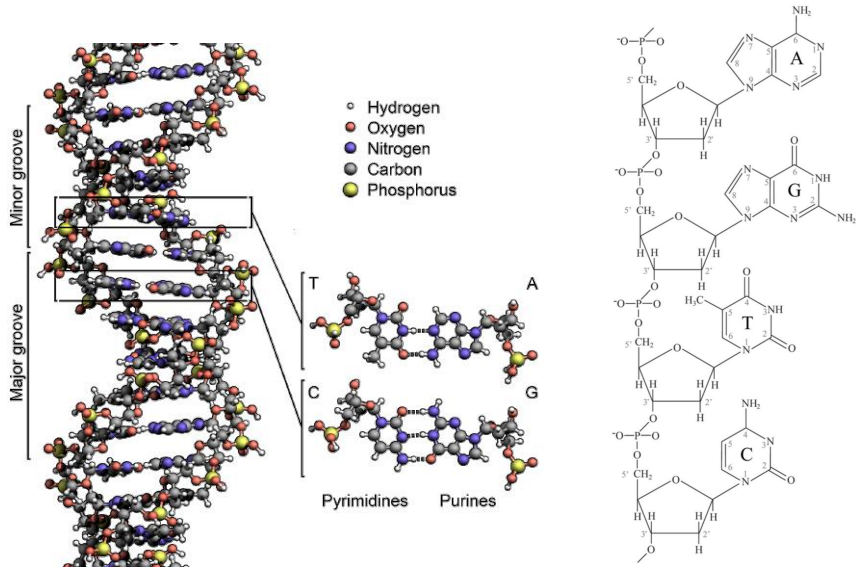

(a) (b)

Figure 1.1.: **(a)** double helix structure of B-DNA. Atoms are colour-coded as specified in the legend. Structural details of base-pairing are reported on the right. **(b)** Chemical structure of each DNA strand. Repeating units of the backbone consist of 2'-deoxyribose and a phosphate residue. The side chains are the four bases: adenine (A), guanine (G), thymine (T), cytosine (C). Figure from [1].

Despite of the great variability of genetic information that each organism carries, DNA molecules always adopt the same base-pairing rule between the two strands, sharing this structural feature with all

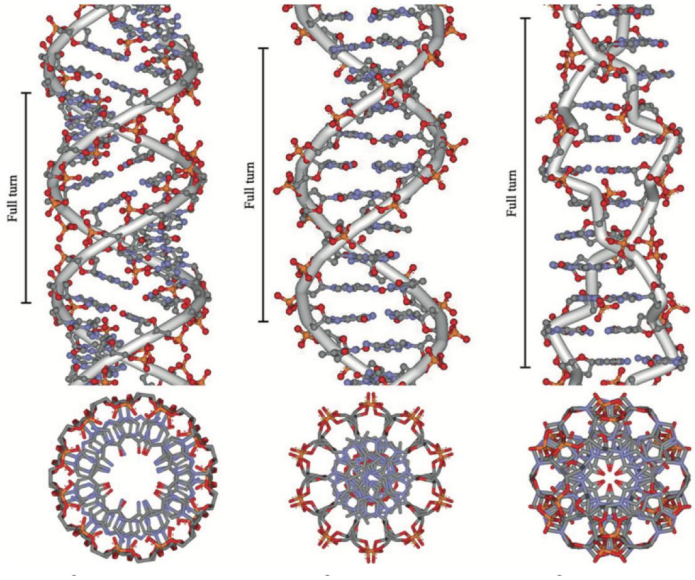

Figure 1.2.: Side and top view of different DNA conformations: A-DNA (left), B-DNA (center), Z-DNA (right). Figure adapted from [2].

double helical forms (Figure 1.2). Each DNA strand is a linear polymer consisting of a sugar-phosphate backbone of repeating units and four different bases attached to these units such as side chains (see figure 1.1(b)). A repeating unit composed of the sugar and a base is called *nucleoside*, while adding the phosphate group to a nucleoside the unit becomes a *nucleotide*. The four bases are classified in purines, *adenine* (A) and *guanine* (G), and pyrimidines, *thymine* (T) and *cytosine* (C). Adenine is always paired with thymine via two hydrogen bonds and guanine is always paired with cytosine via three hydrogen bonds, figure 1.1(a).

The double-stranded DNA (dsDNA) is a biomolecule much stiffer than artificial polymers and than most of other natural polymers [3]. This rigidity comes from two main interactions: the base-pairing, that is the hydrogen bonding between pairs, and the base-stacking, which is even more important for determining the bending stiffness. Moreover, thermal stability of DNA is widely influenced by the screening of negative charges made by the phosphate groups on the backbone.

In the following I will describe the major configurations that DNA can adopt, in terms of structural properties and biological relevance.

1.1.1 *B-DNA*

The canonical form of the DNA double helix in aqueous solution is B-DNA, a right-handed double helix where each base-pair (bp) has an angle of about 34° with the previous one [4, 5] (figure 1.2, center). The helical period is approximately 10.5 bp per turn and the helix rise is ~ 0.34 nm per bp, while the external diameter of the double helix is

about 2 nm [1, 6–8]. The two complementary strands have an antiparallel orientation and base pairs are located in the inner part of the helix while backbones are outside. B-DNA double helix is not perfectly symmetrical, indeed it has two distinct grooves, a major groove 12 Å wide and a minor groove 6 Å wide, see figure 1.1(a). The geometry of the grooves has a very important biological role, because there are several proteins or drugs that recognize specific sites on DNA through the binding with these grooves [9]. The interactions involved in double helix stability, the above mentioned base-pairing and base-stacking interactions, confers a very high rigidity to B-DNA, quantified by a *persistence length* (see section 3.3) of about 50 nm, which is about fifty times larger than that one of artificial polymers, such as polystyrene.

1.1.2 *A-DNA*

A-DNA (figure 1.2, left) is another right-handed double helix with the two complementary strands antiparallel, but the helix is shorter and the diameter larger compared to B-DNA. The canonical B-DNA turns into the A-form under dehydration conditions or as a result of the interactions with some proteins [8, 10–13]. This structure is similar to the double-stranded RNA as well, indeed dsRNA cannot adopt B-DNA helix [5, 11]. A-DNA has an helical period of 11 bp/turn, an helix diameter equal to 2.3 nm and the helix rise is 0.25 nm/bp. The twist angle between base-pairs is smaller than that one of B-DNA, in A-DNA it is around 32°. More recently, it has been observed that GC-rich sequences can favor the A-DNA configuration [14, 15]. The authors showed CD spectra suggesting an A-type base-stacking, confirming previous literature findings [16–18], but they did not find relevant differences in terms of the mechanical properties explored by force spectroscopy experiments at the single molecule level.

1.1.3 *Z-DNA*

Z-DNA is a double helical structure dramatically different from the previous two: firstly, this double helix is left-handed and its repeating unit consist of two base-pairs rather than one. The backbone is not a continuous line but zigzags, hence the name Z-form, see the yellow helix in figure 1.2 (right). This structure was first discovered in the '70s by CD spectra [19, 20] and later confirmed by X-ray crystallography [21, 22]. The helical period is 12 bp/turn with an helix rise of 0.37 nm/bp and the diameter is 1.8 nm [1, 10, 11]. Z-DNA is the perfect example of how an alternative dsDNA structure can be different from the conventional B-DNA. The DNA double helix can barely adopt the Z-form, only at very high concentration of sodium or with multivalent ions [23]. Under physiological conditions it is

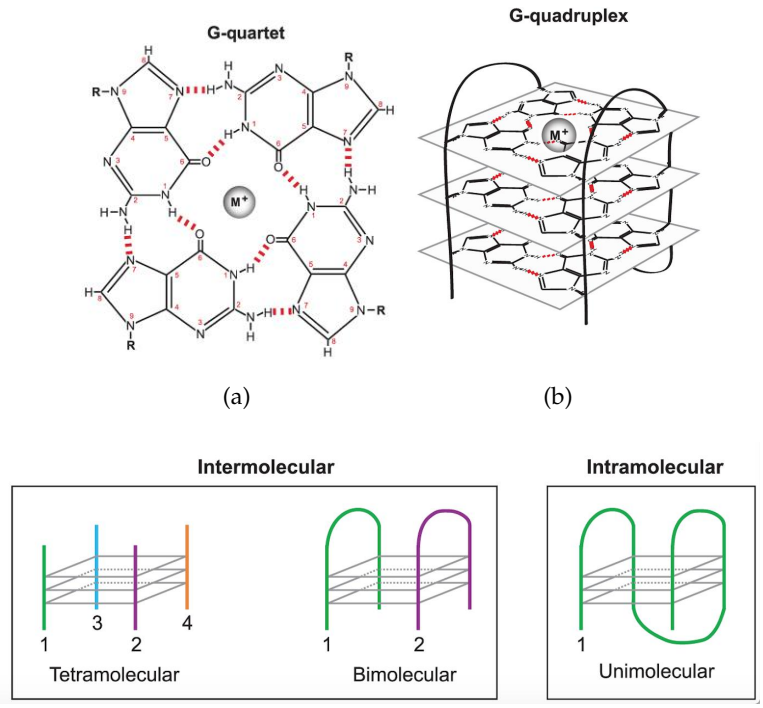

Figure 1.3.: **(a)** Planar structure of a G-quartet with the monovalent cation (M^+) in the middle. Hydrogen-Hoogsteen bonds are shown in red. **(b)** An example of a G-quadruplex structure composed of three G-quartets planes. **(c)** Types of G-quadruplex structures, depending on the number of strands involved. Figures adapted from [**?**].

very difficult to make the B-Z transition, because the rotation of base-pairs has an high energy cost. Nevertheless, with the help of a single molecule technique, namely Magnetic Tweezers, that can apply a torque and induce a negative supercoiling to the DNA molecule, it has been possible to facilitate the transition towards the Z-form in GC tracts [24, 25]. Indeed the most favorable sequences for Z-DNA are GC repeats, as verified by theoretical models as well [26]. The biological function of this structure is still debated, but it can likely have effects on transcription or have a role in absorbing DNA torsional stresses.

1.1.4 *G-quadruplex*

As mentioned above, guanines are the most versatile bases to adopt alternative DNA structures. Single-stranded DNA (ssDNA) with G-repeats can adopt a G-quadruplex conformation in presence of monovalent cations, in particular with potassium. G-quadruplexes are four-stranded structures consisting of a stack of planar G-quartets, see fig-

ure 1.3(a). The biological interest in these structures raised when G-rich tracts were found in human telomeres. Following studies showed that G-quadruplexes are present also in many other situations, with the possibility of becoming useful as therapeutic targets [1, 27]. Guanines in G-quartets planes are held together by *hydrogen-Hoogsteen* bonds, figure 1.3(a)-(b), and the quadruplexes can display a great variety of topologies, depending on loop size and sequence, as sketched in figure 1.3(c). These different topologies can be distinguished by X-ray crystallography and CD or NMR spectroscopy [28]. Negative supercoiling facilitates the formation of G-quadruplex structures, for this reason numerous studies by means of nano-manipulation techniques have been carried out, unravelling the kinetics of folding and unfolding pathways [29–31]. Single molecule FRET is another method of choice to study these structures, as reported in [32].

1.2 DNA TOPOLOGY

Topological properties of DNA double helix firstly came from the multiple interwinding of the two strands around each other. A DNA fragment in which the free rotation of its ends is forbidden is called *topological domain*. The simplest example is the circular DNA, found in most bacteria and viruses, figure 1.4(a). In eukaryotic chromosomal DNA has a linear geometry but it forms large loops representing topological domains. The existence of closed circular dsDNA was discovered in polyoma virus by Dulbecco and Vinograd in the mid-60s [33, 34]. Vinograd and co-workers extracted small circular DNA molecules from viruses, realizing that these compact structures corresponded to superhelical turns of dsDNA. It turned out that these topological domains can be disrupted only by breaking the DNA strands and that negative supercoiling promotes DNA double helix opening [35].

1.2.1 *The linking number*

To quantitively describe DNA topology it is necessary to introduce a parameter called *linking number* (Lk). The Lk can be intuitively defined as the algebraic sum of the number of times a DNA strand crosses an imaginary surface whose contour is the other DNA strand, see figure 1.4(b) [36]. By convention, the Lk of a right-handed closed circular DNA is positive. From Lk definition two important characteristics directly follow: Lk is an integer and it is topologically invariant, i.e. it cannot change as a consequence of deformations of DNA strands.

Lk is a quantity close to N/γ, where N is the total number of base-pairs (bps) while γ is the helical period, the number of bps per turn.

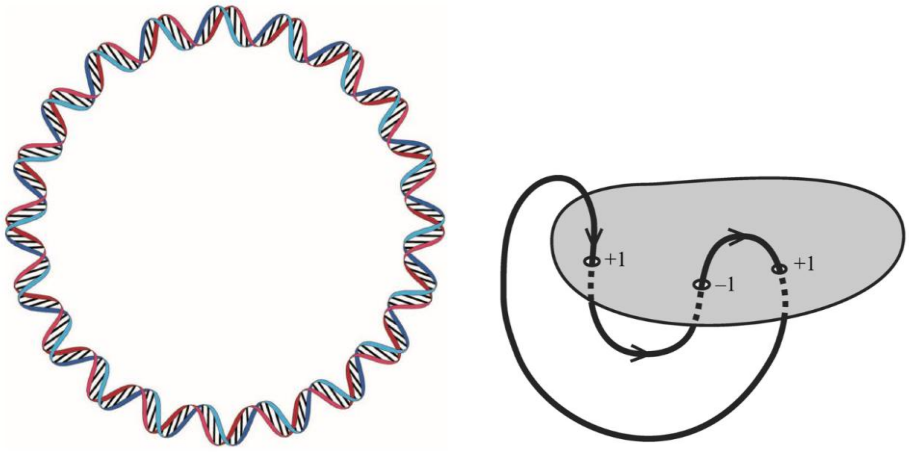

(a) (b)

Figure 1.4.: **(a)** Sketch of a circular closed DNA. This structure represents a topological domain and can be separated only by breaking one of the two strands. **(b)** Imaginary surface for Lk definition. In this example $Lk = +1 - 1 + 1 = 1$. Figures adapted from [1].

It is possible define the linking number for a relaxed DNA molecule (Lk_0) as

$$Lk_0 = \frac{N}{\gamma} \tag{1.1}$$

However, the natural situation is usually different: the double helical structure enables DNA to be overwound or underwound, which may induce the formation of condensed superstructures, such as plectonemic supercoils or solenoidal superhelices (figure 1.5). In general, DNA *supercoiling* affects structural transitions and DNA-ligand interactions. For example, DNA has to be locally underwound during transcriptional and recombinational repair processes, and the strong compaction in chromosomes requires a supercoiled DNA. Therefore, DNA supercoiling is defined in terms of a *linking number difference*

$$\Delta Lk = Lk - Lk_0 = Lk - \frac{N}{\gamma} \tag{1.2}$$

When $\Delta Lk < 0$ DNA is negatively supercoiled and clearly when $\Delta Lk > 0$ DNA is positively supercoiled. The term 'supercoiling' reminds the shape and the size of these DNA structures: they look like a normal DNA helix coiled into a larger helix of a higher order. The plectonemic configuration is typical of procaryotes such as bacteria, while solenoidal supercoils are characteristic structures in eukaryotes where DNA is wrapped around histone proteins (figure 1.5).

A more useful quantity to define the DNA supercoiling is the *superhelical density* σ

$$\sigma = \frac{\Delta Lk}{Lk_0} = \frac{\gamma \Delta Lk}{N} \tag{1.3}$$

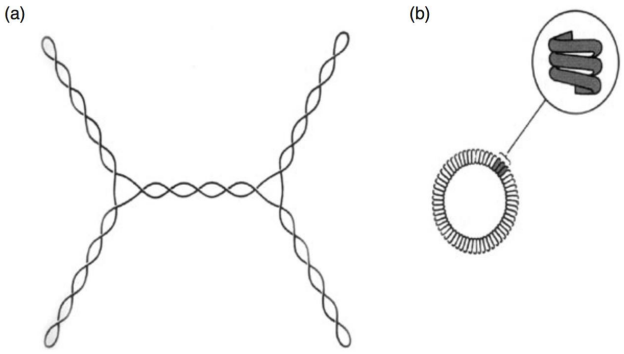

Figure 1.5.: Tertiary structures of supercoiled DNA: **(a)** plectonemes on a supercoiled plasmid. **(b)** solenoidal structure. Figure from [3].

σ is more often used because it is independent on DNA extension and consequently it is more convenient to compare different molecules. The circular DNA isolated from living cells has a slightly negative value of σ, varying between -0.03 and -0.09 [1].

Supercoiling can be applied to a DNA molecule in two ways: by changing the twist and by wrapping DNA molecular axis around itself. These two geometrical properties are analytically expressed by the following quantities: the *Twist* (Tw) and the *Writhe* (Wr) respectively. The first and complete mathematical description was given by White in 1969 [37], with the following theorem linking the three topological quantities above introduced

$$\mathrm{Lk} = \mathrm{T}w + W\mathrm{r} \tag{1.4}$$

note that, as already mentioned, Lk is an integer topologically invariant, while Tw and Wr are not, since they can easily and smoothly change depending on the environmental conditions. Fuller introduced the ribbon theory to mathematically describe DNA topology two years later White's theorem [38].

1.2.2 *Measuring the supercoiling*

DNA supercoiling can be quantitively probed by means of some recent nano-manipulation experiments. In particular the magnetic tweezers, the technique I used for most of this thesis work, are the method of choice to study DNA topology [39, 40]. Indeed, as explained in the Introduction and in detail in section 4.2, a magnetic tweezers setup can easily apply a torsion to DNA single molecules, in addition to forces in the range of pN. Since DNA molecules are torsionally constrained between a chamber and a magnetic bead, the rotation of the magnets in the MT setup induces an over- or underwound supercoiled state in DNA: in figure 1.6 a typical MT twisting experiment is reported, while in figure 1.7 a plectonemic structure is shown, as simulated by a realistic coarse-grained DNA model.

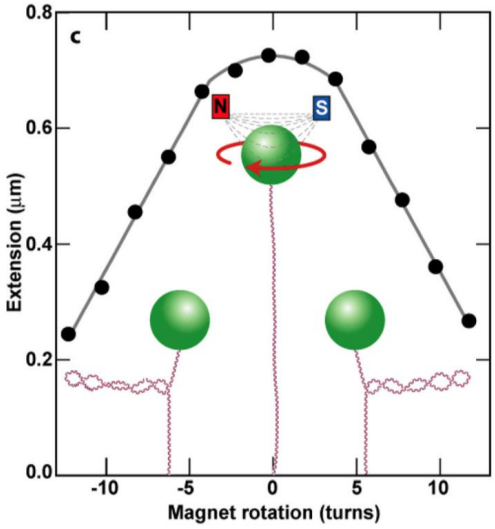

Figure 1.6.: MT twisting experiment at low forces ($F < 0.5\,pN$). After a specific number of turns, the so called buckling number, the DNA molecule starts to forms loops, the plectonemes. In this low force regime the DNA behavior is symmetrical. Figure adapted from [40]

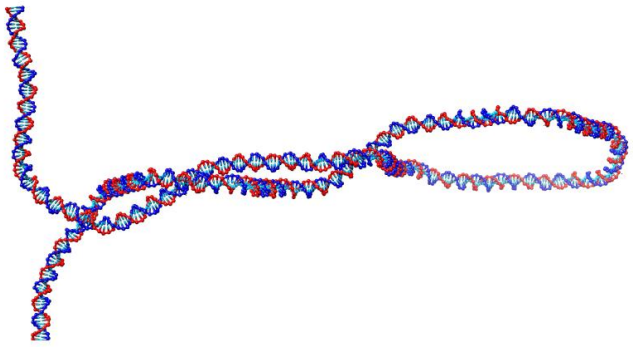

Figure 1.7.: DNA plectoneme simulated by the coarse-grained model OxDNA, developed by T. E. Ouldridge, J. P. K. Doyle and A. A. Louis at University of Oxford [41, 42].

For this reason, one of the first applications of MT technique was the study of DNA topology and topoisomerases [43–47]. The activity of the enzyme can be finely assessed in real time by using a MT setup, with a sensitivity at the single molecule level not achievable by other techniques. A very elegant example is the study carried out by N. H. Dekker and co-workers in [48], where the relaxation of plectonemic supercoils by a topoisomerase has been shown to be a step-wise mechanism with a significantly force-dependence (figure 1.8). In a following interesting work [49], the same authors showed the activity of topoisomerase in combination with a potent anticancer drug, resulting in an asymmetrical supercoil relaxation observed in vivo as well.

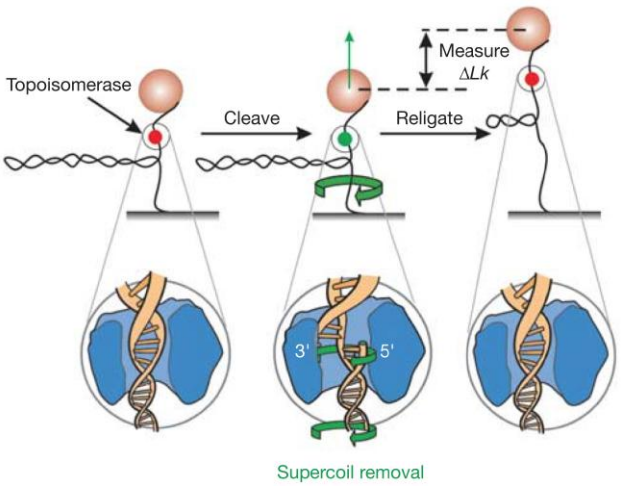

(a)

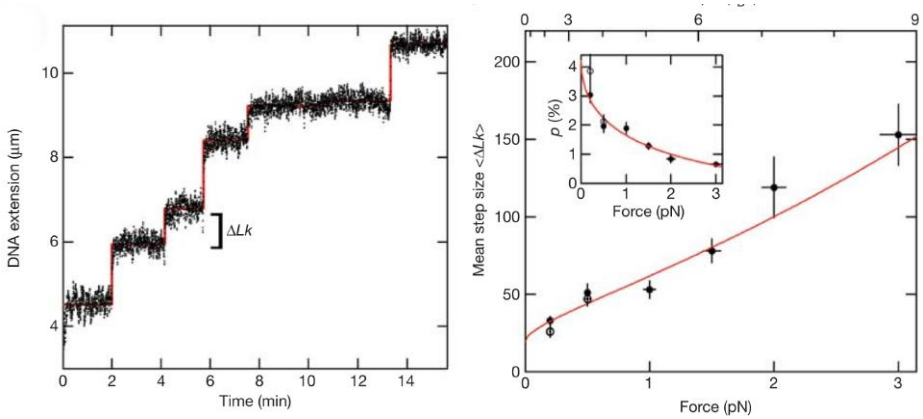

(b) (c)

Figure 1.8.: Single-molecule assay for measuring DNA supercoil relaxation by topoisomerase. **(a)** Type 1B topoisomerase is bound non-covalently to a supercoiled DNA molecule.
(b) Real-time enzymatic activity. Each time TopIB removes supercoils from the DNA, a step is observed in the DNA extension.
(c) $\langle \mathrm{Lk} \rangle$ as a function of applied force and torque. Black circles represent data and red line show the fit. The inset shows the force-dependence of the probability p of TopIB to religate DNA. Figures adapted from [48].

MT has been employed to explore the activity of other enzymes involved in DNA topology, such as helicase [50, 51].

In general, DNA topology has been deeply investigated by means of magnetic tweezers, with the possibility of inducing conformational changes. For example by applying an extremely negative supercoiling to the DNA molecule, a transition to a left-handed DNA occurs. This left-handed double helix is probably the Z-DNA or a structure characterized by a very similar helicity. See for example the twisting experiments carried out at different forces reported in figure 1.9: the slope around $\sigma \approx -1.9$ corresponds to the formation of plectone-

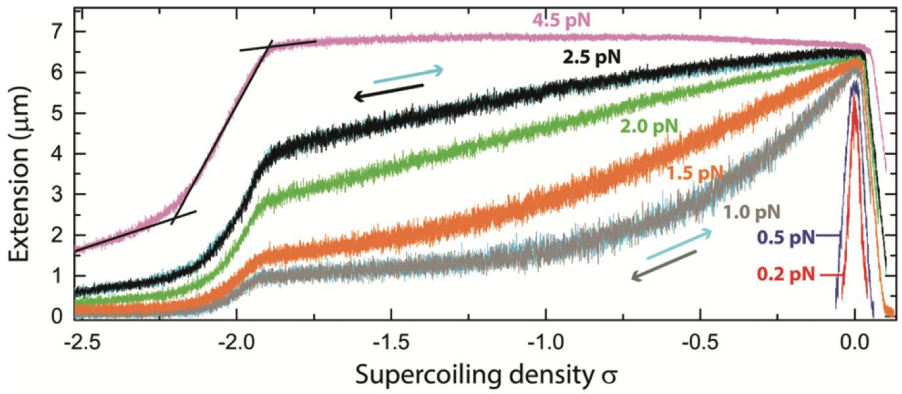

Figure 1.9.: MT twisting experiment in the high supercoiling regime at forces between 0.2 and 4.5 pN. At 1.0 and 2.5 pN the overlapping forward (respectively grey and black) and backward (light blue) trace show the absence of hysteresis. The black lines on the curve at 4.5 pN show how the buckling points are determined. Figure from [52].

mic loops in a left-handed DNA form. These data are taken from a study in which authors experimentally investigated the DNA phase-diagram by using a magnetic tweezer setup in horizontal geometry coupled with a fluorescence system [52].

The transition in figure 1.9 is related to negatively supercoiled DNA molecules, but a conformational transition at highly positive supercoiling has been observed as well, towards a right-handed Pauling-like structure called P-DNA [53]. However, the required forces to form the right-handed P-DNA are much higher compared to the left-handed double helix (see chapter 7).

2

DNA CONDENSATION

DNA has to be organized and highly compacted in the cell in order to store and replicate genetic information. This feature is in common with all three domains: eukarya, bacteria and archaea [54]. Several proteins have the important role of regulating the organization and the structure of the genetic material and they have been found in each kingdom of life. In Eukaryotes these functions are performed by very well known proteins, called *histones*, while in bacteria and archaea these tasks are carried out by a class of proteins called *nucleoid-associated proteins (NAPs)*, that are less known and understood, in particular archaeal NAPs [55, 56]. Actually, the storage and processing of genetic information is controlled by many players which can modify DNA structure. Supercoiling is a perfect example of a DNA property involved in DNA condensation, in particular for bacterial chromosome, where DNA is coiled in plectonemic loops and confined in tiny volumes by stabilising these superhelical structures with bridging proteins, such as H-NS (see section 2.2). Another important agent in DNA packing is the macromolecular crowding, and in this thesis project the effects of a crowding agent on DNA by will be addressed as well (section 2.3).

In particular, I investigated the DNA condensation mechanism in terms of the role of a specific NAP involved in bacterial (*E. coli*) nucleoid structure and organization. This protein is the H-NS protein and I studied both its structural and epigenetic regulatory functions, by means of two completely different but complementary techniques.

2.1 BACTERIAL NUCLEOID STRUCTURE AND NAPS ROLE

There is a number of nucleoid-associated proteins and some of them are not yet well known. In general, NAPs are architectural proteins, since they can induce DNA condensation and vary chromosome organization. These proteins have binding sites in the range of 10-30 bps and they interact with DNA by different binding mechanism, such as bending, bridging or wrapping the double helix. NAPs can also influence the trascriptional activity, in a positive or negative way, it depends on the environmental conditions as well as on the protein.

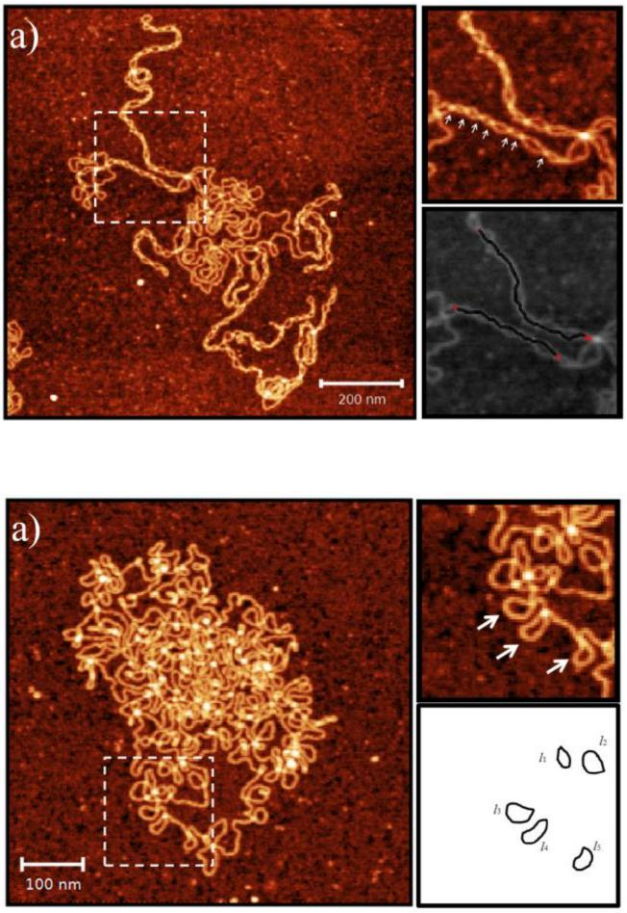

Figure 2.1.: AFM images of H-NS-DNA **(a)** and HU-DNA **(b)** complexes. **(a)** H-NS-DNA superstructure has a periodicity, as shown in the image zoom on the top right, whereas AFM tracking analysis of the filaments is reported on the bottom right. **(b)** HU-DNA complex has an ordered structure consisting of loops, as it is possible to observe on the top right. On the bottom right there is the analysis of loops length. Figures from [57].

First of all, it has been observed that the presence of supercoiled DNA structures, such as plectonemes, is strongly related to the regulation of gene expression. Negative supercoiling of looped domains is needed to reduce the size of the folded bacterial chromosome and it is induced by topoisomerases and locally by the activity of DNA and RNA polymerase [54]. In this scenario, the role of NAPs is to constrain DNA supercoils, thus varying the global level of DNA superhelical density. In figure 2.1 a couple of examples of DNA superstructures formed by the interaction with a NAP are reported, in particular with the H-NS protein (a) and the HU protein (b). The stabilization of these looped structures is of key importance because the activity of many promoters is very sensitive to the local level of supercoiling.

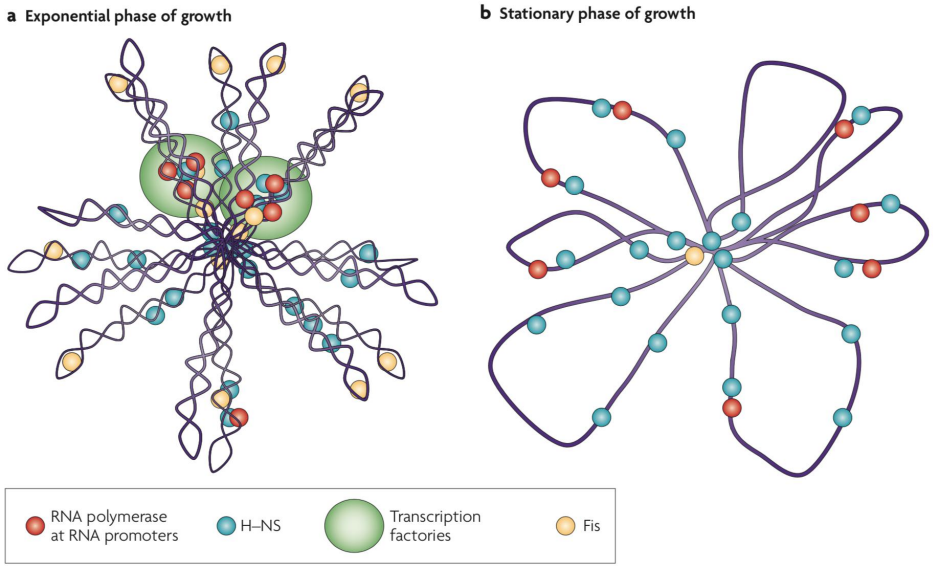

Figure 2.2.: Bacterial nucleoid structure organization during exponential **(a)** and stationary phase **(b)**.
(a) DNA looped domains are negatively supercoiled and the massive presence of NAPs such as H-NS and Fis bound to DNA helps the maintenance of these superstructures. NAPs are associated with other compounds as well, like ribosomal RNA operons.
(b) In this phase most of supercoiled structures are relaxed and Fis is almost absent. Figure adapted form [54].

Moreover, trascriptional activity drastically changes depending on the physiological state of the cell: for example there is an higher activity when bacteria grow fast, in exponential phase, while during a slow growth, as in the stationary phase, there is a relaxation of supercoiled structures and a reduction of the regulatory activity (figure 2.2). The role of cell growth rate in the nucleoid organization will be explored in chapter 10, where single-cell experiments are presented and the gene expression is monitored during a nutrient upshift, that is to say an enrichment of the growth medium.

2.1.1 *NAPs classification*

In this paragraph I am going to briefly describe a few NAPs, illustrating the main properties of the binding mechanisms with DNA and citing some examples of studies reported in literature. The next section is instead entirely focused on H-NS, the protein investigated in this thesis project.

HU: this protein consists of two subunits, HUα and HUβ, and which adopts two forms (homodimer or heterodimer) depending on the bacterial phase. HU-DNA binding mechanism seem to be non-

specific, with a preference for bent DNA regions. HU interacts with topoisomerase I, thus altering DNA superhelicity and influencing both nucleoid structure and gene expression. This NAP can form octameric forms where DNA can be wrapped, as shown in the crystal structure of a modeled DNA-protein spiral structure (figure 2.3). Finally, HU binding mode changes according to the protein concentration: if the concentration is low, the DNA flexibility is increased by reducing the bending stiffness, while at higher concentration the stiffness is increased. These effects are crucial for plectonemic loops formation and therefore for chromosome organization. In [57] authors showed that at low HU concentrations DNA plectonemic structures are partially opened, while increasing the protein concentration the HU-DNA complex form an ordered lattice-like structure with several loops, preferentially left-handed, see figure 2.1(b). Moreover DNA Young modulus decreased of about 75-80% in presence of HU. Another interesting work characterized the kinetics and the thermodynamics of DNA looping induced by a combined effect of Gal repressor and HU protein [58].

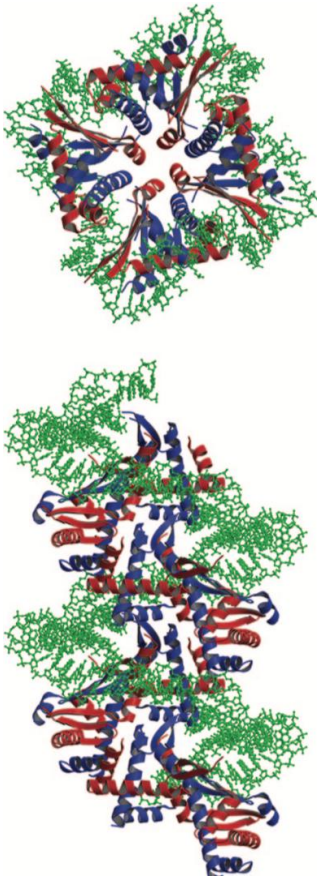

Figure 2.3.: Top and side view of left-handed HU$\alpha\beta$ octamer with DNA double helix as spiral repeating unit. The α-subunit is red and the β-subunit is blue. Figure adapted from [59].

IHF: the Integration Host Factor is a protein with two subunits (α and β) and an amino acid sequence very similar to HU, but despite this it has a different binding mechanism with DNA. Firstly, IHF has sequence specific binding sites and promotes the formation of *U-turn* in DNA structure, see figure 2.4 for IHF structure details. The predominant form of the protein is the $\alpha\beta$ heterodimer. This NAP has also effects on trascriptional activity by means of DNA bending, which can help the contact between regulatory proteins. The deformation of DNA helix by bending it has another important role: prevent the formation of single-stranded DNA bubbles at the IHF binding site [60]. This mechanism occurs through the transfer of the torsional stress collected in supercoiled DNA to the neighbouring regions. In summary, the U-turn structures introduced by IHF into the DNA helix not only merely af-

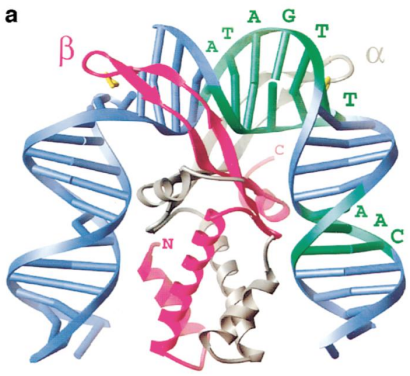

Figure 2.4.: Crystal structure of IHF protein: α-subunit is white while β-subunit is pink. IHF-binding site is shown in green. It is possible to notice that the arm of α and the body of β are the main interacting parts. Figure adapted from [61].

fect the nucleoid structure, but the transcription and the chromosome replication are influenced by the protein activity as well [54].

DPS: Dps, namely DNA Protection during Starvation protein, is a ferritin-like protein involved in cellular responses to stress, such as oxidative, thermal or pH schocks [62, 63]. This NAP is highly expressed during stationary phase, when DNA should be protected, but its effects on trascriptional activity are still largely unknown. Dps forms a dodecamer unit that binds both supercoiled and linear DNA structures. This compact protein structure implies relevant Dps-Dps interactions, see figure 2.5.

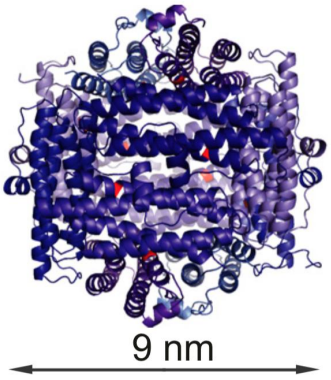

Figure 2.5.: Dps dodecamer shell-structure. The size is between 8 and 9 nm. Figure adapted from [63].

The affinity of Dps for DNA is influenced by buffer conditions: the presence of higher salt concentrations promotes DNA-protein binding, but divalent cations such as Mg^{2+} weaken the binding. The mechanism of DNA-Dps binding has been recently investigated in detail and in real-time by single molecule experiments [63]. The authors observed the kinetics of the DNA-protein complex formation with a fluorescence assay and a magnetic tweezers setup. The main conclusion of this work is the presence of an hysteresis in the formation of the Dps-DNA complex and the cooperativity of the binding mechanism. DNA compaction by Dps is a rapid event and independent on the protein concentration, but it is influenced by buffer

conditions, as mentioned above, and in particular by macromolecular crowding. Indeed, the addition of PEG8000 increased the stability of the Dps-DNA complex. This is interesting for the present discussion, because I studied the crowding effects on DNA-protein interaction as well, observing very similar effects in my case with the H-NS protein (see section 9.2).

FIS: this protein has been extensively studied because of its important role in gene regulation and chromosome organization. It usually has a specific AT-rich binding site ranging from 17 to 21 bp [54, 64], with heterodimer as predominant form, see figure 2.6(a) for Fis dimer crystal structure. Fis interactions consist in the bending of DNA double helix and it has been shown that DNA is unwinded in Fis-DNA complexes, particularly at high concentrations [57], see figure 2.6(b). In addition in the same work, the authors showed how Fis gradually decreases DNA stiffness, measured by AFM imaging experiments. The influence of Fis on the trascriptional activity largely depends on the position of the binding site in relation to RNA polymerase location [54]. A possible binding mechanism is the one already described for IHF protein, the displacement of the torsional stress, whereas another example of Fis binding mode is the maintenance of a micro-domain of negatively supercoiled DNA. Marko, Johnson and co-workers revealed an interesting non-monotonic behavior of Fis effects on DNA condensation as a function of the protein concentration [65]. Same authors tried to quantitatively explain the binding mechanism of Fis and HU protein as well by using a thermodynamic Maxwell relation: their model worked fairly well for HU, while for Fis the agreement with data is not perfect, validating the presence of more complex superstructure ins Fis-DNA complexes [64].

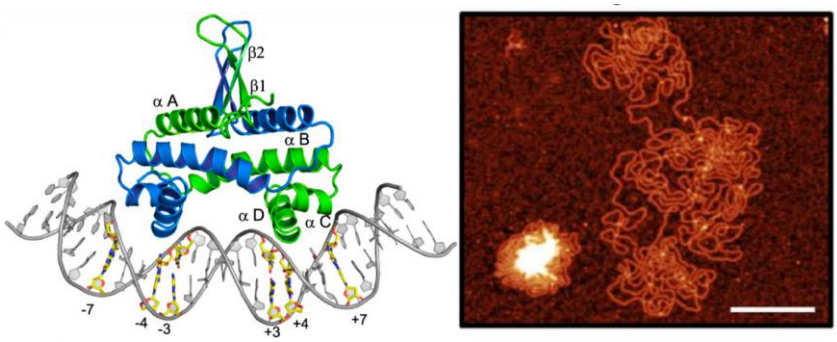

(a) (b)

Figure 2.6.: **(a)** Fis-DNA complex crystal structure. Fis dimer binds to the specific binding site, whose important bases are shown in yellow. Figure from [66]. **(b)** AFM images of Fis-DNA complex: the protein unwinds plectonemic superstructures and condense DNA into simple plectonemes. Figure from [57].

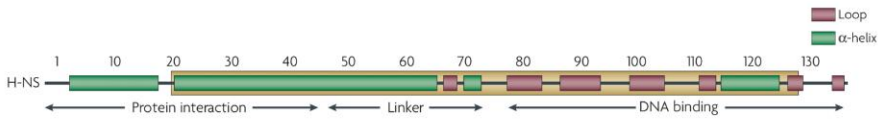

(a)

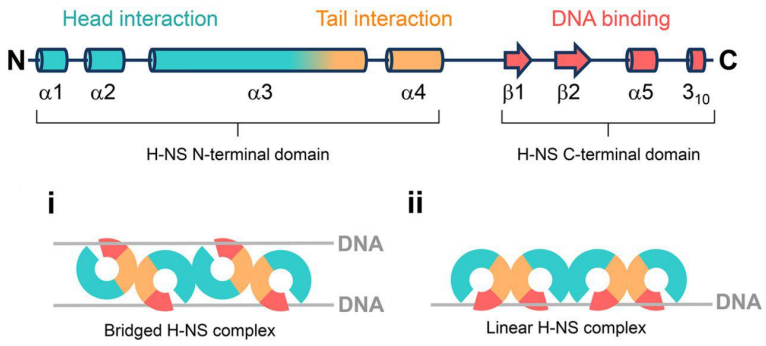

(b)

Figure 2.7.: **(a)** H-NS amino acid sequence. The related secondary structures for each domain are reported as well. Figure adapted from [54]. **(b)** Structure of H-NS protein, including details about each domain: the N-terminus has four α-helices for protein oligomerization. The formation of H-NS dimers can occur by head-to-head interaction (blue) or tail-to-tail interaction (orange). The C-terminus, the DNA binding domain, consists of two β-sheets, an additional α-helix and a 3_{10} helix. Figure from [69].

2.2 THE DUAL ROLE OF H-NS PROTEIN

The family of NAPs called Histone-like Nucleoid Structuring protein (H-NS) is widespread in bacteria. The origin of this name comes from the role of these proteins: they are prokaryotic proteins equivalent to the histones in eukaryotes, namely they compact and organize the chromosomal genome. The protein I studied during this work, the H-NS protein from *Escherichia Coli (E. coli)*, is one of the most studied and characterized proteins of this family. It is a small protein of 137 amino acids and 15.5 kDa, it is composed of a C-terminal domain as DNA-binding part and an N-terminus involved in protein dimerization, a flexible linker connects these two domains [54, 67–70], see figure 2.7. The binding domain consists of two α-helices and two β-sheets and displays a loop which is crucial for the binding to the minor groove of DNA. AT-rich DNA sequences exhibit a narrower minor groove, this is probably the reason of their higher affinity for H-NS. Indeed H-NS does not have a specific binding site but the binding with AT-rich DNA sequences is strongly favoured [71, 72]. On the other hand, the N-terminal domain is organized into four α-heices. The interactions between these helices enables the formation of H-NS dimers, a protein conformation which has been demonstrated to be fundamental for the proper protein functionality [73].

H-NS protein has two different biological roles: the first one is a structural role, the already mentioned condensation of DNA into the bacterial nucleoid, the second one is a regulatory role, i.e. the protein is involved in gene expression regulation, more precisely gene silencing functions [74, 75]. Nano-manipulation techniques enabled to investigate more carefully the structural and conformational deformations induced on DNA by the H-NS protein [76–78]. It has been found that the binding mechanism of H-NS promotes the formation of DNA bridges, this is the so called *bridging binding mode*, involved in the structural role of DNA compaction. This mechanism was clearly explained by Dame and co-workers in 2006 [79]: they used four optical traps [80] to monitor extension changes of two DNA molecules, see figure 2.8(a)-(b). They observed the kinetics of the formation of bridges between these two DNA molecules in presence of H-NS dimers, by means of dynamic force spectroscopy experiments [79]. However, in 2003 magnetic tweezers force spectroscopy experiments did not reveal the formation of condensed DNA structures due to interactions with H-NS [81]. On the contrary, authors observed an increment of DNA bending rigidity as the H-NS protein concentration in solution increased, the so called *stiffenening/coating binding mode*, see figure 2.8(c)-(d).

The explanation for these two completely distinct binding mechanisms belonging to the same protein came in 2010 by Yan group [82]. They noticed that in the previous works authors used two slightly different buffer solutions, in particular the main difference was the presence of Mg^{2+} in Dame's work, while in magnetic tweezers experiment it was absent. It turned out that the switch between the two binding modes is exactly the presence of a divalent cation, such as Mg^{2+} or Ca^{2+}. Yan and co-workers measured force-extension curves of DNA single molecules at different H-NS concentrations in both buffer conditions, with or without Mg^{2+}. They analyzed the temporal dynamics of DNA folding and unfolding in presence of H-NS, by tuning the concentration of $MgCl_2$: if $C_{MgCl_2} < 5\,\text{mM}$ DNA stiffening is observed, while if $C_{MgCl_2} > 5\,\text{mM}$ DNA bridging (folding) occurs. In the stiffening binding mode the saturation was reached at a protein concentration of about 600 nM, and an increase in KCl concentration reduced the H-NS effect. Considering the bridging binding mode, the folding force values were very similar at every protein concentration, and KCl had only a slight effect, weakening the H-NS interaction with DNA at higher KCl concentration (150 mM).

In a following paper the same authors showed the effects of both H-NS binding modes on DNA supercoiling. They used a magnetic tweezers setup to apply a torsion to DNA single-molecules [83]. As expected, the bridging binding mechanism promoted and stabilized the formation of plectonemes, whereas the stiffenining mode, by con-

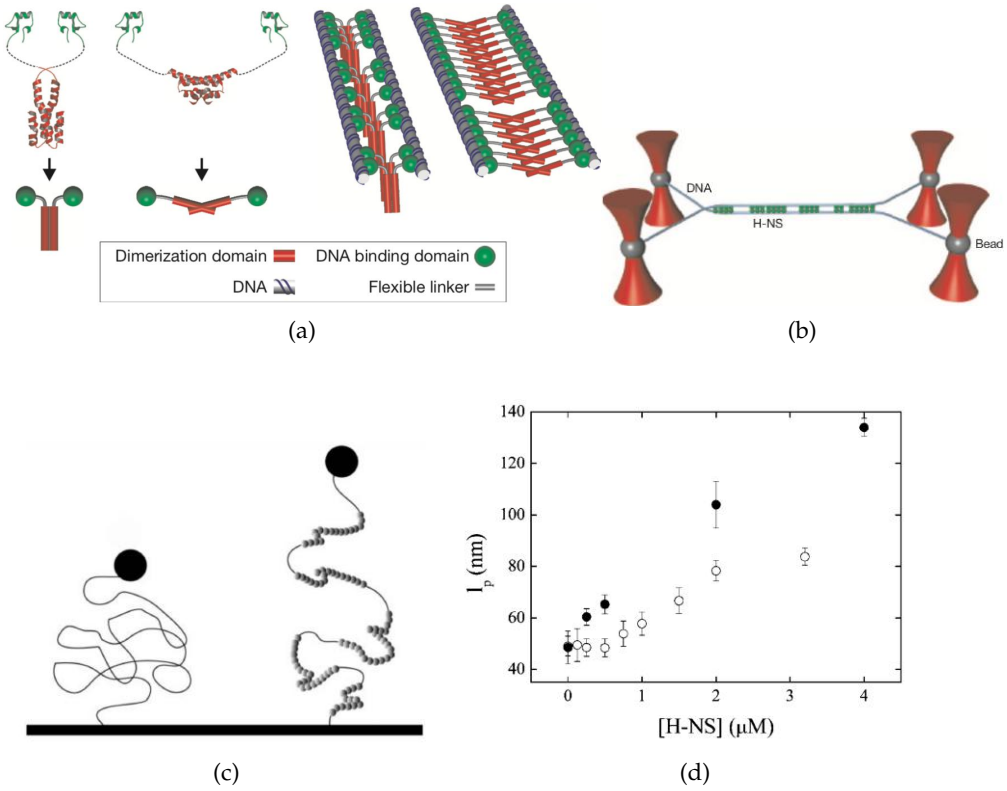

Figure 2.8.: **(a)** Hypothetical H-NS dimer structure in parallel (left) and anti-parallel (right) configuration. **(b)** H-NS bridging interaction with two DNA molecules. Figures from [79].
(c) Schematic representation of bare DNA and H-NS-DNA complex in the coating binding mode during an MT experiment. **(d)** Measurements of DNA persistence length (l_p) as a function of H-NS concentration. Solid circles for 50 mM KCl, open circles for 200 mM KCl. Figures from [81].

trast, suppressed DNA supercoiled structures. A summary of H-NS effects is reported in figure 2.9 .

Finally, some AFM microscopy experiments showed interesting modifications on DNA properties because of the interactions with H-NS, clearly visible AFM images. In the above cited work [57], the authors noticed that at low H-NS concentrations the protein stabilized simple plectonemes by unfolding DNA supercoiled structures, while at higher concentrations DNA molecules are organized into periodic superstructures characterized by a precise helicity of about 20 nm, see figure 2.1(a). Moreover H-NS quickly increases DNA stiffness by a factor ranging between 10% and 50%. Yan group exploited H-NS binding mechanisms by means of AFM as well. In [84] they studied the H-NS protein from *Pseudomonas aeruginosa*: they analyzed the conformations of DNA-H-NS complexes in a wide range of protein concentration. Specifically, they identified a loop and a stem structure, clearly visible from the images at the highest H-NS concentration (3 μM), see figure 2.10.

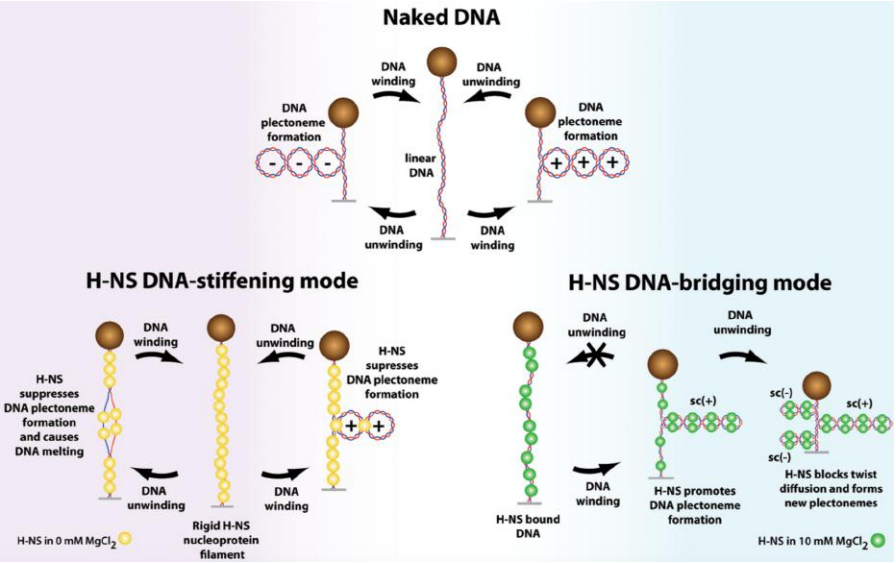

Figure 2.9.: Diagram of H-NS effects on DNA supercoiling, proposed in [83]. Top: formation of negative or positive plectonemes by unwinding and winding a DNA molecule respectively. Bottom left: H-NS in stiffening mode suppresses the formation of plectonemes, but DNA melting is induced by unwinding. Bottom right: bridging mechanism promotes the formation of new DNA plectonemic structures.

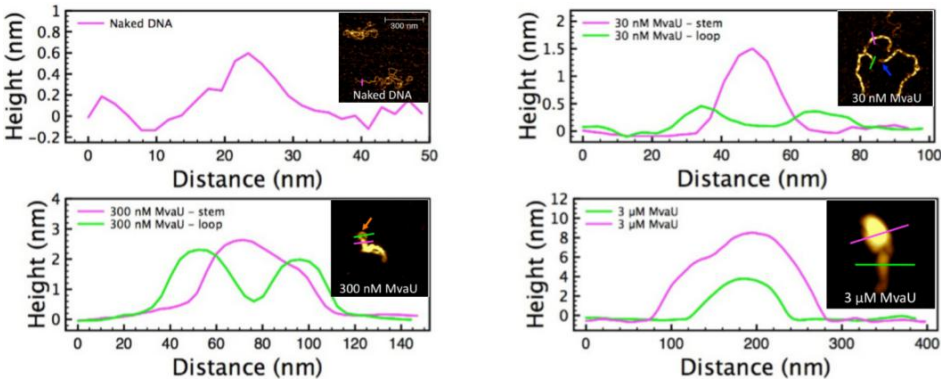

Figure 2.10.: Height of the structures formed by DNA-H-NS complexes at various protein concentrations. The height is extracted from the line profiles indicated in green (loop) and magenta (stem or bare DNA). In the insets examples of AFM images are reported. Figure adapted from [84].

2.2.1 *Regulatory role of H-NS*

As mentioned above H-NS is an abundant prokaryotic protein, present in approximately $20,000$ copies per genome equivalent. This NAP plays two crucial roles in biology, not only the already described DNA condensation , but also the global transcriptional regulatory function, more precisely H-NS has been identified as a gene silencer mostly for horizontally transferred genes [74, 75, 85].

The general idea in literature is that the H-NS activity of binding and affecting several genes is likely due to its preference for specific regions of the genome. These DNA sections usually have a planar curvature associated to AT-rich motifs, commonly found close to bacterial promoters [86]. A number of studies identified the genes where H-NS preferentially binds in different genomes (e.g. *S. typhimurium*, *E. coli*, *V. cholerae*, *S. flexneri*) and all the results agree that these genomic regions have high AT content [87–90]. Here, there are pathogenicity islands encoding many virulence proteins. As a consequence, the following hypothesis has been proposed: the H-NS protein has the biological role of silencing horizontally transferred genes, so that they can be incorporated into the host genome in a basically inert state, leading to a minimal cost for cell fitness.

The repression activity of H-NS could help the initial incorporation of horizontally acquired genes, preventing stress effects on cell physiology. However, in order to benefit from the new genetic information, the host need to be expressed at a certain point. It follows that H-NS activity has to be relieved, immediately or after specific processes with anti-H-NS activity, by removing the protein from its binding sites. The activity of hindering the H-NS-mediated repression could simply result from some structural re-arrangements of DNA or by the competition with other NAP, notably FIS protein, whose binding sites in the *E. coli* genome were found to be very similar to H-NS ones [91]. However, the binding mechanism between H-NS and DNA does not necessarily need another protein to be disrupted, because it is not very specific and strong, leaving the possibility to the DNA of dynamical reorganisation. For instance, if the structure of a curved AT-rich sequence of DNA is altered by increasing the temperature to $37°C$, there is a significant decrease of H-NS bound to these sites. The main reason is that the increment in temperature reduces the bending stiffness of DNA, thus pushing away the binding sites of H-NS and impeding the formation of protein oligomers and bridges with DNA [92].

H-NS is able to trap and immobilize RNA polymerase (RNAP) by DNA-protein-DNA bridges, or by the formation of continuous filaments that wrap themselves around the promoter regions of the genes. In this sense, H-NS acts as a roadblock for RNAP translocation along the DNA filament [93]. The portions of the genome more

repressed by H-NS are some promoter regions, such as its own gene promoter, *hns*, the *virF* virulence gene promoter, the *proU* promoter, and finally a ribosomal promoter involved in RNA synthesis, called *rrnB* [94]. Indeed, the latter is exactly the promoter chosen to monitor the gene silencing activity of H-NS during the single-cell experiments of this thesis work (chapter 10).

2.3 MACROMOLECULAR CROWDING EFFECTS

The chromosomal DNA of prokaryotic cells is highly compacted into a nucleoid structure and, as above mentioned, different factors are involved in this process, more precisely three phenomena: DNA supercoiling (section 1.2), the activity of specific proteins (NAPs) discussed in previous paragraphs, and the *macromolecular crowding*. The crowding effect will be discussed in this section, to introduce the issues addressed during the experiments on DNA in presence of PEG (section 9.3).

DNA inside the cell lives in a crowded environment with a monovalent ion concentration of about 150 mM, surrounded by a high number of molecules of different size, shape and charge, such as nucleic acids, proteins or complex sugars. These macromolecules can reach the extremely high concentration of 400 mg/ml [95] and occupying $30-40\%$ of the cell volume [96, 97]. The poly-ethylene glycol (PEG), a well-characterized neutral polymer purchasable in a wide range of sizes, is the molecule usually chosen to mimic the crowding condition of the cellular environment. In the presence of monovalent salts, PEG can induce DNA condensation, a phenomenon called Ψ condensation, Polymer-Salt-Induced condensation. The Ψ condensation was first described by Lerman in 1971 [98] and then it has been theoretically studied many times, identifying several factors responsible of DNA compaction, such as charge neutralization, DNA bending, and correlated cation fluctuations [99–102]. In addition, numerous experimental studies widely investigated the PEG-induced DNA condensation [95, 103–105] and they focused mostly on the effects of salt concentration or PEG molecular weight. For instance, in [95] and [105] it has been observed that too short PEG molecules do not induce any DNA condensation.

Since macromolecular crowding plays a crucial role in many biological mechanisms, such as DNA replication or transcription, an intense research activity devoted to the study of Ψ condensation had already started many years ago by means of optical microscopy. In [103] the critical PEG concentration for DNA condensation was measured by fluorescence microscopy experiments. The condensation was analysed as a function of PEG size and ionic strength of the solution, in both cases their increment corresponded to a decrease of the critical concentration required for DNA condensation.

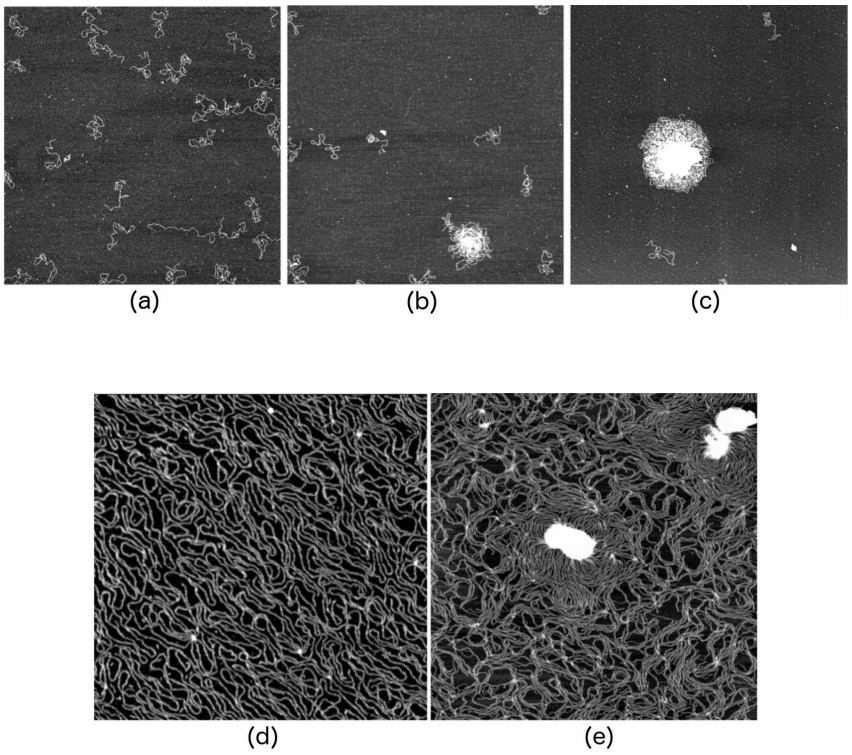

Figure 2.11.: AFM images of linearized pBR322 DNA incubated for 5 minutes with PEG in 300 mM NaCl, 20 mM Tris-HCl, pH 7.5. Top panel: DNA concentration 5 μg/ml, **(a)** 10% PEG1000, **(b)** 10% PEG4000, **(c)** 10% PEG20000. Image areas 3×3 μm.
Bottom panel: DNA concentration 15 μg/ml, **(d)** 15% PEG1000 and **(e)** 15% PEG20000. Image areas 1.5×1.5 μm. Figures adapted from [95].

Single-molecules techniques enabled to achieve more accurate data of Ψ condensation, because of an higher spatial resolution and their ability of studying in greater detail the biomolecular interactions. For example, AFM imaging experiments can clearly show the effects of PEG on DNA, as shown in figures 9.11-9.12. These experiments revealed significant differences in the DNA structures formed after condensation depending on the size of PEG [95]. Particularly, the authors noticed that PEG1000 did not induce DNA condensation even increasing the polymer concentration up to 15% w/v (figure 2.11(a)-(d)), while increasing the degree of polymerization of PEG the condensation effect became more relevant: in presence of PEG4000 DNA formed medium-size aggregates and with PEG20000 large aggregates were observed, see figure 2.11(b)-(c)-(e). Salt concentration effects have also been noticed: the concentration (w/v) of PEG20000 necessary to induce DNA condensation decreased from 30% to 10% with an increase from 50 mM to 300 mM of NaCl [95].

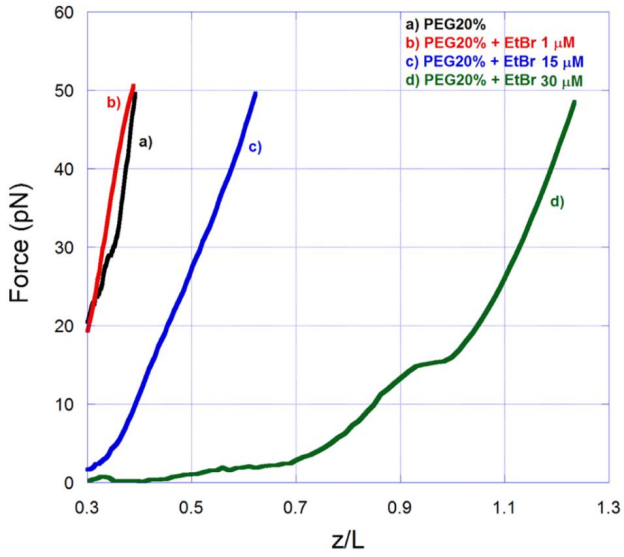

Figure 2.12.: Force versus extension curves of DNA-PEG complexes in presence of different concentrations of EtBr drug: 0 μM (black), 1 μM (red), 15 μM (blue), 30 μM (green). DNA end-to-end extension (z) is normalized to the contour length (L), while PEG8000 concentration is 20% *w*/*v*. Figure from [106].

A number of studies by using optical tweezers are reported. Rocha et al. studied Ψ condensation in presence of a DNA intercalator, namely EtBr [106]. Force spectroscopy experiments were performed at three different concentrations of EtBr and 20% *w*/*v* of PEG8000, results showed that the drug can hinder DNA condensation, especially at higher concentrations, see figure 2.12. The same group further explored the DNA-drug interactions (see also chapter 8) in a crowding condition similar to the real cellular environment where DNA interacts with ligands. It has been shown that the strong DNA stiffening effect of two intercalators drugs is much reduced in presence of PEG8000 [107]. DNA molecule resulted softer in a drug-PEG mixture compared to the DNA-drug complexes alone, more precisely the authors showed that the persistence length was around 90 nm in presence of 3 μM EtBr or 4 μM GelRed, but only 1% *w*/*v* of PEG was enough to recover the standard ~ 50 nm value of bare DNA.

A very interesting work analysed the effects of using monovalent or divalent salts, namely NaCl and $MgCl_2$, on Ψ condensation were used [108]. Force extension measurements by means of a magnetic tweezers setup were carried out on solutions of PEG600 and PEG6000: a critical force (F_c) at which DNA abruptly collapses to zero extension was observed, in addition a concentration dependence was revealed, as shown in figure 2.13. In solutions of 30% *w*/*v* PEG600 the DNA condensation was detected only if Na^+ concentration was at least 300 mM, on the other hand, in presence of the same concentration of PEG6000 the condensation is observed even without adding salts.

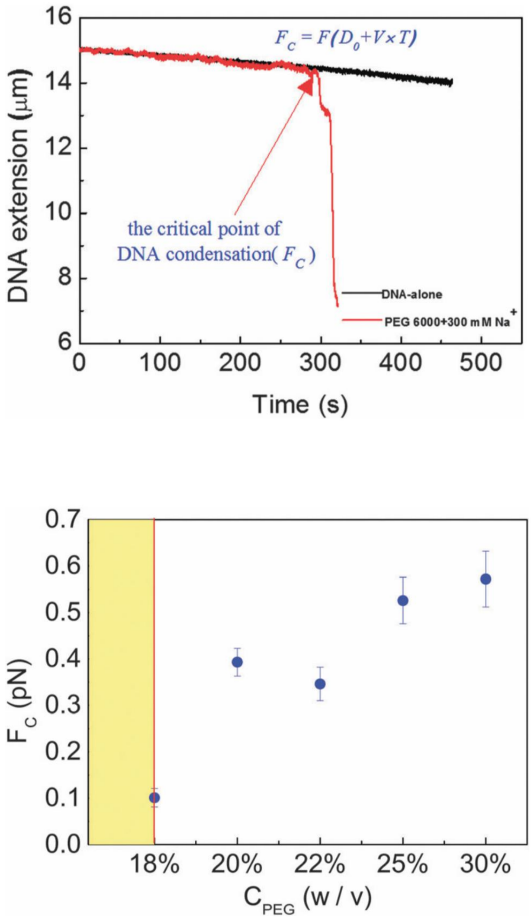

Figure 2.13.: **(a)** Force-extension measurements. Black curve for bare DNA, red curve for DNA in presence of PEG6000, where a steep collapse of DNA extension is observed at a critical force F_c. D_0 is the position of the starting magnet, V the velocity of the magnet and T the elapsed time at the critical point.
(b) Critical force F_c variations as a function of PEG6000 concentration, in 100 mM Tris-HCl. Figures adapted from [108].

These findings support the hypothesis of the important role of PEG size in Ψ condensation. The most striking results of this work concern the differences between the behavior of Ψ condensation as a function of the monovalent salt or the bivalent salt concentration. As reported in figure 2.14, the critical force F_c had a linear dependence with salt concentration in the case of monovalent ions, such as Na^+, while bivalent ions like Mg2+ produce a parabolic curve of F_c, reaching a maximum at ~ 3 mM $MgCl_2$ for the 30% PEG6000 solution. This parabolic trend of Ψ condensation in presence of divalent ions suggests that DNA underwent a reentrant condensation, which means that higher $MgCl_2$ concentrations inhibit DNA condensation by promoting the formation of less compact structures. Authors confirmed this result by morphological studies of PEG-induced DNA complexes

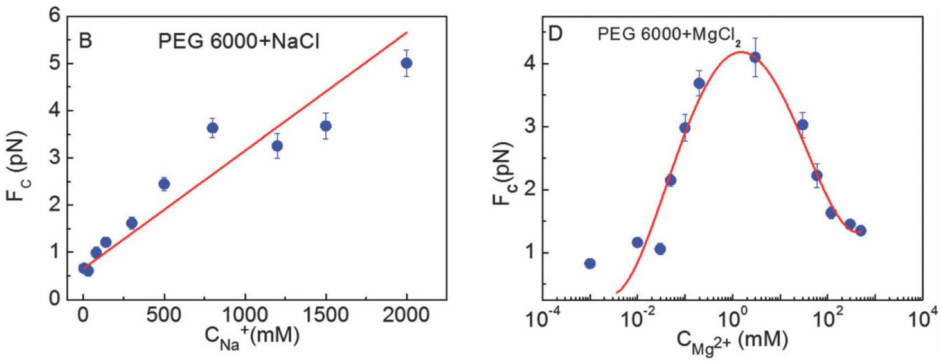

Figure 2.14.: Critical force (F_c) values as a function of NaCl (left) or $MgCl_2$ (right) concentration, in PEG6000 solutions at 30% w/v. Data from monovalent salt solutions were fitted with a linear function, whereas bivalent salt solutions data with a polynomial function. Figure adapted from [108].

achieved with AFM imaging experiments. The height of DNA complexes in 30% PEG6000 solutions had a very similar parabolic shape as a function of $MgCl_2$ concentration [108]. Reentrant condensation was discussed by other groups as well, from both the theoretical [102] and experimental [101] point of view.

3

THEORETICAL BACKGROUND

3.1 INTRODUCTION TO POLYMER PHYSICS MODELS

DNA molecules, such as any other polymer, adopt a random coil configuration when they are free in solution, because the entropy is thus maximized. Stretching a molecule with an external force lowers the number of possible configurations of the system and reduces the entropic contribution. This reduction of entropy has an energetic cost, supplied by the work done by the external force.

Guth and Mark and Kuhn have set the bases of the polymer elasticity theory in 1934, explaining through a simple model the elastic properties of a polymer chain. This description requires a statistical approach and several models have been developed over the years [109]. The simplest approach considers the polymer as a chain discretized into a series of rigid segments (Kuhn segments), each of the same length (a) and connected by links that can rotate in arbitrary directions (figure 3.2). Macromolecules are thus described by random walks: in one-dimension every single segment of the polymer can be oriented on the left or on the right with an equal probability of 0.5. Consequently, there are $2N$ different possible configurations for a polymer chain of N segments, each with a probability $\frac{1}{2N}$. The probability of the end-to-end distance (L_e) of a certain macromolecular state is given by the following binomial distribution

$$p(L_e, N) = \binom{N}{\frac{N-L_e}{2a}} \left(\frac{1}{2}\right)^N \tag{3.1}$$

See [110] for details about calculations.

3.1.1 *Stretching a DNA molecule*

The elastic properties of an isolated molecule are quite simple to analyse from the theoretical point of view, but it has been much more difficult to study them experimentally. Indeed, the first experiment applying a force on individual molecules was carried out in 1992, much later than Guth and Kuhn theory. Bustamante and co-workers were able to stretch DNA and study its elasticity, comparing data with existing theoretical models [111].

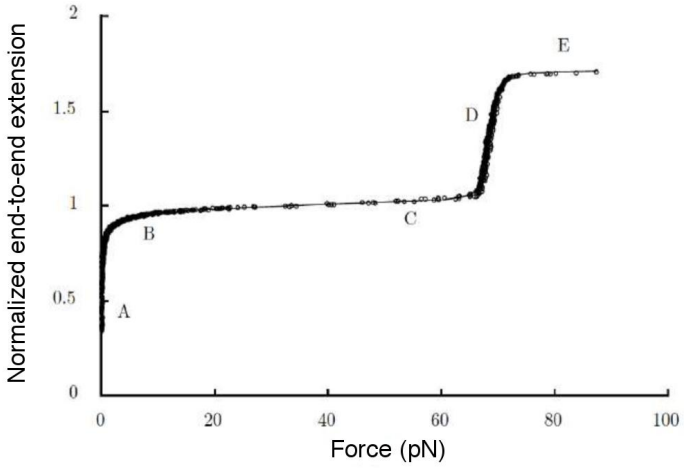

Figure 3.1.: Example of stretching experiment on an individual DNA molecule. In this force-extension curve it is possible to distinguish five regimes, each characterised by a different behaviour of DNA: A) random coil, B) entropic regime (worm-like chain), C) elastic regime (spring-like behaviour), D) overstretching regime, and finally E) elasticity of the overstretched DNA phase. Figure adapted from [112].

Different regimes of force have been identified during the stretching of DNA molecules [113, 114], as shown in figure 3.1.

As above mentioned, DNA is approximately a random coil for very low forces, below 0.01 pN. The end-to-end distance of DNA in such a condition is determined by the mean square displacement of the random walk configuration previously introduced.

The first regime in which it is possible to study elastic and mechanical properties of DNA is the *entropic regime*, with forces ranging from 0.01 to $\sim$ 10 pN. The parameters describing the nanomechanics of DNA in this regime are the contour length (L_0) and the persistence length (L_P). L_0 is the length of the completely extended molecule, while L_P provides information about the bending rigidity. These quantities will be derived from the models in the following sections.

When the forces are are between 10 pN and 50-60 pN, DNA enters in an *elastic regime*. Here the molecule behaves like a spring, described by an elastic constant called stretch modulus. The DNA extension increases linearly with the force.

Around 65 pN DNA exhibits a particular structural transition during which its extension increases by roughly 70%. This phenomenon is called *overstretching transition* and it was first reported in 1996 [115]. The precise nature of this transition phase is still debated. Many experimental studies tried to unravel if DNA undergoes a melting process involving the unpeeling of the strands or if a base-paired structure called S-DNA is formed [116–118]. Additionally, several theoretical models have been proposed as well [119–123]. It seems that a sequence-dependent process is involved. I addressed this prob-

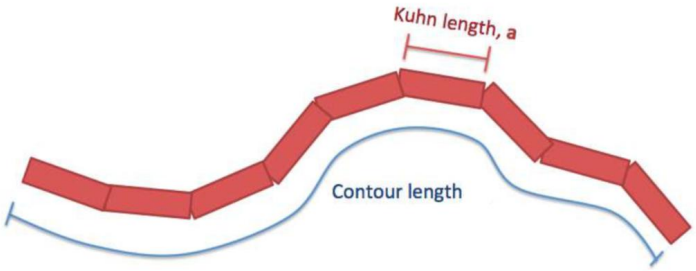

Figure 3.2.: Polymer chain divided into Kuhn segments accordingly to the freely-jointed chain.

lem during the single-molecule experiments at high forces described in chapter 6.

Finally, beyond this transition, the elasticity of the overstretched DNA is explored, until the complete melting of he double helix is achieved around 150 pN or 300 pN, depending on the GC content [124]. When forces are even higher the breaking of the covalent bonds of DNA backbone can occur [113].

In the next section I am going to focus on DNA models concerning the entropic regime, below 10 pN. I will first present two models used to describe the force-extension curves obtained by stretching individual molecules, and then I will explain a more realistic model including the torsional stress, necessary to describe the mechanics of twisted DNA molecules.

A polymer without the torsional contribution is usually described by the Kratky-Porod model: a chain divided into N Kuhn segments of length a and orientation vectors $\mathbf{t}_i$, with nearest-neighbour interactions [3]. A polymer under tension has an energy for each configuration consisting of two terms

$$\begin{aligned} E_{K\text{-}P} &= -\frac{B}{a}\sum_{i=2}^{N}\mathbf{t}_i\cdot\mathbf{t}_{i-1} - Fa\sum_{i=1}^{N}\mathbf{t}_{i,z} \\ &= -\frac{B}{a}\sum_{i=2}^{N}\cos\vartheta_i - Fa\sum_{i=1}^{N}\cos\phi_i \end{aligned} \tag{3.2}$$

where B is the bending modulus of the polymer chain, ϑ_i is the angle between subsequent $\mathbf{t}_i$ vectors, F is the force applied along the z-axis and ϕ_i is the angle between $\mathbf{t}_i$ and the z-axis. The first term represents the bending energy while the second one is the external work done to stretch the molecule.

The FJC and WLC models described below are specific limits of the Kratky-Porod chain.

3.2 THE FREELY-JOINTED CHAIN MODEL (FJC)

The first and simplest model adopted to describe the elasticity of DNA molecules in the entropic regime is the freely-jointed chain (FJC) model. It is a Kratky-Porod model in the limit $B = 0$, that means each segment of the chain can freely rotate in random orientations. The energy of the system becomes

$$E_{FJC} = -Fa \sum_{i=1}^{N} \cos\phi_i \tag{3.3}$$

with the following partition function

$$\begin{aligned} Z &= \sum_{t_i} e^{-\frac{E_{FJC}}{k_B T}} = \sum_{t_i} \prod_{i=1}^{N} e^{\frac{Fa\cos\phi_i}{k_B T}} \\ &= \left(\frac{2\pi k_B T}{Fa} \sinh \frac{Fa}{k_B T} \right)^N \end{aligned} \tag{3.4}$$

Now, by using the relation between free energy and partition function of statistical mechanics, the equation $A = -k_B T \log Z$, I can compute the average end-to-end extension of the polymer as

$$\langle L_e \rangle = -\frac{\partial A}{\partial F} = L_0 \left(\coth \frac{Fa}{k_B T} - \frac{k_B T}{Fa} \right) \tag{3.5}$$

where L_0 is the contour length. In the small force limit, namely if $Fa \ll k_B T$, the extension L_e becomes linear with the force, similarly to a Hookean regime. On the other hand for larger forces, when the end-to-end extension approaches the contour length, the FJC model does not describe accurately the experimental force-extension curve of DNA, as first noticed in [111]. In such force regime a more precise model is needed to describe the elastic behavior of a polymer.

3.3 WORM-LIKE CHAIN MODEL (WLC)

The model enabling a better prediction of the experimental data is the worm-like chain (WLC) model. The WLC model is basically the continuous limit of the FJC model: $a \to 0$ and a bending stiffness is introduced, $B \neq 0$, as clearly shown in figure 3.3. This model was first introduced in 1994 [126] and succeeded in describing accurately the data presented in [111] two years earlier. The mathematical details of the model were then explained by Marko and Siggia the following year [127, 128].

The energy of the system in the WLC model considers both terms of the Kratky-Porod mode (equation 3.2):

$$E_{WLC} = \frac{B}{2} \int_0^{L_0} \left(\frac{dt}{ds} \right)^2 ds - \frac{F}{k_B T} \int_0^{L_0} \cos\phi(s)\, ds \tag{3.6}$$

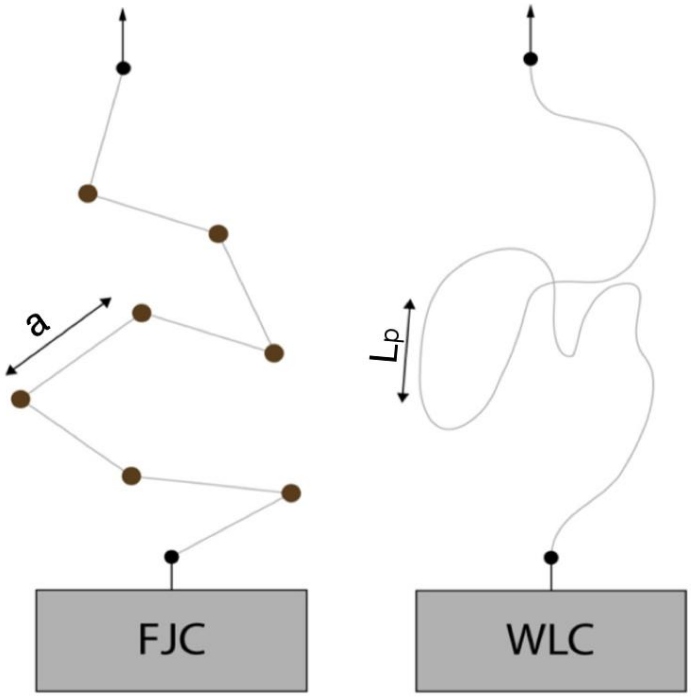

(a) (b)

Figure 3.3.: Polymer elasticity models commonly used in single molecule manipulation. **(a)** FJC model: chain of Kuhn segments of length a connected by freely-rotating joint. **(b)** WLC model: polymer chain described as a flexible rod with defined stiffness, namely the persistence length L_P. Figure adapted from [125].

where s is the curvilinear coordinate along the polymer chain and it is integrated over the total contour length of the molecule, L_0, thus substituting the discretized Kuhn segments of length a of the FJC model. Additionally, the bending modulus is related to the persistence length by the following equation $B = k_B T \cdot L_P$.

A relation between L_e and F equivalent to equation 3.5 is much more complicated to obtain in this case, and an approach similar to the calculation of the quantum mechanical problem of a dipole in an electric field is required. These calculations have been addressed in detail elsewhere [3, 109, 126–129].

However, there is no analytic formula describing the WLC behaviour of the molecule extension in the whole range of forces, but only two functions working for the extreme cases of low and high forces [3]. An approximate numerical solution with a precision of 0.1% has been interpolated, leading to the following WLC equation

$$F = \frac{k_B T}{L_P}\left(\frac{L_e}{L_0} + \frac{1}{4}\frac{1}{\left(1 - L_e/L_0\right)^2} - \frac{1}{4}\right) \tag{3.7}$$

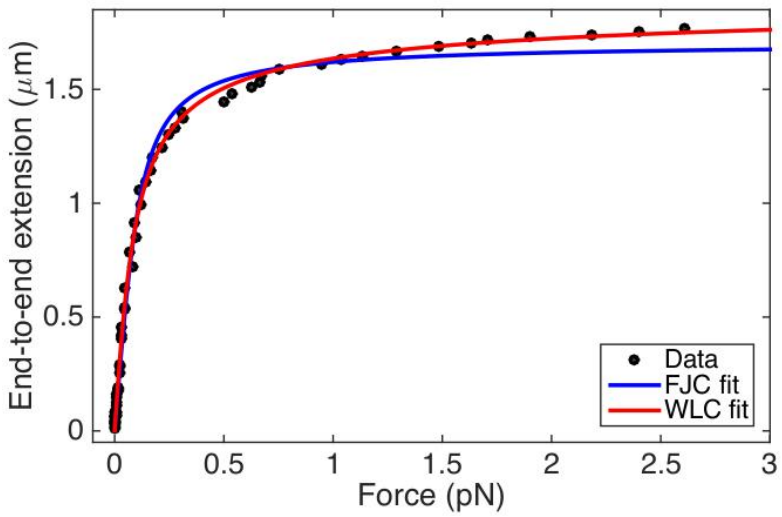

Figure 3.4.: Comparison between FJC and WLC model. The agreement with low forces data is very good for both models, that are almost perfectly superimposed at the beginning, while above ~ 1 pN the FJC fails in properly predicting the experimental curve. Data from a force-extension experiment on a 4.6 kbp DNA molecule.

Figure 3.4 shows the comparison of the accuracy of FJC and WLC model in describing experimental force-extension data. Both models work fairly well for very low forces, but above 1 pN the the discrepancy between data and FJC curve (blue) becomes significant, whereas the WLC curve (red) has a perfect agreement with data in the whole range of forces. The comparison between FJC and WLC models will be briefly addressed in section 12.2 as well, in the Discussion part.

3.4 ROD-LIKE CHAIN MODEL (RLC)

The FJC and WLC models just discussed, derived from the Kratky-Porod approach, did not consider the torsional stress, but DNA is one of the natural polymers capable of storing torsion. Indeed, in most of the living organisms, the DNA double helix is slightly untwisted. This likely occurs to promote local unravelling and open melting bubbles, for the DNA replication for instance. As a consequence, a more realistic polymer model taking into account the torsional energy contribution is needed. This model is named rod-like chain (RLC) model and has been discussed in detail in 1997 [130, 131].

The RLC model considers the DNA molecule as a homogeneous rod with a finite torsional modulus C, not a chain free to rotate along its axis as in the WLC model. The energy of the system is thus ob-

tained by adding a twist energy term (E_{twist}) to the energy of the WLC model defined in equation 3.6:

$$E_{RLC} = E_{WLC} + E_{twist} = \frac{B}{2}\int_0^{L_0}\left(\frac{d\mathbf{t}}{ds}\right)^2 ds - \frac{F}{k_B T}\int_0^{L_0}\cos\phi(s)ds + \frac{C}{2}\int_0^{L_0}\Omega^2(s)\,ds \tag{3.8}$$

with $\Omega(s)$ the local twist angle of the polymer chain.

3.4.1 *The buckling transition*

The RLC model enables to describe the behaviour of DNA under torsional stress, for example during the typical DNA twisting experiments of a magnetic tweezers setup (figure 1.6). This kind of experiments are a very useful tool to study the formation of DNA supercoiled structures and understand their biological relevance, as already mentioned in section 1.2.

A DNA molecule subject to a twist deformation initially stores torsional energy without changing its extension, as shown in figure 1.6 (flat region around zero turns). Under this condition, the torque Γ increases linearly with the twist angle ($\Gamma = \frac{C}{L_0}\Omega$) and consequently the twist energy E_{twist} increases quadratically. The twist angle is related to the experimentally measured number of turns (n_t) by the relation $\Omega = 2\pi n_t$.

After a certain amount of twist, the molecule begins to buckle and a loop, called plectoneme, is formed. During this buckling transition the twist energy is transferred into bending energy and a further torsional stress does not increase the torque. The plectoneme formation causes an extension decrease of the polymer of $2\pi R$ per turn, where R is the radius of the plectoneme supposed to be circular. Therefore, the torsional energy produced by the external torque Γ is balanced by the bending energy and the work done by the force applied by the MT setup to stretch the polymer:

$$2\pi\Gamma_b = 2\pi RF + 2\pi R\frac{B}{2}\frac{1}{R^2} \qquad \text{with} \quad \Gamma_b = \frac{C}{L_0}2\pi n_b \tag{3.9}$$

where the first term is the torsional energy at the buckling transition, the second term is the bending energy for a plectoneme with circular geometry and the last one is the energetic cost to extend a molecule by $2\pi R$, expressed as an external work.

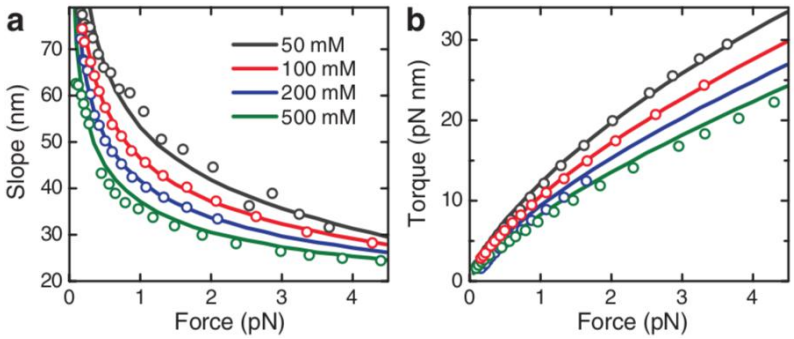

Figure 3.5.: Comparison of the predictions from the theoretical model developed in [132] with data from [136]. Slopes **(a)** and torque **(b)** after buckling transition as a function of force for different Na^+ concentrations. Circles represent experimental data and solid lines the theoretical prediction. Figure from [132].

The minimization of this equation with respect to R leads to the relation $2\pi F = \frac{\pi B}{R^2}$, that can be rewritten in terms of the following equations

$$\Gamma_b = \sqrt{2BF} \implies n_b = \frac{L_0}{\pi C}\sqrt{\frac{BF}{2}} \tag{3.10a}$$

$$R = \sqrt{\frac{B}{2F}} \implies \frac{dL_e}{dn_t} = \pi\sqrt{\frac{2B}{F}} \tag{3.10b}$$

where in second equation I considered that in this simple model the plectonome formation induces an extension decrease of $2\pi R$ per turn, that is to say $\frac{dL_e}{dn_t} = 2\pi R$.

These equations will be used for the description of twisting experiments reported in chapter 8. However, some limitations of this model in predicting the experimental findings will be revealed.

As a matter of fact, new models describing the buckling transition and in general the formation of plectonemes have been recently introduced [132–135]. These models include a more sophisticated and realistic description of the plectonemes, thus enabling to predict with higher accuracy the values of n_b and the slope $\frac{dL_e}{dn_t}$, see figure 3.5 for example. To improve the description of the supercoiled DNA an electrostatic interaction energy term was added to equation 3.8, because the circular geometry of the plectonemes above discussed is an oversimplification which does not provide a quantitative agreement with the expected results. The electrostatic potential of these models has been calculated by using the Debye-Huckle approximation within the framework of the Poisson-Boltzmann equation, the details are included in [132, 133].

3.4.2 *Mechanical denaturation*

The models discussed so far did not consider the double-helical structure of DNA, in particular its chirality. Twisting experiments has indeed revealed an asymmettrical behaviour of DNA molecules depending on the orientation of the twist angle: when the force is high enough ($> 1\,pN$), the unwinded molecules did not form plectonemes and maintain an extended state, whereas overwound molecules keep on forming loops even at higher forces, both for negative or positive σ (figure 3.6). More precisely, this applies for forces lower than 5-6 pN, above which DNA relaxes plectonemes in favor of an extended state even for positive supercoiling (see experiments of chapter 7 for details).

For low forces ($F \leqslant 0.5\,pN$) the DNA molecule begins to form plectonemes after the buckling transition and its extension symmetrically decreases with supercoiling (σ). For intermediate forces ($0.6 < F < 0.8\,pN$) an asymmetry appears: at $\sigma > 0$ plectonemes are still formed, whereas at $\sigma < 0$ the DNA extension is larger than zero, as is typical for the plectonemic state. Finally, for forces even higher ($F \geqslant 1\,pN$), the DNA is fully extended at negative superhelical density.

The reason of this phenomenon is the positive (clockwise) helicity of the double-stranded DNA (dsDNA) backbone. A negative applied twist has a destabilizing effect on this chiral structure and, instead of the plectoneme formation, part of the twist is absorbed by the local opening up of the dsDNA helix into two single DNA strands, i.e. melting the DNA (see green and orange curves with the related cartoons of figure 3.6).

In order to systematically measure this force-induced melting transition, Mantegazza group observed that the fluctuations of DNA extension becomes larger for the intermediate forces, see figure 3.7. Therefore, a quantitative analysis can be performed by calculating the variance of these fluctuations as a function of the applied force [137, 138]. It was also verified that the standard deviation (and hence the variance) is not dependent on the total averaging time, because that time is much longer than the characteristic time of the correlation function of the data (more than 100 times) [137]. Another method to quantitatively measure the mechanical denaturation is the calculation of the characteristic time (τ) of the temporal autocorrelation function ($g(\tau)$) related to the end-to-end extension. The time τ is derived by computing the half width at half maximum (HWHM) of the correlation function. I show two representative examples of the temporal traces of L_e fluctuations in figure 3.8(a), with the corresponding autocorrelation time, figure 3.8(b). The characteristic correlation time is negligible compared to the frame acquisition time ($\approx 20\,ms$) for the measurements at $F = 0.5$ pN, while it is appreciable with $F \approx 0.8$ pN.

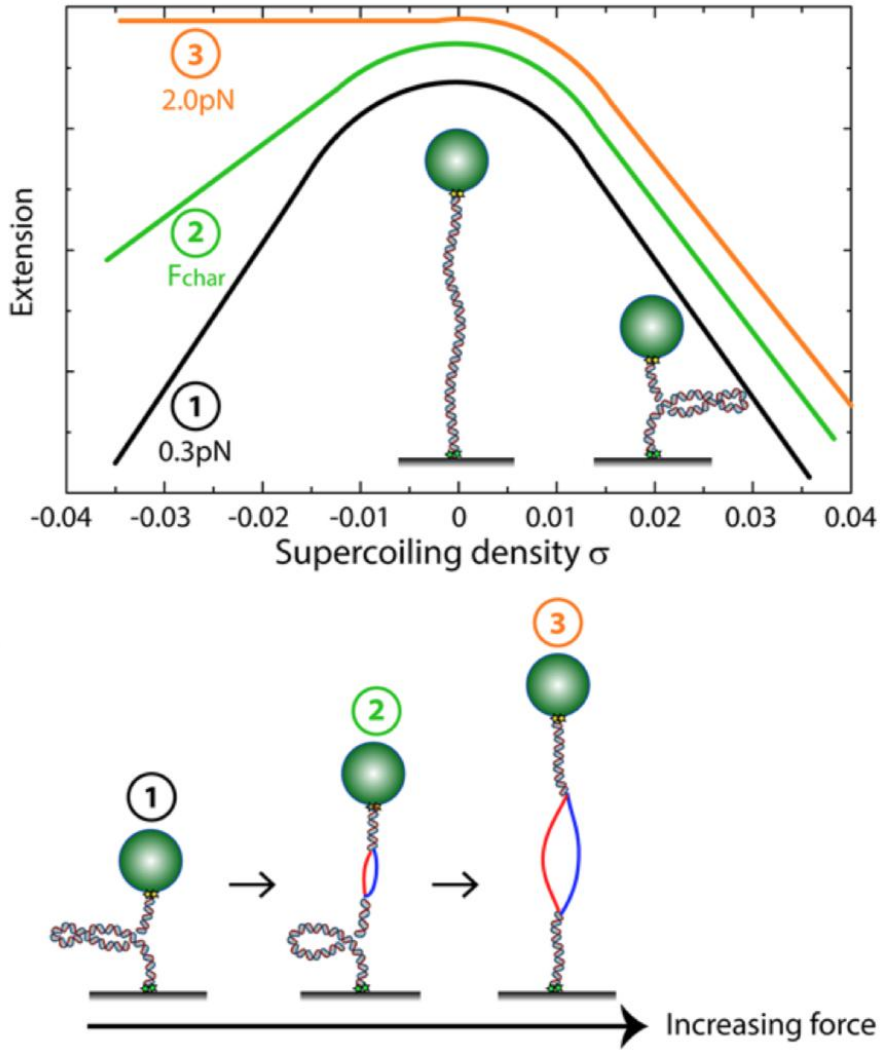

Figure 3.6.: Top: twisting experiments at different forces: low (black), intermediate (green) and high (orange). The behaviour of DNA is symmetrical only for low forces ($\leqslant$ 0.5 pN), while an asymmetry is introduced for higher forces. Particularly, for high forces ($\geqslant$ 1 pN) DNA is fully extended. In the intermediate force regime the DNA extension is between the previous extreme situations. Bottom: schematic representation of DNA state during the twisting experiments at different force. Figure adapted from [207].

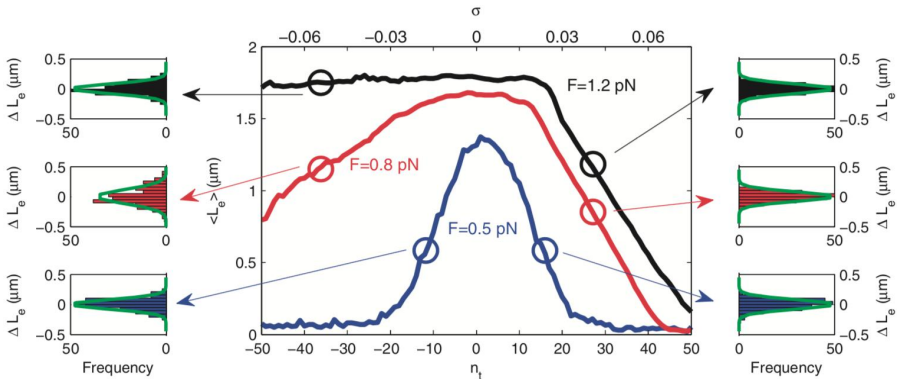

Figure 3.7.: Average DNA extension ($\langle L_e \rangle$) measured as a function of the number of imposed turn n_t (lower axis) or degree of supercoiling σ (upper axis). The data are taken at three different values of force and the lateral histograms show the fluctuations of DNA extension, by means of the statistical distribution of $\delta L_e = L_e - \langle L_e \rangle$ (μm). Figure from [138].

This observation for intermediate forces is a strong suggestion of the presence of a DNA coexistence phase between the plectonemic structure and an extended denaturation state. In fact, when the forces are higher the brownian motion of the tethered bead is expected to be smaller and consequently the extension fluctuations should be lower, but it has been observed that at $F \approx 0.8\,\mathrm{pN}$ fluctuations are significantly bigger than those for lower forces.

Finally, I show on page 41 an example of these two strategy for the quantitative analysis of the mechanical denaturation: in figure 3.9(a) the variance $\sigma^2_{L_e}$ is reported as a function of the force, whereas in figure 3.9(b) the autocorrelation time τ behaviour is shown. Both curves show a peak corresponding to the force values at which the extension fluctuations were higher. The maximum force at which this peak occurs represent the *characteristic force* of the plectonemic-denaturation transition. In next section this quantity will be described in detail, within the framework of simple model.

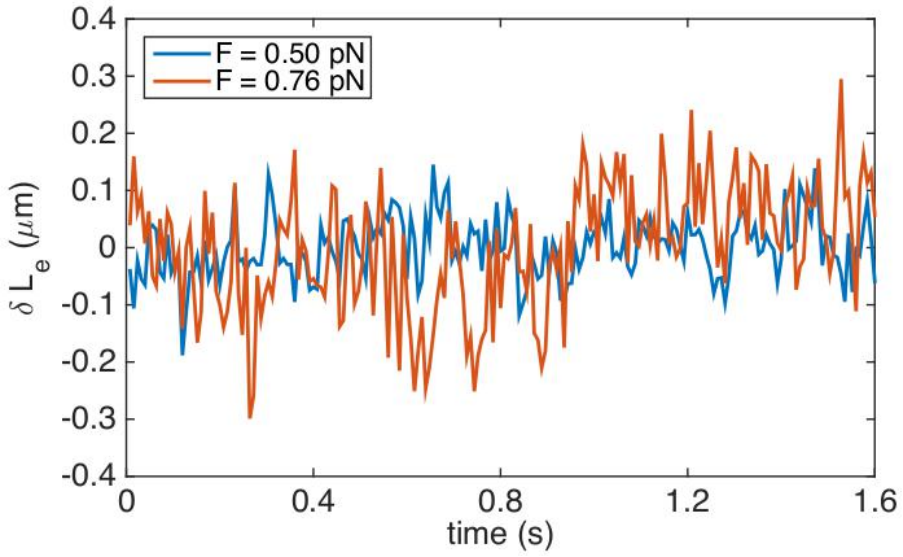

(a)

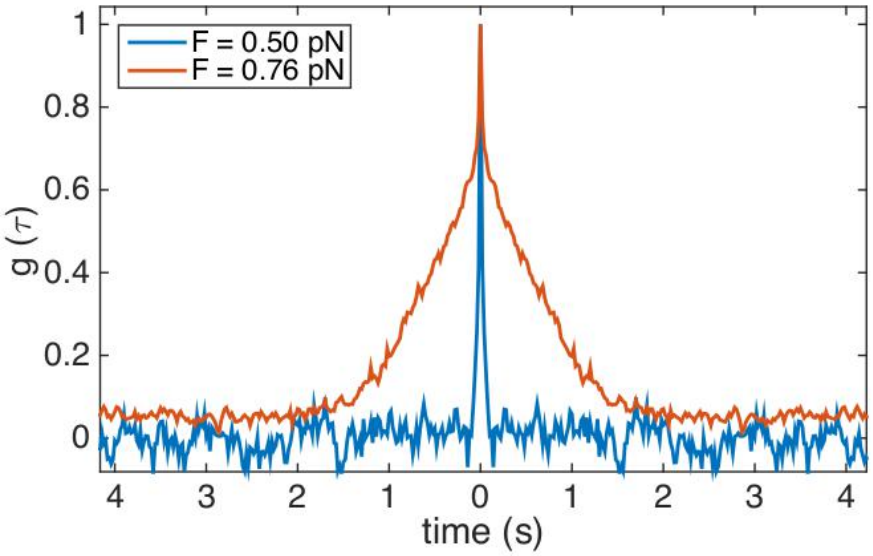

(b)

Figure 3.8.: **(a)**: two examples of the temporal traces of DNA end-to-end extension at different force. Extension fluctuations are represented as $\delta L_e = L_e - \langle L_e \rangle$. Data obtained at $F \approx 0.8\,pN$ (orange) show larger fluctuations compared to data at $F \approx 0.5\,pN$ (blue), as confirmed by the autocorrelation functions $g(\tau)$ shown in **(b)**: the width of the normalized temporal autocorrelation function for $F \approx 0.8\,pN$ is much larger than the width for $F \approx 0.5\,pN$. Both measurements were taken for a normal DNA molecule at $\sigma = -0.09$ and in physiological conditions.

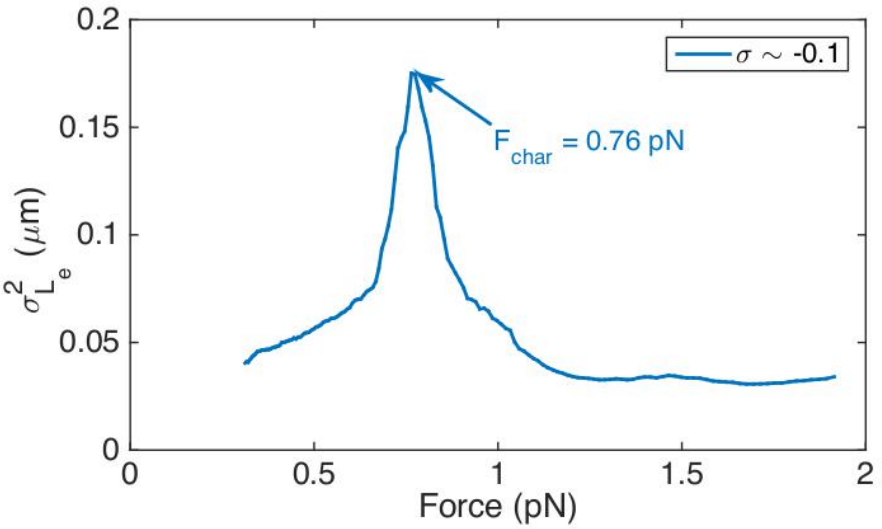

(a)

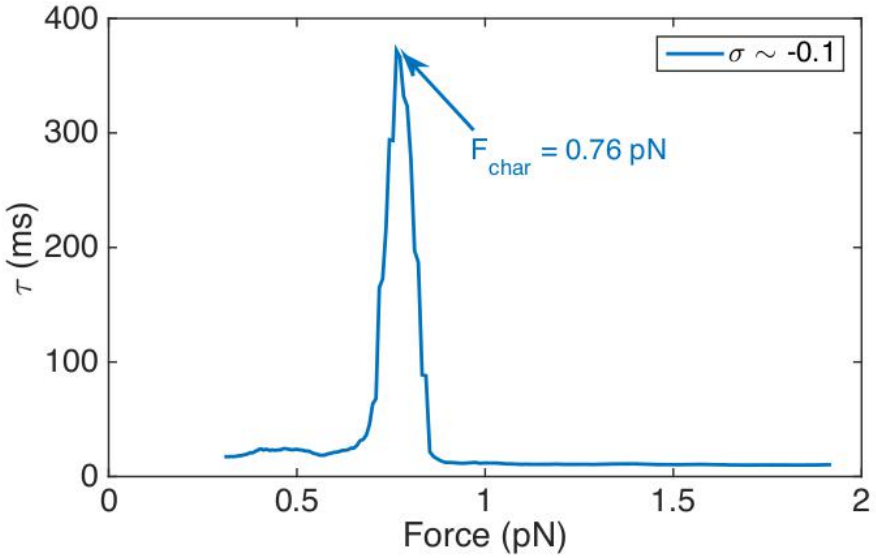

(b)

Figure 3.9.: Quantitative analysis of fluctuations of DNA extension. Variance $\sigma^2_{L_e}$ and autocorrelation time τ measured as a function of the applied force F. The peak of these plots represent the value of the characteristic force.

3.5 DENATURATION MODEL

The model presented here is an extension of the classical theory of plectonemes formation of the RLC model, section 3.4, and it quantitatively explains the increase of L_e fluctuations observed in the experiments. In the previous paragraph I showed that this phenomenon occurs for a characteristic value of force, which is called F_{char}. This model was first derived by Salerno and co-workers [137] and provides a relation between F_{char} and the binding energy between base-pairs, i.e. the denaturation energy.

A DNA molecule can relax an external work, such as an applied torque Γ or a force F, in three different ways: by storing twisting energy E_{twist}, by forming plectonemes, E_{plect}, or by locally denaturing the double helix, E_{den}. These three energy contributions can be defined as follows:

$$E_{twist} = \frac{1}{2}\frac{C}{L}(2\pi n_e)^2 \tag{3.11a}$$

$$E_{plect} = W + E_{bend} = 2\pi R n_p \cdot F + \frac{B}{2}\frac{1}{R^2}2\pi R n_p \tag{3.11b}$$

$$E_{den} = \alpha n_d \tag{3.11c}$$

where C is the torsional modulus, the work W and the bending energy E_{bend} for plectonemes formation were previously introduced in equation 3.9, and α is a phenomenological constant which represents the denaturation energy per turn, namely the energy for opening a certain number of base-pairs required to relax one turn. n_e, n_p and n_d correspond to the number of turns stored in torsional energy, the number of plectonemes, and the number of turns relaxed by denaturation respectively. The total energy thus results

$$E_{tot} = E_{twist} + E_{plect} + E_{den} \tag{3.12}$$

To solve this model it is assumed that the variations in DNA extensions are mainly due to the plectonemes formation, while denaturation bubbles involve a negligible number of base pairs and do not induce length variations. This hypothesis is valid if the explored value of the total number of turns n_t is very low and consequently a small fraction of single-strand DNA is present. In chapter 7 the high supercoiling regimes will be investigated, where this hypothesis is no longer correct, and a new model will be introduced to describe the data (chapter 11).

The aim of this model is to derive an analytical expression for F_{char}. In order to do that, E_{tot} is minimized with respect to the three variables R, n_p and n_d, by imposing a topological condition as well

$$n_t = n_e + n_p + n_d \tag{3.13}$$

This equation states that the total number of applied turns must necessarily be equal to the sum of the three ways to relax them. If the total energy were minimized without considering the E_{den} term, I obtain the plectoneme radius R and the buckling number n_b derived in equation 3.10a. On the other hand, the minimization of E_{tot} becomes more complicated by taking into account the denaturation process. The system of equations involved is the following

$$\begin{cases} n_e = n_t - n_p - n_d \\ \frac{\partial E_{tot}}{R} = 0 \\ \frac{\partial E_{tot}}{n_d} = 0 \\ \frac{\partial E_{tot}}{n_p} = 0 \end{cases} \tag{3.14}$$

which leads to the equation

$$2\pi\sqrt{2BF} - \alpha = 0 \tag{3.15}$$

From the last equation a relation between the force F and the energy α can be derived, thereby defining the characteristic force:

$$F_{char} = \frac{\alpha^2}{8B\pi^2} \tag{3.16}$$

The characteristic force and its relation with the denaturation energy α will be used for the analysis of the experimental findings presented in chapters 7, 8, 9.

The behavior of DNA under an applied force and torque can be overall analysed with a phase-diagram in n-F space, as shown in figure 3.10. Different colours are used to describe regions where DNA behaves differently according to the values of F and n. The white region is the entropic regime of DNA (page 30) well described by the WLC model. Lateral blue regions correspond to the plectonemes formation process, when DNA extension progressively decreases down to zero, represented in green regions. The most interesting regions that denaturation model just described enables to explain are the red and the yellow one, which are not predicted by the RLC theory: the red region describes a condition in which all the torsional stress applied to the DNA molecule is released with the formation of denaturation bubbles, and no stable plectonemes exist. The yellow zone shows the coexistence phase between the plectonemes and the denaturation bubbles. The model just presented focused on the transition between yellow and red zone. In figure 3.10 black lines indicate measurements carried out in [137]. The horizontal line delimiting the red zone correspond to a value of force of $\approx 0.8\,pN$, where fluctuations of DNA extensions are high. That line, at the boundary between red and yellow regions, is the only one characterised by step-like variations in the DNA extension: from a reduced extension due to the

plectonemic state to an extended structure in denaturation state. This discontinuity in the end-to-end extension L_e is precisely the cause of wider extension fluctuations during the plectonemic-denaturation transition occurring at $F = F_{char}$.

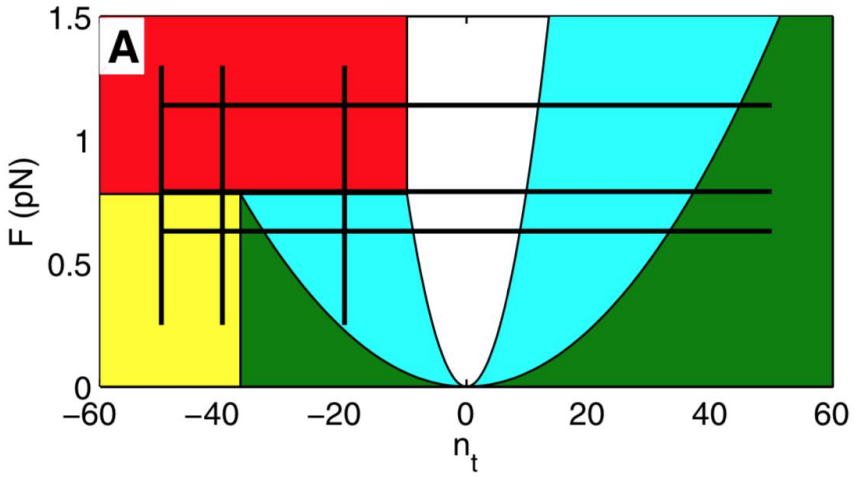

Figure 3.10.: Phase diagram describing DNA structures in the torsion-force space (n, F). The colours correspond to the different phases of DNA: the white parabola is the entropic regime of DNA, the lateral blue regions correspond to the plectonemic state, green regions are related to the zero extension configuration due to plectonemes formation, yellow region is the coexistence phase of denaturation bubbles and plectonemes at zero extension, and finally the red region is the denaturation state. The black lines represent measurement presented in [137].

Part II

MATERIALS & METHODS

4

EXPERIMENTAL SETUP

4.1 INTRODUCTION TO SINGLE MOLECULE TECHNIQUES

Over the last twenty years single molecule techniques attracted interest in the field of biophysics and they have been used for many applications. The main reasons are the limitations of traditional biophysical methods: canonical microscopy techniques enable to carry out only bulk experiments, that means studying big ensembles of molecules. It follows that the properties of a molecule under investigation are known as average values. Because of the complexity of some molecular or cellular processes, it became essential the possibility of studying one molecule at a time for a detailed comprehension of the biology behind an experiment.

In some situations, single molecule methods are also often called nano-manipulation techniques since they can apply small forces at the molecular level. Just to give an idea, the typical energy in biology is given by the hydrolysis of ATP, equal to $\approx 20\, k_B T$ and the characteristic size is the diameter of a protein, in the range of nanometers. As a result, the forces necessary to monitor biological processes are therefore between hundreds of femtonewtons to ten of piconewtons [139]. These techniques allow the biophysicist to analyze the elasticity of single biopolymers, such as nucleic acids or proteins, to measure the strength of bonding between ligand and receptor, and finally to observe the activity of enzymes or proteins in real time. The application of a force at the molecular scale gives the possibility to unravel some hidden features of nanosized biomolecules. For example, several biological phenomena take place by the formation of chemical bonds and by breaking them it becomes possible to understand the internal organization of the studied system and the order of magnitude of the forces necessary to maintain a specific biological structure. Moreover, the nano-manipulation provides new insights into the kinetics and mechanochemistry of macromolecules.

The first experiment measuring the elasticity of a single molecule was performed in 1992 by Bustamante and co-workers [111]. They used a combination of magnetic fields and hydrodynamic drag to pull with a certain force different superparamagnetic beads tethered to a surface by a DNA molecule. The precision of this experiment

was enough to invalidate the FJC model and to show the need of a more realistic model to describe polymers, the WLC model (section 3.3). Nowadays, the most commonly used single molecule techniques are magnetic tweezers (MT), optical tweezers (OT) and atomic force microscopy (AFM) [40, 140–142]. These three techniques are complementary and usually each of them is more suited for particular studies, depending on the range of forces needed and on the investigated biological sample. The force that can be applied by these nano-manipulation methods can vary between 10^{-14} and 10^{-8} N, and the length of the molecules ranges from 10^{-10} to 10^{-4} m. For example magnetic tweezers are usually used to study biological processes involving nucleic acids, which are molecules characterised by an helix rise of 0.34 nm and with typical forces of folding or unfolding in the range of pN. AFM is more suited for the investigation of cell ($\approx$ 100 µm) mechanics or protein unfolding, which involves higher forces of hundreds of pN and in case of covalent bonds in the range of nN.

In the following, I will focus on the description of a magnetic tweezers setup since it is the technique I used for most of the experiments, and I will briefly describe the AFM as well, because it was necessary for some complementary measurements.

4.2 MAGNETIC TWEEZERS TECHNIQUE

The first magnetic manipulator was developed by Amblard et al. [143], but it was just a precursor of the magnetic tweezers, the first modern MT setup is reported by Strick and co-workers in 1996 [144]. They bound one end of DNA molecules to a functionalized glass cover slip, and the other end to a magnetic bead. By using small magnets to create a magnetic field they exerted forces to the DNA-tethered beads. It was possible to pull and stretch DNA single molecules at forces ranging from 6 fN to 20 pN and they were also able to induce a supercoiling state to the torsionally constrained DNA by rotating the magnets. The most striking result of this paper was the observation of a transition from the supercoiled plectonemic state to the extended denaturation state, which confirmed the intrinsic chirality of DNA: if the molecules were underwound this transition occurred at $\approx$ 0.45 pN, while for overwound molecules the transition force was around 3 pN in their buffer conditions (10 mM of phosphate buffer). It became clear later that the transition for a positively supercoiled DNA is completely different from the melting, see section 1.2.2 and chapter 7 for details about DNA phase transitions.

Among single molecule techniques the MT have several advantages: first of all it is the most straightforward and cheapest setup to build, it has a simple and robust experimental configuration, without the need for a feedback to control the applied force. This method

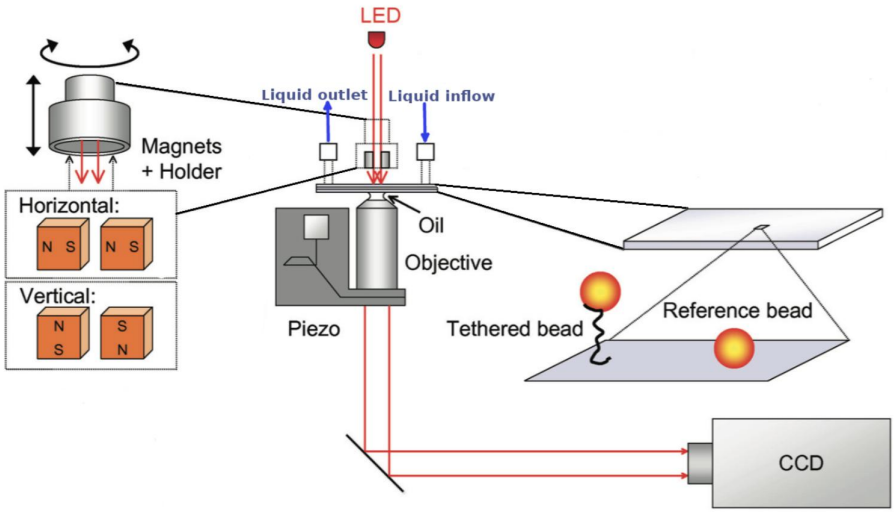

Figure 4.1.: Scheme of a typical magnetic tweezers setup. The two possible configurations of the magnets are reported, the horizontal geometry is that one used in this work. Figure adapted from [145].

can be easily applied for multiplexing measurements and can be readily integrated with fluorescent microscopy. Finally, as previously described, MT is the only instrument capable of inducing a torsion to DNA molecules and finely monitoring supercoiling dependent processes.

A typical magnetic tweezers setup consists of an optical inverted microscope coupled with a micro-movement apparatus of permanent magnets and an illumination system equipped with a LED as light source, see figure 4.1 for a scheme of MT configuration. A camera collects the images from the focal plane. A piezoelectric crystal is used to move the objective with an axial accuracy of up to 10 nm and two motors are usually employed for movements in x-y directions, see section 4.2.2. In order to apply a stretching force and a torque, the DNA molecules have to be connected to the surface of a glass coverslip by one end and to a magnetic bead by the other end. DNA fragments tails are properly functionalized to link the coverslip and the bead, as described in the next chapter.

There is also an alternative MT configuration with electromagnets creating a magnetic field with the possibility of 3D manipulation of the magnetic beads and thus the DNA molecules. Main disadvantages of this setup are a smaller magnetic field gradient, implying smaller forces, and an heating of the biological sample because of the electric current.

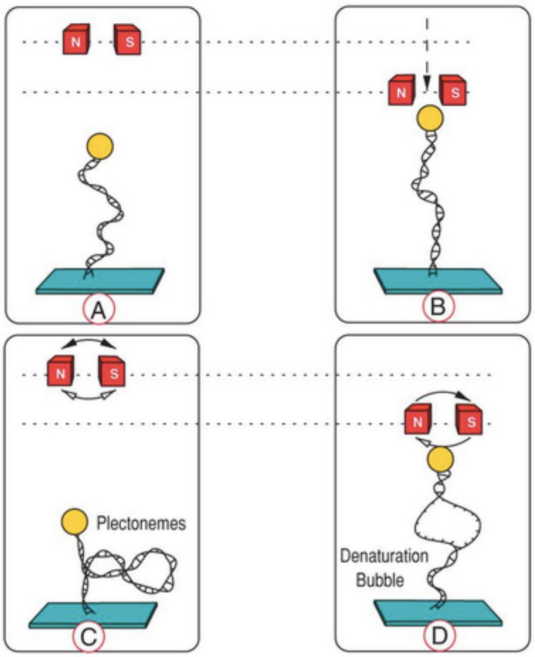

Figure 4.2.: The two operation principles of magnetic tweezers: a stretching force is applied to a DNA molecule by vertically moving magnets (A-B). A torsion is induced to the DNA molecule by rotating the magnets: when the force is low plectonemes are formed (C), whereas if the force is high melting bubbles are created (D). Figure from [138].

4.2.1 *Working principle and setup description*

A MT setup can basically work through two operation principles:

- **Pulling force experiment**: magnets have a fixed angle and they are moved up or down. In this way the applied force varies as a function of the magnets position (see section 4.2.3). The force exerts a mechanical deformation of stretching on DNA molecules.

- **Twisting experiment**: magnets are held at constant height, i.e. constant force, while they are rotated to apply a torque to the torsionally constrained DNA molecules.

These two working principles are schematically shown in figure 4.2 .

A few pictures of the magnetic tweezers setup used for this thesis project are reported in figure 4.3 and it has been previously described [138, 146]. The setup consists of an optical inverted microscope equipped with an oil-immersion objective (NIKON 100x, $NA = 1.25$) mounted on a piezoelectric focusing system (PIFoc, Physik Instrumente, Italy). The objective is coupled with a 15 cm focal-length lens leading to a real 75x magnification. The light source is a green light-emitting diode (LED), or alternatively it is possible to use a su-

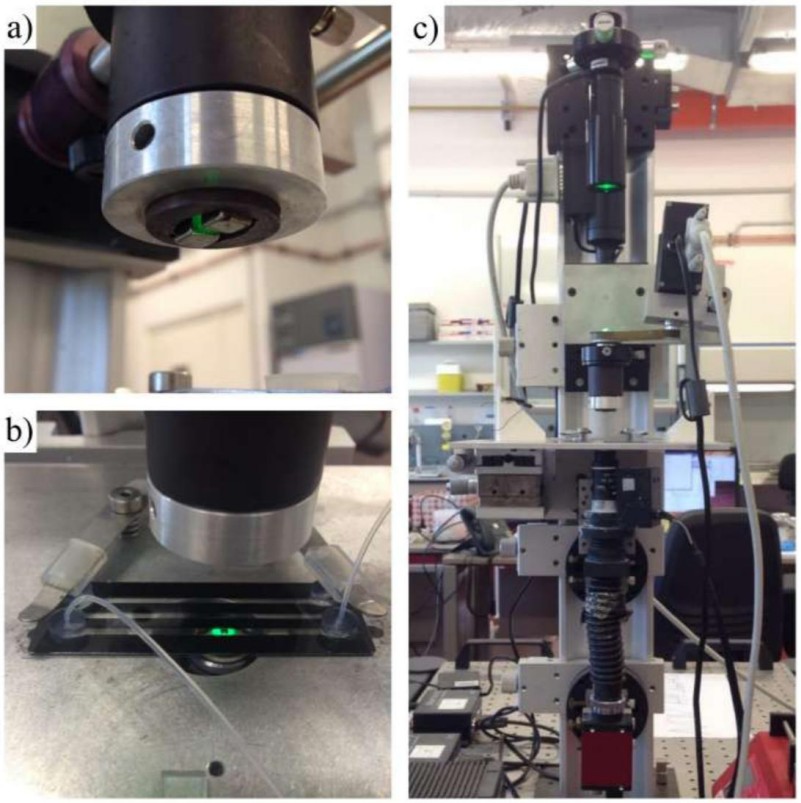

Figure 4.3.: Pictures of the MT setup used for the experiments of this thesis project.

perluminescent diode in order to reduce the exposure time of the camera and study faster kinetics. The charge-coupled device (CCD) camera (Marlin, Allied Vision Technologies) collects images at a frame rate of 50 Hz and it is connected to a computer to analyze them in real time .

The magnetic field is generated by a micro-movement apparatus of two permanent magnets placed above the flow chamber. Two motors control the position of the magnets along the optical axis (z-direction) and the rotation around the same axis. The magnets are two cubes of 3 mm by side separated by a 2 mm gap and they are in horizontal configuration (see figure 4.1). The magnetic material is neodymium iron boron ($Nd_2Fe_{14}B$), the strongest available alloy that enables to reach a magnetic field higher than 1.3 T. An iron ring surrounds the two magnets to create a magnetic circuit that conveys the magnetic flux and to reduce stray fields. The magnetic field decreases exponentially moving away from the magnets, therefore generating a gradient field along the optical axis [147].

The flow chamber is connected to a fluidics system and inserted into an home-made alluminium sample holder. The channels where the biological sample is loaded are created by sandwiching a glass coverslip and an adhesive polycarbonate film shaped with three flow

channels, see figure 4.3(b). The plastic film is 250 μm thick and custom-made by Grace BioLabs. There are inlet and outlet holes at each end of the channels, with the possibility of glueing press fit tubing connectors. In this way it is possible to connect the flow chamber with tubings (0.455 mm thick) and a syringe pump enabling the monitoring of the flow rate into the channels. The glass coverslip of the camber must be properly functionalized to bind DNA molecules: firstly it is carefully cleaned by a sonication for 10 minutes in potassium hydroxide (KOH), deionized water and ethanol. After that, a solution of 0.02 μg/ml anti-digoxigenin in 150 mM PBS (Phosphate Buffered Saline) is incubated for 2 hours at room temperature and in a wet chamber to avoid evaporation. The chamber is then rinsed with PBS and the surface of the glass coverslip is passivated with 10 mg/ml or 100 mg/ml of bovine serum albumine (BSA) for two hours at room temperature or overnight at 4°C. Finally, the chamber is rinsed again with PBS and dried with compressed air. These chambers can be stored at −20°C for several months.

4.2.2 *Optical calibration*

The MT setup can measure the extension of DNA molecules in real time by exploiting an optical calibration method based on the diffraction pattern generated by the magnetic beads tethered to DNA.This method of detecting DNA extension was first described by Gosse and Croquette in 2002 [139]. The objective focal plane is accurately shifted along the axial direction by finely moving the objective mounted on the piezoelectric. This process creates a series of diffraction rings of the magnetic beads and the images thus created change as a function of the axial position of the beads, see figure 4.4(a). These images are recorded by a camera and a calibration profile can be generated by correlating the diffraction pattern to the distance of the bead from the objective focal plane, figure 4.4(b)-(c). The difference between two measured distances gives the vertical extension of a DNA tether. This calibration procedure enables to determine the axial position with an accuracy of ∼ 10 nm. A diffraction pattern easy to calibrate needs an illumination source fulfilling the following requirements: monochromaticity, incoherence and relatively high intensity, such as the LED used in my MT setup, such as in most of these experimental setups.

An analogous calibration is performed for a reference bead attached to the surface of the glass coverslip and close to the tethered bead, thus obtaining the distance of the glass surface from the objective focal plane. In figure 4.5 an example of a typical field of view including the tracking of a tethered and a reference bead. The advantage of a differential measurement between these two optical calibration profiles is the strong minimization of thermal drift effects, mainly due to the oil between the objective and the flow chamber. As will be shown

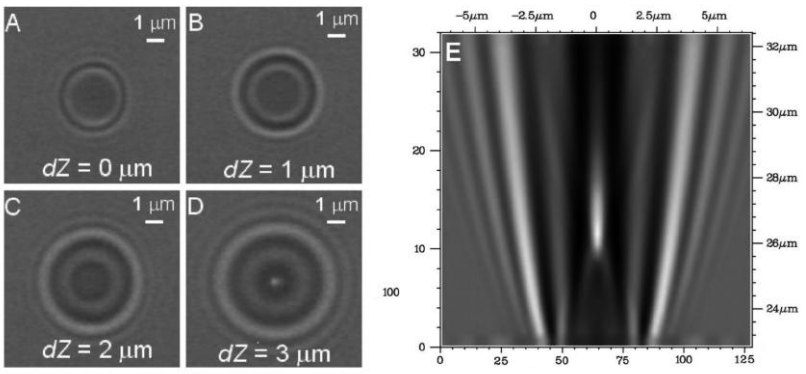

(a)

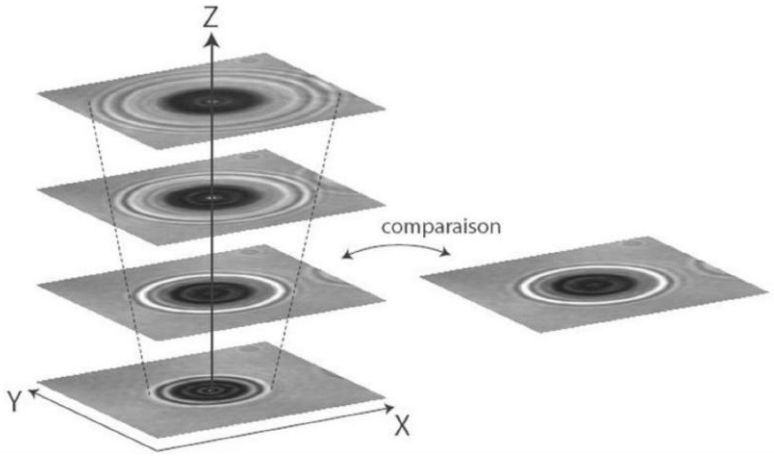

(b)

Figure 4.4.: **(a)** Left: diffraction rings formed by a 3 μm magnetic bead at four different positions along the axial direction. Right: Calibration profile related to the intensity of the diffraction rings at several positions.
(b) Schematic representation of the stack of images recorded by the camera. Figures adapted from [145].

in the next paragraph, the fluctuations of the beads are necessary to calculate the applied force, not only the tether vertical extension. These calculations are computed by a cross-correlation analysis of the calibration intensity profiles. The tracking on the x-y plane can be carried out with the same accuracy of the vertical one, with a resolution of a few nanometers.

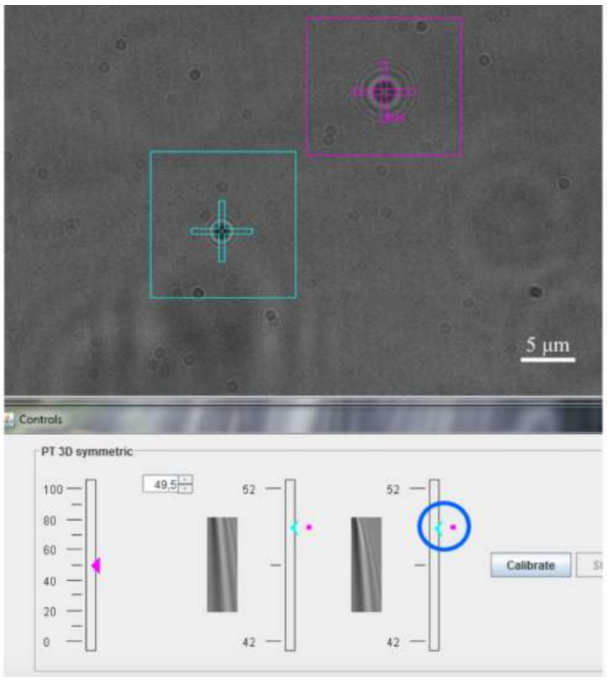

(a)

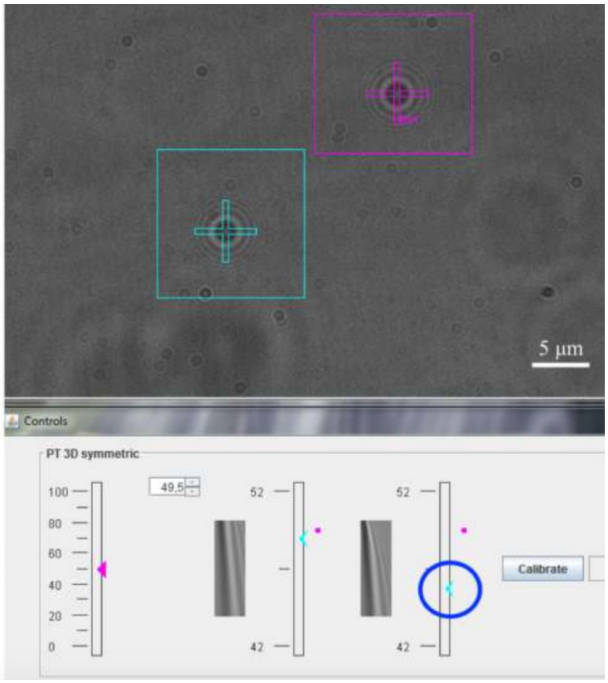

(b)

Figure 4.5.: Field of view with tethered (blue cross) and reference bead (pink cross). Crosses indicate the tracking of the beads by an home-made software. The field of view is recorded at high force **(a)** and low force **(b)**, as shown by bottom panels reporting calibration profiles. The blue arrow is the real-time measurement of the distance from the objective focal plane, while the pink one corresponds to the intensity value recorded in the objective focal plane during calibration (at high forces). At low force the distance from the objective focal of the reference bead does not change, while in the tethered bead a distance of about 3 µm is observed (blue circle), corresponding to the expected DNA extension.

4.2.3 *Calculation and calibration of the force*

The magnets of a MT setup (figure 4.3(a)) create a magnetic field that is applied to the magnetic beads, thus generating the following force

$$F = \frac{1}{2}\nabla(\mathbf{m} \cdot \mathbf{B}) \tag{4.1}$$

where $\mathbf{m}$ is the magnetic moment of the bead induced by the external magnetic field $\mathbf{B}$. This equation shows the relation between the applied force and the local magnetic field gradient: the movement of the magnets along the axial direction changes the field gradient in the proximity of the beads, particularly if the magnets are moved downward (closer to the flow chamber) the applied force increases, while moving the magnets upward the force decreases, see figure 4.6. The variations of the magnetic field are in the range of millimeters, consequently it can be considered constant for the micron-sized magnetic beads.

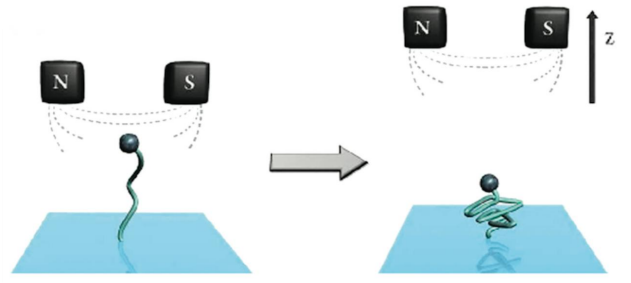

Figure 4.6.: The movement of the magnets in a MT setup along the axial direction (z-direction). When magnets are lowered towards the chamber the force is higher and DNA is stretched (left), while they are far from the sample the force is low (right).

An MT setup is usually used to investigate nucleic acids, or possibly proteins, whose diameter is a few nanometers. In biology the typical reference value of the energy at the single-molecule level is the hydrolysis of ATP, around $20\,k_BT \approx 80\,pN \cdot m$ [139]. It follows that the resulting forces needed during an MT experiment should be in a range between fN and pN. The experimental configuration adopted during this thesis work can apply forces between tens of fN up to $\sim 5\,pN$ by using the 1 µm magnetic beads, while for higher forces applications it has been possible to use 4.5 µm magnetic beads, enabling to reach about 100 pN.

Since before applying a magnetic field the magnetization of the beads have a slight anisotropy, there is a small part of (m) not aligned with $\mathbf{B}$ at the beginning. The external magnetic field tends to align the magnetic moments, which generates the torque

$$\Gamma = \mathbf{m}_0 \times \mathbf{B} \tag{4.2}$$

where $\mathbf{m}_0$ is the initial magnetic moment.

Let us consider now the total energy of the system studied during MT measurements, the DNA-tethered bead. There are two main forces acting on the magnetic bead: the external magnetic force applied by the magnets, F, and the restoring force exerted by the DNA molecule. The latter can be approximated with the elastic force of a spring for reasonably low values of F.

$$U_{tot} = U_{DNA} + U_{mag} = U_{DNA}(L_e) - Fz \tag{4.3}$$

where $U_{DNA}(L_e)$ is the mechanical energy stored by the nucleic acid, depending on the end-to-end extension of the molecule L_e, and z is the position of the bead along the axial direction. When the bead reaches the equilibrium, the partial derivatives of the total potential energy along each axis are equal to zero

$$\frac{\partial U_{tot}}{\partial x} = \frac{\partial U_{tot}}{\partial y} = \frac{\partial U_{tot}}{\partial z} = 0 \tag{4.4}$$

in particular considering the z direction the following condition holds

$$\frac{\partial U_{tot}}{\partial z} = \frac{\partial U_{DNA}(L_e)}{\partial z} - F = 0 \implies F = \frac{\partial U_{DNA}(L_e)}{\partial z} \tag{4.5}$$

The equilibrium position of the bead is $\mathbf{r_0} = (x, y, z) = (0, 0, L_e)$, but the the Brownian motion continuously pushes the bead out of equilibrium, see the schematic in figure 4.7. When the force along the axial direction is high enough the fluctuations in x-y plane are small, this makes it possible to compute a Taylor expansion around the equilibrium position

$$\frac{\partial^2 U_{tot}}{\partial x^2} = \frac{\partial^2 U_{tot}}{\partial y^2} = \frac{F}{L_e} \tag{4.6a}$$

$$\frac{\partial^2 U_{tot}}{\partial z^2} = \frac{\partial F}{\partial L_e} \tag{4.6b}$$

resulting in the following equation for the total energy around the equilibrium position

$$U_{tot}(\mathbf{r}) \approx U_{tot}(\mathbf{r_0}) + \frac{1}{2}\left(\frac{F}{L_e}\right)\delta x^2 + \frac{1}{2}\left(\frac{F}{L_e}\right)\delta y^2 + \frac{1}{2}\left(\frac{\partial F}{\partial L_e}\right)\delta z^2 \tag{4.7}$$

The equation 4.6a derives from the analytical form of the potential energy of the system, equivalent to an inverted pendulum (figure 4.7A) of length L_e and having an elastic energy

$$U_{tot}(L_e) = \frac{1}{2} k L_e^2 \tag{4.8}$$

which corresponds to the energy stored in a spring with elastic constant k. As well known the elastic constant, or the stiffness, of a spring is $k = \dfrac{F}{L_e}$.

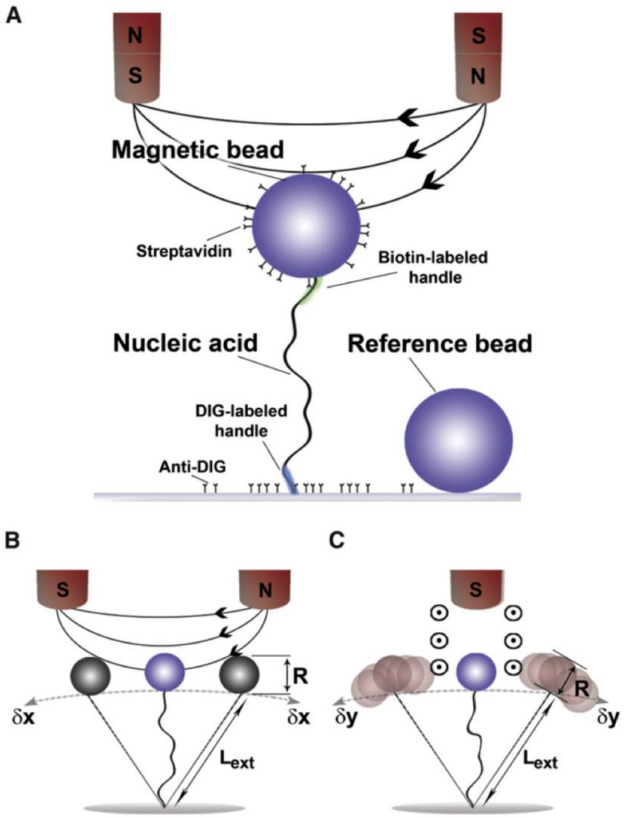

Figure 4.7.: Schematic of the oscillations of a magnetic bead during Brownian motion. **A.** Representation of the DNA-tethered bead, the reference bead and the magnetic field lines (black lines). **B.** Fluctuations of the bead in the x direction, along the major component of the magnetic field. **C.** Fluctuations in y axis, perpendicular to field lines and producing lower oscillations. Figure from [148].

Now, if the potential energy in the equilibrium position $\mathbf{r}_0$ is set to zero, the average potential energy as a function of the small displacements in the objective focal plane can be written in one dimension as follows

$$\langle U_{tot} \rangle = \frac{1}{2}\left(\frac{F}{L_e}\right)\langle \delta x^2 \rangle \tag{4.9}$$

Observing this equation it is clear that the quantity $\dfrac{F}{L_e}$ is the effective stiffness of the magnetic trap, equivalent to the elastic constant of a spring, while δx^2 is the variance of the bead oscillations in the x direction around the equilibrium position.

$$\sigma_x^2 = \langle \delta x^2 \rangle - \langle \delta x \rangle^2 = \langle \delta x^2 \rangle \qquad (\langle \delta x \rangle = 0) \tag{4.10}$$

The *equipartition theorem* enables to balance equation 4.9 to the energy $\frac{1}{2}k_BT$ corresponding to one degree of freedom. Finally, this yields to the following expression of the force

$$F = \frac{k_BT}{\sigma_x^2}L_e \tag{4.11}$$

that can be easily calculated by measuring the extension of the studied DNA molecule and the variance of the bead motion in x direction. As the fluctuations of the bead in the objective focal plane increase, the applied force F decreases. This is clearly represented in figure 4.8.

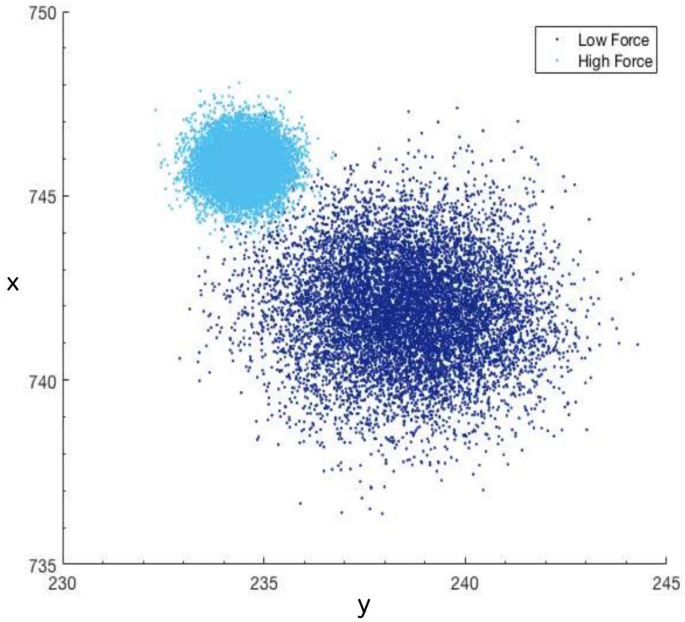

Figure 4.8.: Example of the fluctuations of a bead in the x-y plane, at high forces (light blue) and low forces (dark blue). The elliptic shape of the clouds confirms that oscillations in x direction, i.e. along magnetic field lines, are bigger (see figure 4.7).

One of the most important quantities to know for precise MT measurements is the applied force F. Therefore, an accurate calibration of the force is crucial for the experiments. In equation 4.11 we observed that the calculation of the force requires the measurement of DNA end-to-end extension and bead fluctuations in x-y plane. These fluctuations induced by Brownian motion show an asymmetry: in the x axis, the direction of magnetic field lines, the oscillations of the bead are smaller, that means the resulting force is higher, whereas along y direction fluctuations are bigger and force lower (see figure 4.8). This detail is very useful when a more precise measurement of the force is necessary, because the measurement of bigger fluctuations is easier. Therefore, the axis perpendicular to magnetic filed is often preferred for the calculation of the force during some experiments.

The calibration of the force firstly needs to associate each magnets position (MP) to the values of the applied force F. MP is defined as the distance between the magnets and the flow chamber. The calibration procedure consists in recording a pulling force experiment at null torque: magnets are moved in the axial direction by keeping the rotation fixed. DNA extension L_e and the applied force F are measured as a function of MP, see figures 4.10 (red curve) and 4.9. Force data points (blue circles in figure 4.9) are fitted with a decreasing exponential law and a calibration curve is computed. This enables to study the behavior of DNA extension as a function of the force, the $L_e(F)$ reported in figure 4.10 (black curve), the typical data from force-extension experiments.

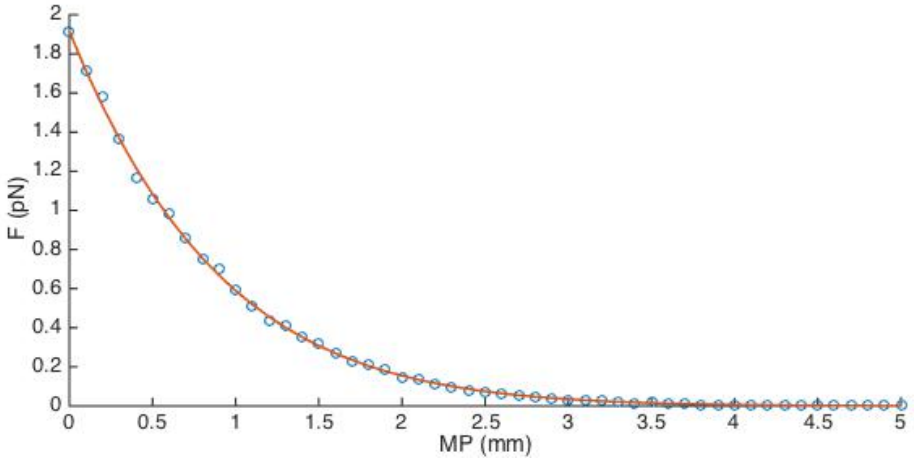

Figure 4.9.: Measured force (F) as a function of magnets position (MP). Blue circles are the data points while the red solid line is the decreasing exponential fit.

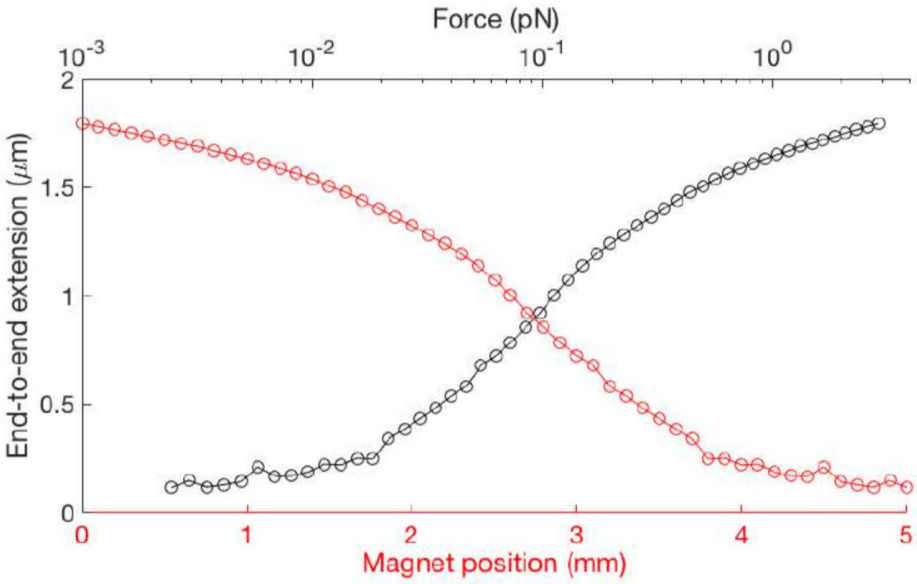

Figure 4.10.: End-to-end extension of a DNA molecule (L_e) as a function of magnets position (red curve) and applied force (black curve).

4.3 ATOMIC FORCE MICROSCOPY

The first Atomic Force Microscopy was realized in 1986 by Binnig, Quate and Gerber [149] and its principles are based on the Scanning Tunneling Micrscope (STM), an AFM precursor discovered in the early 1980s thanks to which Binnig won the Nobel Prize for Physics together with Rohrer in 1986. In a STM setup the measured physical quantity is the distance between the surface and a specific probe. After having recorded two-dimensional profiles at very high frame rate, the topography of the surface is reconstructed in three-dimensions. On the other hand, an AFM setup monitors the bending of a cantilever in the vertical axis: the instrument works as a nanoscale phonograph.

The first application of this instrument was the investigation of surface morphology, but several applications emerged in a wide variety of fields over time, such as in microelectronics or biology. Indeed nowadays the AFM is one of the most powerful tools for probing biological systems proprieties. It is extremely sensitive to forces, so it has become one of the main techniques to measure cell mechanics or to nanomanipulate single biomelocules. For example AFM is the method of choice to study the unfolding mechanism of proteins [150] and it was the first single-molecules technique to observe the overstretching transition in DNA molecules [124].

4.3.1 *Setup description*

A conventional AFM setup consists of a cantilever with a sharp tip on one end, a laser beam that hits the back of the tip and is reflected in the direction of a four-quadrant photodiode detector, see figure 4.11.

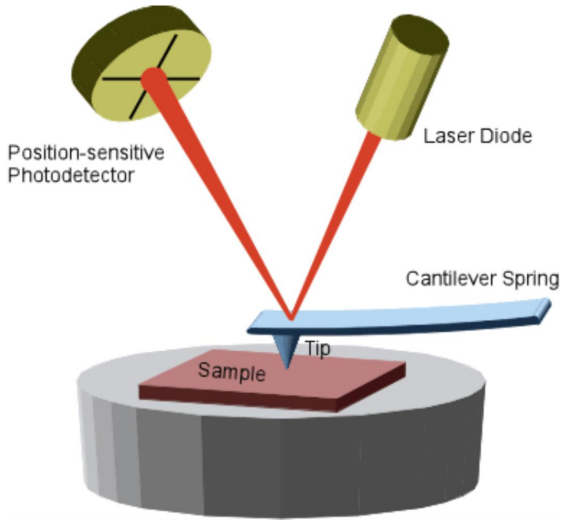

Figure 4.11.: Schematic of a conventional AFM setup.

Figure 4.12.: Picture of the commercial AFM setup used for this thesis, the Life Science Nanowizard II ®from JPK Instruments, Berlin.

The photodiode collects and converts the laser light in electrical signal which enters in a feedback process. The setup is completed by a stage on which the sample is positioned, a camera and an optical or fluorescence microscope in some versions, as the instrument used for this thesis, shown in figure 4.12. The Life Science Nanowizard II (JPK Instruments, Berlin) is mounted on an inverted microscope, the Zeiss Axiobserver A1. The whole instrument is positioned on an active vibration isolation platform and it is enclosed into an airtight chamber that minimizes external noises. The chamber is fitted on an optical table insulated from the ground by four air bearings. These arrangements serve to have an optimal insulation of the instrument from external agents.

The cantilever and the tip are usually made of Silicon Nitride (Si_3N_4), since this material has a good uniformity which enables a proper reproducibility of results [151]. Cantilevers could be coated by gold in order to increase the reflectivity of the laser beam. Basically there are two possible geometries of the cantilever: rectangular arm or triangular arm, whose length is of the order of 100 µm (see figure 4.13). The geometry of the cantilever determines its mechanical properties, therefore the choice of the proper cantilever is crucial and depends on the investigated sample. The tip is attached on one end of the cantilever and it is very sharp, available in different sizes and shapes. As with the cantilever, the selection of the tip is important according to the analysed sample. The properties of the probe could be varied, for instance the length of the arms on which the tip is mounted or

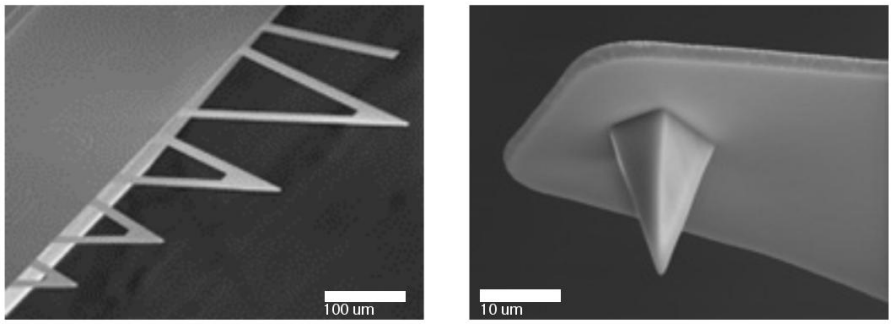

(a)

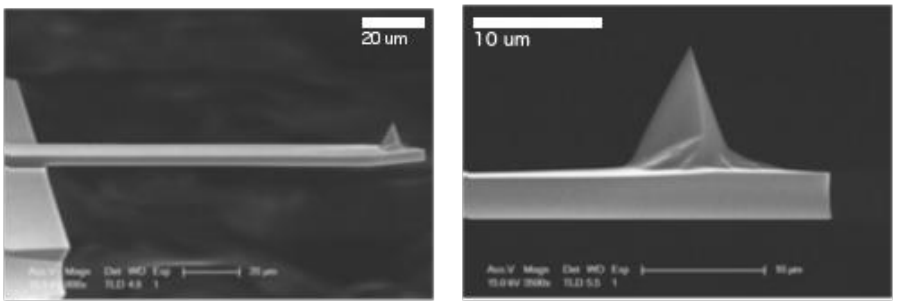

(b)

Figure 4.13.: Pictures of cantilevers for different applications, from imaging in contact mode or force spectroscopy (top) to imaging in tapping mode (bottom). Figures adapted from Bruker official website.

their width. The physical parameters define the elastic constant of the probe: a very soft cantilever results in a higher resolution in the detection of laser deflection, i.e. the more the cantilever bends the more the laser beam is deflected. However, the use of soft cantilevers, with low spring constant, has the disadvantage of having a probe very sensitive to thermal noise. It is therefore necessary to balance appropriately these two conflicting requirements, sensitivity and thermal noise, by means of proper calibration procedures.

4.3.2 *Working principle*

The standard procedure to perform an AFM experiment is the following: the tip approaches the surface of the sample under investigation and then it is retracted by a piezoelectric actuator which records the position with a subnanometer resolution. The displacements of the laser on the photodiode detector, induced by the deflections of the cantilever, enables to achieve quantitative information about the surface features or about the interactions between the tip and the sample. The deflections of the cantilever are caused by interaction forces between the tip and the substrate, occurring while the tip is approaching the sample. These interactions could have different origins, when

electrostatics is involved, such as in the case of the topographically mapping of surfaces, the tip undergoes a van der Waals interaction attractive force. However, moving closer and closer to the surface of the sample, the interactions become repulsive and they are not described by van der Waals laws, but by a Lennard-Jones repulsive potential. The probe therefore switches from a weak attraction to a strong repulsion from the surface. The scanning of the surface allows to map the topology of the surface, whereas pushing the tip on the surface and then raising it back enables to measure the local force interactions between the tip and the sample [152].

These interactions induce a change in the position of the reflected laser beam on the photodiode detector, forming an optical lever system. As above mentioned, the laser beam reflected by the cantilever hits a photodiode recording the displacement (in Volts) of the beam from a reference point. The distance between the cantilever and the detector is much greater than the size of the cantilever, as consequence small movements of the cantilever can be translated into displacements of the reflected beam large enough to be visualized. The cantilever is modelled as a Hookean spring with a known elastic constant, so it is possible to convert the measured voltage to a force. The deflection is measured within a nanometer accuracy, and the force sensitivity is in the pN scale. The piezoelectric actuator is able to move the cantilever in the 3D space with a resolution of ~ 1 nm.

An AFM can be used in two main modes:

- **imaging mode** the AFM probe scans the surface of the sample line after line and a proportional derivative (PD) feedback corrects instantaneously its vertical position. This mechanism guarantees that the force is kept during the scanning of the sample.
- **force spectroscopy** the cantilever is moved along the vertical direction, perpendicularly to the sample plane, with a constant speed between 30 and 3000 nm/s, while its position is recorded. Another method to work in force spectroscopy mode is keeping constant the bending, the deflection of the cantilever by adjusting the position of the tip. This method is called force clamp mode.

In both cases, the accuracy of the experiments relies on the response time of the feedback process. During the experiments presented in this thesis project I only used the AFM in the imaging mode, this is why I am going to describe it in more detail.

4.3.3 *AFM imaging mode*

In the previous paragraph I have already explained that when the tip of the cantilever is close enough to the specimen it is attracted or repelled from its surface, and this phenomena induces deflections

of the cantilever. The related variations in the voltage of the piezoelectric crystal controlling the vertical position of the cantilever are recorded and converted, in order to produce a 3D image of the surface topography.

The most common strategy to carry out AFM imaging experiments is the *contact mode*: the tip and sample are maintained in close contact during the scanning process, consequently they feel a repulsive Lennard-Jones potential. The major drawback of this imaging strategy is the presence of large lateral forces on the sample due to the dragging of the tip in contact with the specimen. These lateral forces often causes damages to the tip and to the sample, especially for soft biological specimens, for crystalline surfaces these damages are generally not a big issue.

Therefore, an alternative imaging strategy has been developed: the *tapping mode*: the cantilever is oscillated at the resonant frequency, in the range of hundreds kHz, so when it is approached to the surface of the sample the contact occurs only for a small fraction of its oscillation period. The interaction regime is still repulsive as the contact mode, but the very short times over which the contacts occurs dramatically reduce the lateral forces acting on the sample and on the tip.

In this work, AFM imaging technique was employed during the analysis of the mechanical properties of the DNA analogue (chapter 6) and to observe the crowding effects on DNA induced by PEG (section 9.2). In the DNA analogue project, images were acquired in tapping mode, in air, using stiff silicon cantilevers (RTESO-Veeco) with a spring constant of about 40 pN/m and resonant frequencies of 300-350 kHz. 8×8 μm images were collected at a 0.5-1 Hz scan rate and 2048×2048 pixel resolution. Several hundred DNA molecules were recorded from several widely-spaced areas of each sample and processed with a standard "flatten" filter in the JPK Data Processing software. The morphological characterization of the DNA samples relies on the tracing of individual DNA fragments by means of a custom-tracing routine described in [153] and enabling the calculation of DNA contour length values [154]. The analysis of the distance between points along DNA molecules plotted as a functions of their separation along the contour length provided an estimation of the persistence length [155–157].

Concerning experiments of DNA in presence of PEG1500, the tip needs to be sharp enough to obtain the desired resolution. Probes (RTESP-300, Bruker Nano) are composed of 0.01-0.025 Ohm-cm Antimony (n) doped Si and without coating. The cantilevers have a spring constant of 40 pN/m and a nominal resonance frequency of 300 kHz. Experiments are performed in air. The 4×4 μm images had

a 1024×1024 pixel resolution and they were collected at a 0.5-1 Hz scan rate.

4.4 INTRODUCTION TO SINGLE-CELL MICROSCOPY METHODS

Bacterial cells contain proteins and other molecules, such as mRNAs, in low and varying numbers per cell, this condition randomizes the cellular behavior and strongly affects the cell cycle. The stochastic feature of numerous biological processes inside the cell has limited for many years the comprehension and analysis of some aspects of microbiology: the cell growth, the mutation rate, the cell senescence or the DNA damage responses, to name a few. The development of new microfluidic devices, together with more reliable and faster imaging technologies, enabled to monitor individual cells over long time periods and perform image-based analyses of the kinetics of cellular mechanisms [158]. Moreover, by means of these methods it is possible to grow cells under precisely controlled conditions and to count fluorescent molecules inside the cells, for example.

The first strategy to monitor the cell growth over time has been to seed bacteria on agar pads and observe the behavior of micro colonies [159–163]. The issues of this technique are the low throughput and the limitations in recording long time series, implying difficulties of monitoring cell lineages. The advantages of using agar pads still remain their simplicity and low cost of fabrication. However, alternative methods are increasingly preferred to agar pads because of their inability of easily acquiring time-lapse measurements. There are several alternative methods based on microfluidic devices developed in recent years, I will briefly mention a few of them.

4.4.1 *Linear trench and monolayer*

The first study reported in literature to follow the cell growth of individual bacteria in a microfluidic device is based on linear trenches engraved in PDMS (Polydimethylsiloxane), where a small number of cells are seeded [164]. Trenches are enclosed in a permeable membrane, in this manner cells are fed by diffusive flow, see figure 4.14(a). This strategy enables to feed cells more uniformly compared to agar pads and additionally to change media is more straightforward and fast. The limitation of this technique is still related to the difficulties of collecting long time series, because trenches filled up with cells during the experiment.

The monolayer growth chamber chip finally enabled to carry out long time-lapse experiments [165, 166]. The bacterial cells are confined into a two-dimensional monolayer and continuously fed by flowing media on both sides of the colony, see figure 4.14(b). This

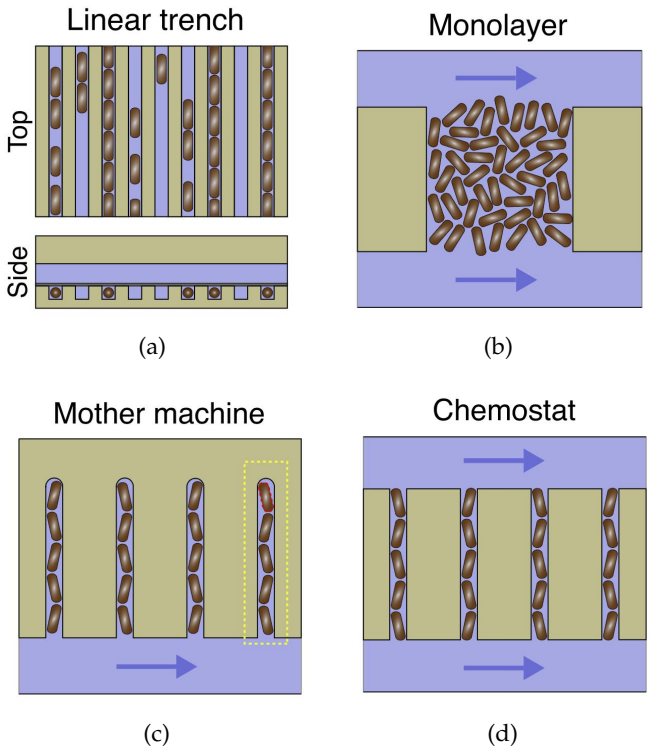

Figure 4.14.: Examples of microfluidic devices for single-cell experiments: **(a)** linear trench, **(b)** monolayer growth chamber chip, **(c)** mother machine, **(d)** chemostat. Figures adapted from [158].

technology made it possible to observe oscillations in gene expression over several generations and community behaviors [167]. The most severe limitation of this device is the lack of suitable uniform conditions in the chamber.

4.4.2 *Mother machine and chemostat*

The mother machine is one of the most successful methods for single-cell experiments and it was developed by Jun in 2010 [168]. This device consists of a series of channels oriented at right angles to a trench through which the growth medium flows at a constant rate, see figure 4.14(c). After the bacterial cells fill up the channels, they start to emerge from the channels and consequently are washed away from a continuous flow of fresh medium, figure 4.15. This technique enables to monitor the growth and the division of a small linear colony of constant size, following up to 700 consecutive generations [169].

The device developed by Jun group has channels closed on one end and the cell at this end is called "mother cell", because one of its poles, the old pole, is inherited to all the subsequent generations, figure 4.15A-B. There is an alternative design, where channels are open on both ends, called single-cell chemostat [170, 171], see figure 4.14(d).

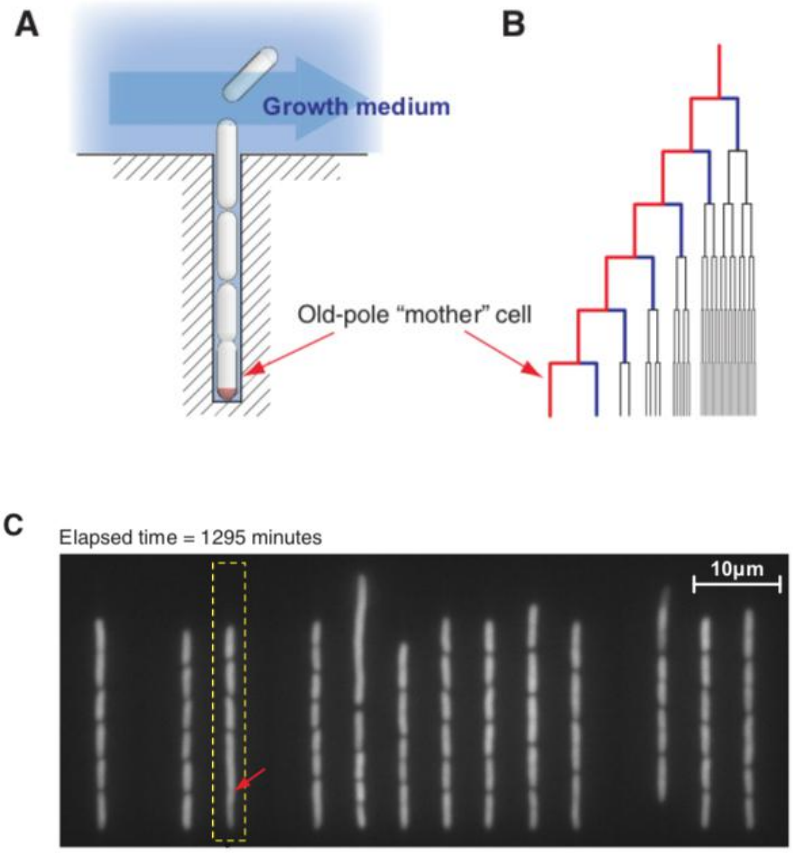

Figure 4.15.: The mother machine device. **(A)** Schematic of a channel of the mother machine, with the mother cell is trapped at its end.
(B) Lineages tree reporting the old-pole mother cell and the progeny.
(C) Typical field of view during a mother machine experiment, with a number of channels filled with bacterial cells. Figure adapted from [168].

In this device there is not an old pole of the mother cell and daughter cells are washed away from both ends, thus avoiding aging.

The channels of these microfluidic devices are usually slightly deeper than the cell diameter, so as to avoid to squeeze cells, and can be placed very close to each other to achieve a larger statistics or well separated to reduce the spill-over fluorescence. Moreover, shorter channels have a more uniform feeding but cells are washed away more easily.

4.5 THE MICROFLUIDIC CHAMBER

The microfluidic device I used for the experiments of this thesis is a sort of compromise between the agar pads and the mother machine, aiming to gain the advantages of both methods: the fabrication is eas-

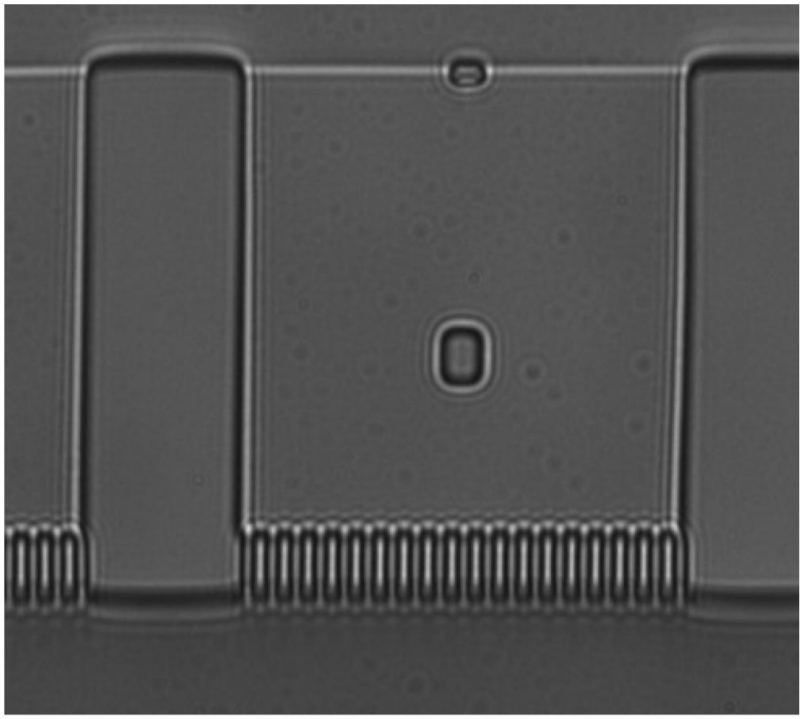

Figure 4.16.: Picture of the PDMS microfluidic chamber used for single-cell experiments. In this example a $30 \times 30\,\mu m$ channel separated from neighbouring ones is reported. On the bottom end there is the filter, while the object in the center of the channel is a pillar necessary to support the structure of bigger channels. Figure adapted from Bianca Sclavi Lab (Debayan Saha's thesis).

ier and faster compared to mother machine devices, but at the same time it enables to monitor the cell growth over long time intervals and under controlled conditions, similarly to the mother machine. This device is the PDMS microfluidic chamber reported in figure 4.16: a series of micron-sized channels perpendicular to a couple of trenches where the growth medium flows at a constant rate. This design is conceptually very similar to the mother machine, but channels are an order of magnitude wider and both their ends are open. More precisely, the channels are asymmetric at their ends: one end is large to promote bacterial cells flowing inside the channel, whereas the other end has half micron spaced micro-pillars acting as a filter for the cells, that theoretically are too big to fit through. A similar design has already been discussed in [172], where authors investigated the ordering parameter of *E. coli* cells in two channels of different geometry.

The channels of this microfluidic chamber have different sizes and geometries, the width and the length range from 15 to 60 μm, in figure 4.17 three examples are reported. Each combination of size and geometry has its advantages and disadvantages.

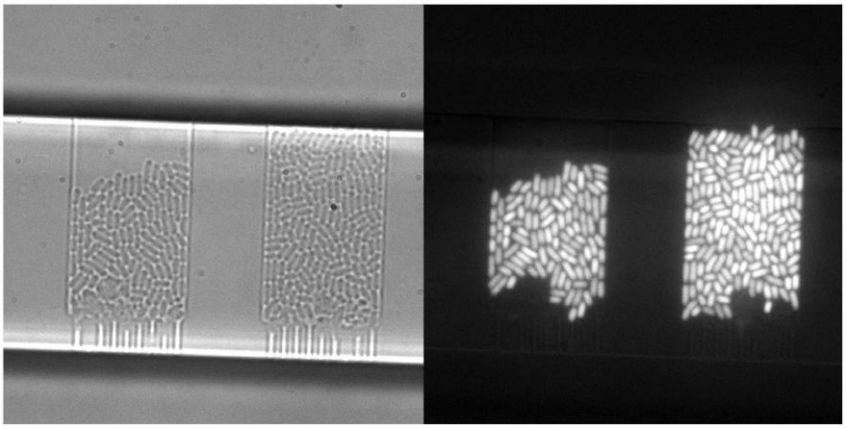

(a)

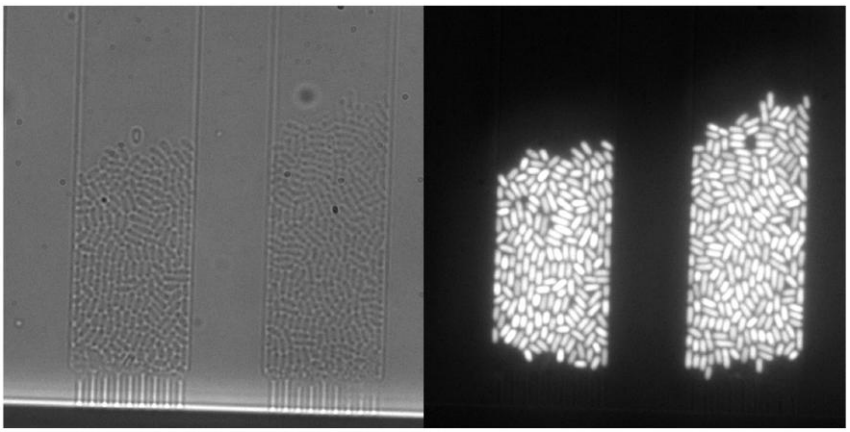

(b)

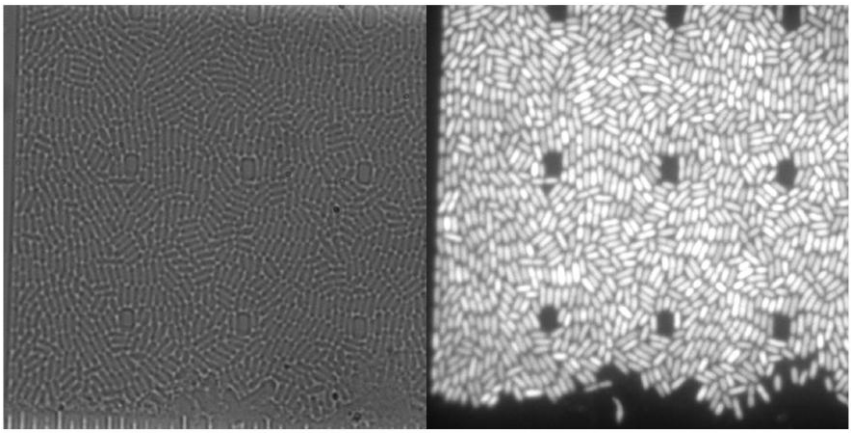

(c)

Figure 4.17.: Bright-field (left) and fluorescence (right) images of bacterial cells filling up channels of different geometries (length × width): **(a)** 30 × 15 µm, **(b)** 60 × 15 µm, **(c)** 60 × 60 µm.

For example in short channels (15 μm) bacterial cells are washed away very readily compared to 30-60 μm long channels. On the other hand, in wider channels bacteria are less aligned in average, adopting more random orientations, thus leading to a more complicated cell segmentation and tracking. All the channels are 1-1.2 μ deep, while the two trenches for the growth medium are 19 μm deep and 50 μ wide.

In comparison to the mother machine, this microfluidic device has still more problems in achieving long time dependent lineages, because cells can move a bit faster and in a more random orientation in contrast to the small linear colonies of mother machine. Nevertheless, the microfluidic chamber has the clear advantage of a much larger statistics compared to mother machine or chemostat devices, thereby increasing the probability to observe rare events such as cell mutations, which maybe could not have occurred in a mother machine due to the spatial constraints of thin channels (see section 10.4). The presence of the filter on one end, instead of a closed or a completely open end, makes it possible to have a continuous flow of fresh medium along the whole channel, this limits gradients of nutrient and at the same time prevents a too fast motion of the cells that cannot escape from both ends.

4.5.1 *Protocol preparation of the chambers*

The starting mould of the microfluidic chamber is made of silicon and was produced by Kevin Dorfman, at the University of Minnesota (USA), a collaborator working on the microfluidics devices for these single-cell experiments. The PDMS for the chambers is prepared and poured on the mould by following a standard procedure, in supplementary material (section A.1) I included the details of the protocol. Once the PDMS substrate is ready the chamber is cut from the mould and inlet and outlet holes are created with a surgical punch. The PDMS chamber is then cleaned by removing dust with tape and by a plasma cleaning procedure. Before the plasma cleaning, a glass coverslip is prepared: its surface is cleaned by 5 minutes ultrasonication in acetone and another 5 minutes in isopropanol. The glass coverslip is then rinsed with distilled water and dried with nitrogen flow. The plasma cleaning procedure consists of cleaning the glass coverslip alone first, and after it is cleaned for a second time along with the PDMS chamber. Finally the microfluidic device is assembled by sticking the PDMS chamber to the coverslip glass. The PDMS chambers can be stored at room temperature for a month before the channels start to degrade.

Prior to the experiment, the prepared microfluidic chamber is passivated with 10 mg/ml BSA and incubated for one hour at 30°C. The BSA is filtered (0.2 μm filters) to prevent that protein aggregates at

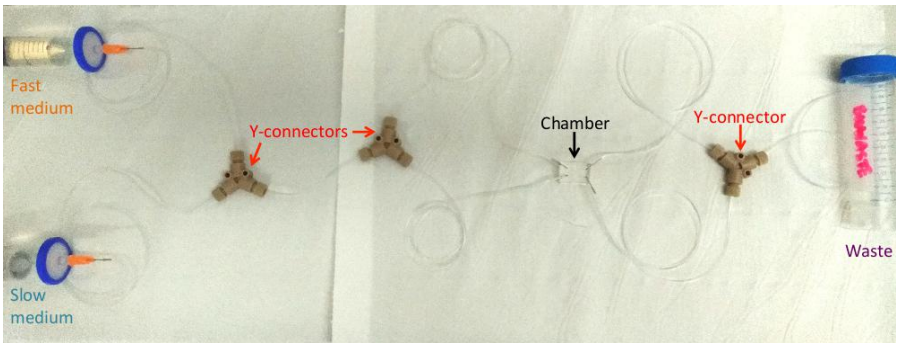

Figure 4.18.: Picture of the microfluidic system adopted for the single-cell experiments. From left to right: two syringes containing different media, tubings and two y-connector, the PDMS microfluidic chamber, the third y-connector and finally the waste tube.

this high concentration lead to clogs in the microfluidic device. The chamber is then rinsed with ethanol and distilled water.

The microfluidic system is completed by tubings, cleaned together with the glass coverslip, and 90 deg needles for inlet and outlet holes of the chamber. Needles are cleaned by 10 minutes ultrasonication in ethanol. Finally two syringes are connected to the tubings and mounted on two syringe pumps during the experiments in order to have and constant flow rate and the possibility of changing the medium (see chapter 10). In figure 4.18 I reported a picture of the complete microfluidic system, including the syringes, the waste tube, and the y-connectors used to assemble it.

The bacterial culture is gently loaded into the chamber by using a 1$ml insulin syringe mounted on a syringe pump, in order to better control the pressure.

4.6 MICROSCOPY

The optical microscope used for the single-cell experiments of this thesis is a Nikon Eclipse Ti-E inverted microscope (figure 4.19) equipped with a 60X oil immersion objective with NA 1.4 (Nikon CFI Plan Apo VC 60X Oil). The acquired images were further magnified with a 2.5X TV adapter before detection on an Andor iXon EM-CCD camera. This EM-CCD camera employs a UltraVac vacuum technology which ensures a deep cooling at $-60°$ and a complete protection of the sensor, thus enabling a low thermal noise and a high signal-to-noise ratio.

Additionally, the microscope is coupled with a Nikon Perfect Focus System (PFS), an autofocus hardware system, to rectify drifts during the imaging scanning process.

A temperature controller keeps the microfluidic chamber at the desired temperature, in my experiments 37°C. Particularly, the microfluidic device is enclosed in an heating chamber whose temperature is

Figure 4.19.: Picture of the commercial optical microscope used for this thesis, the Nikon Eclipse Ti-E inverted microscope (Nikon Instruments, Tokyo).

monitored by a thermocouple (figure 4.21), and the objective has a thermal ring and a second thermocouple to measure the temperature. In figure 4.20 I reported the experimental setup used for the time-lapse single-cell microscopy experiments.

4.6.1 *Image acquisition and analysis*

A fully motorized stage is used for the movement in x-y plane and for the field of views acquisition at specified time intervals. During a typical experiment about 20-30 field of views are scanned at a frame rate ranging from 2 to 3 minutes, the exposure time of the camera is set to 150 ms. Bright field, fluorescence and dark dark field images have been acquired automatically for each field of view by using a custom-written software. Dark field images have been used to subtract the real background from the images. I reported an example of a field of view including two channels filled up with fluorescent bacterial cells, where the bright field and fluorescent images have been superimposed, figure 4.22.

The collected images are processed by using Fiji (ImageJ) software: they are cropped and the dark field frame is subtracted from every image to remove the background signal. I used SuperSegger software for the cell segmentation and cell tracking, a powerful Matlab-based image processing suite for time lapse fluorescence experiments, developed by Wiggins Lab and particularly tailored for the analysis of *E. coli* cells [173, 174]. I always used fluorescence images for the cell segmentation because the signal-to-noise ratio is much higher compared to the bright field images, which is a crucial factor to distinguish

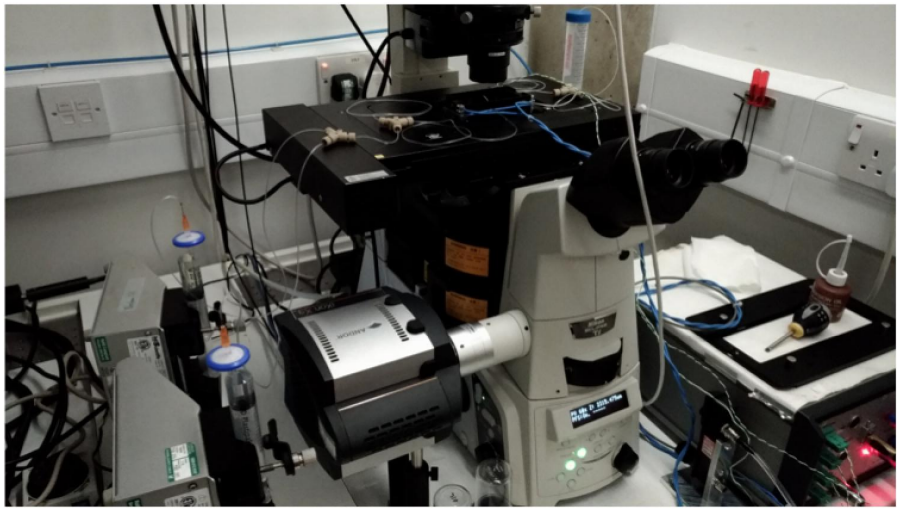

Figure 4.20.: Picture of the experimental setup used during my research activity in Pietro Cicuta laboratory, at the University of Cambridge. On the left there are the two syringe pumps with the syringes containing different media. The Andor EM-CCD camera is connected to the lateral port of the microscope. On the right there is the temperature controller connected to the thermocouples (green and white wires), to the heating chamber and to the objective thermal ring (blue wires). On the microscope stage there is the microfluidic system: the PDMS chamber in the heating chamber, the tubings along with the y-connectors and the waste tube. During the experiments y-connectors have been placed in petri dishes to avoid damaging leakages for the microscope and fixed to the stage with tape.

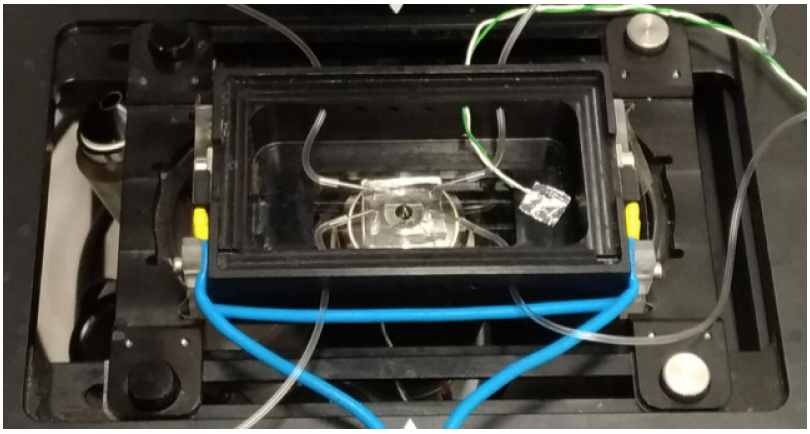

Figure 4.21.: Microfluidic PDMS device fixed to the heating chamber with transparent waterproof tape. The thermocouple (green and white wire) is glued to the heating chamber by conductive tape. There are two inlet (left) and two outlet (right) holes corresponding to the two growth medium trenches above mentioned. During the experiments the heating chamber has been covered with a lid for better thermal insulation.

neighbouring cells. In figure 4.23 I reported an example of a snapshot of fluorescent bacterial cells segmented as a result of SuperSegger analysis during an experiment. The output data of the segmented images are then processed by an homemade Matlab code calculating all the average quantities needed for the analysis of cells growth: the geometrical parameters, e.g. length, width, area, the fluorescence or the growth rate.

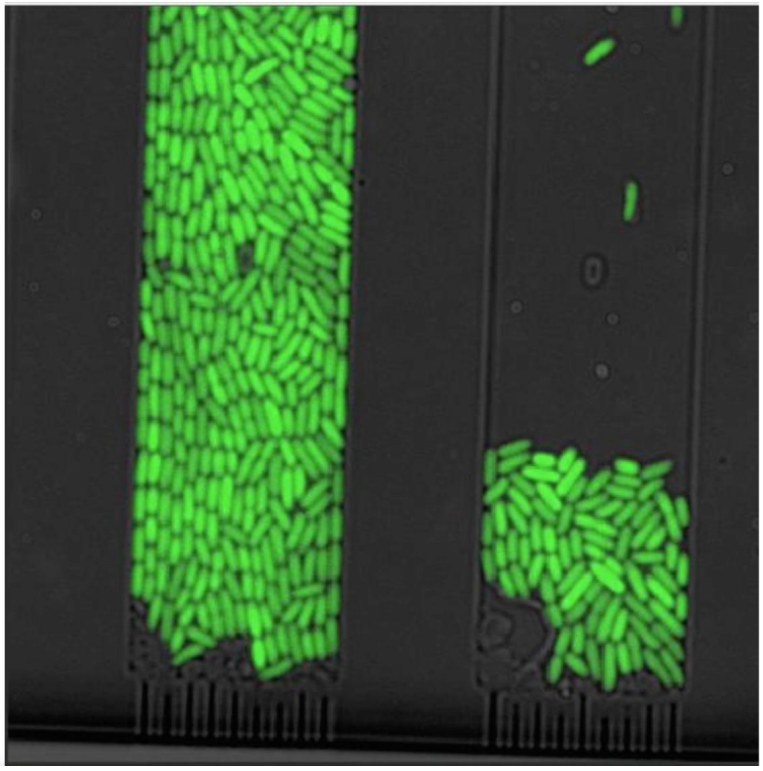

Figure 4.22.: Example of a field of view with bright field and the fluorescence images superimposed. Snapshot taken prior to the beginning of the experiment, when bacterial cells are filling up the channels. The size of these two channels is $60 \times 15\,\mu m$.

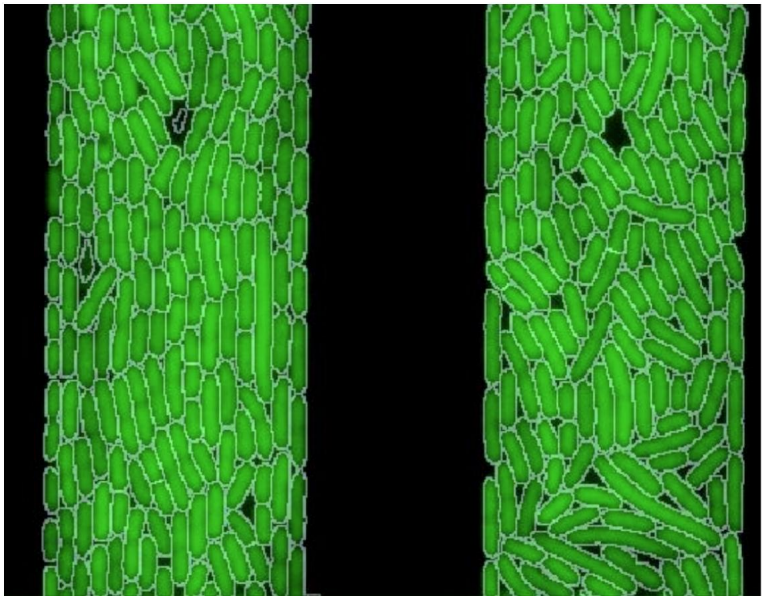

Figure 4.23.: Example of cell segmentation analysis performed by SuperSegger on a snapshot of a time-lapse experiment. The quality of segmentation is very good and almost all the cells are identified by the software. The cell tracking efficiency can be equally high as far as the fluorescent bacterial are bright enough.

5

BIOLOGICAL SAMPLES

5.1 DNA CONSTRUCTS PREPARATION FOR MT AND AFM

The DNA samples used in this thesis during MT experiments had to be conjugated to a supermagnetic bead on one end and to a fixed support on the other end, the surface of the flow chamber. DNA molecules result torsionally constrained in this way, and by rotating the magnets a torsion can be applied to the DNA double-helix.

As it will be explained in detail in the next sections, one end of DNA fragments is modified with digoxigenin to provide a connection to the anti-digoxigenin coated surface of the flow chamber (see paragraph 4.2.1), whereas the other end has a biotin-modification enabling the binding with the streptavidin coated superparamagnetic beads (Dynabeads, Invitrogen, Milan).

The concentration of the beads suspended in stock solution is around $7 \cdot 10^6$ per microliter. A 1.5-2 µl of beads solution is washed three times in 500 µl of 150 mM phosphate-buffered saline (PBS), after adding 5 µl of 10 mg/ml BSA. Magnets are used to separate the beads from the solution. The aim of this washing procedure is to remove the buffer solution of the initial stock, and BSA inhibits the non-specific adhesion of the beads to the walls of the vial. After this step, magnetic beads are re-suspended in 10 µl of PBS and an equal volume of digoxigenin/biotin-modified DNA is added, to have a solution of $\sim 10^7$ molecules. The incubation between magnetic beads and DNA lasts 15-20 minutes and then the solution is diluted in 500 µl of 150 mM PBS supplemented with 0.1 mM EDTA and 0.1% Tween20. This solution is finally loaded into the flow chamber and incubated for 45-60 minutes before flushing out with ~ 8 ml of PTE buffer the excess, unbound DNA tethers and beads [138, 146].

The AFM nano-scale imaging measurements are performed on DNA molecules deposited onto mica surfaces. DNA fragments are diluted in a 5 mM $MgCl_2$ buffer solution to a final concentration between 0.2-0.3 µM. 10 µl of this solution are deposited onto freshly cleaved mica substrates and incubated at room temperature for 5-10 minutes. Samples are then rinsed with 0.22 µm-filtered deionized ultra-pure water and dried with a gentle nitrogen flow.

5.2 DNA ANALOGUE PROJECT

DNA fragments used to study the DNA analogue were produced by polymerase chain reaction (PCR), both for wild-type and DAP-substituted DNA. DAP DNA was produced by replacing dATP with 2,6-diaminopurine-5′-triphosphate (Trilink Biotechnologies, San Diego, CA) at the same concentration (200 μM) as the other three dNTPs (Fermentas, Waltham, MA).

5.2.1 *DNA for melting temperature experiments*

Melting temperatures of wild-type and DAP substituted sequences were determined from fluorescently detected melting curves. Three portions of 155, 147 and 156 bp of the pBR322 plasmid were selected, containing 40%, 54%, and 65% GC-content, respectively. See section B.1 for complete sequences. The sequences were amplified using Taq DNA Polymerase (New England Biolabs, Ipswitch, MA) in ThermoPol buffer. The primer pairs used to produced 40%, 55%, and 65% amplicons were:

5′-TCTTTTACTTTCACCAGCGTTT, 5′-CCGCTCATGAGACAATAA
5′-TTCCGGCTGGCTGGTTTATTGC, 5′-TTCGTTCATCCATAGTTG
5′-GTTTCGGCGAGAAGCAGG, 5′-ACAGCATGGCCTGCAACG

respectively. Following PCR amplification, DNA samples were purified with a Qia Quick PCR cleanup kit (Qiagen, Germantown, MD) and eluted in 10 mM Tris-HCl pH 8.5. Amplicon lengths were verified by gel electrophoresis and concentrations measured by UV absorption using a Nanodrop Lite (Thermo Scientific). DNA was diluted to 10 ng/μl in 10 mM Tris-HCl pH 7.4, with 15 mM KCl and a range of 0.0005 - 0.01% v/v 10,000x Sybr-Green I dye (Thermo Scientific). Fluorescently detected melting was recorded using a BioRad C1000 qPCR machine (BioRad, Hercules, CA) over a temperature range of 60-95°C in 0.5°C increments.

5.2.2 *DNA for MT and AFM experiments*

MT and AFM experiments were performed using 4642 bp (hereafter 4.6 kb) long DNA fragments. For MT experiments, tethers were constructed from three components: a 4.6 kb long core fragment containing either wild-type or DAP-DNA, and two ~ 1 kb flanking tails containing biotin- or digoxigenin- 11-dUTPs. The core fragment was prepared by PCR with Long AmpTM(New England Biolabs) using the pKLJ12wt plasmid [**?**] and the following primers:

5′-AGCGTTGGCGCCGATTGCAGAATGAATTT and
5′-TGGGATCGGCCGAAAGGGCAGATTGATAGG,

which contain KasI and EagI restriction sites, respectively. The biotin and digoxigenin-labeled tail fragments were also produced by PCR using Taq polymerase in standard buffer (NEB). PCR solutions were supplemented with biotin-11-dUTP (Fermentas) and digoxigenin-11-dUTP (Roche, Indiannapolis, IN) in a 1:9 ratio with respect to dTTP [183]. The biotin-labeled fragment was amplified from pUC19 using the primer pair

5′-ATGATCCCCCATGTTGTGCA
5′-TCAAGACGATAGTTACCGGATAAG

to create a 1.8 kb biotin-labeled amplicon with a central KasI site. The digoxigenin-labeled fragment was amplified from pBluKSP using the primer pair

5′-TGGGTGAGCAAAAACAGGAAGGCA
5′-GCGTAATCTGCTGCTTGCAA

to create a 2 kb dig-labeled amplicon with a central EagI site.

Following PCR amplification and column purification (Qia Quick PCR cleanup; Qiagen) the core and tail fragments were digested with KasI and EagI-HF restriction enzymes (New England Biolabs), purified again, and concentrations were measured by UV absorption. Restriction of the tails yields roughly 1 kb fragments with a single KasI or EagI sticky-end. Restriction of the core fragment produces a 4.6 kb sequences with KasI and EagI sticky-ends at opposite ends. To assemble the final tether, approximately 600 ng of the core fragment was mixed with 250 ng of each tail along with 30 U of T4 DNA ligase (NEB) and the recommended buffer to a total volume of 30 µl and incubated at 16°C for 4 hours. After heat-inactivation at 65°C for 20 min, the ligation mixture was used directly in the micro-chambers.

5.3 HIGH SUPERCOILING PROJECT

5.3.1 *DNA for MT experiments*

The DNA constructs used for the MT experiments at high supercoiling are engineered by the assemble of three different DNA sequences: a central portion and two flanking tails, suitably modified in order to provide connections to the functionalized surfaces. One of the tails needed to be functionalized with biotin, to link a strepavidin coated magnetic bead, while the other one with digoxigenin, to bind the anti-digoxigenin coated surface of the coverslip. Low GC-content DNA

used for this work consists of a 5396 bp DNA with a sequence at 30% GC content, hereafter to as the low-GC DNA. The central portion of the molecule was obtained by PCR amplification using Q5High-Fidelity DNA Polymerase (NEB), Lambda DNA N6-methyladenine-free (Sigma-Aldrich) as template, and the following primers:

5′-actCCCGGGTTGTGAGGCTTGCATAATGG -3′
5′-ctaGGGCCCAGTGAATGTCTGTTATGAGCGAGG-3′

The DNA here referred to as normal-GC DNA used for this work consists of a 6740 bp DNA with sequence 50% GC content. The central portion of the molecule was obtained by PCR amplification using LongAmpTaq DNA polymerase (NEB), plasmidic pL6 DNA as template, and the following primers:

5′- acaCCCGGGACCAGGACGCAGATATAGCC-3′
5′-ctaGGGCCCGCCGTAGAAGAACAGCAAGG-3′

The DNA here referred to as high-GC DNA used for this work consists of 5811 bp bp DNA sequence at 77% GC content. The central portion of the molecule was obtained by PCR amplification using Q5 High Fidelity DNA polymerase (NEB), psC-tC.GC vector plasmid (gently gifted by Prof. Dekker, Delft University of Technology) and the following primers:

5′-ttttGCGGCCGCCCAGGCCCACCCCCTCGTGGA -3′
5′-ttttCTCGAGGGGACCACAAAGGCCAGAATTCACGGCTG-3′

The low-GC DNA and the normal-GC DNA constructs were built up using the same tails. Both are amplified PCR from the pBR322 plasmid (NEB). The reaction was carried out in the presence of biotin 16-dUTP or 6-dUTP or digoxigenin-11dUTP-labeled nucleotides, using the same reverse primer and two different primers (Roche), as follows:

5′-gcttGGGCCCAGAGTTCTTGAAGTGGTGG -3′
5′-ggagtCCCGGGCAGAGTTCTTGAAGTGGTGG-3′
5′-ggtccagTCGTCGGGTCTCGCGGTATCATTGC-3′

In the case of high-GC DNA construct both tails were amplified PCR from the pBR322 plasmid (NEB). The reaction was carried out in the presence of biotin 16-dUTP or 6-dUTP or digoxigenin-11dUTP-labeled nucleotides, using the same reverse primer and two different primers (Roche), as follows:

5′-gcgcCTCGAGCAGAGTTCTTGAAGTGGTGG -3′
5′-gcgcCTCGAGCAGAGTTCTTGAAGTGGTGG -3′
5′-catatgGCGGCCG CATGCGCGCATCTCCTTG
CATGCACCATTCCTTGCG-3′
5′-CTGTCCCTGATGGTCGTCATCTAC-3′

For all the construct the effective presences of the amplicons was detected by 1% agarose gel electrophoresis. The samples were then purified by QI- Aquick PCR Purification Kit. The resulting fragments were subjected to extensive digestion (16 h) using the appropriate restriction enzymes and further purified to stop the reaction and remove any trace of contaminants. Finally, the central fragment and the two tails were ligated using T4 DNA ligase at 16° for 48 h. The presence of the final construct was confirmed by 1% agarose gel electrophoresis.

5.4 DNA-DRUGS INTERACTIONS PROJECT

5.4.1 *DNA for MT experiments*

The DNA sequence used for MT measurements is a 6964 bp long fragment including biotin- and digoxigening-modified tails. The central portion is 5780 bp long and was obtained from NotI/SacII restriction digests of the pCMV6-neo plasmid (Origene, Rockville, MD). The tails, 537 bp and 647 bp long, were obtained by polymerase chain reaction using the pBR322 plasmid (Stratagene, San Diego, CA) as a template. PCR reactions were performed using two oligonucleotides annealed to the pBR322 plasmid and carrying the restriction enzyme sites NotI and SacII at their 5′ ends. The oligonucleotides are

5′-CATATGGCGGCCGCATGCGCGCATCTCCTTGCATGCACCATT
CCTTGCG,
5′-CATATGCCGCGGATGGCGCCATGCGGCCGCATCTCCTTGCAT
GCACCATTCCTTGCG,

respectively, in the presence of two different reverse primers

5′-CTGTCCCTGATGGTCGTCATCTAC
5′-ATCCATGCCAACCCGTTCCATGTG

Polymerase chain reaction was performed using biotin-16-dUTP-labeled nucleotides (Roche, Basel, Switzerland) for the 537 bp sequence or digoxigenin-11-dUTP-labeled nucleotides (Roche) for the 647 bp sequence in the reaction mixture. After amplification, the sticky ends were obtained by digesting with either NotI or SacII at 37°C for 2 hours. The central sequence (5780 bp) obtained by NotI/SacII di-

gestion of pCMV6-neo plasmid (Origene) was ligated to the tails overnight at 16°C with T4 DNA-ligase (Promega, Madison, WI) with a 5:1 excess of the ends with respect to the central sequence. The effectiveness of the ligation reaction was verified using gel agarose electrophoresis. The ligation products were diluted to a final concentration of 0.2 ng/ml in TE buffer, aliquoted in volumes of 10 ml and stored at −20°C.

5.4.2 *DNA for UV experiments*

For the thermal melting studies by UV absorption, a calf-thymus DNA (Sigma-Aldrich, st. Louis, MO) without any purification was used, both for DNA and DNA-drug complexes experiments. The concentration of DNA was 1.5 mM during these bulk measurements, and a 1 day incubation in the presence of a drug molecule/DNA bp ratio of 0.5, in 50 mM $NaClO_4$. Finally, DNA solution is diluted in 150 mM PBS to reach a final concentration of 150 μM.

5.4.3 *Drug compounds preparation*

Platinum-based drug compounds were kept inactivated by using high concentrations of Cl^- ions [175]. A reasonable concentration of Na^+ ions, 50 mM, with a low concentration of Cl^-, was maintained by diluting all platinum compounds in an activating buffer solution including 50 mM $NaClO_4$. Na^+ ions are necessary to avoid non-specific binding of the magnetic beads to the glass surface. Drug compounds were diluted in physiological solution (154 mM NaCl) and stored in the dark at room temperature for CIS and at −20°C for BBR-compounds.

For MT experiments drugs were diluted in a $NaClO_4$ buffer solution to reach a final concentration of 1 μM. This concentration greatly exceeds the base-pair concentration of the DNA present in the flow chamber. Furthermore, considering the binding kinetics reported in literature, that concentration is high enough to almost saturate all the cross-linking sites. The very low concentration of Cl^- ions enabled to study the most reactive form of the platinum-based drugs, as explained in other protocols [175].

The cross-linking reaction occurred during an overnight (14-16 hours) incubation of the drugs with the DNA attached to the surface of the flow chamber, a time much longer than the binding kinetics half-period. This half-period should have been around 1.5 hours for CIS and BBR3005 and 15 minutes for BBR3464. Therefore, this reaction time is another guarantee of the saturation of cross-linking reaction. The incubation was carried out under a pulling force of about 1 pN, in order to prevent attachment of the bead to the glass surface.

5.5 H-NS ROLE PROJECT

5.5.1 *DNA and PEG for MT experiments*

The DNA analyzed for this work by MT consists of a 5396 bp long sequence with a 37% GC content, hereafter lowGC DNA. This DNA construct is a fragment assembling three different portions: a 4380 bp core sequence and two 508 bp flanking tails, suitably modified with biotin and digoxigenin in order to provide linking to the anti-digoxigenin functionalized glass surface and to the streptavidin coated magnetic bead, respectively.

The central fragment was obtained by PCR amplification using Q5 DNA polymerase, Lambda DNA N6-methyladenine-free (Sigma-Aldrich, st. Louis, MO) as template, and the following primers:

5′ - ACTCCCGGGTTGTGAGGCTTGCATAATGG
5′ - CTAGGGCCCAGTGAATGTCTGTTATGAGCGAGG

that contain XmaI and ApaI restriction sites. DNA tails were amplified by PCR from the pBR322 plasmid (Roche, Basel, Switzerland). PCR reactions were carried out in the presence of biotin-16-dUTP or digoxigenin- 11-dUTP-labeled nucleotides (Roche), using two different forward primers and the same reverse primer, which are

5′-GCTTGGGCCCCAGAGTTCTTGAAGTGGTGG
5′-GGAGTCCCGGGCAGAGTTCTTGAAGTGGTGG
5′-GGTCCAGTCGTCGGGTCTCGCGGTATCATTGC

respectively. The effective presence of the amplicons was detected by 1% agarose gel electrophoresis. The samples were then purified by QIAquick PCR Purification Kit (Qiagen, Germantown, MD). The resulting fragments were subjected to extensive digestion (16 hours) using the appropriate restriction enzymes and further purified to stop the reaction and to remove any trace of contaminants.

Finally, the three molecules were ligated using T4 DNA ligase (NEB) at 16°C for 48 hours. The molar ratio between core fragment and tails was of 1:2 and 800 ligase units were used for 500 ng of core fragment. The presence of the final construct was confirmed by 1% agarose gel electrophoresis.

The crowding conditions during MT experiments were induced by adding poly(ethylene glycol) (PEG) with an average molecular weight of 1500 ($M_W \sim$ 1400-1500), purchased from Sigma-Aldrich. PEG solutions were prepared by dissolving the crowding agent in H-NS buffer (see section D.1) and used for experiments without any further purification [**?** **?**].

5.5.2 *H-NS protein purification*

The H-NS protein was purified as previously described [176], and its concentration was measured according to a previous studies [176, 177].

E. Coli BL21 (λDE3)/pLysS (Invitrogen) cells were transformed with pBSK H-NS, plated on LB with ampicillin, and used for H-NS protein overexpression. A single clone was picked and inoculated in 10 ml of LB with ampicillin, this preculture was grown to an optical density at 600 nm (OD_{600}) of 0.5, and kept at 4°C overnight. Subsequently, 1 liter of culture is prepared in two 500 ml flasks by inoculating 5 ml of preculture in 500 ml of LB with ampicillin and kanamycin, these cells were then grown at 37°C to an OD_{600} of 0.3/0.4. Protein production was induced by adding 1 mM isopropyl-β-d-thiogalactopyranoside (IPTG), at 30°C for one hour. After that, cells were harvested on ice and a pellet was obtained by centrifugation at 5000 g for 15 minutes at 4°C, the supernatant is discarded. Cells from the 1 liter culture were resuspended in 20 ml of Lysis buffer (see supplementary section D.1) and they were disrupted using a French press at 20000 psi, followed by a centrifugation at 12000 g for 25 minutes at 4°C. The supernatant was applied to a HiTrap chelating column (Amersham Biosciences), equilibrated with the loading buffer (section D.1). The supernatant was loaded manually and repeatedly by using a 2 ml syringe (a larger syringe tends to block), the column was mounted on a FPLC and washed with the loading buffer. A gradient was made with loading buffer and elution buffer (section D.1), then the protein was eluted at 0.5 ml/min with 10 ml of total gradient volume and 0.4 ml per fraction were collected. The sample was run from the eluted peak on a 15-25% acrylamide gradient SDS gel and the protein fractions were pooled. These fraction were dialyzed against a buffer with Tris HCl pH 8.0, 300 mM NaCl and 20% glycerol. Finally the protein was quantified with the Bradford assay and aliquots were frozen in liquid N_2 and stored at -20°C until further use.

For MT experiments the H-NS protein was diluted in a buffer solution containing 10 mM of $MgCl_2$ (H-NS buffer), in order to have the molecule in the bridging binding mode state [82].

5.5.3 *Strains for single-cell experiments*

The cells analysed during the time-lapse microscopy experiments are *E. coli* cells. The investigated promoter is a shortened version of *rrnB*P1 (P1 short), see figure A.1, and its activity was measured by cloning the promoter upstream of the mut2-gfp. The promoter-gfp KanR cassette was amplified by PCR from the pDoc-K plasmid [**?**] and inserted at specific positions of the genome of the BW25113 *Escherichia coli* strain by the lambda Red recombination protocol [**?**].

The kanamycin resistance cassette (KanR) was removed by Flp-FRT recombination. The insertion positions were chosen to correspond to the position of the ParS sites in the work by Espeli [**?**] and are within intragenic regions, as defined by the gene positions in the Ecocyc Genome browser [**?**].

The studied strains in this project have the P1 short promoter inserted in two positions: *ori*3 and *nsr*3 (figure A.2). Particularly, two strains in *nsr*3 position were studied, one including the KanR cassette (P1nsr3-Kan) and the other one without KanR (P1nsr3-NoKan). On the other hand, two strains were inserted in *ori*3 position, a strain with a knockout of *hns* gene (P1ori3-δ*hns*), compared with a control strain including the *hns* gene. Both P1ori3 strains include KanR cassette.

The bacterial strains were stored at $-80°$C and they were spread, directly from the $-80°$C stock or from an overnight 2 ml LB culture, on LB (Lysogeny broth) agar plates supplemented with kanamycin as selective bacterial antibiotic. The agar plates are then incubated overnight at 37°C. The preparation of agar plates and bacterial cultures I am going to describe was always performed under sterile conditions.

The next day, a single colony from the agar plate is inoculated in 2 ml of slow growth medium (M9 salts+glucose) and incubated overnight at 37°C, see section A.3 for details about growth media. This pre-culture is finally diluted $1:200$ in 2 ml of fresh slow growth medium and incubated for 3-4 at 30°C, to reach an optical density at 600 nm (OD_{600}) of $\sim$ 0.05-0.06. These bacterial cells in exponential phase are thus ready to be loaded into the microfluidic device for the single-cell time-lapse microscopy experiments.

Part III

RESULTS

6

NANOMECHANICS OF A DNA ANALOGUE

The investigation of DNA structural polymorphism started from the study of a chemically modified nucleic acid, namely the diaminopurine substituted DNA. The aim of this work is to assess if a chemical modification of DNA double helix could induce relevant conformational changes, involving different biological functions as well.

2,6-Diaminopurine (DAP, alternatively 2-aminoadenine) is a nucleotide analog of adenine, bearing an additional amine group at position 2 of the purine molecule. When incorporated into double-stranded DNA, its additional amine enables it to form three hydrogen bonds with thymidine, see figure 6.1. Despite this difference, incorporation of DAP during PCR amplification yields no loss in sequence specificity and this DNA modification is interesting both biologically and structurally for nanoscale engineering [178, 179]. While nature has generally chosen to use the canonical bases, there are instances, such as in the genome of cyanophage S-2L, where DAP substitution occurs [180, 181]. The biological advantages (or disadvantages) of DAP substitution are not entirely understood. From a biophysics perspective, DAP substitution offers a way of manipulating the physical characteristics of a DNA molecule without altering the sequence, with applications including the study of the interactions between DNA and proteins or drug candidates [182–187], investigations of RNA-related mechanisms [188, 189], and even as novel dopants in DNA-based nanoelectronics [190]. The characterization of DAP substitution effects on the physical properties of DNA yields insight into the relationship between the specific properties of individual bases and the biochemical characteristics of the whole double-helix assembled with such bases.

The nanomechanics of this DNA analogue has been studied from a thermal and a mechanical point of view, by using a fluorescence method and single-molecules techniques respectively. A fluorescent dye intercalating DNA was adopted to measure the melting temperature of short DNA sequences and, on the other hand, AFM imaging experiments and MT force spectroscopy measurements were carried out to analyse the mechanical properties. Particularly, the nanomechanics was examined in a wide range of forces, from null values

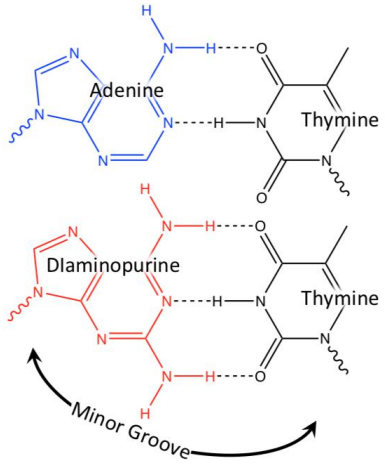

Figure 6.1.: Chemical structures of Adenine-Thymine base-pair (top) and 2,6-Diaminopurine-Thymine base-pair (bottom).

(AFM imaging) to low force regime (WLC), and finally to high force regime (overstretching), as it will be described in the following sections. All the collected data about DAP DNA were compared with the results of a wild type (WT) DNA sample having the same sequence.

The results I am going to describe here have been presented in a couple of conference talks [191, 192] and a paper about these finding is currently under review [193].

6.1 THERMAL CHARACTERIZATION

As already explained in the first chapter, the two backbones of a DNA are held together by hydrogen bonds formed between the base pairs, following the Watson-Crick rules. Consequently, on first approximation, one would naïvely expect melting temperature to be proportional to the total number of base pair hydrogen bonds in a given sequence. However, the stacking interactions between A/T and G/C duplexes produce sequence dependent effects [194, 195]. Indeed, two relatively short sequences with same length and GC content can have different melting temperatures. Since DAP DNA has all the base-pairs linked by three hydrogen bonds, it is a useful tool to probe the roles of stacking and hydrogen bonds.

The melting temperature (T_m) of three sequences containing 40%, 54%, and 65% GC were compared, as shown in figure 6.2, where measured (red and blue) and calculated (yellow and purple) values of T_m are presented as a function of GC percentage. The sequences were roughly the same length (155, 147, 156 bp). The DNA melting temperature was measured by fluorescence in the presence of the intercalating dye Sybr Green I. Because Sybr Green intercalation stabilises double-helical DNA, titrations ranging from 0.0005 to 0.01% v/v were measured so that the resulting melting temperature shifts could be

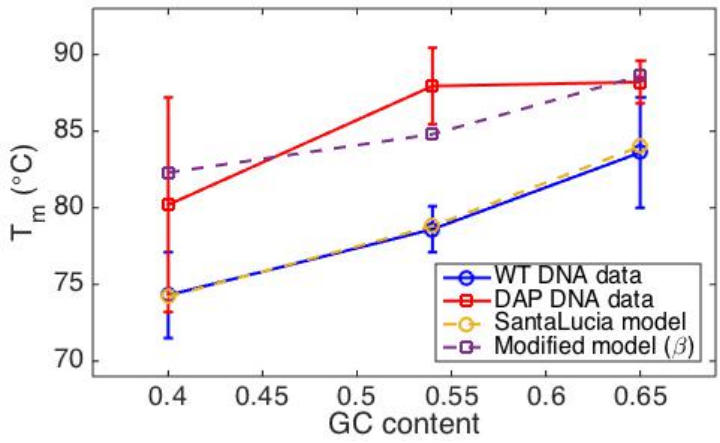

Figure 6.2.: Melting temperatures of WT (blue) and DAP DNA (red) sequences having three different GC- fractions: 0.4, 0.54 and 0.65. T_m values were measured using fluorescence over a range of Sybr Green concentrations, yielding estimates of the dye-free melting temperatures from intercepts of linear fit (see section B.2). Yellow dots are T_m values predicted by SantaLucia Nearest-Neighbour model, while purple dots are the prediction from modified version of SantaLucia model, by adding the enthalpy term β (see text for details).

fit with a line and projected to the dye-free (0% v/v) condition, see figure B.2, [196]. Fluorescence curves were normalized to account for temperature dependence of the fluorescent dye [197, 198]; details are included in supplementary material, section B.2. For short sequences, melting approximates a binary process and melting temperatures can be estimated by

$$T_m = \frac{\Delta H}{\Delta S + R \ln \frac{[dsDNA]}{2}} - 273.15 \tag{6.1}$$

where T_m is the temperature at which 50% of dsDNA molecules will be melted, ΔH is the sequence dependent enthalpy, ΔS is the sequence dependent entropy, R is the gas constant and [dsDNA] is the concentration of dsDNA in solution. ΔH and ΔS are equal to the sum of empirically determined nearest-neighbour terms and are corrected to account for salt-dependent effects, according to the SantaLucia model [199, 200]. Despite the SantaLucia model is intended for short sequences, it yielded predictions within ± 0.5°C of the measured melting temperatures for this study, see blue and yellow dots of figure 6.2.

To a rough approximation, one might assume that stacking interactions, which dictate the discrepancies between nearest-neighbour terms of the SantaLucia model, to remain largely unchanged for DAP-T containing duplexes. With that assumption, the simplest modification to the SantaLucia model accounting for the effect of DAP

substitution is to supplement the enthalpy of each AT pair with an additional factor corresponding to the enthalpy of the extra hydrogen bond (represented here as β). For example, under the modified scheme the example sequence 5′-GATCG-3′ would have the following total enthalpy

$$\begin{aligned}\sum \Delta H &= (\Delta H_{GA} + \beta) + (\Delta H_{AT} + 2\beta) + (\Delta H_{TC} + \beta) + (\Delta H_{CG}) \\ &= \sum \Delta H_{WT} + 4\beta\end{aligned} \tag{6.2}$$

where ΔH_{WT} is the enthalpy for the corresponding wild type sequence. I used this modified SantaLucia to predict the melting temperatures of DAP DNA sequences, the least-squares fit of the melting data yielded $\beta \sim -0.16\,\text{kcal/mol}$. The modified model did not perfectly capture T_m data as the original SantaLucia model with WT DNA, particularly the 54% GC content DAP sequence was not predicted very well. However the general trend of the model was still preserved accordingly to the data.

6.2 MECHANICAL CHARACTERIZATION

6.2.1 *Zero-to-low force regime*

To measure the mechanical properties of the DNA analogue, AFM imaging experiments were first carried out. WT and DAP DNA molecules were deposited onto freshly cleaved mica surfaces and imaged in tapping mode, so as to obtain the values of contour length (L_0) and persistence length (L_P). Representative images of both WT and DAP samples are shown in figure 6.3. Contour lengths were calculated by tracing each DNA filament using an image recognition algorithm and computing the integrated length [153]. Molecules that were significantly shorter or longer than the expected 1.1-1.8 μm range were excluded from the data set. A histogram of contour lengths for WT and DAP molecules is included in figure 6.4(a). As indicated, DAP-substitution decreased the average contour length from 1.45 μm to 1.30 μm, corresponding to an axial rise per base pair of 3.12 Å/bp and 2.80 Å/bp respectively.

Persistence length was estimated from the measured mean square displacement between points along the contours of molecules in two-dimensions [153]. For a worm-like chain confined to two dimensions, the average squared distance $\langle R_L^2 \rangle$ between two points along the chain is given by

$$\langle R_L^2 \rangle = 8L_P^2 \left(\frac{L}{2L_P} - 1 + e^{-\frac{L}{2L_P}} \right) \tag{6.3}$$

where L is the curvilinear distance along the chain [155–157]. Using the x-y coordinates generated by the tracing routine, it is relatively

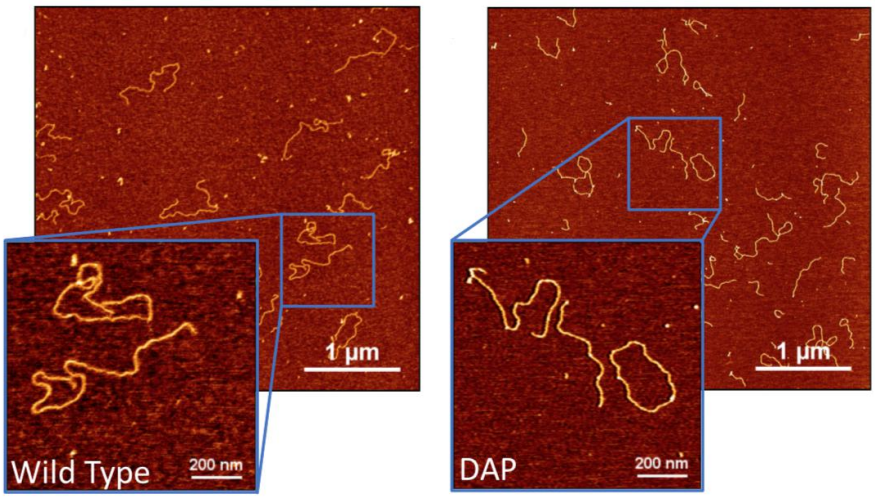

(a) (b)

Figure 6.3.: Representative AFM images of wild type **(a)** and DAP DNA **(b)** molecules.

straight forward to compute the distance between points separated by increasing contour lengths. Aggregating the data of all the molecules from each sample (WT or DAP), the mean of the squared Euclidean distance was computed as a function of contour length separation and fit to equation 6.3, results are shown in labels of figure 6.4(b). WT-DNA yielded $L_P \approx 58\,nm$, while DAP substitution increased the persistence length to $\approx 83\,nm$.

After the zero-force AFM experiments, the next step was the analysis of the mechanical properties in the low force regime, by means of MT force spectroscopy measurements. DNA tethers were subjected to tensions ranging 0.001-5 pN and their time-averaged end-to-end extensions were measured. Below 10 pN, DNA acts as an entropic spring and it is well described by the worm-like chain model (WLC), introduced in theory chapter, section 3.3. An example of force-extension curves in the low force regime with the related WLC fits are represented in figure 6.5, for WT DNA (blue) and DAP DNA (red). The difference between the two types of DNA can be seen in this plot, particularly for intermediate forces around 0.1 pN. The downward shift of DAP DNA curve in figure 6.5 means higher bending rigidity. The WLC equation enables to extract two parameters describing the DNA mechanics: the persistence length and the contour length. In figure 6.6 the histograms of the resulting values of L_0 (a) and L_P (b) are reported: DAP substitution increased persistence length from $45 \pm 4\,nm$ to $56 \pm 5\,nm$. On the other hand, the contour length is, within the experimental errors, the same for the two DNAs.

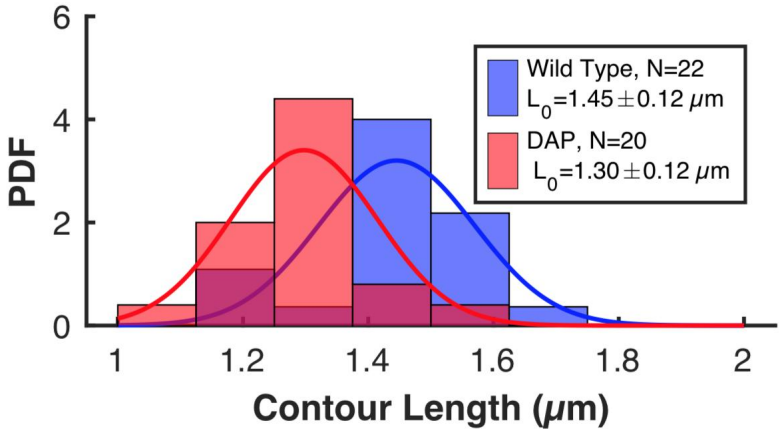

(a)

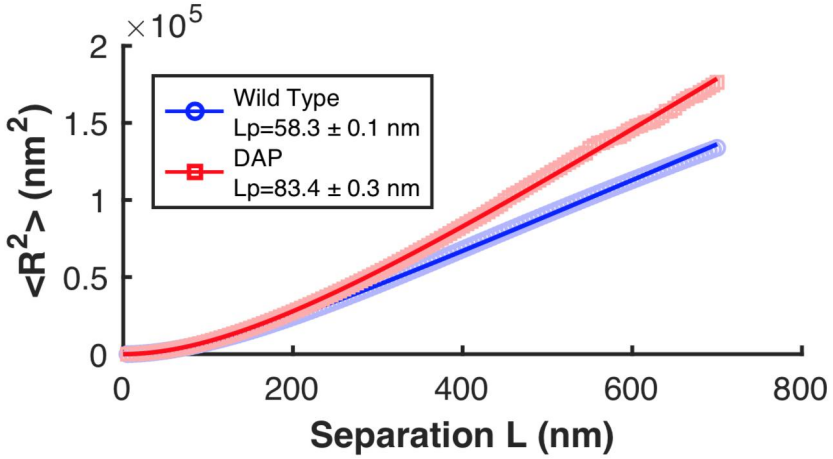

(b)

Figure 6.4.: Contour length (L_0) and persistence length (L_P) resulting from the analysis of AFM images.
(a) Histograms of L_0 values calculated by tracing individual WT (blue) and DAP (red) DNA molecules. Average and standard deviation of L_0 are reported in labels.
(b) Mean squared distance $\langle R^2 \rangle$ versus separation L along each molecular contour. Data points correspond to average square distance, aggregated for all WT (blue) and DAP (red) molecules. Data were fit to equation 6.3, yielding averages and standard deviations of L_P.

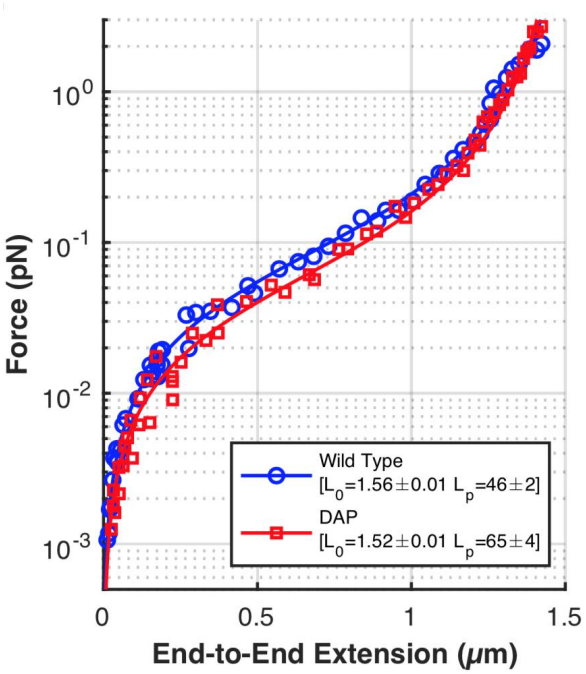

Figure 6.5.: WLC curves of WT DNA (blue circles) and DAP DNA (red squares), measured by MT. Circles and squares are force (F) vs DNA extension (L_e) data points, the solid line of the corresponding colour is the WLC fit of the data. Fitting parameters are reported including the standard deviation in the inset.

Both samples showed the expected value of ≈ 1.5 µm for 4.6 kbp long DNA fragments (section 5.2).

6.2.2 *High force regime: overstretching transition*

In the high force regime, i.e. above the elastic regime between 10 and 50 pN, DNA undergoes a particular phase transition around 60-70 pN, called overstretching (see section 3.1.1). As already explained, DNA can exhibit this transition basically in two ways: separation, or unzipping, of the two DNA strands, namely a melting process, or to assume a new structural form, called S-DNA, where hydrogen bonds are still intact.

To investigate how DAP affects overstretching transition we analyzed the force-extension behavior of several molecules in the high force regime. Un-nicked molecules (verified by a twist versus extension curve) were excluded from the analysis because torsional constraint forces hyper-extended molecules to adopt a P-DNA configuration [24, 53, 201–203], a structure which is beyond the scope of this study (see next chapter).

Remarkably, DAP DNA exhibited an overstretching transition at a significantly lower force than WT-DNA. As shown in figure 6.7, DAP-

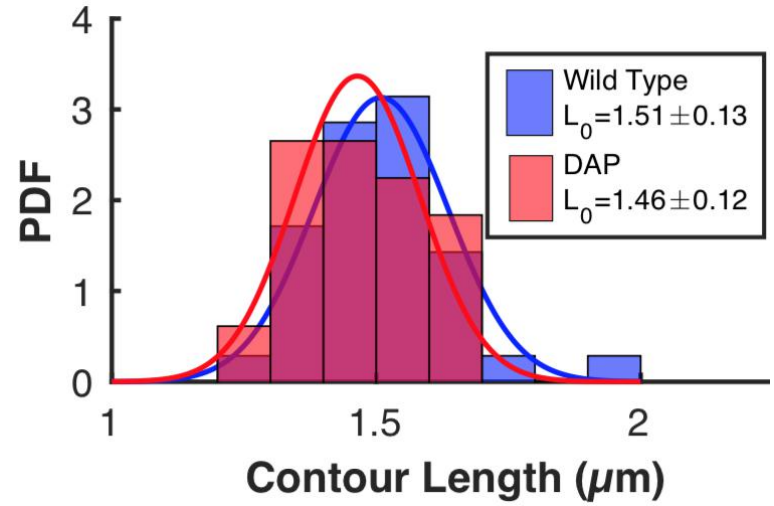

(a)

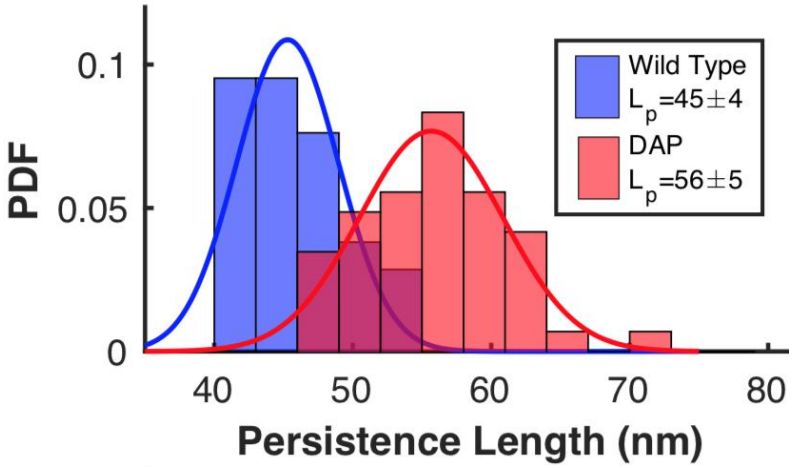

(b)

Figure 6.6.: Histograms of the contour length L_0 **(a)** and the persistence length L_P **(b)** values extracted from the WLC fit of F vs L_e MT data. Average values and errors (standard deviation) are reported in the inset. The values were calculated over 35 and 48 DNA molecules for WT and DAP DNA respectively.

substitution lowered the transition force to $F_{os} = 54\,pN$ compared to the 62 pN for WT-DNA consistent with the literature.

Cyclic extension and relaxation also revealed that DAP DNA exhibited very little hysteresis through the overstretching transition, whereas nearly all WT molecules showed significant hysteresis, as it has been widely reported in literature [115, 204–206]. To quantify the difference in DAP and WT behavior I computed the area between the extension and relaxation traces for each molecule, see in figure 6.8 illustrative force-extension curve cycles for both DNA samples.

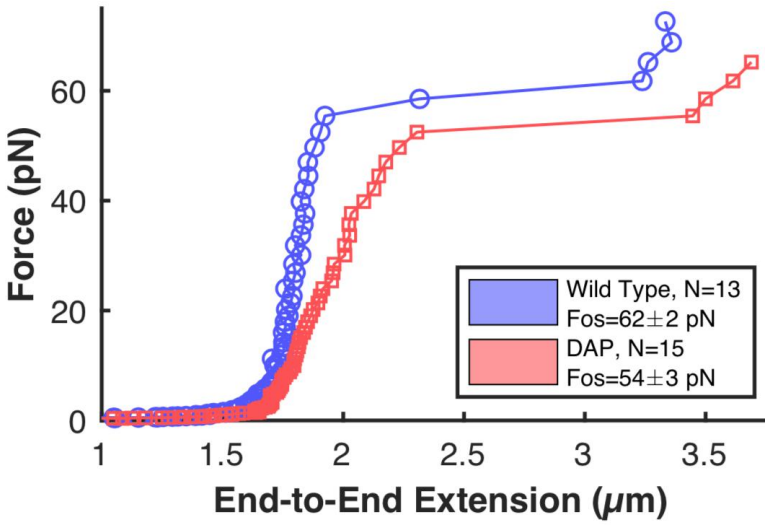

(a)

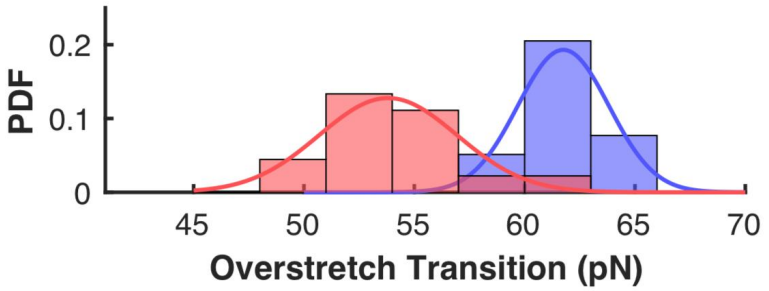

(b)

Figure 6.7.: DNA behaviour in the high force regime ($F > 10\,pN$).
(a) Representative pulling traces for WT (blue) and DAP (red) molecules collected with MT.
(b) Histograms of the overstretching transition force (F_{os}) for WT (blue) and DAP (red) DNA.

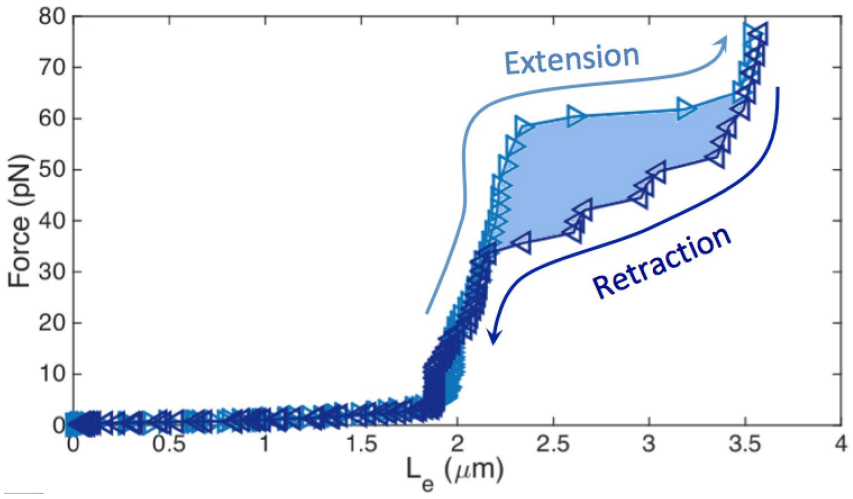

(a)

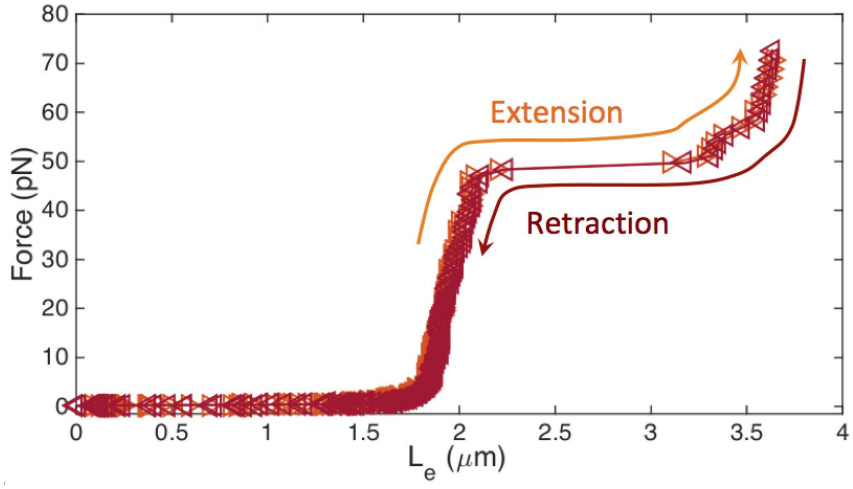

(b)

Figure 6.8.: Hysteresis observed upon overstretching transition. Example force-extension cycles for WT DNA **(a)** and DAP DNA **(b)**. Extension and retraction curves are represented in dark and light blue respectively for WT DNA, while in red and orange for DAP DNA. No hysteresis has been shown in DAP DNA, on the contrary for WT the typical hysteretic behavior occurred.

7

HIGH SUPERCOILING REGIME

A second strategy adopted to investigate the structural polymorphism was to carry out DNA twist experiments so that the formation of supercoiled structures could promote alternative DNA forms. Indeed, DNA has a double-helical structure with a well defined helicity and mechanical properties, the application of certain torsions and forces can create loops or melting bubbles. These local structures can act as nucleation centers for a phase transition to an alternative DNA structure. In particular in the theory chapter, page 29, I already introduced a model describing the nanomechanical denaturation of the double helix. To make that transition happen it is necessary to induce a counter clockwise torsion to the DNA molecule before applying a force in the range of 0.5-1 pN [137, 138, 207]. The physical observable of this phenomenon is simply the end-to-end extension of DNA (L_e), ranging from zero in the plectonemic state to the maximum value of the extended molecule in the denaturation state. This phase transition has been identified by looking at fluctuations of DNA extension, which significantly increase in a narrow range of forces and for certain twist values (section 3.4.2). I clarify this concept in figure 7.1(a), where I reported a number of extension-twist curves performed at different forces: the measurement of DNA extension becomes noisier at negative turns for intermediate force values, in particular for $F \approx 0.8$ pN (red curve), which indeed roughly corresponds to the characteristic force F_{char} of the plectonemic-denaturation transition (see section 3.5) [137]. Note that counter clockwise torsions correspond to negative number of turns, where the increment of L_e fluctuations is observed.

The aim of the experiments that will be presented in this chapter is to study this phase transition at very high supercoiling, under extreme conditions promoting the formation of an alternative double helix. When a DNA molecule is strongly underwound and the applied force value is high enough, the fraction of denatured DNA regions becomes significant and an additional (counter clockwise) twist can lead to the formation of a left-handed DNA, called L-DNA. This structure has been already reported in literature [24, 208] and a few similarities with Z-DNA have been found [25, 209]. However, the

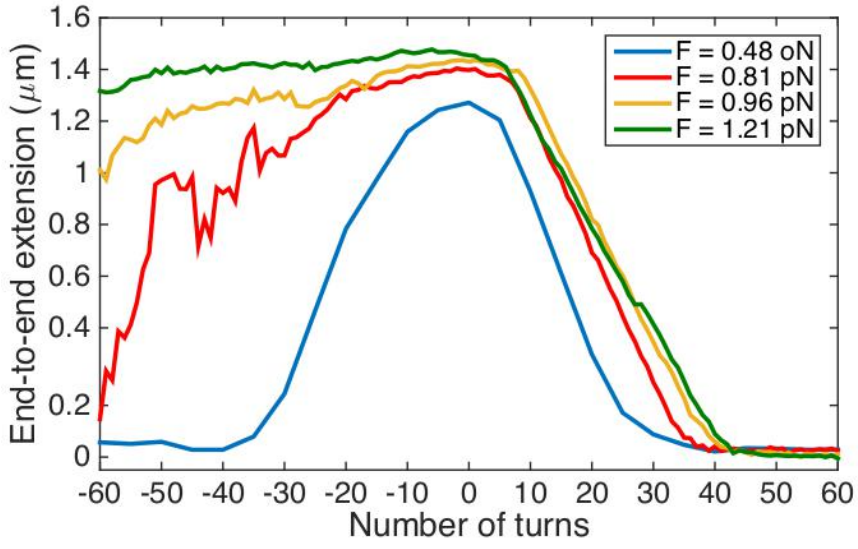

(a)

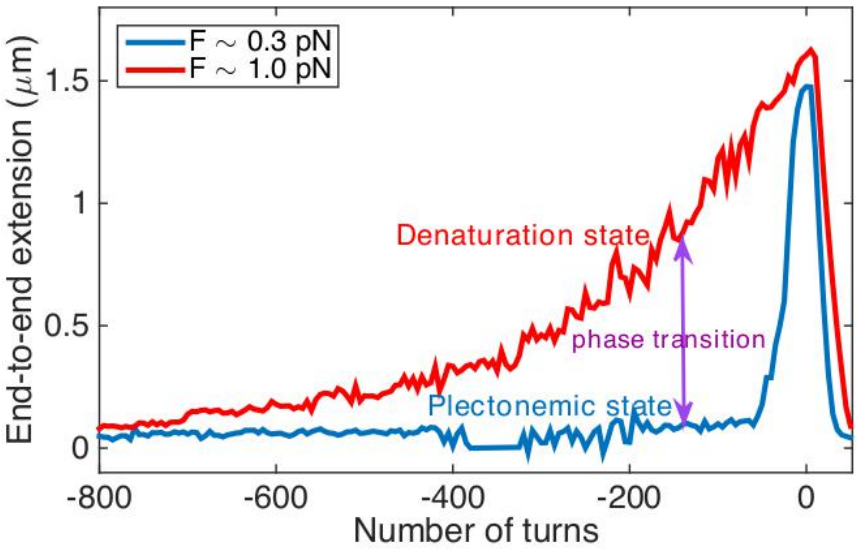

(b)

Figure 7.1.: Representative examples of twisting experiments on a ≈ 1.5 μm long DNA molecule.
(a) End-to-end extension (L_e) measured as a function of low number of turns (n_t). In the legend the values of the applied force F for each measurement are reported. At $F = 0.81$ pN the extension fluctuations are larger for negative n_t.
(b) Twist experiments in the high supercoiling regime at low force (blue) and high force (red). Blue curve represents the plectonemic state, red curve includes a fraction of denatured DNA increasing with n_t.

behavior of this particular DNA form is not completely associable to the left-handed Z-DNA, because it is a metastable structure living in a coexistence state between supercoiled B-DNA and DNA melting bubbles, probably lacking of a complete base-pairing. Figure 7.1(b) represents a twist experiment in the highly negative supercoiling regime clearly showing the occurrence of this phase transition: the L_e extension of a DNA molecule at $F \sim 1\,pN$ constantly decreases with the number of turns n_t, despite the molecule should be completely denatured and extended at such a value of force. The only explanation is the presence of an increasing fraction of DNA with lower persistence length, that means a more flexible molecule having lower extension compared to B-DNA at the the same force. This flexible DNA form is likely a left-handed DNA, a mixed phase of supercoiled and melted B-DNA. Some preliminary results about this topic have been presented for a conference abstract [210].

Similar experiments have been carried out for positive turns, namely clockwise torsions, but in this case the superhelical density and the values of the applied force required to induce a phase transition are much higher. Indeed, the canonical structure of DNA is the right-handed B-form, and consequently the double helix can absorb more clockwise twist and form more compacted and numerous plectonemes along the chain compared to the equivalent phenomenon for counter clockwise twist. The phase transition occurring in this regime is different from the strand separation and formation of the left-handed helix. An extremely overwound DNA stretched with enough force enters in a state with sugar-phosphate backbones in the middle of the double helix and the unpaired bases exposed. This DNA form was named P-DNA, after a model of Pauling for the double helix with a somewhat similar structure [53, 201]. The force necessary to make this phase transition occur is around 6 pN [24, 211], an order of magnitude higher than the corresponding force of L-DNA, and some similarities between P-DNA and the overstretched S-DNA form have been found [202, 203].

Finally, I will describe the experiments aimed to discover a sequence dependence behavior of the denaturation transition to L-DNA. I measured the characteristic force of the transition for three DNA sequences with different GC content, similarly to the study in [207]. A paper about these findings is currently in preparation.

7.1 F_{CHAR} BEHAVIOUR AT HIGH SUPERCOILING

The main parameter adopted to quantify these phase transitions of DNA is the characteristic force F_{char} introduced in section 3.5. As already described, the characteristic force can be measured in two

different ways: the most straightforward strategy is to compute the variance of the DNA extension fluctuations, alternatively it is possible to extract a characteristic time of the autocorrelation function related to each temporal trace of the experiment (figure 3.8). Both quantities plotted as a function of the applied force F exhibit a curve with a characteristic peak (figure 3.9) at the force value corresponding to F_{char}.

I recall that the characteristic force is defined as the force at which there is an equal probability for a DNA molecule to be in the zero-extension plectonemic state or in the extended denaturation state (here L-DNA or P-DNA). Therefore, it is reasonable to expect a dependence of F_{char} with the superhelical density σ, because an increment of the DNA twist leads to a greater fraction of more flexible DNA regions, such as melting bubbles of parallel ssDNA, that require higher forces to be extended. In figure 7.2 I reported some examples of F_{char} measurements by means of the fluctuations variance ($\sigma^2_{L_e}$) analysis, both for negative (a) and positive (b) supercoiling. Colours represent experiments performed at different σ: for negative supercoiling there is a clear dependence, F_{char} increases with σ, whereas for positive supercoiling does not seem to be a similar behaviour.

I have already defined the quantity σ in the first chapter (equation 1.3), but in order to better quantify the experimental results I clarify the relation between the number of turns n_t of figure 7.1 and the superhelical density σ:

$$\sigma = \frac{n_t \cdot 10.4}{N_{bp}} \tag{7.1}$$

where 10.4 is the number of base pairs per turn in B-DNA and N_{bp} the total number of base-pairs of the investigated DNA molecule.

I summarised the resulting F_{char} values calculated from all the analysed molecules in the plots on page 104. From figure 7.3(a) the σ dependence of F_{char} for negative supercoiling can be noticed: the characteristic force increases when DNA is more supercoiled, ranging from 0.7-0.8 pN, the typical value of nanomechanical denaturation [137, 138], to about 1.5-1.6 pN. So, the F_{char} value is roughly doubled by exploring all the available space of negative σ, before the formation of left-handed loops at $\sigma \approx -1.9$ attributable to a Z-DNA transition (paragraph 1.2.2). In the positive supercoiling regime the behavior of DNA is different and surprisingly no apparent σ dependence was identified. The characteristic force did not show a well defined trend, such as for the example of figure 7.2(b). Data in figure 7.3(b) are more widespread compared to those for negative supercoiling, but the cloud of F_{char} values is around 5-6 pN consistently with literature values. The spreading of the data is likely due to the fact that there are experimental issues in measuring the phase transition at $\sigma > 0$: firstly, higher forces require larger magnetic beads,

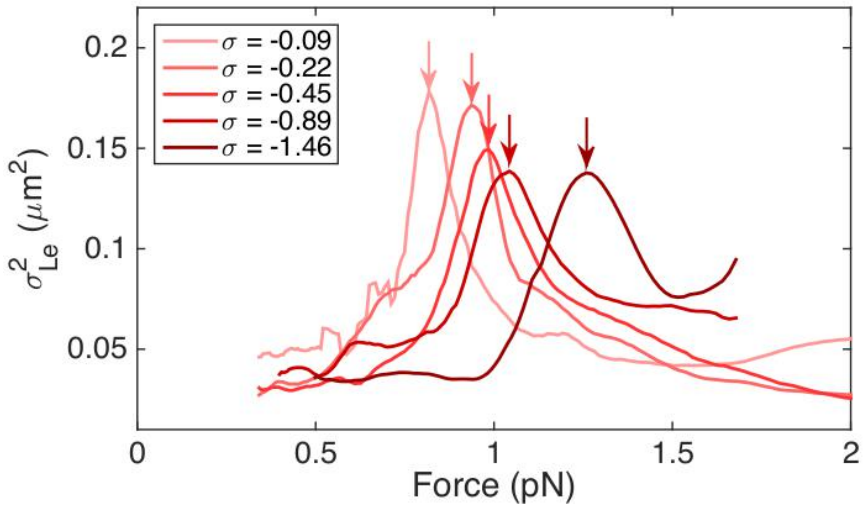

(a)

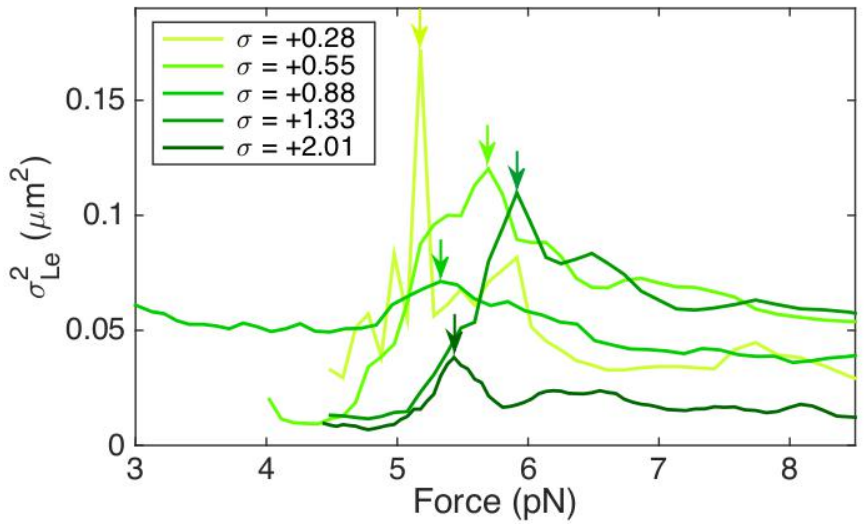

(b)

Figure 7.2.: Example of F_{char} measurement at negative **(a)** and positive **(b)** superhelical density (σ). The variance of DNA extension fluctuations ($\sigma^2_{L_e}$) is calculated as a function of the applied force (F). Each colour is related to a different σ. The forces at which the peaks occur correspond to the values of F_{char}, indicated by the arrows.

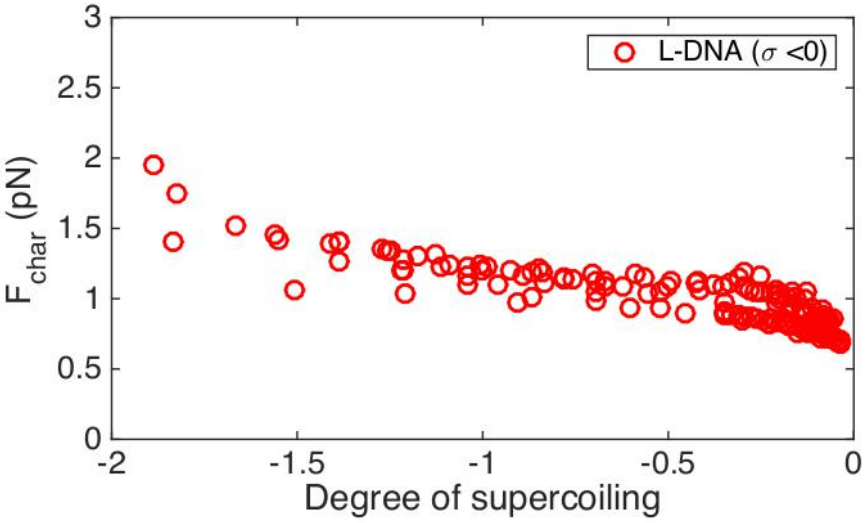

(a)

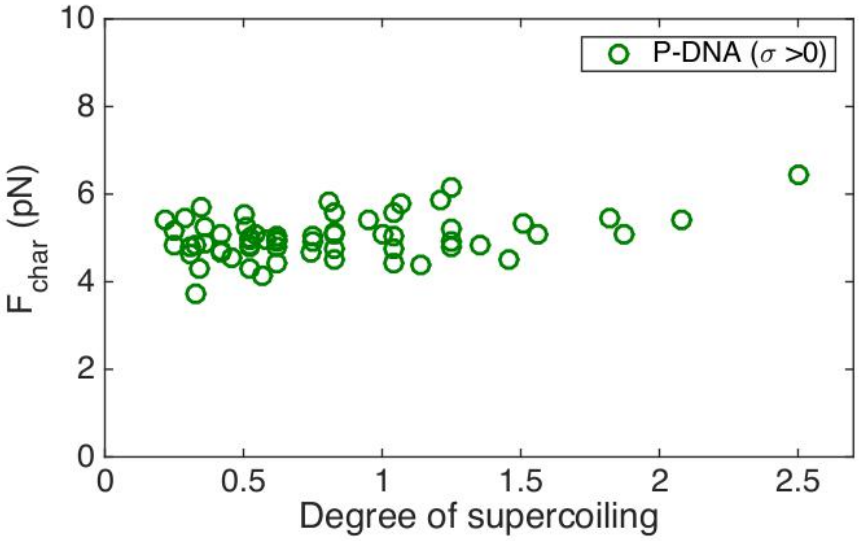

(b)

Figure 7.3.: F_{char} values measured as a function of σ from all the collected data, both for negative **(a)** and positive supercoiling **(b)**. Measurements performed in physiological conditions, 150 mM PBS, by using MT.

namely 2.8 µm beads, which cause a lower precision in the measurement of DNA extension compared to the conventional 1 µm MyOne beads, because of a decrease in signal-to-noise ratio and an increase of Stokes friction with the bead radius [147, 212, 213]. Secondly, a higher number of turns is required to form P-DNA, from $\sigma = 0.2$ - 0.3 to $\sigma \approx 2.8$ [53, 214], and this could introduce additional problems related to the tethered bead-glass surface interactions.

7.2 SEQUENCE DEPENDENCE OF L-DNA TRANSITION

During more recents experiments I analysed a possible sequence-dependent behavior of these conformational changes. Particularly I focused on L-DNA phase ($\sigma < 0$), since it is better known in literature and easier to measure compared to P-DNA transition. I compared the results obtained from three different DNA sequences with the following GC content: 30% (low-GC), 50% (normal-GC) and 77% (high-GC), see paragraph 5.3.1. The normal-GC DNA sequence is the same studied in previous section.

The force-extension measurements enable to observe relevant differences, as shown in figure 7.4: the blue curve represents the typical WLC behavior of a relaxed DNA molecule ($\sigma = 0$) stretched by an external force, while the orange line corresponds to a denaturation curve ($\sigma = -0.11$) describing the transition from the zero-extension plectonemic state to the extended state relaxed by melting bubbles (see the cartoons).

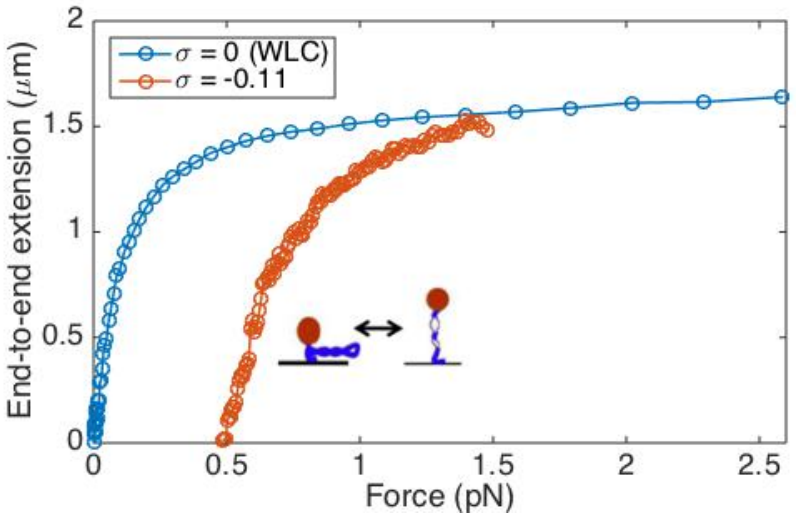

Figure 7.4.: Example of force-extension experiments on a relaxed DNA molecule ($\sigma = 0$, blue) and on a supercoiled DNA molecule ($\sigma = -0.11$, orange). On the y axis the normalized extension of DNA is reported, namely $\frac{L_e}{L_0}$.

I explored the behaviour of the three different DNA sequences in a range of σ between -0.08 and -1.8, and by applying a force F up to 3.6 pN. The resulting denaturation curves are reported in figure 7.5 and they exhibited a clear tendency: the higher GC content is the steeper the transition is. This can be noticed especially for highGC DNA, which seems also characterized by lower F_{char} values, approximately corresponding to the midpoint of the denaturaton curves.

Indeed, I calculated the characteristic force of the three different DNA sequences as a function of the superhelical density, as described above, and I observed some differences depending on the GC content (figure 7.6). For this preliminary analysis I excluded the F_{char} values obtained at the highest σ shown in figure 7.3(a), because the statistics was too low and the results not completely reliable. Two main information can be extracted these curves: the F_{char} of the B-L-DNA transition increases with $\sigma(<0)$ regardless the DNA sequence. In fact, low-GC and high-GC constructs confirmed the general behaviour observed in the previous section for 50%GC DNA. The most interesting result here is the systematically lower value of the characteristic force for the DNA with the highest GC content, a behaviour additionally exhibited in the whole range of supercoiling.

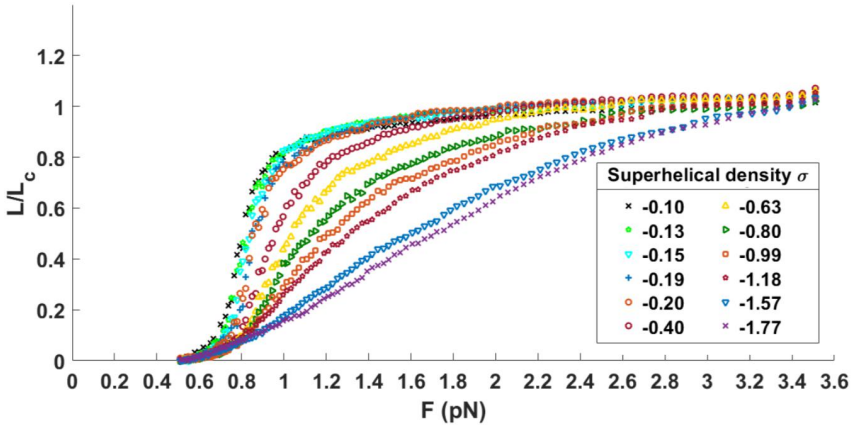

(a)

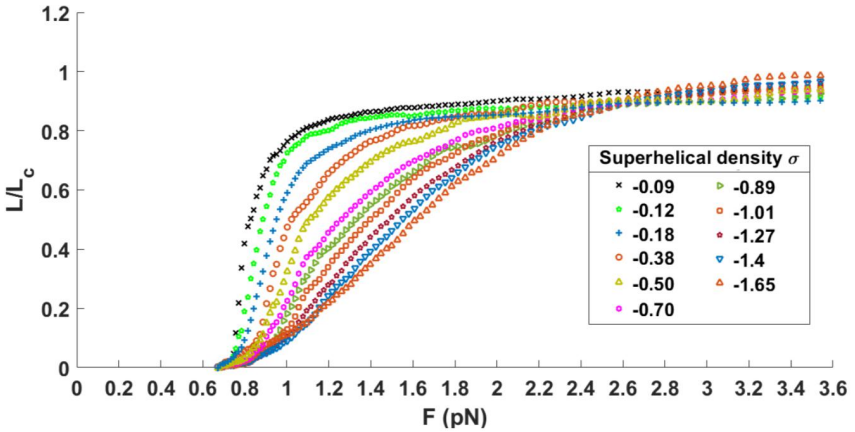

(b)

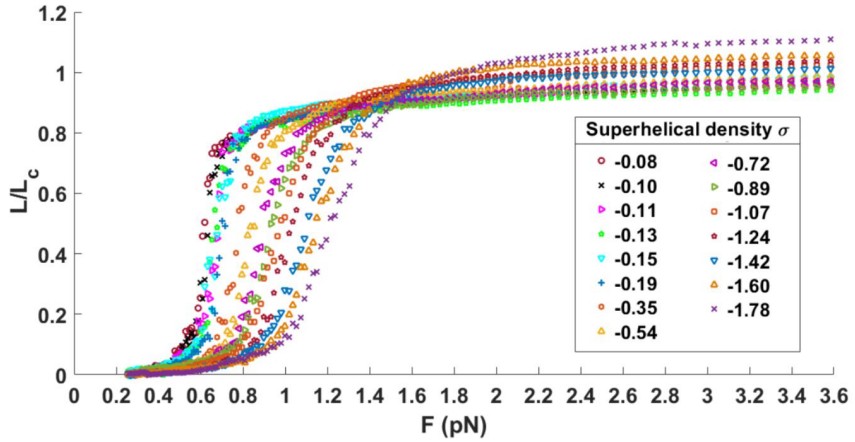

(c)

Figure 7.5.: Force-extension measurements of supercoiled DNA molecules with different superhelical density. σ values are reported in the legend. Data for low-GC DNA **(a)**, normal-GC DNA **(b)**, and high-GC DNA **(c)**.

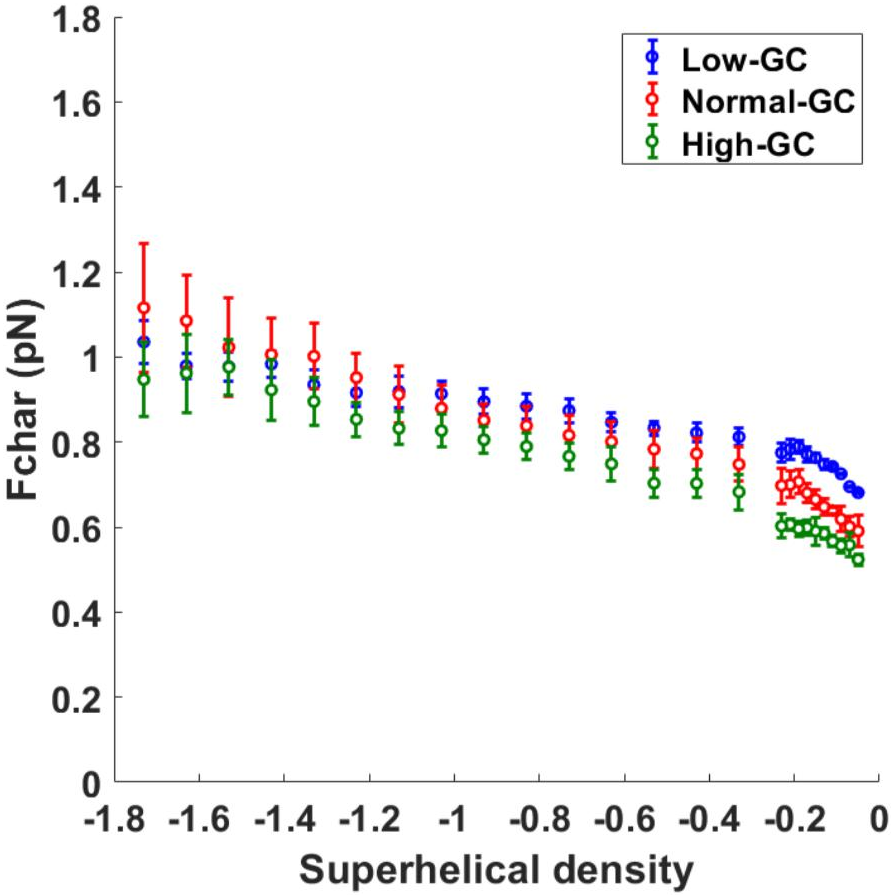

Figure 7.6.: Characteristic force values (F_{char}) as a function of the superhelical density (σ) for different GC content DNA sequences: low-GC (blue), normal-GC (red) and high-GC (green). Measurements performed by MT in physiological conditions, 150 mM PBS.

8

DNA-DRUG INTERACTIONS

The first research project in which I was involved in my PhD was the study of the nanomechanical interactions between DNA and some anticancer drugs, particularly platinum-based molecules. The results I am going to present have been published in [175].

Platinum-based compounds are frequently prescribed in clinics for the treatment of solid tumors, for example Cisplatin (cis-diamminedi chloroplatinum(II)), hereafter CIS, have been used to produce several drugs and because of its efficacy and versatility it has been often referred to as the penicillin of cancer. See figure 8.1A for CIS chemical structure. This molecule exerts cytotoxic effects by forming cross-links with DNA [215, 216], mostly intermolecular links, but sometimes DNA adducts are produced by CIS intramolecular links, which are more relevant for cytoxicity. In literature it was shown that CIS binding is favored with DNA sequences including adjacent purines, especially guanines [217, 218]. The cross-linking reaction between CIS and DNA hinders the opening of DNA and, as a consequence, DNA replication and transcription are significantly hampered. The impeding of these crucial DNA functions results in an irreversible DNA damage and the induction of apoptosis. However, despite the wide use of CIS in clinical practice, a number of drawbacks in using this drug are still persistent.

This is why there is an important research of new platinum-based compounds, such as multinuclear Pt(II) molecules instead of the monofunctional Pt complexes, hoping to find more efficient and less toxic anticancer drugs. These multinuclear platinum compounds form long range inter- and intra-strand cross-links with DNA molecules, leading to different kind of DNA adducts. A stronger binding mechanism to DNA could lead to an higher antitumoral efficacy and overcome CIS resistance. The two multinuclear complexes investigated in this project are BBR3005 and BBR3464: BBR3005 is a dinuclear platinum compound containing two monofunctional platinum groups separated by six methylene groups, see figure 8.1B. This characteristic confers a high flexibility to the Pt nuclei and the drug molecule is thus free to adopt the best geometry for interacting with DNA [219]. BBR3005 forms inter-strand cross-links with an efficiency of $\sim$ 70-90% of the total DNA adducts, while its ability to twist and unwind

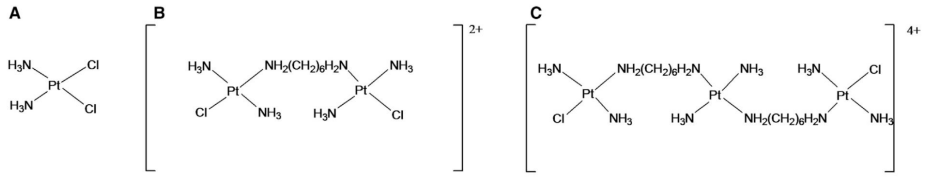

Figure 8.1.: Chemical structures of CIS **(A)**, BBR3005 **(B)** and BBR3464 **(C)**. Figure from [175].

DNA is not very different from that one of CIS [175]. BBR3464 is the more complex molecule studied here, indeed it has three monofunctional Pt groups (see figure 8.1C). This multinuclear platinum compound has a faster binding kinetics compared to CIS because of its high positive charge and bigger structural flexibility, forming more DNA adducts as well. As above mentioned, CIS forms rigid, short range and intra-strand adducts, on the contrary cross-links formed by BBR3464 are flexible and long range, including also inter-strand links. By comparing the two multinuclear drugs, BBR3005 has an higher efficiency of inter-strand cross-links formation, because BBR3464 has a frequency of only about 20% of the the total DNA adducts; whereas as regards the binding kinetics, BBR3464 is much faster during cross-linking reaction [215].

In the current work we analysed the effects of these three drugs on single DNA molecules by means of a magnetic tweezers setup. Mechanical modifications in DNA structure and DNA stability after the formation of DNA-drug complexes were monitored. Specifically, it was observed how the two multinuclear platinum-based compounds affects DNA stability as compared with CIS binding, in terms of nanomechanical denaturation induced by torsional stresses applied with MT and thermal stability studied with spectrophotometric melting assays, namely UV absorption measurements.

8.1 MECHANICAL EFFECTS

8.1.1 *Plectonemes formation*

The first two analysed parameters concern the formation of plectonemes, and they give information about the mechanical properties of DNA-drug complexes: the *buckling number* n_b, corresponding to the number of turns necessary to begin the formation of plectonemes, and the *plectoneme radius* R, derived from the quantity $\frac{dL_e}{dn_t}$, which is the slope of twisting measurements (section 3.4).

The resulting values of n_b and $\frac{dL_e}{dn_t}$ were plotted as a function of the force F, thus making it possible to observe potential power law dependencies, as clearly shown in log-log plots reported in figure 8.2 and 8.3, for n_b and $\frac{dL_e}{dn_t}$ respectively. In all the cases, the power law

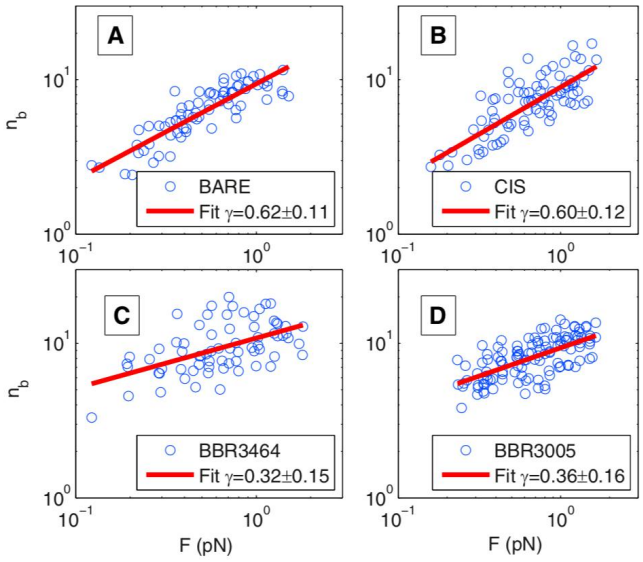

Figure 8.2.: n_b values extracted from MT rotation measurements (section **??**), as a function of the force F. The four log-log plots show the behavior of bare DNA (**A**), CIS-DNA complex (**B**), BBR3005-DNA complex (**C**) and BBR3464-DNA complex (**D**). Blue circles are data points and red lines the linear fit on the log-log plots. The fit parameter γ is the value of the exponent, assuming that $n_b \propto F^{\gamma}$. Figure from [175].

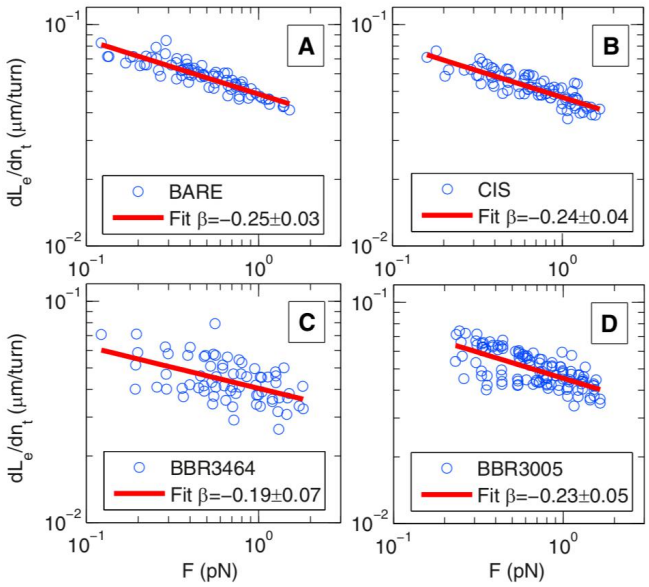

Figure 8.3.: $\frac{dL_e}{dn_t}$ values extracted from MT rotation measurements (section **??**), as a function of the force F. The four log-log plots show the behavior of bare DNA (**A**), CIS-DNA complex (**B**), BBR3005-DNA complex (**C**) and BBR3464-DNA complex (**D**). Blue circles are data points and red lines the linear fit on the log-log plots. The fit parameter β is the value of the exponent, assuming that $\frac{dL_e}{dn_t} \propto F^{\beta}$. Figure from [175].

behavior was confirmed, indeed there is a small dispersion of data points (blue circles) around the red lines representing the linear best fit.

Once data are described by a power law behavior, it is possible to assume that the following equations hold

$$n_b \propto F^{\gamma} \tag{8.1a}$$

$$\frac{dL_e}{dn_t} \propto F^{\beta} \tag{8.1b}$$

and thus extracting the exponents γ and β from the linear fit. Values and related errors of the exponents in each condition are reported in the inset of log-log plots. Errors are the standard deviations computed during the fitting procedure of Matlab. The resulting values of the exponent γ related to n_b can be divided into two groups: bare DNA and CIS-DNA complex showed an exponent γ of about 0.6, while in presence of the two BBR compounds $\gamma \approx 0.3$. This seems to suggest that the multinuclear Pt compounds weakens the buckling transition dependence on the force. As regards the slope, the exponent β is negative and around -0.2 for each condition.

8.1.2 *DNA length and bending stiffness*

The second part of the mechanical properties study was focused on the analysis of the worm-like chain behavior of DNA in presence of the drugs. In figure 8.4 three examples of WLC curves of DNA-drug complexes are reported, when the drugs had already reached the saturation concentration (see figures C.1 and C.2 in supplementary material). Black dots are data points representing the applied force F (in log scale) versus the measured end-to-end extension of DNA, L_e, while the red line is the WLC fit, introduced in equation 3.7. In section C of supplementary material additional F vs L_e data for different concentrations of the drugs are reported.

It is immediately clear that the drugs have different effects on DNA: the contour length L_0 basically does not change in presence of CIS and BBR3005, whereas with BBR3464 there is a significant decrease. More precisely, $L_0 \approx 1.8\,\mu m$ and $\approx 1.7\,\mu m$ for CIS-DNA and BBR3005-DNA complexes respectively, values consistent with the contour length of bare DNA, around $1.8\,\mu m$. On the contrary, $L_0 \approx 1.2\,\mu m$ when BBR3464 binds DNA. The persistence length L_P is reduced in each of the three cases, but BR3464 is again the most effective drug. $L_P \approx 33\,nm$ with CIS and BBR3005 and $\approx 27\,nm$ in presence of BBR3464. These average values are calculated from the concentration at which drugs seem to start inducing some effects on DNA, in our case $\geqslant 0.2\,\mu M$.

Figure 8.5 illustrates the histograms summarizing the results about L_0 and L_P. Mean values were obtained from a few tens of DNA

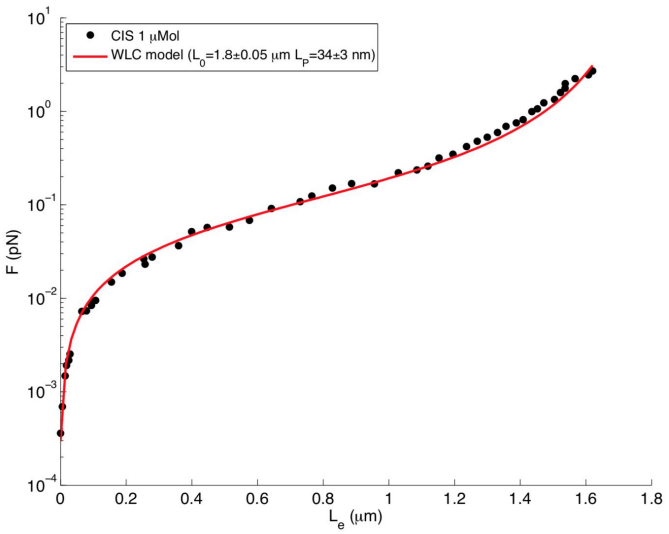

(a)

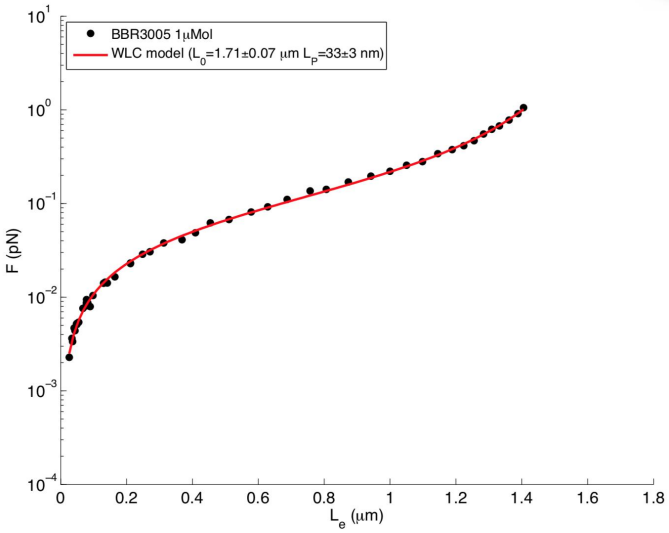

(b)

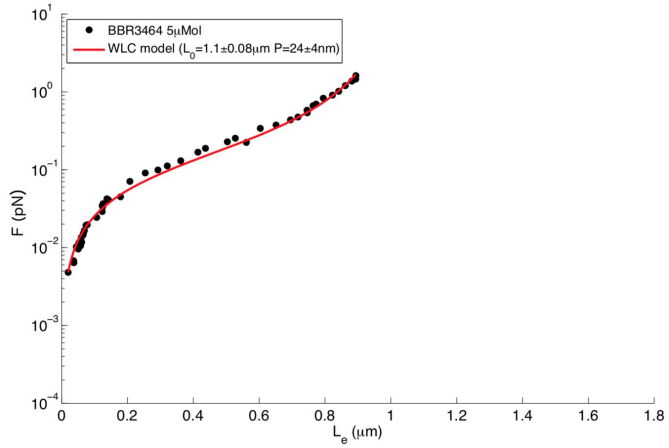

(c)

Figure 8.4.: WLC curves of DNA in presence of CIS **(a)**, BBR3005 **(b)** and BBR3464 **(c)**. Black dots are data points, red lines the WLC fits. In the insets concentration of the drug and fitting parameters are reported. Figures from [175].

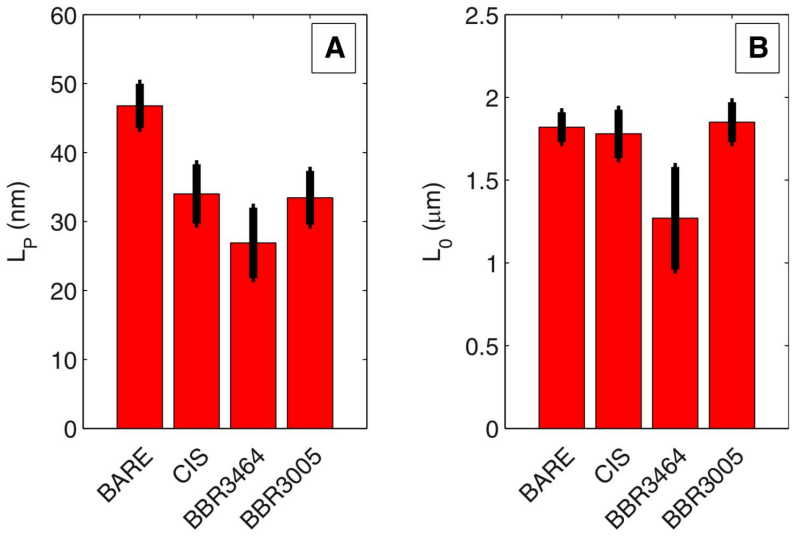

Figure 8.5.: Histograms of the persistence length L_P **(A)** and the contour length L_0 **(B)** values extracted the WLC fit of F vs L_e data. Average values are calculated over a few tens of DNA and black error bars corresponds to the standard deviations. Figure from [175].

molecules, each one measured about five times, and the error bars correspond to the standard deviations of the data.

8.2 DNA STRUCTURAL STABILITY

8.2.1 *Nanomechanical denaturation*

The most interesting effects of the drugs on DNA were observed during the experiments testing DNA double-helix stability. Specifically, a denaturation process was nanomechanically induced to DNA by applying torsion and force to the molecules, as already described in section 3.4.2. This analysis could distinguish even better the different interactions of the three platinum-compunds with DNA. The characteristic force of denaturation, the F_{char} introduced in equation 3.16, was derived by calculating the standard deviation σ_{L_e} and the autocorrelation characteristic time τ_{char} of DNA extension fluctuations. These two quantities were plotted as a function of the applied force and the F_{char} can be extracted from the typical peak of these plot, see figure 8.6. The F_{char} value is heavily dependent on the specific drug interacting with DNA, indeed the three drugs can be easily distinguished during this experiment: CIS-DNA complex shares a very similar value with bare DNA, namely $F_{char} \approx 0.8\,pN$, but the two BBR compound are characterized by much lower values, $F_{char} \approx 0.5\,pN$ for BBR3005 and $F_{char} \approx 0.2\,pN$ for BBR3464, indicating again a major effect on DNA from this last drug.

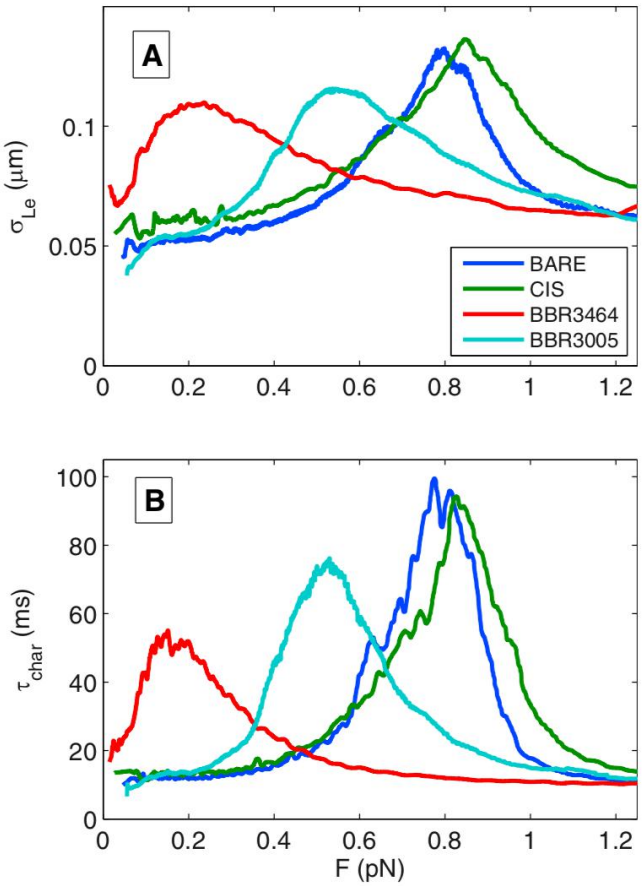

Figure 8.6.: Standard deviations σ_{L_e} **(A)** and autocorrelation characteristic times τ_{char} **(B)** of DNA extension fluctuations. They are plotted as a function of the applied force F. Different colors indicate the four conditions (bare DNA and three drug-DNA complexes), see labels for the names. The F_{char} values are extracted from the maximum values of the curves. Figures from [175].

8.2.2 *Thermal denaturation*

The nanomechanical denaturation experiments were combined with traditional biophysical techniques, that is to say spectrophotometric melting assays, in order to have complementary information about the denaturation process of DNA, in terms of thermal stability. Experiments consisted in temperature ramps from 40°C to 90°C applied to DNA samples and in measuring the UV absorption at 260 nm. Melting profiles can be obtained from the well-known increment in UV absorption when DNA is under denaturation conditions, see figure 8.7A.

Melting transition is usually described with two parameters: the melting temperature, T_m, and the temperature range of the transition,

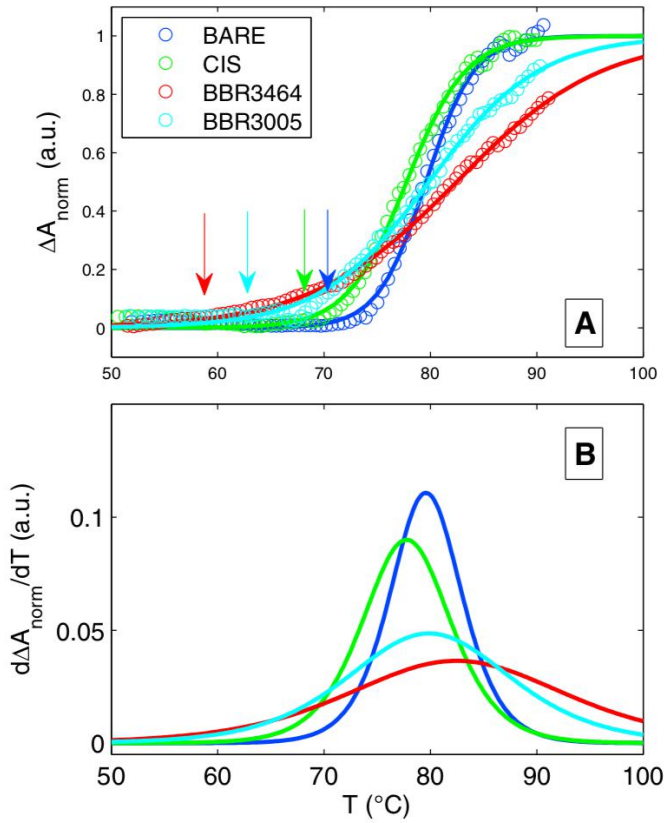

Figure 8.7.: Melting curves of bulk thermal denaturation experiments. Every color indicates a condition, bare DNA, CIS-, BBR3005-, BBR3464-DNA complexes, see labels. **(A)** Normalized differential UV absorption at 260 nm, ΔA_{norm}, measured as a function of the temperature T. Solid lines are the fit described by equation 8.2 and arrows indicate T_s values at which melting transition begins. **(B)** Derivatives of melting profiles reported in figure 8.7A, more precisely derivatives of fitting curves. Figures from [175].

ΔT [5, 110]. The normalized UV absorption data can be fitted with the following equation

$$\Delta A_{norm} = \frac{1}{1 + e^{-\frac{T - T_m}{\Delta T}}} \tag{8.2}$$

where ΔA_{norm} is the normalized difference between the 260 nm absorption at low and high temprature

Different behaviors were observed depending on the drug binding to the DNA, as regards the melting temperature: CIS interactions produced a slight negative shift in T_m, from 79.6°C of bare DNA to 77.8°, BBR3005 did not produce any shift (79.9°) and BBR3464 induced a positive shift, 82.5°. The temperature range showed a more peculiar behavior, indeed all the three drugs increased this quantity as compared to bare DNA, indicating that the melting transition occurred over a wider range of temperature. Particularly, $\Delta T = 2.3$°C for bare

DNA, 2.8°C for CIS, 6.9°C for BBR3005 and finally 5.1°C for BBR3464. In figure 8.7B the significant broadening of the transition, especially for BBR compounds, is clearly visible by the derivatives of the fitting curves of figure 8.7A. An additional parameter was used for the analysis of the thermal denaturation, the temperature at which the transition begins, T_s, indicated by the coloured arrows in figure 8.7A. T_s has been defined as the temperature at which only 3% of DNA is melted. Lower T_s values for DNA-drug complexes suggest that there are small regions of DNA more easily to denature in presence of the drugs with respect to bare DNA.

9

H-NS PROTEIN STRUCTURAL ROLE

The main research project of this PhD thesis has been the study of the roles of H-NS protein in bacterial nucleoid structure and organization, more precisely the investigation of the dual role of this NAP (sections 2.1 and 2.2). In this chapter I am going to present the experimental findings concerning the structural role, studied in terms of the nanomechanics of the interaction between DNA and H-NS. In the next chapter I will describe the other function of H-NS, the regulatory role, by time-lapse fluorescence experiments at the single-cell level. This project is part of a collaboration with Bianca Sclavi (ENS Paris-Saclay and CNRS), who deals with the biological details of this research activity and provided both the H-NS protein sample used for MT experiments and some of the cell strains studied during the single-cell experiments; Marco Cosentino Lagomarsino (IFOM and University of Milan), who develops the theoretical models with the aim of predicting the experimental findings, and Pietro Cicuta (University of Cambridge), whose group works with microfluidic devices to study gene expression of bacterial cells, I carried all the single-cell experiments in his laboratory. A paper about the results of H-NS-DNA nanomechanical interactions is currently in preparation.

The structural role of H-NS was studied by force spectroscopy experiments performed with the MT setup described in chapter 4. These experiments were carried out in the conditions required to observe the structural binding mechanism of the protein, namely the bridging binding mode. In literature it was found that the presence of divalent ions induces the formation of DNA-H-NS-DNA bridges, therefore the buffer solution in which DNA and H-NS were suspended contains 10 mM of $MgCl_2$ (see section D.1) [82, 83]. The analysis of the force-extension curves of single DNA molecules is the method of choice to accurately understand the molecular interaction between the protein and the DNA [220, 221]. Indeed in this way it is possible to estimate the rupture the force and the stability of the formed DNA-protein complex, as well as the kinetics of the the binding mechanism [79, 222]. There are many examples in literature not only by using MT setup, but also OT or AFM [223–225].

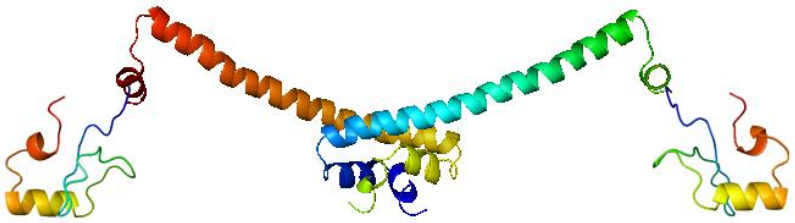

Figure 9.1.: Crystal structure of H-NS dimer in antiparallel configuration (see figure 2.8(a) for comparison of parallel and antiparallel configuration). Figure from iGEM2011, HKU team.

The pulling force experiments I am going to present have been always performed from high to low forces at the beginning, i.e. starting from an extended state of the DNA molecule, in order to favor the H-NS binding to DNA. The statistics and the accuracy of these experiments were significantly increased compared to the typical experiments, as the WLC data shown in chapter 6 and 8: if usually the step size of the magnets movement during a force-extension curve is 50-100 μm, with each data point equal to an average of 300-500 measurements of DNA extension (figure 6.5), in the case of DNA in presence of H-NS protein the step size is reduced to 20 μm and the extension per data point is calculated by averaging 1500-2000 measurements. These settings are required to effectively observe the DNA-protein interaction with sufficient statistics, including the kinetics. The drawback is obviously a much longer time for every individual measurement.

9.1 THE BRIDGING BINDING MECHANISM

A first experiment showing DNA condensation as a result of the interaction with H-NS is the force-extension plot reported in figure 9.2. The green curve is the conventional behavior of a bare DNA described by the WLC model (section 3.3), while the blue curve is related to DNA in presence of the H-NS protein: DNA extension drops to zero in a very narrow range of forces as a consequence of the bridging mechanism promoted by H-NS. From this curve it is already clear that H-NS binding process has a strong effect on DNA and it occurs relatively quickly. The relevant modification on DNA structure produced by this binding mechanism can be also attributed to the dimeric structure of the protein, which enables to easily bind two points along the DNA sequence and connect them to form a loop, a 'bridge', reducing DNA extension. See figure 9.1 and the figure 2.8(a) previously introduced for H-NS structure.

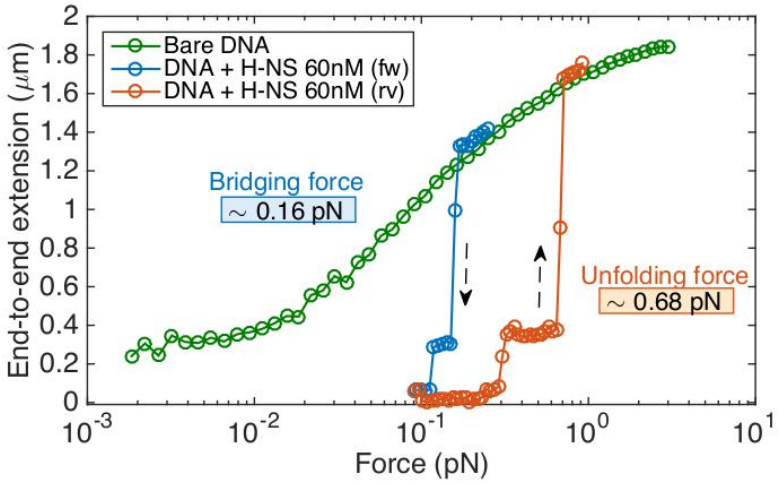

Figure 9.2.: DNA bridging resulting from the interaction with H-NS protein. Force-extension curves of bare DNA (green) and DNA in presence of 60 nM H-NS (blue and orange). Blue curve represents the bridging (folding) event, forces are gradually decreased from high values to lower ones (fw), whereas in the orange curve the unfolding process of the H-NS-DNA complex is observed, forces are increased from low to high values (rv). The two black arrows indicate the direction of the measurements. Folding and unfolding forces are also reported.

9.1.1 *Hysteresis and concentration dependence*

In figure 9.2 a first interesting feature is observed: a hysteresis during the DNA-protein binding. The orange curve is in fact a force-extension measurement carried out right after the blue curve, but in the reverse way, from low to high forces, while the blue curve is performed from high to low forces as indicated by the black arrows, starting from a completely extended DNA molecule. The two curves of DNA in presence of H-NS are distinct and not overlapping, because the H-NS-DNA complex required a much higher force to be disrupted (*unfolding force*) compared to the force necessary to form it (*bridging/folding force*).

The second aspect investigated is the possible concentration dependence of the bridging mechanism. In figure 9.3 the same curve of bare DNA is reported in green together with many other curves of different colors, corresponding to measurements of DNA molecules in solution with different concentrations of the H-NS. The protein concentrations spans about two orders of magnitude, ranging from 15 nM to 1 μM. The experiments in presence of 5 nM H-NS did not show a clear DNA folding event, see the figure supplementary material (section D.2), consequently those data were not included in the analysis of the bridging force discussed in chapter 13. All the force extension measurements at different protein concentrations collapse

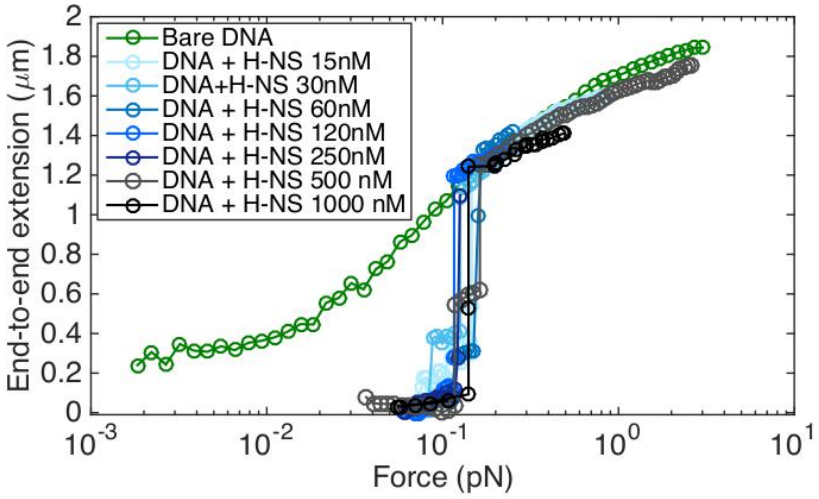

Figure 9.3.: Concentration dependence of H-NS bridging binding mechanism. Force-extension curve of bare DNA (green), and the blueish coloured curves corresponding to DNA in presence of different H-NS concentrations, ranging in a wide range between 15 nM and 1 μM.

approximately on the same curve, and the same applies to the unfolding curves, just with a a bigger spreading that means a higher noise, particularly for the 15 nM curve (figure D.2).

9.1.2 *Temporal kinetics*

A very useful advantage of these single-molecule experiments is the possibility of analysing the temporal kinetics of this molecular interaction. Each data point of the force-extension curves reported above is an average of 1500-2000 measurements, leading to a time step of about 30-40 s considering the ≈ 50 Hz frame rate of the camera (paragraph 4.2.1). In figure 9.4 this concept is clearly explained: in the top right inset an enlargement of a force-extension measurement similar to that one shown in figure 9.2 is reported. The five temporal traces of the DNA extension shown in the main figure correspond to the five data points highlighted with coloured circles.

Other two examples of temporal traces related to experiments on DNA and lower concentration H-NS are reported in page 124. The bridging/folding (figure 9.5) and the unfolding (figure 9.6) multistep binding mechanisms are more evident in these examples. In that specific case there were three steps both during DNA folding and unfolding, probably corresponding to three binding events (loops/bridges) by the H-NS proteins.

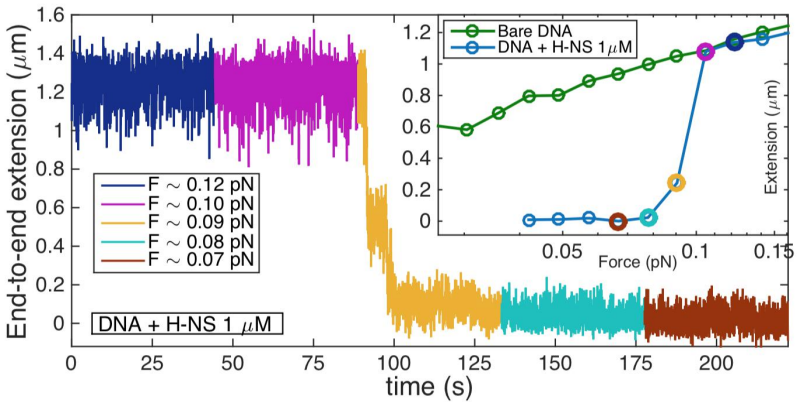

Figure 9.4.: Temporal traces of the DNA end-to-end extension during a bridging binding event. Each coloured trace is collected at a different force, indicated in the legend, and corresponds to the data point highlighted with the same colour in the top right inset, an enlargement of a force-extension curve.

9.1.3 *Mechanical denaturation*

An additional strategy to explore the binding mechanism of H-NS protein is to analyse the stability of DNA structure against the denaturation applied by nanomechanical stresses. The nanomechanical denaturation has been introduced in chapter 3 and already discussed for the experimental findings of the high supercoiling and DNA-drugs interactions studies. Particularly, the characteristic force F_{char} behavior was investigated in presence of H-NS, to understand if the activity of the protein stabilizes or destabilizes the formation of plectenomic structures. In figure 9.7 force extension curves of bare DNA and DNA+H-NS are reported: the green curve is the canonical WLC behavior of DNA without applied torsion, the yellow curve is still related to bare DNA but the molecule underwent a certain degree of torsion, expressed in number of turns, and in the same way the dark blue curve represents an H-NS-DNA complex subject to an identical torsion, required to mechanically induce the denaturation. The presence of H-NS considerably shifted the value of the F_{char} and introduced a multistep mechanism, very well quantifiable by the autocorrelation characteristic time analysis, as shown in figure 9.8. The related temporal trace is reported in supplementary material (figure **??**), to be compared with the typical traces observed during denaturation of bare DNA (figure 3.8(a)).

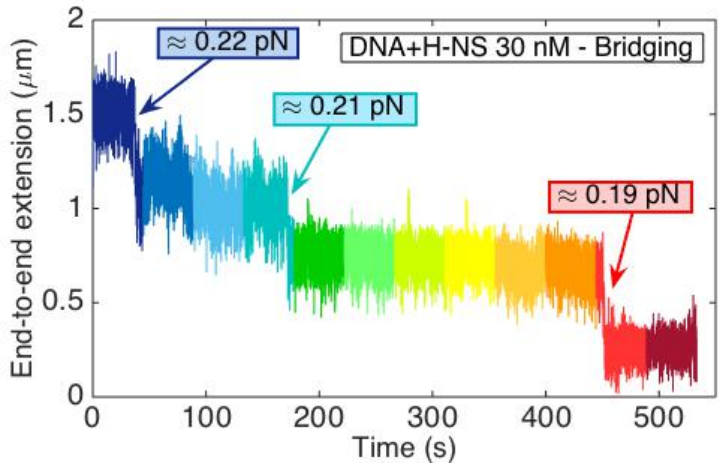

Figure 9.5.: Temporal traces of a force-extension experiment during a DNA folding process in presence of 30 nM H-NS. Each coloured trace is collected at a different force, in the three labels the forces at which binding events occur are reported. The binding events are shown by a quick and significant decrease in DNA extension.

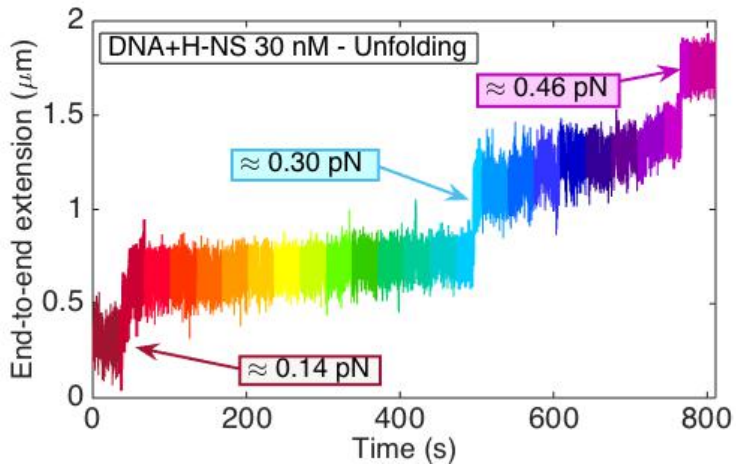

Figure 9.6.: Temporal traces of a force-extension experiment during the unfolding event of a H-NS-DNA complex (30 nM H-NS). Each coloured trace is collected at a different force, in the labels the forces at which a binding events occur are reported. The binding events are shown by a quick and significant increase in DNA extension.

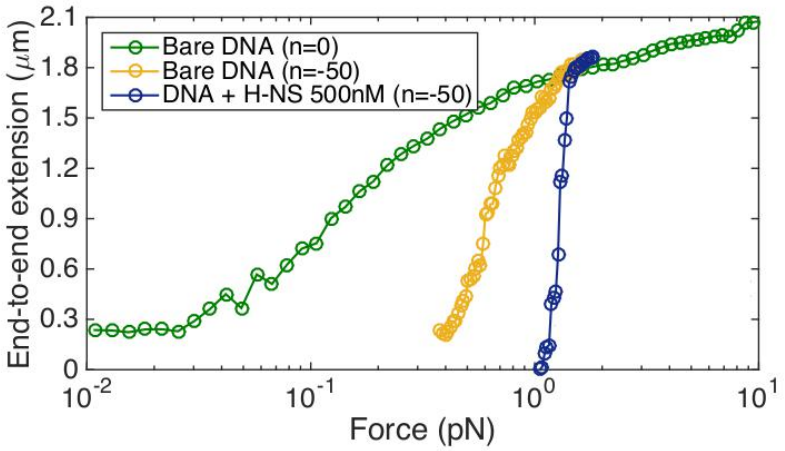

Figure 9.7.: Nanomechanical denaturation of a H-NS-DNA complex, with 500 nM of H-NS. Green curve is the standard WLC behavior of bare DNA without any applied torsion, included for comparison. Yellow and dark blue curves are the effective denaturation experiments, a certain torsion was applied to the bare DNA (yellow) and to the H-NS-DNA complex (dark blue) in order to induce the denaturation at a specific force (see section **??**).

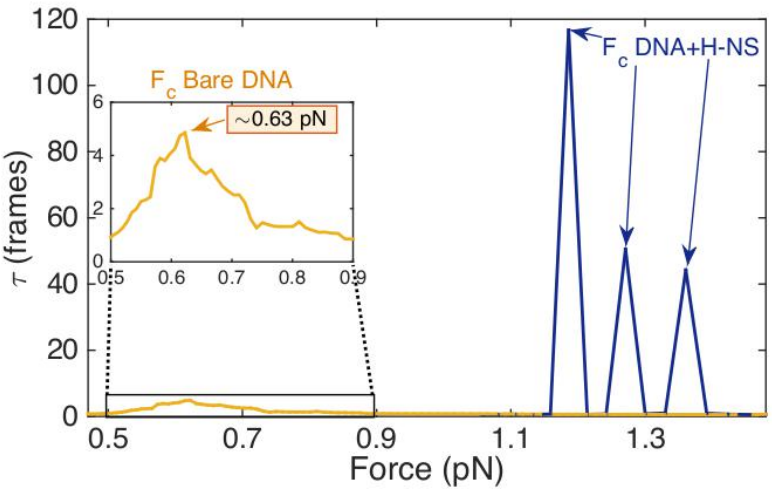

Figure 9.8.: Autocorrelation characteristic times of the denaturation curves reported in figure 9.7. The force values of the maxima correspond to the F_{char}. The presence of H-NS protein induces a stronger correlation, higher value of τ, and introduced intermediate states, three in this case.

9.2 MACROMOLECULAR CROWDING EFFECT

The main goal of this research project has been to study the activity of H-NS in conditions as close as possible to the cellular environment, that is a crowded space as above explained (section 2.3). To meet this requirement, a crowding agent was introduced in the solutions containing DNA molecules and H-NS proteins, in order to mimic the macromolecular crowding inside the cell. Before introducing the crowding agent together with the protein, it was necessary to study and analyse the effects on DNA of this crowder alone. The chosen crowding agent is the widely used neutral polymer poly-ethylene glycol, otherwise known as PEG, for this experiments PEG1500.

9.2.1 *Hysteresis and concentration dependence*

PEG1500 induced a DNA condensation apparently similar to that one observed in presence of H-NS and described in the previous pages. However, a more in-depth analysis shows that the DNA collapse deriving from the crowding effect have a completely different origin: first of all, there is not an evident hysteresis in this mechanism, since the folding and the unfolding curves are almost perfectly overlapped, see figure 9.9. Secondly, this DNA condensation strongly depends on the concentration of the crowding agent, in figure 9.10 you can notice how the PEG+DNA curves are increasingly shifted to the right for higher PEG concentrations.

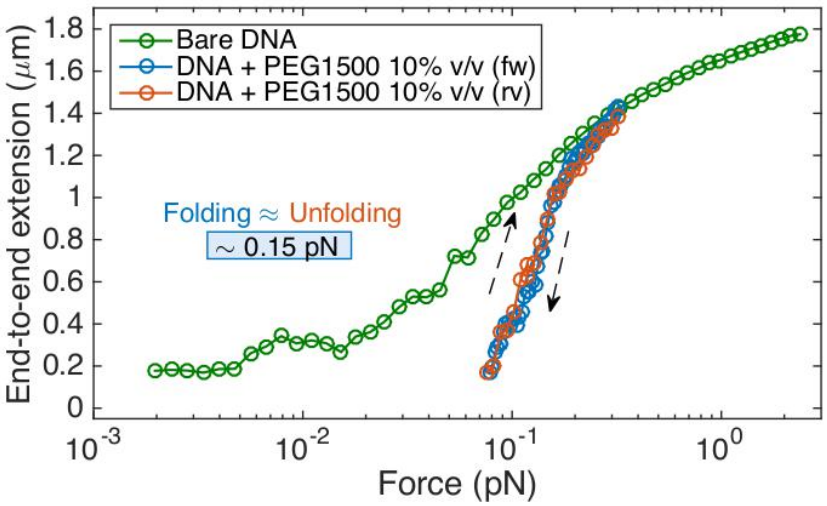

Figure 9.9.: DNA condensation resulting from the interaction with PEG1500. Force-extension curves of bare DNA (green) and DNA in presence of 11% *v*/*v* PEG (blue and orange). Blue curve represents the folding event, whereas the orange curve is the unfolding process. The two black arrows indicate the direction of the measurements. Folding and unfolding force values are reported.

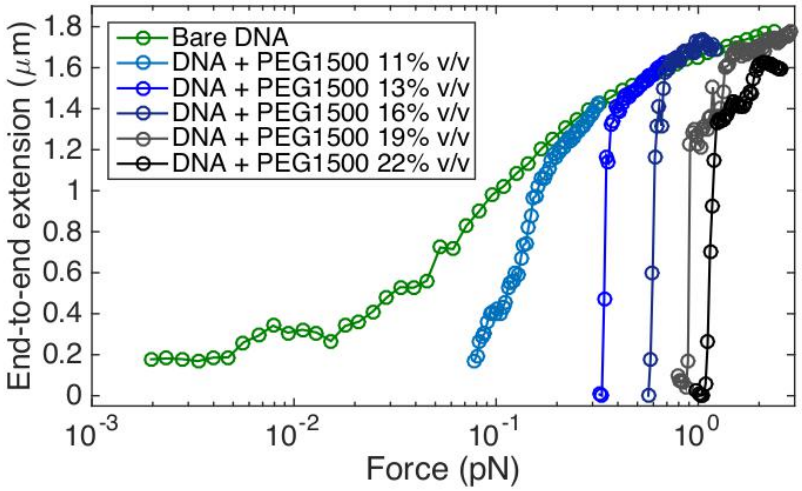

Figure 9.10.: Concentration dependence of PEG-induced DNA condensation mechanism. Force-extension curve of bare DNA (green), and the blue-ish coloured curves corresponding to DNA in presence of different PEG concentrations, ranging from 11% to 22% v/v.

The reason is probably that the PEG-DNA interaction does not involve a real binding mechanism such as that one with the protein, but depletion force effects are instead involved, a process intrinsically concentration-dependent [95, 107, 108].

The concentration dependence of this type of DNA condensation, hereafter Ψ condensation (see section 2.3), can be also observed by the differences in the shape of the DNA collapse curves: at low concentrations DNA collapses more gradually, as for the ~ 11% v/v PEG measurements, whereas at higher concentration the transition is much steeper, see the curves of figure 9.10 for concentrations $\geqslant$ 13% v/v. Furthermore, at concentrations higher than or equal to 13% v/v I could not measure the force extension curve in the reverse way (rv), to look for a potential hysteresis, because the chamber surface became 'sticky' and tethered magnetic beads got stuck to the bottom of the flow chamber. Even under an applied and persistent force of a few of piconewtons it was impossible to detach the stuck beads from the surface and it was necessary to flush out several milliliters of buffer solution to remove PEG and recover freely moving tethered beads. On the other hand, for lower PEG concentrations there is a different behavior: if the volume fraction is less than or equal to 5% no DNA condensation or other effects were observed, if the concentration is between 8-11% v/v a coexistence region was present, i.e. sometimes Ψ condensation occurred and sometimes did not, even on the same DNA molecule and under the same conditions, see figure 13.5.

The effect of macromolecular crowding has been visualized by using AFM imaging technique as well. This is the most direct way to see DNA condensation in presence of macromolecular crowding and how this process heavily depends on the concentration. In figures 9.11 and 9.12 images of DNA incubated with three different concentrations of PEG1500 are reported. 7.5% v/v PEG1500 did not induce any condensation on DNA, and this results fairly consistent with MT data, while in presence of 10% v/v PEG1500 some DNA aggregates begin to form. Finally at 15% v/v the PEG-induced DNA condensation is particularly evident and DNA aggregates are large, especially at higher DNA concentration, figure 9.12.

9.2.2 *Temporal kinetics*

The temporal traces are very helpful also in this case, to improve the comprehension of the molecular mechanism behind the Ψ condensation. On page 130 I reported two examples of the temporal kinetics of force-extension experiments of DNA in presence of PEG1500 at 11% v/v (figure 9.13) and 19% v/v (figure 9.14). Firstly, these temporal traces highlight the differences between the DNA condensation induced by H-NS bridging and the DNA condensation in presence of PEG. Indeed, the clear multistep feature typical of the formation of multiple loops by the protein is absent with PEG. The two figures describing the kinetics of Ψ condensation confirm its concentration dependence behavior: DNA condensation in presence of 11% v/v PEG was relatively gradual and slow, preceded by an increase in the noise of DNA extension measurement, while at 19% v/v PEG induced an abrupt and quick condensation of DNA.

9.2.3 *Mechanical denaturation*

The denaturation process of DNA was mechanically studied in crowding conditions too, to further investigate the effects of a crowded environment on DNA structural properties, figure 9.15. For example, by means of this kind of experiments it is possible to assess if the crowder promotes supercoiled DNA structures, the plectonemes, or the formation of melting bubbles. In this case the results are very similar, at least qualitatively, to those obtained for H-NS: the crowding condition favors the formation of plectonemic structures, indeed the F_{char} became higher as better shown by figure 9.16. Looking at this figure it can be seen that a multistep process appears for DNA under the effect of a crowding agent, exactly like the denaturation of H-NS-DNA complex, the only slight difference are higher F_{char} values for PEG. The temporal trace of the denaturation process of DNA in presence of PEG in included in supplementary material (figure D.12).

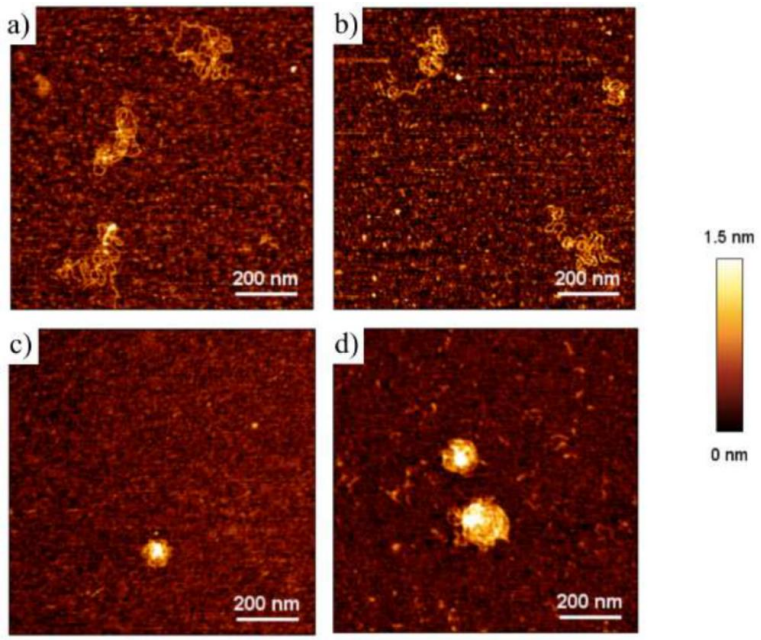

Figure 9.11.: AFM images of bare DNA **(a)** and DNA in presence of PEG at 7.5% *v*/*v* **(b)**, 10% *v*/*v* **(c)**, 15% *v*/*v* **(d)**. In all these experiments the concentration of DNA was 0.3 ng/ µl.

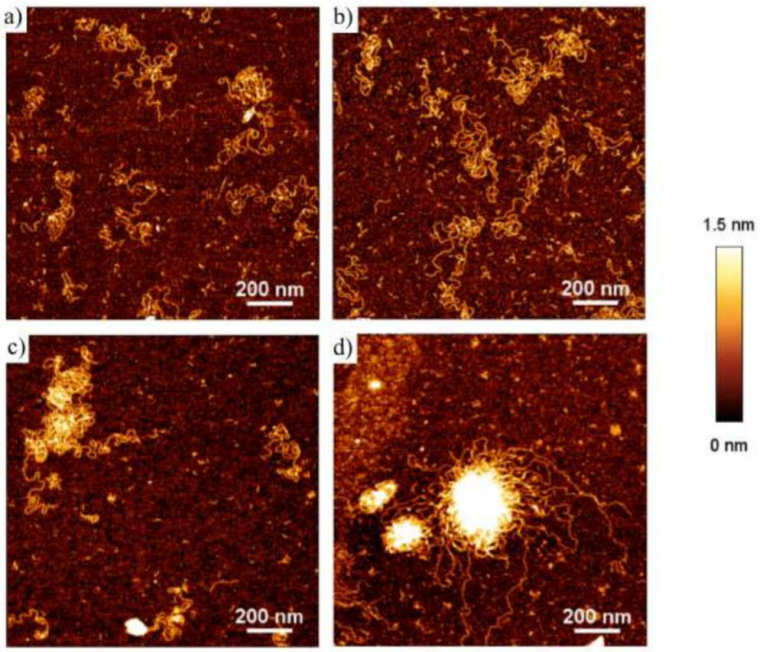

Figure 9.12.: AFM images of bare DNA **(a)** and DNA in presence of PEG at 7.5% *v*/*v* **(b)**, 10% *v*/*v* **(c)**, 15% *v*/*v* **(d)**. In all these experiments the concentration of DNA was 1.25 ng/ µl.

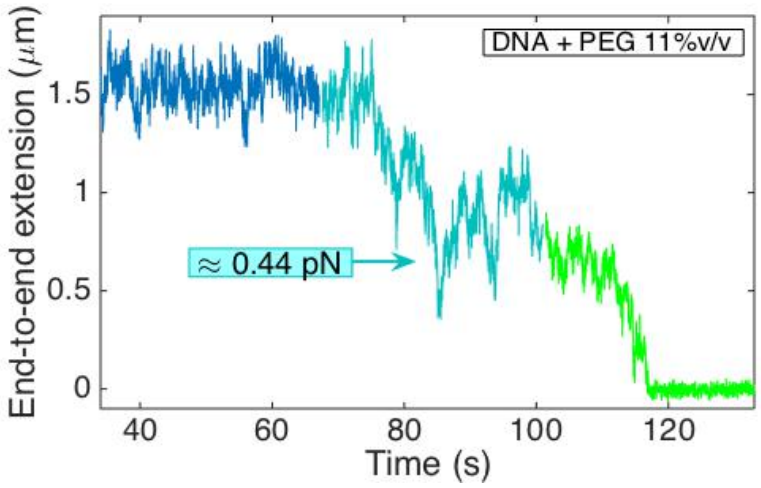

Figure 9.13.: Temporal traces of a force-extension experiment during DNA folding in presence of 11% *v*/*v* PEG. Each coloured trace is collected at a different force.

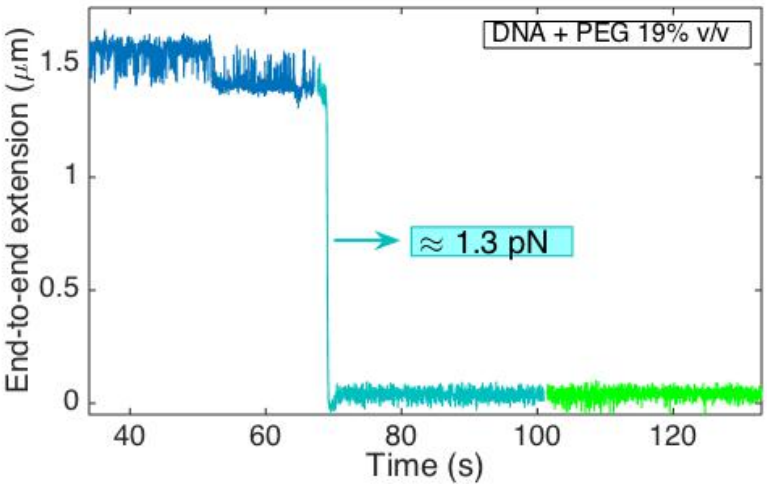

Figure 9.14.: Temporal traces of a force-extension experiment during DNA folding in presence of 19% *v*/*v* PEG. Each coloured trace is collected at a different force.

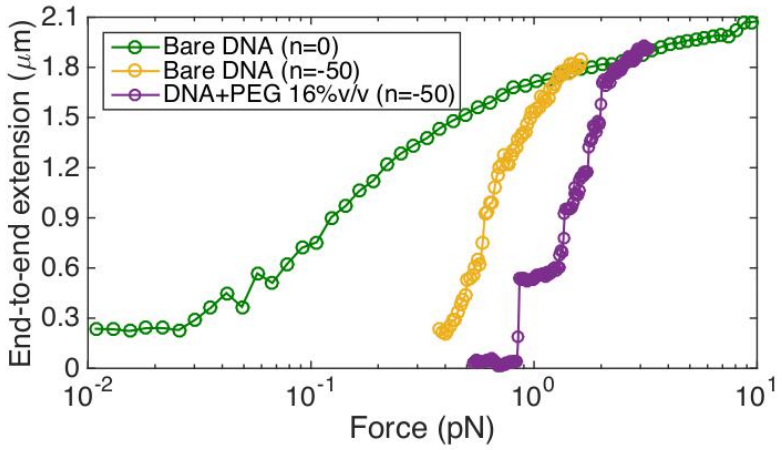

Figure 9.15.: Nanomechanical denaturation of DNA in presence of 11% v/v. Green curve is the standard WLC behavior of bare DNA without any applied torsion, included for comparison. Yellow and purple curves are the effective denaturation experiments, a certain torsion was applied to the bare DNA (yellow) and to the PEG-DNA complex (purple) in order to induce the denaturation at a specific force.

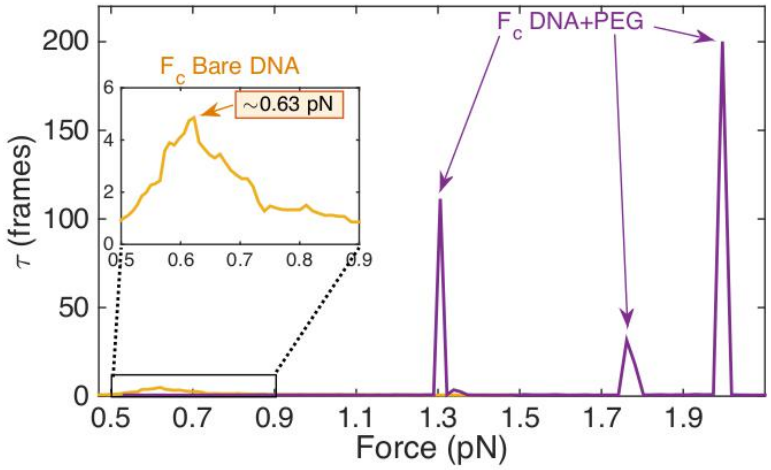

Figure 9.16.: Autocorrelation characteristic times of the denaturation curves reported in figure 9.15. The force values of the maxima correspond to the F_{char}. The presence of the crowding agent PEG1500 induces a stronger correlation, higher value of τ, and introduced intermediate states, three in this case.

9.3 COMBINED EFFECT OF H-NS AND PEG

Once the effects of H-NS and PEG have been examined individually, the combined and potentially cooperative effects on DNA condensation of the protein and the crowding agent can be investigated. These experiments investigating the nanomechanics of the interaction between DNA and H-NS and PEG at the same time are the most important data for this project, because they are carried out under the more realistic conditions, very similar to the cellular environment.

In figures 9.17 and 9.18 two useful examples are reported: in the first figure the combined effect of H-NS and PEG is explored in the low concentration regimes, H-NS at 30 nM and PEG at 8% volume fraction. This concentration is included in the coexistence region above mentioned, and indeed in this experiment the crowding agent did not induce any effect on DNA. This is why the measurement is very interesting: a low level of crowding did not induce DNA condensation alone but the combination with H-NS improved the effects of the protein, by increasing both the folding and unfolding forces by a factor of 3-4, see discussion for details. In figure 9.18 both H-NS and PEG concentrations are higher, more precisely 120 nM and 13% v/v respectively, which are intermediate values in the chosen concentration ranges. The cooperative effect becomes more evident here: the DNA collapse curve in presence of H-NS+PEG (purple) is shifted to much higher forces. The DNA folding force is more than eight times higher compared to the bridging force of H-NS alone, and four times higher than the sum of the two folding forces related to H-NS or PEG alone.

The temporal traces of DNA condensation provides information also in this case. As shown in figure 9.19, the kinetics of DNA folding induced by H-NS bridging and depletion forces seems to have very similar feature to the kinetics of DNA bridging in presence of H-NS alone. The presence of a multistep temporal trace is a fairly clear signature of the protein binding, different from the crowding effect, see figures 9.5 and 9.4 previously presented. This suggests that the folding curves observed in presence of both the protein and the crowder are still determined by H-NS activity on DNA, but carried out in a more favorable environment.

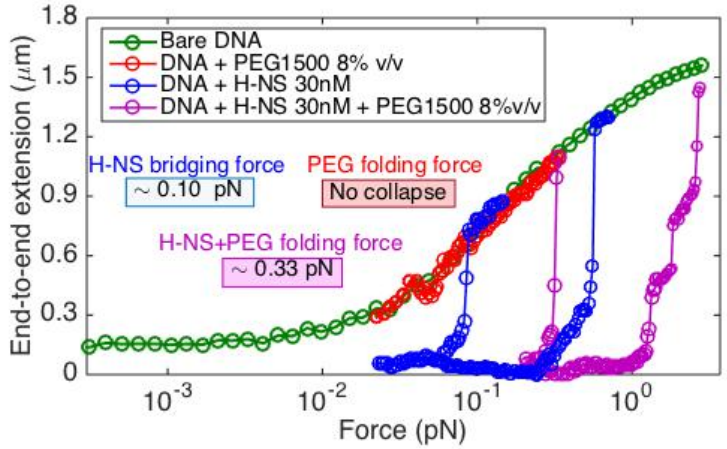

Figure 9.17.: Force-extension curves describing the combined effect of H-NS protein and the crowding agent PEG1500 on a DNA molecule. Green curve is related to the WLC behavior of bare DNA, red curve to DNA in presence of 8% v/v PEG1500, blue curves are related to the bridging and unfolding events for the DNA-HNS (30 nM) complex, and purple curves are the experiments in presence of both H-NS and PEG, at the same concentration of previous curves. The DNA interacting with H-NS and PEG shows an increase of the folding and unfolding force values, indicated in the labels. This experiments is significant because PEG alone did not induce any DNA condensation.

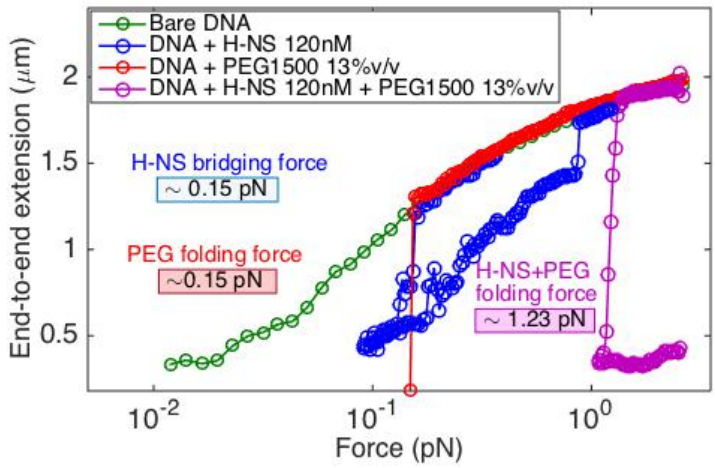

Figure 9.18.: Force-extension curves describing the combined effect of H-NS protein and the crowding agent PEG1500 on a DNA molecule. Green curve is related to the WLC behavior of bare DNA, red curve to DNA in presence of 13% v/v PEG1500, blue curves are related to the bridging and unfolding events for the DNA-HNS (120 nM) complex, and purple curves are the experiments in presence of both H-NS and PEG, at the same concentration of previous curves. The DNA interacting with H-NS and PEG showed a significant increase of the folding and unfolding force values, as indicated in the labels.

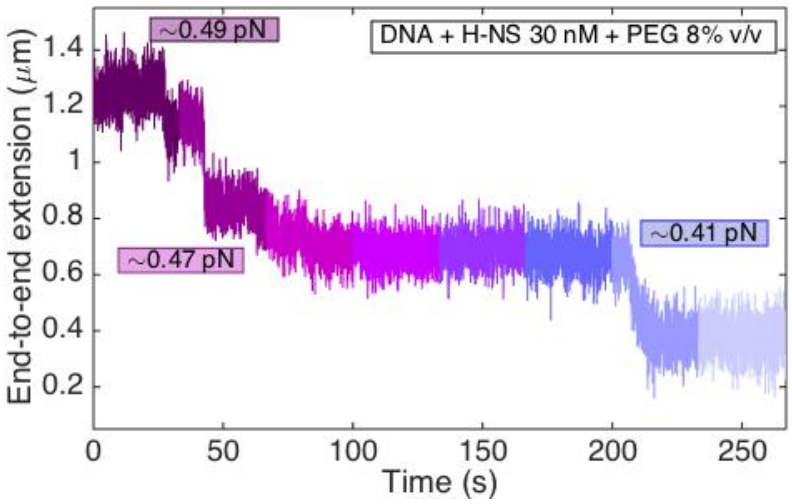

Figure 9.19.: Temporal traces of a force-extension experiment during DNA folding in presence of 30 nM H-NS and 8% v/v PEG. Each coloured trace is collected at a different force, in the labels the forces at which a binding events occur are reported. Binding events are represented by a quick decrease in DNA extension, this multistep folding is very similar to the bridging binding kinetics, figure 9.5.

10

H-NS PROTEIN REGULATORY ROLE

In this chapter I will present the experimental results aimed at the investigation of the second role of the H-NS protein: the regulatory role involved in gene silencing functions [74, 75, 85–87, 226]. The method adopted to study the influence of H-NS on gene expression has been to observe in real time the activity of a specific promoter regulated by H-NS, by means of time-lapse microscopy experiments on bacterial cells. Basically, I monitored the level of expression of a fluorescent reporter protein under the control of this H-NS-regulated promoter, that is to say I measured the fluorescence of individual bacterial cells subjected to certain stimuli. In order to analyse the promoter (and H-NS) activity at the single-cell level I employed a microfluidic device technique, previously described in section 4.5. The whole research activity I am going to describe in this chapter has been carried out during the visiting research period in Pietro Cicuta laboratory, at the University of Cambridge (Cavendish Laboratory).

The chosen promoter is a shortened version of *rrnB*P1, a well characterized ribosomal promoter regulated by a few global regulators, such as ppGpp, DNA topology and NAPs, specifically Fis and H-NS [77, 227, 228]. The shortened *rrnB*P1 promoter used here, hereafter P1 short, lacks of the three binding sites of Fis and one of the three H-NS binding sites (see figure A.1 in supplementary material), in this way it is regulated by only one NAP, the H-NS protein under investigation in this thesis.

The promoter activity was monitored by measuring the expression of the mut2-gfp gene under control of the *rrnB*P1 region. The resulting construct was inserted in different positions along the genome of *E. coli*, including a divergently oriented kanamycin resistance cassette as well. This strategy has already been used in literature to explore the potential local and genomic level changes in the activity of the regulators. This represents a method to observe the genome position influence on the gene expression [229–234]. In particular in [230], an interesting work by Sclavi at al., it was revealed revealed how the regulatory activity of H-NS is strictly related to the genomic position. The authors analysed the activity of H-NS by measuring the gene expression of a fluorescent reporter under control of the P*hns*

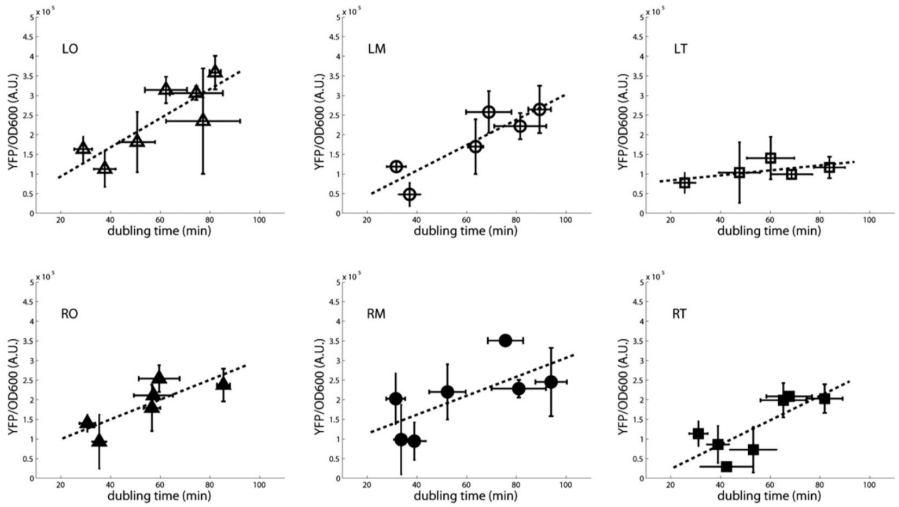

Figure 10.1.: Gene expression measured as the concentration of fluorescent reporter YFP, resulting from the fluorescence divided by the optical density (OD_{600}). The faster is the growth rate (smaller doubling time) the faster is the YFP dilution rate, that means lower protein concentration. In the left terminus (LT) position (top right) there is a strong repression: the YFP concentration does not increase. Figure from [230].

promoter, inserted in six mirror sites along the genome, see figure 1 in [230]. This promoter is clearly regulated by H-NS protein and it also enables to probe the regulation of *hns* gene. The gene expression, namely the fluorescence of the reporter (YFP), was measured as a function of the growth rate: for a particular chromosomal position near the terminus (LT) a stronger promoter repression by H-NS was observed, see figure 10.1.

I similarly studied the H-NS regulatory role by measuring the activity of the P1 short promoter in two specific genomic sites: the first one close to the origin (*ori*3) and the other within an extended H-NS binding domain (*nsr*3), about 15 kbp long [235]. The *ori*3 position is not expected to significantly alter the promoter activity, so the P1*ori*3 strain is used as a control for the P1*nsr*3 strain, where H-NS activity should be strong. Moreover, I explored the effects of the kanamycin resistance cassette (hereafter KanR) because it has been shown that the transcription of *Kan* gene can create a negative DNA supercoiling, thus promoting P1 short promoter activity [236, 237]. Additionally, the presence of KanR cassette could also "protect" the promoter from the repression by H-NS, probably increasing the local level of supercoiling and disrupting the H-NS cluster. Therefore, I measured the gene expression of P1 short in the position more affected by H-NS, *nsr*3, with and without the kanamycin cassette. Finally, I will describe gene experiments carried out on a bacterial strain with an *hns* gene knockout, in *ori*3 position, and I compared the results with the

control experiments on P1*ori*3. The idea here is to see how the complete lack of H-NS protein influences the global regulatory dynamics of the cell.

10.1 THE UPSHIFT EXPERIMENTS

In order to measure the gene expression, I performed time-lapse fluorescence microscopy experiments on individual bacterial cells in temperature controlled condition. These cells were loaded into the microfluidic device described in section 4.5 and their growth dynamics was monitored. More precisely, the experiments consisted of measuring changes in gene expression and cell growth in response to a *nutritional upshift*: the growth medium is switched from a slow growth medium containing only glucose (Glu) to another containing both glucose and casamino acids (CAA), which induce an increase in gene expression and cell growth rate. With this technique, I have been able to analyse and quantify the cell adaptation to an upshift stimulus, in terms of cell physiology and transcriptional activity.

The details about the growth media used to induce the upshift are included in supplementary material (section A.3), the important difference are the nutrient sources: the slow growth medium has only 0.4% of glucose, while the rich, or the fast growth, medium has 0.4% of glucose and 0.5% of casamino acids. In figure 10.2 I reported an example of an upshift experiment, to show how the gene expression and the size growth of the cell are influenced by a nutrient stimulus. The dotted line in the figures represents the time when the fast growth medium reaches the chamber and when the cells start to adapt to the stimulus. The data I am going to present are always normalized to the average values before the upshift, so as to prevent external biases, such as the non-uniformity of the power intensity of the light source. Moreover, the main interest of this work is purely the cell behavior in response to an external stimulus and to understand how the cellular adaptation is regulated by H-NS protein.

The first plot, figure 10.2(a), shows the most directly measurable quantity: the fluorescence of the bacterial cells. The fluorescence signal is proportional to the level of expression of the GFP fluorescent reporter and consequently it is related to the promoter activity. Actually, the fluorescence depends also on the size growth of the cell and a "correction" should be made to evaluate the gene expression (see next section). In the reported fluorescence curve a peculiar feature is clearly visible, an overshoot after the upshift stimulus. The causes of this interesting phenomenon are still debated and not fully understood.

The nutrient upshift stimulus induced a significant increment in the fluorescence signal, reaching a maximum value about 2.5 times higher than the average fluorescence in the slow growth medium.

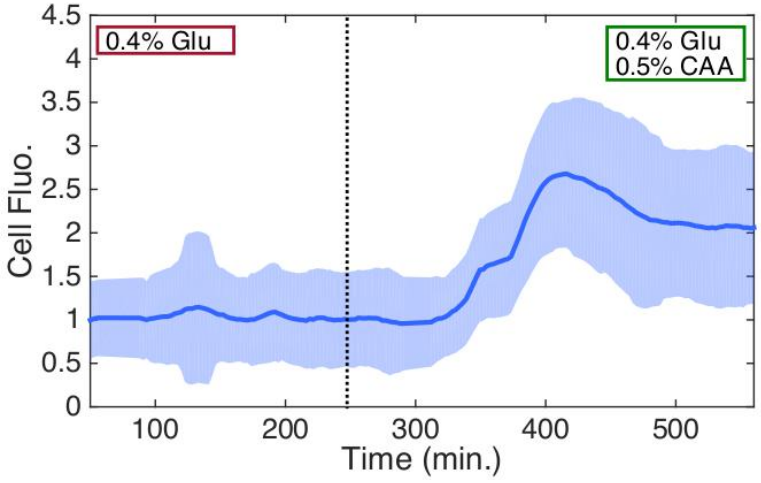

(a)

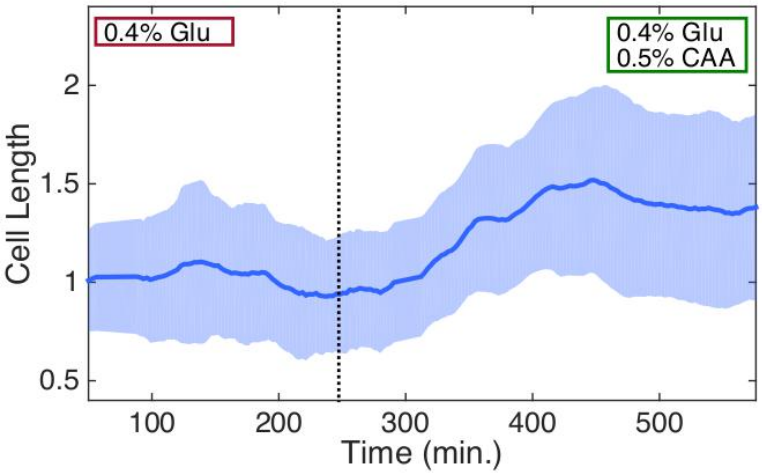

(b)

Figure 10.2.: Example of an upshift experiment from a slow growth medium (M9 + 0.4% Glu) to a rich medium (M9 + 0.4% Glu + 0.5% CAA). The dotted line approximately represents the time when the rich medium reached the chamber. This experiment lasted about 16 hours, here ≈ 8.5 hours are shown. Two quantities are reported: the cell fluorescence **(a)** and the cell length **(b)**, as a function of time. Solid lines and shaded areas represent the average and the standard deviation over ~ 3500 cells, respectively. Data are normalized to the average value before the upshift.

After the overshoot, the fluorescence stabilised around an increment factor of 2.

The cell segmentation software introduced at page 73 enabled to quantify not only the fluorescence but also a set of other geometrical properties of the analysed single cells, such as the length, the width, the area or the volume, information that can be used to study the coupling between gene expression and the growth rate. For example, in figure 10.2(b) I show the measurement of the cell length. The increment in response to the upshift is lower in this case compared to the fluorescence curve, the length increases of about the 50% during a slight overshoot, before stabilising to a factor of $\approx 35\%$.

10.2 EFFECTS OF GENOMIC POSITION

The first investigated effect playing a role in the regulatory activity of H-NS is the genomic position, recently discussed in literature [229, 230, 234]. I compared the gene expression and the size growth of P1 short promoter inserted in a position affected by H-NS binding (*nsr*3) with the same quantities measured for the P1*ori*3 strain, as a control experiment, since the *ori*3 region of the genome does not include any H-NS binding site. The data concerning the gene expression showed the expected results: H-NS had a stronger repression activity on promoter activity when the promoter itself is very close to binding sites of the protein. The curves reported in figure 10.3 illustrate level of expression of the the promoter-gfp construct in terms of fluorescence (a) and concentration of the fluorescent protein (b), in this case GFP. Indeed, as previously mentioned in section 10.1, the fluorescence intensity is related not only to the level of gene expression, but also to the cell volume, as clearly shown from some snapshots of microfluidic channels (e.g. figure 4.22, 13.8(a) or 13.13(a)): bigger cells have a higher total fluorescence. As a consequence, to measure more precisely the real gene expression activity of the promoter, these fluorescence data are usually normalized to the cell area or volume, thus isolating the effective contribution of the promoter activity from the cell morphology contributions. The GFP concentration provides information about the change in the density of fluorescent reporters during the upshift stimulus, a quantity independent from the size heterogeneity, as confirmed by the smaller errors (shaded area) of figure 10.3(b) compared to those of 10.3(a).

From a quantitative analysis of the fluorescence curves turned out that in P1*ori*3 the average fluorescence of the cells increased by a factor of ≈ 3.7, whereas in P1*nsr*3 by a factor of ≈ 2.5. As regards the measurement of GFP concentration the difference is even more pronounced, the increment factors are ≈ 2.6 and ≈ 1.6 for P1*ori*3 and P1*nsr*3 respectively.

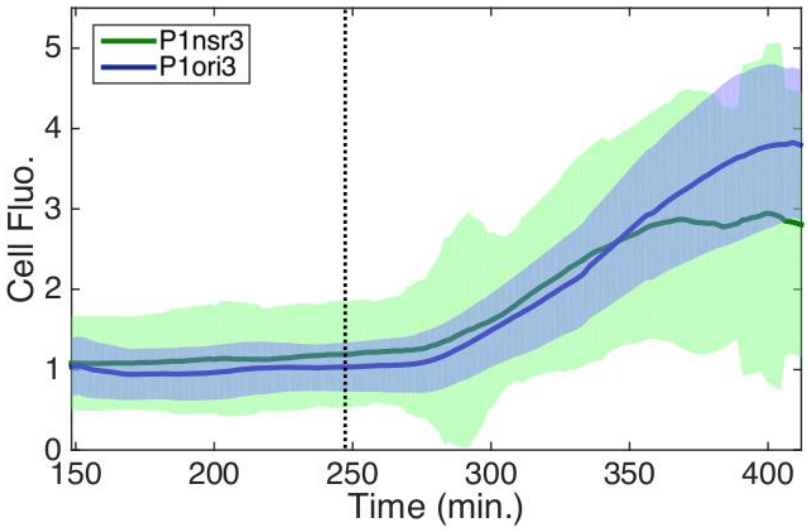

(a)

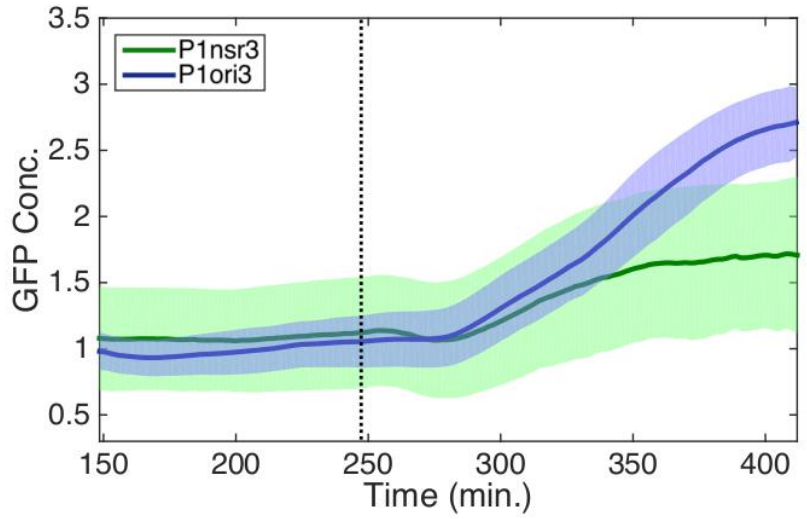

(b)

Figure 10.3.: Upshift experiments showing the cell average fluorescence **(a)** and the GFP average concentration **(b)** as a function of time for P1*ori*3 (blue) and P1*nsr*3 (green) strains. Solid lines and shaded areas represent the average and the standard deviation over 3000-4000 cells. Data are normalized to the average value before the upshift. The dotted line approximately represents the time when the rich medium reached the chamber.

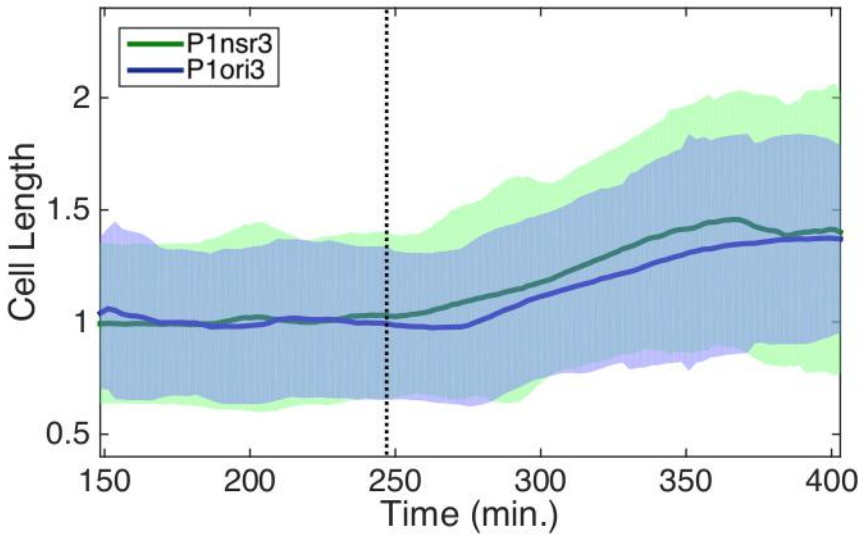

(a)

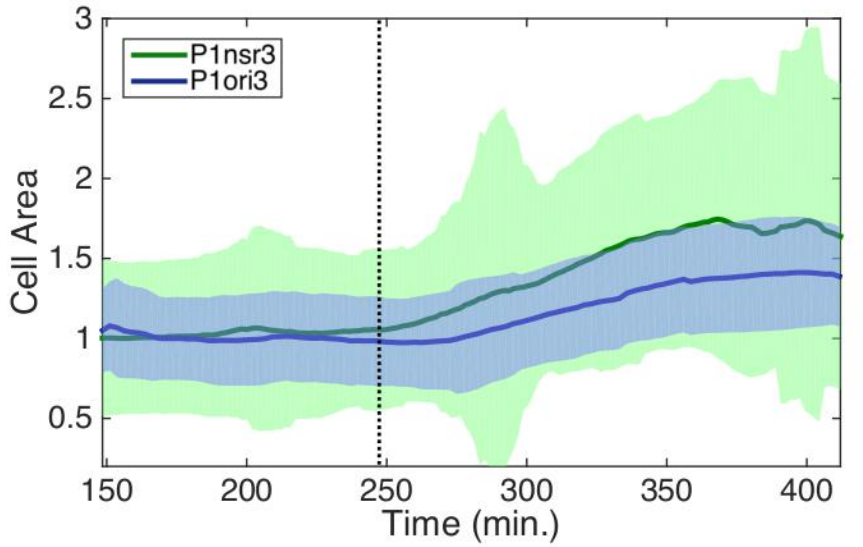

(b)

Figure 10.4.: Upshift experiments showing the cell average length **(a)** and the cell average area **(b)** as a function of time for P1*ori*3 (blue) and P1*nsr*3 (green) strains. Solid lines and shaded areas represent the average and the standard deviation over 3000-4000 cells. Data are normalized to the average value before the upshift. The dotted line approximately represents the time when the rich medium reached the chamber.

The size growth displayed less evident effects as a response to the upshift, but above all an opposite behavior was observed, i.e. P1*nsr*3 showed higher increases of cell size. For example, the average length of the cells initially increased slightly more for P1*nsr*3, despite after about two hours from the upshift the length stabilized to a value around 1.4 for both strains. Instead, looking at the upshift curves of average area, it can be noticed how the size growth of the bacterial cells of P1*nsr*3 is constantly higher than the area of P1*ori*3 cells. Specifically, the increment factor in *nsr*3 is ≈ 1.6, while in *ori*3 is ≈ 1.4. Since the average length did not show any relevant difference between the two strains, the results concerning the area should derive from another geometrical cell parameter: the width, whose curves are reported in figure E.1.

10.3 PROTECTION EFFECT OF *kan*R CASSETTE

The data presented in the previous section concerns bacterial strains including the KanR cassette, now I want to assess the effect of the transcription of *Kan* gene, that is likely protecting the P1 short promoter from H-NS activity by increasing the negative supercoiling of DNA [236, 237]. I measured the gene expression of the promoter inserted in the genomic position more influenced by H-NS, *nsr*3, lacking of the KanR cassette, to see if the repression by H-NS is even more pronounced without this kind of transcriptional protection.

The figure 10.5 shows again the gene expression of P1*nsr*3 described in the previous section, but compared with the same strain without kanamycin P1*nsr*3(NoKan): both fluorescence and GFP concentration exhibited a smaller increase in response to the upshift when *Kan* is absent, confirming a higher repression activity of H-NS if there is not this protection of the promoter. Particularly, the lack of KanR cassette induced a further decrease in the average fluorescence signal compared to the results of section 10.2, the increment factor was shifted from 2.5 (green curve) to 2.1 (ochre curve), but with an overshoot maximum values of about 2.6. This overshoot feature is very interesting for the GFP concentration data, which additionally provide more significant information about gene expression. Indeed the maximum value reached during the overshoot of P1*nsr*3(NoKan) exceeded the increment of the strain including *Kan*, albeit the final saturation value of the GFP concentration in P1*nsr*3(NoKan) is lower: the increment factor is ≈ 1.5 compared to the ≈ 1.6 of P1*nsr*3 strain.

This phenomenon can be better understood by observing the size growth. Unexpectedly, the size of the bacterial cells lacking of KanR increases less during the upshift stimulus, see for example the curves related to the cell area reported in the supplementary material (figure E.2).

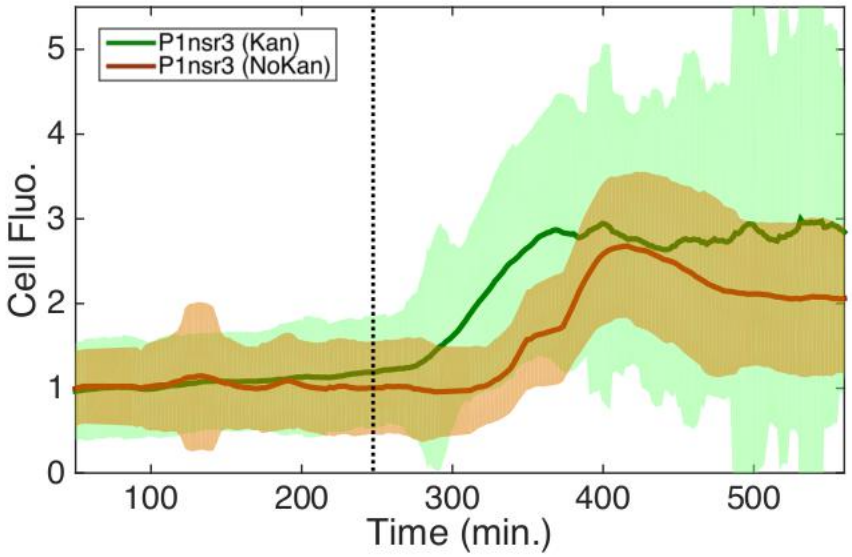

(a)

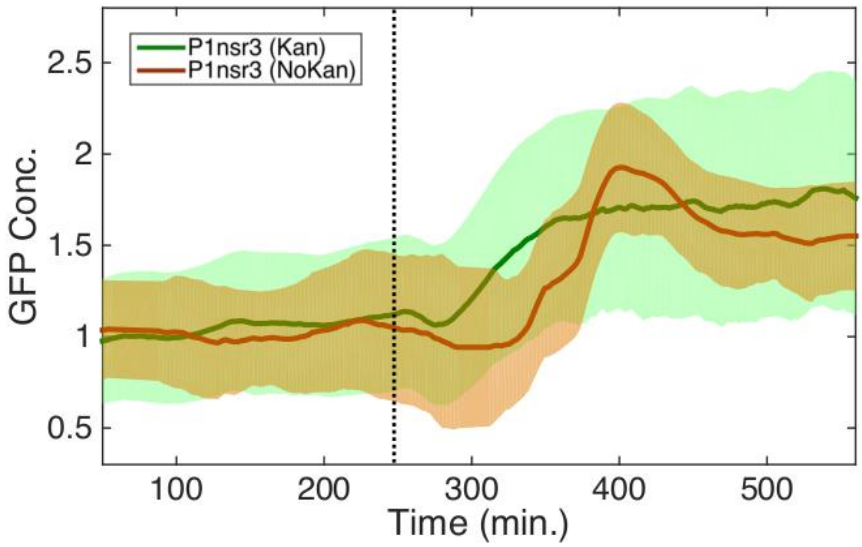

(b)

Figure 10.5.: Upshift experiments showing the cell average fluorescence **(a)** and the GFP average concentration **(b)** as a function of time for P1*nsr3* strain including kanamycin cassette (green) and without Kan (ochre). Solid lines and shaded areas represent the average and the standard deviation over 3500-4000 cells. Data are normalized to the average value before the upshift. The dotted line approximately represents the time when the rich medium reached the chamber.

10.4 THE *hns* GENE KNOCKOUT

Finally, another strategy to evaluate the regulatory role of H-NS at the single-cell level is to completely remove this protein from bacteria, by deleting the *hns* gene. I measured the activity of the P1 short promoter in a bacterial strain with an *hns* gene knockout, comparing these resulting data with the control strain P1*ori*3. The measurement of the gene expression of P1*ori*3-Δ*hns* enabled to observe directly how the H-NS protein influences the cell behavior, both in terms of regulatory or structural functions.

Once again, I begin from the gene expression analysis by showing the fluorescence and the GFP concentration, see figure 10.6. Unfortunately, as it can be seen from the red curves, during upshift experiments of P1*ori*3-Δ*hns* strain a problem occurred, causing a drop of fluorescence just a few minutes before the upshift, probably because an air bubble emptied most of the channels of the camber. Nevertheless, I can still analyse these data because I have to calculate the relative increment of the fluorescence from approximately the upshift time (dotted line) to the the final saturation value. Figure 10.6 illustrates that in the strain with *hns* gene knockout the fluorescence increased by a factor between 3.3 and 4.3 and the GFP concentration by a factor ranging from 2.3 to 2.7 (depending on the uncertainties of the exact upshift time), to compare with the ≈ 3.7 and ≈ 2.6 values for P1*ori*3. From the comparisons between these two strains turned out that the gene expression levels are similar, within the experimental errors, but the relative increment of fluorescence of Δ*hns* strain is slightly higher in average (~ 3.8) than the fluorescence increment observed in the control strain. On the contrary, the GFP concentration increment of Δ*hns* strain is slightly lower (~ 2.5). Here again, this effect can be explained by the cell size data. The strain with the *hns* gene knockout is characterized by an initial faster size growth, before stabilising to a value very similar to that one of P1*ori*3 strain, see figure E.3 in supplementary material.

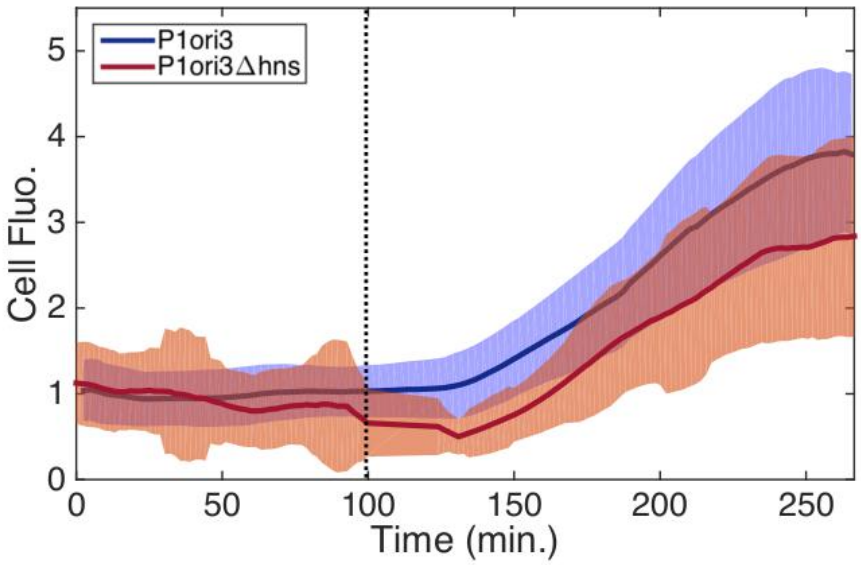

(a)

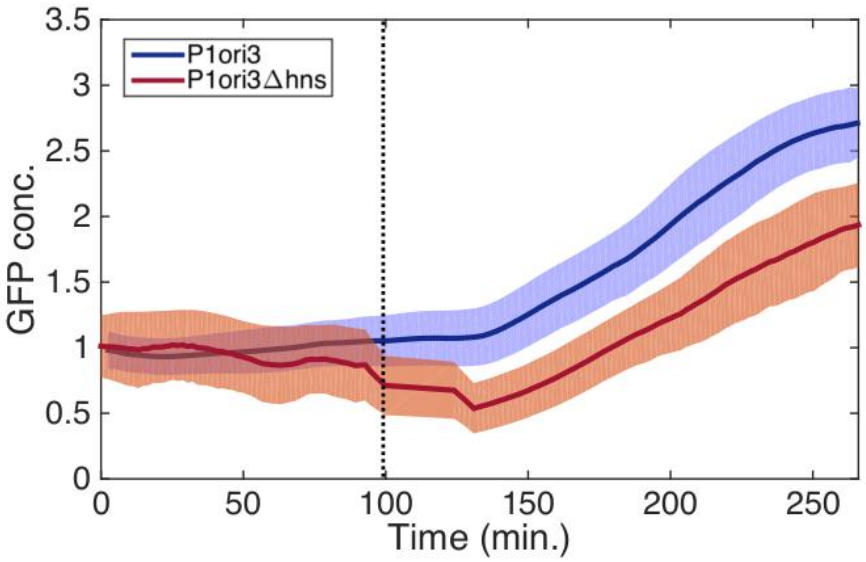

(b)

Figure 10.6.: Upshift experiments showing the cell average fluorescence **(a)** and the GFP average concentration **(b)** as a function of time for P1*ori3* (blue) and P1*ori3*-Δ*hns* (red) strains. Solid lines and shaded areas represent the average and the standard deviation over 3000-3500 cells. Data are normalized to the average value before the upshift. The dotted line approximately represents the time when the rich medium reached the chamber.

Part IV

DISCUSSION

11

STRUCTURAL POLYMORPHISM OF DNA

The first main topic addressed in this thesis is the ability of DNA of easily changing conformation, depending on the biological function involved. This property can be referred as to structural polymorphism of DNA. I studied this phenomenon from two different perspective: the first one is how a chemical modification can alter the structural conformation of the DNA double helix, by changing some mechanical properties or by favouring some phase transition, such as DNA melting or alternative DNA forms, namely A-like or S-DNA structures (chapter 6). The second strategy to study the structural polymorphism of DNA is the analysis of the high supercoiling regime (chapter 7), because under specific topological stress conditions some alternative DNA structures are energetically favoured. The study of the mechanical properties of these alternative forms, such as L-DNA or P-DNA, can help to understand which are the necessary requirements to exhibit a structural phase transition and why this is important in some biological situations.

The chemical modification has been achieved by using an adenine nucleotide analogue, namely the diaminopurine. The study of this DNA analogue concerned the thermal and mechanical properties of this molecule. Specifically, the melting temperature at different GC content has been explored, and the rigidity along with the extension of DNA were studied by nano-manipulation techniques. The nanomechanical characterization included also the analysis of a phase transition at very high forces, i. e. the force-induced melting or the S-DNA formation during overstretching.

The investigation of DNA under high supercoiling regimes enabled to associate the topology of the DNA double helix to its structural polymorphism, that is to say its propensity to form alternative structures with different helicity, helix rise, or also rigidity. Particularly, underwound DNA molecules were analysed by applying counter clockwise torsions, in the same way usually adopted to study the mechanical denaturation (see sections 8.2.1 and 9.2.3). However in this case the formation of melting bubbles competing with plectonemic structures is explored in a much wider range of superhelical density, so that it was possible to investigate the phase transition to a left-handed

DNA (L-DNA). A sequence-dependency of this structural transition has been studied as well. Similarly, this approach of applying torsions and forces to promote the formation of alternative DNA structures has been adopted for clockwise twisted molecules. In this way an exotic DNA structure was revealed, with a Pauling-like structure called P-DNA.

11.1 CHEMICAL MODIFICATION: DAP-SUBSTITUTION

11.1.1 *Thermal and force-induced melting*

The melting experiments clearly demonstrated that DAP substitution increases the thermal stability of double-stranded molecules. The melting temperature of each sequence with different GC content was increased in a range between 5 and 10°C (figure 6.2), but interestingly, sequence dependence still appeared to play a significant role in dictating melting temperature, implying that nearest-neighbour interactions persist in DAP DNA as well. Despite having nearly the same number of hydrogen-bonds adjoining the two ss-DNA backbones (all the base-pairs are connected by triple hydrogen bonds), the melting temperature of the DAP-substituted 40% and 65% GC sequences differed by roughly 8°C. This suggests that the base-stacking interactions of GC/CG repeats are the leading factor driving the melting temperature, more than the interactions between other base-pair duplexes and regardless of the number of hydrogen bonds [200]. In fact, the increase in melting temperature roughly corresponds to a constant decrease in the base pairing enthalpy of (DAP-substituted) adenosine bearing nucleotides. In other words, DAP DNA has a higher T_m than WT DNA because of the additional hydrogen bond, but the stacking interactions of GC base-pairs remains the most important factor determining the melting point. These statements are confirmed by the T_m of 100%GC DNA sequences of approximately the same length, with expected values ranging between 95-100° [238], whereas the DAP DNA samples investigated here had always a T_m below 90°.

The thermal stabilisation effect seems opposite to the force-induced melting observed during the overstretching transition. One of the ways in which DNA can overstretch is indeed through the phosphate backbones separation, enabling the stretching of individual nucleotide strands, and this process is the force-induced melting. The alternative overstretching mechanism is the formation of a new double-helical structure called S-DNA. The propensity of a DNA molecule to form S-DNA rather than undergo force-induced melting is sequence dependent. Simulations have shown that while G-C base pairs persist through the transition, A-T pairs loose registration, eventually form-

ing melted bubbles [239, 240]. Similarly, various pulling force experiments and theoretical models have also demonstrated that AT-rich sequences tend to melt more easily than GC-rich sequences [118, 122, 123, 204, 206, 241–244]. Finally, cyclic pulling experiments demonstrated that force-induced melting is associated with hysteresis, such that once melted, the complementary strands re-anneal slowly [115, 204–206]. In particular, a detailed study conducted by Nordén comparing the overstretching behavior of short 70% AT and 60% GC oligos found that while AT-sequences melt and GC-sequences form S-DNA, the transition threshold for GC oligos was similar to AT oligos [204, 241]. Other authors had previously argued in a similar way that S-DNA formation likely required more energy than AT-separation but less than GC-separation [121, 124, 245].

The high-force cyclic extension/retraction experiments shown in chapter 6 revealed that while WT molecules exhibited significant hysteresis after crossing the overstretching transition, DAP molecules had little to no hysteresis. The lack of hysteresis suggests that two strands of DAP molecules remain base-paired throughout the transition and therefore, unlike the WT molecules, do not need to re-anneal once the tension is reduced [243]. I quantified this hysteresis by computing the area between the extension and relaxation curves, such as those shown in figure 6.8, and I obtained the values reported in the boxplot of figure 11.1. The hysteresis area in WT DNA molecules has an average value of $19 \pm 9\,\mathrm{pN{\cdot}\mu m}$, whereas DAP DNA molecules showed a nearly zero hysteresis, the average area is $2 \pm 1\,\mathrm{pN{\cdot}\mu m}$. Therefore, from this analysis I can conclude that the application of high forces to the DNA analogue does not induce melting, which is instead a typical phenomenon occurring in WT DNA, but promotes a structural phase transition to the S-DNA form. As a consequence, thermal and force-induced melting are very different process, exploring distinct mechanisms and interactions.

On the other hand, the analysis of overstretching transition can help to understand the roles of base-pairing and stacking interactions in DNA structural stability. Indeed, the most interesting and surprising result of this work is probably the lower value of the overstretching force F_{os} for DAP (54 pN) compared to the expected 62 pN of WT DNA. Since the overstretching of DAP consists in the formation of S-DNA without breaking hydrogen bonds, the interaction involved during this transition is the base-stacking. In particular, despite the DAP-substitution increases the number of hydrogen bonds, DAP-T base-pairs are less stable than AT base-pairs during overstretching, thus suggesting that the the driving factor during this phase transition is the stacking. This conclusion is confirmed by literature experiments showing GC DNA oligos overstretching at the same force of AT oligos, as above mentioned.

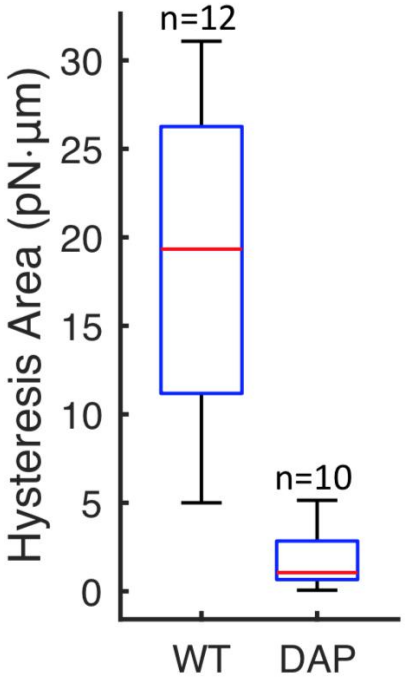

Figure 11.1.: Hysteresis during overstretching transition. Box and whisker plot of area between extension and relaxation curves (see figure **??**). Box edges 25th and 75th percentiles. Whiskers indicate extent of data. Red line indicates median.

11.1.2 *The A-like-form conformational change*

Several studies have shown that DAP substitution stiffens the molecule against lateral bends [183, 246, 247]. The low-force AFM and MT experiments presented here confirm that finding. In line with the previous reports, our low-tension MT and AFM experiments demonstrate that DAP substitution increases persistence length. It has been argued that DAP's extra amine group which protrudes into the minor groove shifts the molecule towards an A-like DNA conformation and resists flexural bends that would compress the minor groove [246, 248]. Indeed, DAP-substitution would seem to add steric clashes between the exocyclic amine and the nitrogen at position 3 of adjacent purines, as already observed in [11, 249]. The lower helical twist and base pair tilt of the A-form likely minimize steric clashes between adjacent purines in the minor groove of DAP-substituted DNA. Interestingly, while DAP substitution resulted in a significant reduction in contour length as measured by AFM, namely from 3.12 ± 0.03 Å/bp down to 2.80 ± 0.03 Å/bp (a 10% decrease), it did not have an effect when measured by MT, where the helix pitch values are 3.25 ± 0.03 Å/bp and 3.15 ± 0.03 Å/bp for WT and DAP respectively. Although the zero-tension AFM results suggest that DAP decreases the helix pitch, the change does not persist once low-to-moderate tension is applied. One explanation for the discrepancy is simply that an un-

perturbed DAP molecule adopts the A-like form, but quickly reverts back to B-DNA when mildly stretched. Alternatively, it is possible that DAP-DNA natively adopts a traditional B-form but is more susceptible to dehydration and surface charge effects than WT-DNA. In either case, the AFM results indicate that DAP substitution not only stabilizes base pairing and increases flexural rigidity but also alters the helical conformation.

If DAP DNA more readily adopts an A-like form at zero-tension to minimize steric clashes between adjacent purines, one might expect those steric clashes to also facilitate other conformational changes. The overstretching results above discussed has indeed indicated that DAP-substitution also lowers the energetic barrier separating B- and S-form DNA.

11.2 DNA SUPERCOILING

11.2.1 *L-DNA and P-DNA structures*

In chapter 7 I presented an analysis of two phase transitions occurring for negatively and positively supercoiled DNA, where negative means counter clockwise while positive means clockwise. The alternative structures involved are respectively a left-handed double helix, named L-DNA, and a Pauling-like structure, named P-DNA. The quantitative analysis consisted of measuring the characteristic force (F_{char}) of the transition from a zero-extension state (plectonemic DNA) to a fully extended state (denatured DNA), for different superhelical density (σ).

First of all, a crucial difference was revealed between these two transitions in terms of the dependence on the superhelical density. More precisely, the B-L-DNA mixed phase ($\sigma < 0$) exhibited a relevant increment of F_{char}, whereas the B-P-DNA phase ($\sigma > 0$) did not. In figure 11.2 I show a comprehensive plot describing the global behaviour of DNA during both transitions , from the left-handed structure for negative supercoiling, to the normal B-DNA form roughly in the range $-0.05 < \sigma < +0.25$, until the molecule adopts a Pauling-like helix for highly positive supercoiling.

I begin the discussion from the simplest phenomenon to explain, the L-DNA form. The experiments at negative supercoiling summarised by figure 7.3(a) are basically an extension of the nanomechanical denaturation analysis introduced in the theoretical chapter and addressed in other projects of this thesis (chapters 8 and 9). Additionally, the nanomechanical denaturation has been reported elsewhere [137, 138, 207]. Extending the range of supercoiling to higher σ values enables to analyse the nanomechanical properties of this left-handed DNA, which is likely present in the conventional experiments at low σ as well, but in a very small fraction. When the twist applied

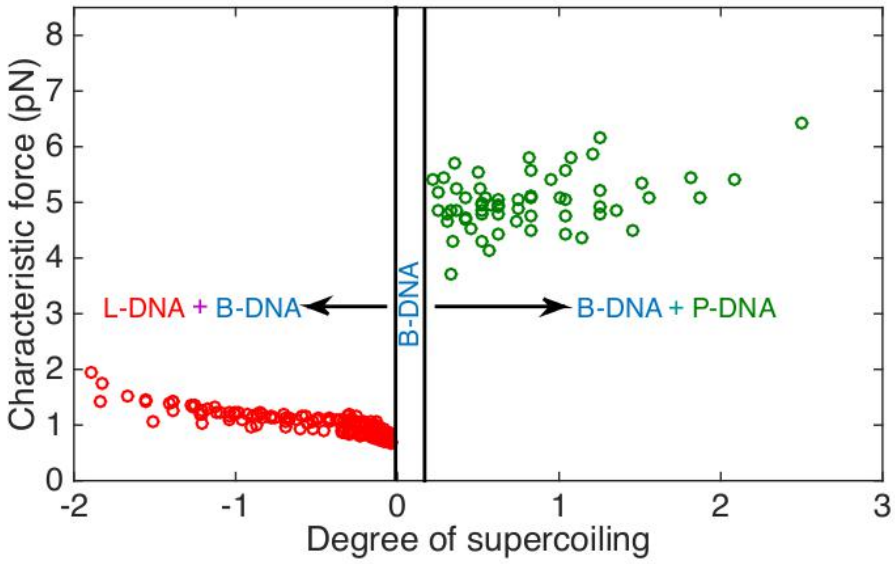

Figure 11.2.: Global F_{char} diagram with DNA supercoiling ranging from about $\sigma = -2$ to almost $\sigma = +3$. In this wide range of σ two structural transition were observed: L-DNA ($\sigma < -0.05$) and P-DNA ($\sigma > 0.25$). Data from figure figure 7.3.

on DNA becomes large, this fraction is increased until having a dominant left-handed structure. As already explained, this left-handed DNA is not a well defined double-helical structure, such as a Z-DNA with hydrogen bonds along whole chain, but it is a mixed phase including ssDNA regions and consequently characterised by a very low persistence length. The reported value of L_P for two parallel ssDNA strands in a melting bubble is indeed around 2-3 nm [208, 250], approximately 20 times lower than the typical $\approx$ 50 nm of double-stranded B-DNA. This argument about DNA flexibility clarifies the decrease of the end-to-end extension with the number of turns observed in figure 7.1(b). The consequence is that the entropic contribution becomes more important for this mixed phase of flexible DNA and the applied force needed to fully extend the molecule increases. Accordingly, since the F_{char} is a parameter measuring the difference between the extended and the plectonemic DNA, its value should increase with the superhelical density for such a DNA structure with increasingly lower persistence length, as shown by red dots of figure 11.2.

The phase transition observed for positive supercoiling is expected to involve a different mechanism in order to explain the lack of σ dependence for F_{char}. A mechanism without the formation a new structure or, alternatively, an alternative DNA phase with very similar mechanical parameters to the canonical B-DNA is created. In literature it can be found that the first hypothesis is that one closer

to the truth: the transition identified around 5-6 pN for positive σ involves a mixed phase of supercoiled B-P-DNA and an extended B-DNA form [53, 214]. As a consequence in this case the extended state is not a new structure with a different flexibility and consequently giving rise to an increasingly greater entropic contribution, such as the L-DNA form, but it is the canonical B-DNA exhibiting the same mechanical properties for the whole range of supercoiling. That is why a σ dependence of F_{char} was not observed for positive supercoiling. There is a partial mixed phase between B- and P-DNA in the plectonemic form at zero extension, but this state is "invisible" for MT force spectroscopy experiments and, most of all, does not affect F_{char} value since a DNA extension change is not involved. The force required to see the extended P-DNA structure is much higher, around 20-25 pN in physiological conditions [53, 214], and this characteristic force is probably dependent on σ value, similarly to the L-DNA transition observed in this work.

11.2.2 *Modeling the mixed phase*

In order to improve the understanding of the structural polymorphism phenomenon observed during these phase transitions, a semi-empirical model has been developed within the same framework of the denaturation model described in section 3.5. This model has been applied only on the B-L-DNA mixed phase, because this transition is more interesting for a couple of reasons: it really quantifies the presence of a new DNA structure in the extended form and, for this reason, a well-defined trend of F_{char} with σ is identified. Moreover, a sequence-dependent behaviour can be also investigated.

The free energy of this mixed phase model is introduced in a general and simple form including two terms: the external work applied by MT and the entropic contribution of the system, $A = W - H_{entr}$. In the following I will prove that the entropic contribution increases with the number of turns n_t (or $superhelicaldensity\sigma$). This fact, along with the hypothesis of a constant free energy A, is sufficient to justify an increment of F_{char}.

In the first step of this discussion I consider only the extended B- and L-DNA phases by neglecting the entropic contribution. The aim is to demonstrate that the L-DNA fraction increases with the number of turns. Under these conditions, the total energy of the system is given by three contributions:

$$E_{ext} = \frac{C_B}{2}\left(\frac{n_B}{b_B}\right)^2 b_B + \frac{C_L}{2}\left(\frac{n_L}{b_L}\right)^2 b_L + \varepsilon_L \cdot b_L \qquad (11.1)$$

where C is the torsional modulus, n is the number of turns and b is the number of base-pairs. The subscript $_B$ and $_L$ identifies the corresponding phase, B- or L-DNA respectively. The first two terms

represent the torsional energy term and ε_L is the activation energy per base-pair of the L-DNA phase [121, 214].

It is necessary to define also some boundary conditions for the total number of turns (n_t) and the total number of base-pairs b_t

$$n_t = n_B + n_L + \delta_L \cdot b_L \tag{11.2a}$$

$$b_t = b_B + b_L \tag{11.2b}$$

where δ_L is the difference of helicity between B-DNA and the new mixed phase, expressed as number of turns per base-pairs. Obviously, $\delta_B = 0$, while δ_L is a negative value that can range between -0.1 and -0.2 [25, 208, 209].

An additional relation holds:

$$C_B \frac{n_B}{b_B} = C_L \frac{n_L}{b_L} \tag{11.3}$$

that means the external applied torque is constant along the DNA molecule.

The energy E_{ext} can thus be expressed as a function of n_t and b_L, because the other parameters, namely the torsional moduli, b_t, δ_L and ε_L, have a known and constant value. The minimization of E_{ext} leads to a linear relation of the following form: $b_L = k_1 n_t + k_2$, with k_1 and k_2 two constants, see supplementary material for details. In figure 11.3 an example of the linear relation of b_L as a function of n_t is reported for a DNA 5000 bp long. n_{max} and $\mathrm{Max}(n_B)$ are two quantities which can be easily observed during experiments: n_{max} is identified by a change in slope of twist experiments (figure 1.9), when the left-handed form of DNA begins to form loops, while $\mathrm{Max}(n_B)$ corresponds to the point at which the torque applied to DNA becomes constant, when B-DNA absorbed the maximum twist stress. Between these two extreme experimental points b_L can be expressed in a very simple form

$$b_L = \frac{n_t - \mathrm{Max}(n_B)}{n_{max}} \tag{11.4}$$

and the fraction of L-DNA phase become

$$\chi = \frac{n_t - \mathrm{Max}(n_B)}{n_{max}} \tag{11.5}$$

with χ value ranging from 0 to 1.

Now, I can introduce the entropic contribution as the following integral

$$H_{entr} = \int_0^{L_e(F)} F \, dL_e \tag{11.6}$$

the relation between F and L_e is given by the WLC model, but in the mixed phase at high supercoiling the end-to-end extension becomes

$$L_e(F) = L_{eB}(F) \cdot (1 - \chi) + L_{eL}(F) \cdot \chi \tag{11.7}$$

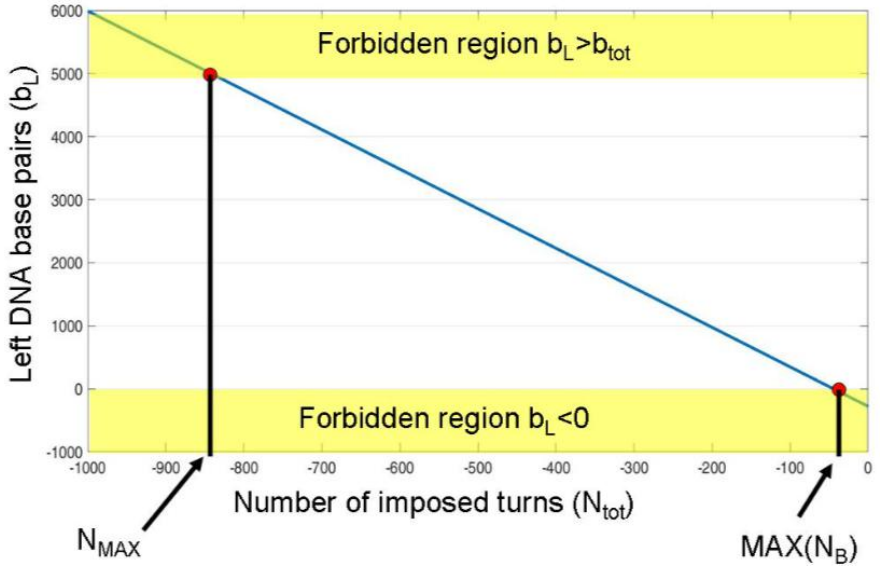

Figure 11.3.: Linear dependence of L-DNA fraction with supercoiling. The number of base-pairs of L-DNA (b_L) plotted as a function of the number of turns (n_t). This curve resulted from the minimization of equation **??**, with the following parameters: $b_t = 5000$, $\delta_L = -0.12$, $C_B = 109 \cdot 10^{-9} \cdot 2\pi/(0.34 \cdot 10^{-9})$, $C_L = 20 \cdot 10^{-9} \cdot 2\pi/(0.34 \cdot 10^{-9})$ and $\varepsilon = 2.5 \cdot k_B T$.

where L_{eB} and L_{eL} are the end-to-end extension for the pure B-DNA or L-DNA phase respectively. It could be shown that for any value χ this L_e has the functional form of the WLC with effective parameters L_{0mix} and L_{Pmix} for the contour length and the persistence length respectively

$$L_{0mix} = L_{0B} \cdot (1 - \chi) + L_{0L} \cdot \chi \tag{11.8a}$$

$$L_{Pmix} = \frac{L_{0B} L_{0L} \left((\chi - 1) - L_{0B} \cdot \chi\right)^2}{\left(L_{0L} \sqrt{LPB \cdot (1 - \chi)} - L_{0B} \sqrt{L_{PL} \cdot \chi}\right)^2} \tag{11.8b}$$

The expression for the total energy of the mixed phase including the entropic contribution of equation 11.6 becomes

$$E_{mix} = \frac{C_B}{2} \left(\frac{n_B}{b_B}\right)^2 b_B + \frac{C_L}{2} \left(\frac{n_L}{b_L}\right)^2 b_L + \varepsilon_L \cdot b_L + \int_0^{L_e(F)} F \, dL_e \tag{11.9}$$

The last term, the entropic contribution H_{entr}, becomes analytically complicated due to the form of the mixed persistence length (equation 11.8b), but it can be numerically computed or alternatively written in a simpler analytic form by approximating the WLC equation. The H_{entr} thus defined is an increasing quantity with χ, namely the entropic contribution increases with the fracion of L-DNA. This concept is graphically straightforward to understand, see figures on page 159: the WLC curves at higher χ values have a lower end-to-end extension

than the WLC at $\chi = 0$ for forces below 2 pN (figure 11.4), which roughly corresponds to the maximum F_{char} values of the B-L-DNA transition, figure 7.3(a). The reason is a lower persistence length, i.e. higher flexibility, as previously explained. Since the entropic contribution is an integral defined as the area under the WLC (figure 11.5), its values decreases for WLC curves at higher χ.

Finally, the last step is to extract the values of F_{char} from the free energy A. Figure 11.5 shows a WLC curve (red line) normalized for both axes: L_e is normalized to the contour legth L_0 and the force is normalized to the quantity $\frac{k_B T}{L_P}$, in order to have a master curve independent on the mechancal properties of the individual DNA molecule. At the beginning of this pararaph I introduced the free energy in a general form, the can be expressed as

$$W = A + H_{entr} \tag{11.10}$$

The work is always defined as force times distance, the DNA extension in this case. From figure 11.5 I can notice that: the work W is the area of the rectangle enclosing the WLC curve, the entropic contribution is the area under the WLC curve and therefore, from equation 11.10, the free energy A should necessarily be the the remaining area of the rectangle, the difference area between W and H_{entr}.

Now, if I call $\overline{x}$ and $\overline{y}$ the normalized extension and the normalized force respectively, it is possible to calculated a normalized free energy by the integral

$$\overline{A} = \int_0^{\overline{y}} x \, dy = \int_0^{\overline{F}} \frac{L_e}{L_0} \frac{L_P}{k_B T} \, dF = \frac{L_e}{L_0} \frac{L_P}{k_B T} \int_0^{\overline{F}} L_e \, dF = \frac{L_P}{L_0 k_B T} A \tag{11.11}$$

where $\overline{F} = \frac{F L_P}{k_B T}$.

Now I have to substitute L_e, L_0 and L_P with the corresponding values of the mixed phase, so that to obtain the A_{mix}

$$A_{mix} = \int_0^{\overline{F}} L_{eB}(F) \cdot (1-\chi) + L_{eL}(F) \cdot \chi \, dF = A_B + A_L \tag{11.12}$$

where, from equation 11.11, the free energies of the pure phases are

$$A_B = \overline{A_B} \frac{L_{0B} k_B T}{L_{PB}} (1-\chi) \tag{11.13a}$$

$$A_L = \overline{A_L} \frac{L_{0L} k_B T}{L_{PL}} \chi \tag{11.13b}$$

Finally, the resulting free energy of the mixed phase becomes

$$A_{mix} = k_B T \left(\overline{A_B} \frac{L_{0B}}{L_{PB}} (1-\chi) + \overline{A_L} \frac{L_{0L}}{L_{PL}} \chi \right) \tag{11.14}$$

where normalized free energy values, $\overline{A}$, are computed from the green area shown in the example of figure 11.5 for the different experimental WLC curves, while the mechanical parameters of pure B- and

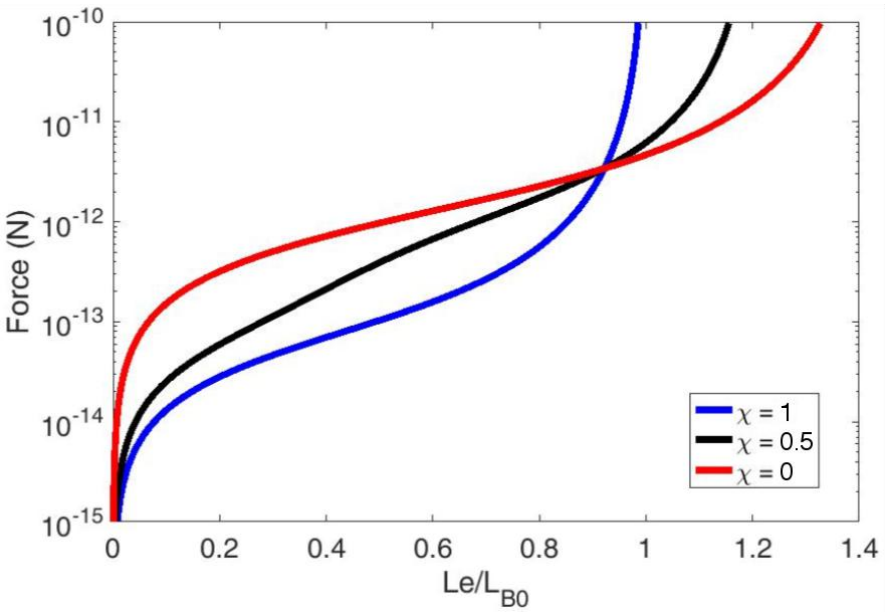

Figure 11.4.: WLC curves at different fraction χ of L-DNA: $\chi = 1$ (blue), $\chi = 0.5$ (black) and $\chi = 0$ (red). The DNA end-to-end extension is normalized to the contour length of the B-DNA form.

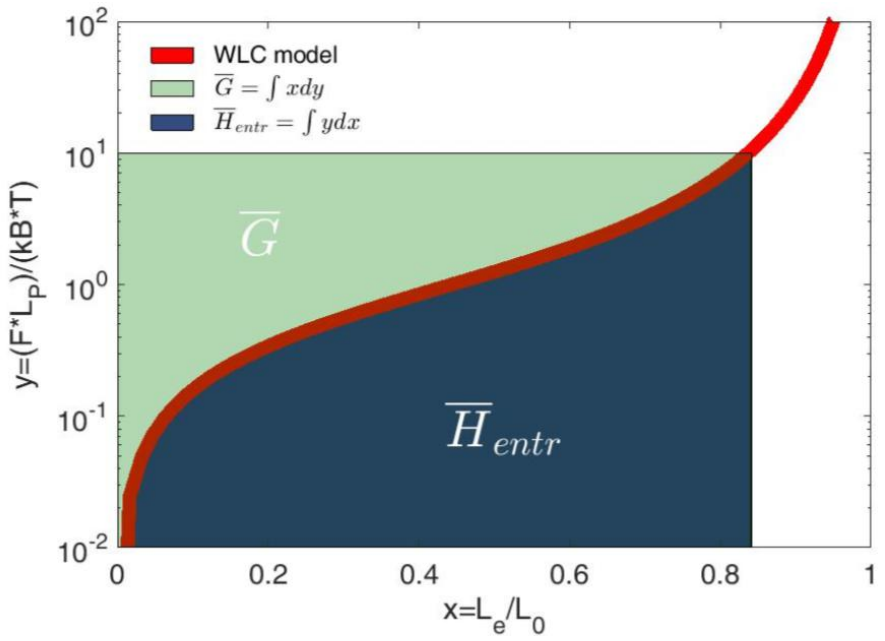

Figure 11.5.: Graphical representation of the energetic terms of equation 11.10: the whole rectangle is the external work (W), the dark blue area is the entropic contribution (H_{entr}) and the light green area is the free energy (A). The red line is a normalized WLC curve: the end-to-end extension (x-axis) by the contour length, whereas the force (y-axis) by the factor $k_B T/L_P$.

L-DNA can be calculated by fitting the denaturation curves shown in figure 7.5 with the WLC of the mixed phase (equation 11.7).

Since the free energy is expected to be a constant for each value of χ, I first calculated the initial A_{mix} for $\chi = 0$ (A_{start}), by substituting F with the experimentally measured F_{char} at low supercoiling, when the fraction of L-DNA is likely negligible (section 3.5). Under this approximation, I then calculated the F_{char} values from the following equation

$$A_{mix}(F) = A_{start} \tag{11.15}$$

The resulting F_{char} values are reported on page 161, where the model prediction is compared with the experimental data of the three different GC-content DNA sequences. The agreement of the experimental findings presented in section 7.2 with the semi-empirical model discussed here is reasonable in each of the three studied cases.

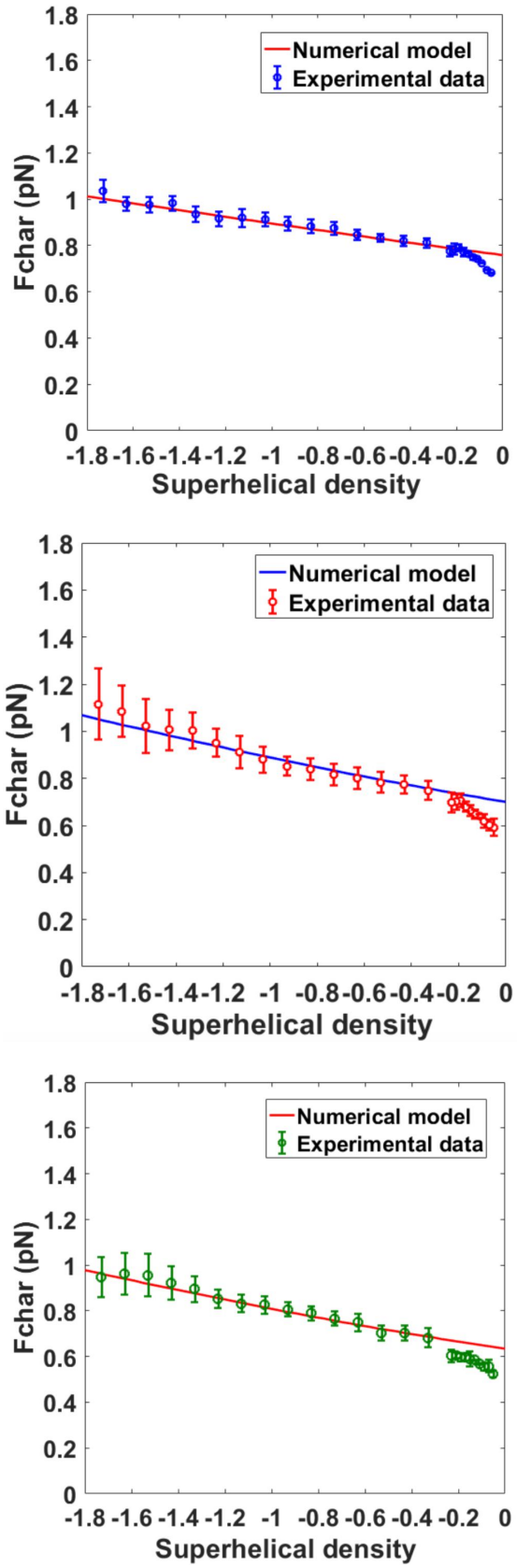

Figure 11.6.: Comparison between F_{char} values measured from the experiments (section 7.2 and prediction of the semi-empirical model discussed in this section. **(a)** low-GC, **(b)** normal-GC and **(c)** high-GC.

12

NANOMECHANICS OF DNA-LIGAND INTERACTIONS

In this second chapter of the discussion part I will deal with the experiments where DNA interacted with other small molecules, i.e. ligands. In this thesis work the DNA-ligands interactions issue has been addressed in two particular projects: the DNA-drugs project, whose results were presented in chapter 8, and the project concerning the H-NS protein binding to DNA, including also the interactions with PEG1500 as crowding agent, chapter 9. The analysis of the nanomechanics of DNA interactions with ligands, such as drugs or proteins, is fundamental for a complete understanding of the relation between the mechanical properties of DNA double-helix and its biological functions [220, 221]. As a matter of fact, DNA is often required to bind other molecules during cellular life, thus involving changes in mechanical properties, such as torsional properties, length or bending stiffness, or even varying the topological state of DNA: some ligands can increase the twist of the double-helix, promote or penalise the formation of supercoiled structures, the DNA loops called plectonemes [83, 146, 211]. Finally, the most interesting aspect explored here is the influence of these ligands on DNA stability , how some drugs or a specific protein or a crowding agent can affect the opening of the DNA double helical structure, inducing the creation of melting bubbles. These molecular mechanisms are of the utmost importance for many crucial biological phenomena, like DNA transcription or DNA replication.

In the following sections I will discuss the results presented in chapter 8, regarding the nanomechanics of DNA with some anticancer Pt-based drugs, and a part of the results of chapter 9, dealing with the molecular mechanisms involved during the binding between DNA and H-NS or PEG.

12.1 NANOMECHANICS OF DNA-DRUG COMPLEXES

12.1.1 *Mechanical effects*

In section 8.1 I started to analyse the DNA-drugs complexes by presenting the data concerning the effects on the formation of DNA plectonemes. Particularly I focused on two parameters: the buckling number n_b and the slope $\frac{dL_e}{dn_t}$, which is related to the plectoneme size.

I studied the force dependence of both quantities, indeed, accordingly to the rod-like chain model introduced in section 3.4, n_b and $\frac{dL_e}{dn_t}$ have a $\sqrt{F}$ and a $\frac{1}{\sqrt{F}}$ dependence respectively. As a consequence, recalling the equations of page 112, the expected exponents γ and β should be equal to 0.5 and -0.5 [110, 251]. From figures 8.2 and 8.3 it becomes immediately clear that the value of γ is reasonably confirmed for bare DNA, whereas β is appreciably underestimated in all the cases, bare DNA and the three DNA-drugs complexes. The discrepancy between experimental findings and theoretical predictions have already been observed many times in literature [136, 144, 252], in fact new and more precise models have been introduced to describe the plectonemes formation [132–135, 253, 254], see section 3.4.1. However, the focus of this analysis is to quantify possible differences between bare DNA and DNA in presence of Pt-based drugs: the measured values of γ are lower for the DNA-BBR complexes compared to bare DNA and CIS-DNA, namely BBR drugs roughly halved γ. As regards β, on the contrary, it seems the drugs do not induce any significant effect. Overall, the buckling transition is the only parameter influenced by the multinuclear drugs, but not by cisplatin, thus suggesting a greater effectiveness of the new BBR compounds in mechanically affecting DNA activity.

The second class of mechanical quantities studied in this project concerns the parameters of the WLC model: the contour length L_0, the length of DNA, and the persistence length L_P, which is related to the bending rigidity. A good agreement between data and theoretical fit is detected not only in bare DNA measurements but also for DNA-drugs complexes, see figure 8.4 and chapter C of supplementary information. These results are summarised by the histograms reported in figure 8.5: CIS did not affect affect the extension of DNA at all, the contour length of CIS-DNA complexes is the same of the expected and measured extension of bare DNA. On the other hand, the persistence length is reduced, consistently with previous studies [255, 256]. This mechanical effect of the drug has been explained with the formation of kinks. It should be pointed out that other studies reported a larger reduction of the persistence length, resulting in a L_P ranging from 10 to 25 nm, while in my experiments the persistence

length of CIS-DNA complex was approximately 33 nm. The reason is likely related to the experimental protocol adopted during the experiments, consisting in an incubation of the drug with DNA under an applied force > 1 pN. This procedure was compulsory to avoid the attachment of the tethered beads to the surface of the flow chamber in presence of BBR drugs causing an abrupt DNA collapse. In order to have experiments performed in equivalent conditions for all the three drugs, this procedure was applied to CIS-DNA complexes as well, even if it was not necessary.

The reduction of L_P was observed in presence of the BBR drugs too, especially for BBR3464 that decreased the value to ≈ 27 nm from the ≈ 48 nm measured for bare DNA, typical L_P value reported in literature for DNA in physiological conditions. So, BBR3464 reduced L_P more than 40% and its strong effects on DNA are evident from the measurement of the contour length as well: BBR3464 complexes were significantly shorter, with $L_0 \approx 1.2$ μm, compared to the contour length around 1.8 μm of bare DNA, a $\approx 33\%$ difference in this case. Instead, BBR3005 had less relevant effects on DNA: firstly, the contour length was basically unchanged, while the reduction of the persistence length is similar to that one of CIS, BBR3005-DNA complexes had $L_P \approx 33$ nm. The more relevant effects of BBR3464 are likely due to its capability of forming long range interactions with DNA double-helix, thanks to a high positive charge and a bigger and flexible structure including three Pt groups, as already explained at the beginning of chapter 8. However, I have also mentioned that the efficiency of forming DNA adducts is much lower for BBR3464 ($\approx 20\%$) compared to that one for BBR3005 (70-90%), confirmed by the higher error bars of L_0 and L_P average values, shown in figure 8.5.

12.1.2 *DNA structural stability*

The mechanical effects just discussed, induced by the cross-linking reactions between DNA and anticancer drugs, can induce both an enhanced compaction of DNA and a local denaturation of the double helix. This is the reason why I investigated the stability of the dsDNA structure by means of nanomechanical denaturation experiments. The characteristic force F_{char} introduced in section 3.4.2 turned out to be a very useful parameter to distinguish the effects on DNA of the three investigated drugs: in figure 12.1 the values of F_{char} are plotted as a function of the L_P values presented before, the data points of the three drugs cluster in well separated regions, contrary to the analysis of L_0 and L_P alone. Particularly, the introduction of the F_{char} parameter enabled to distinguish BBR3005 from CIS, because by considering only the analysis of WLC behavior these two drugs looked similar. On the other hand, the greater effect of BBR3464 is even more pronounced in this scatter plot.

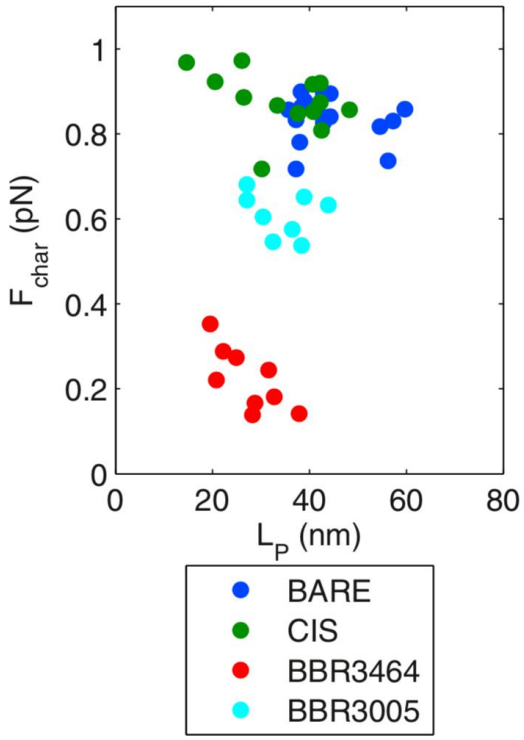

Figure 12.1.: Scatter plot of the F_{char} and L_P values obtained from MT experiments. The different colors of the dots identify bare DNA (blue) and the three DNA-drug complexes: DNA-CIS (green), DNA-BBR3005 (red) and DNA-BBR3464 (light blue). Figure adapted from [175].

The characteristic force depends on a number of quantities, the most important are the persistence length and the denaturation energy α (see equation 3.16), representing the binding energy of the number of basepairs required to relax one turn [137, 138]. Therefore, from this latter parameter it is possible to quantify the effect of the drugs on the destabilization of DNA, in terms of energy necessary to denature a dsDNA. In the histogram of figure 12.2(a) the values of α energies are reported, calculated from the averages of the F_{char} obtained in each of the case study (see figure 8.6). The lower values of α for DNA-BBR complexes suggests that the multinuclear drugs are more effective than cisplatin in destabilizing and locally open the DNA double-helix, leading to a higher ability of weakening and consequently damaging DNA, especially for BBR3464 case. The sizable effects of BBR3464 on overall structural properties of DNA are likely dependent on an enhanced cytotoxicity of this drug [257–259]. Additionally, these results indicate that the DNA basepairs opening at the beginning of the denaturation are probably the bases between the binding sites involved in the formation of the cross-links with the drug molecule. Indeed CIS did not significantly alter the DNA structural stability and it is the smallest molecule binding adjacent

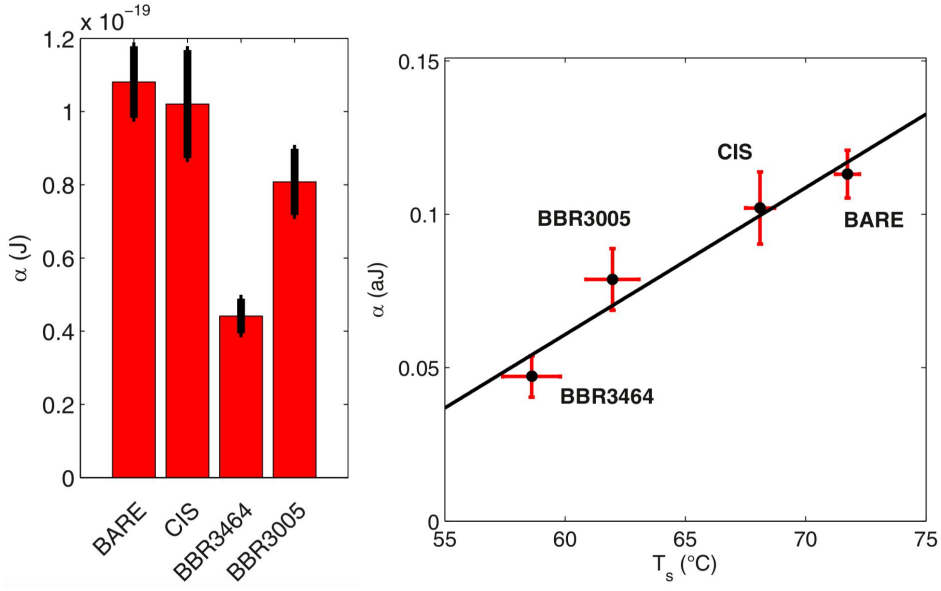

(a) (b)

Figure 12.2.: Resulting values of the denaturation energy α measured during MT experiments and comparison with thermal denaturation.
(a) Histogram of the values of α extracted from F_{char} by using equation 3.16.
(b) Comparison between bulk and single-molecule denaturation experiments. A linear relation between the nanomechanical parameter α and the thermal parameter T_s is shown. T_s is defined as the starting melting temperature, when only about the 3% of DNA is melted. Black points and red bars are data with standard deviations, the black line is the linear fit. Figures adapted from [175].

basepairs, whereas BBR3464, the most destabilizing drug, forms long range cross-links involving larger portions of the DNA molecule.

To conclude, I considered the thermal denaturation experiments and compared those results with the nanomechanical analysis, the values of α energies. Apparently, the bulk melting experiments showed opposite results, particularly for BBR compounds: the DNA double helix was not destabilized by the interaction with the drug (BBR3005) or DNA was even stabilized (BBR3464). This discrepancy between bulk and single-molecule techniques can be easily explained by recalling that thermal melting is a measurement of the denaturation involving the whole DNA molecule, it is a *global* phase transition. On the contrary, the nanomechanical melting involves a few basepairs and measures a *local* denaturation transition. As previously reported in other studies of my group [137, 138], the number of base-pairs opened during the nanomechanical denaturation is a linear function of the number of turns n applied to the DNA molecules. Furthermore, the melting bubbles involve approximately six or seven basepairs per

turn. In this work the DNA fragment used for MT experiments was about 6 kbp long (see section 5.4.1) and the twist applied to the DNA molecules to induce the denaturation was equal to $n = -30$, corresponding approximately to 200 bp$\simeq$ 3% of the total base-pairs. Therefore, the calculated values of α should be compared with the temperature related to the melting of only the 3% of the DNA molecule, which is different from the T_m, defined as the temperature at which 50% of DNA is denatured. In paragraph 8.2.2 I introduced a parameter measuring exactly this quantity, the temperature T_s. The linear dependence between α and T_s shown in figure 12.2(b) corroborates the hypothesis that nanomechanical single-molecules experiments are very sensitive to the local and initial denaturation of a few base-pairs, whereas the bulk thermal measurements takes into account the global phase transition, the denaturation involving the entire molecule. Overall, the interactions between DNA and these Pt-based drugs, particularly the multinuclear BBR compounds, can promote a local denaturation as well as a global average stabilization of the double helix. This highlights the complementarity of bulk and single-molecule techniques, and the importance of combined their information for a better understand of some DNA ligands, such as drugs or proteins.

12.2 INTERACTIONS BETWEEN DNA AND H-NS

12.2.1 *Hysteresis*

The discussion of the structural role of H-NS protein starts from the mechanical analysis of the binding process described by the data presented in chapter 9, namely the bridging binding mechanism. How H-NS activity is involved in DNA condensation, particularly in crowding conditions, will be addressed in the next chapter. A paper about the experimental findings discussed in this section is currently in preparation.

The first result related to H-NS binding mechanism is the presence of hysteresis, figure 9.2. The simplest strategy to quantify the hysteresis is to calculate the corresponding area, in this case the area enclosed by the bridging and unfolding curves, i.e. the blue and orange curve of figure 9.2 respectively. See also section D.2 for additional curves.

Taking inspiration from [63], where authors studied DNA condensation induced by Dps protein and developed a theoretical model to describe their data, I computed the *work difference* W_{diff}, which is basically the hysteresis area, and the *average work* W_{ave}, which is the average of the works done by the protein during folding and unfolding.

In figure 12.3 I reported the W_{diff} and W_{ave} values as a function of Dps protein concentration calculated in [63]: the different colours cor-

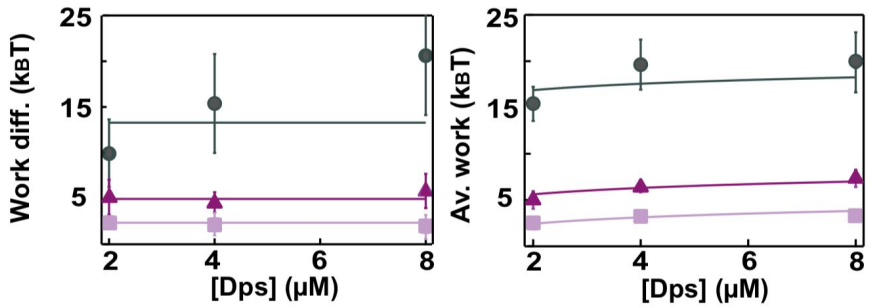

Figure 12.3.: Average values of work difference (W_{diff}) and average work (W_{ave}) as a function of Dps protein concentration at different NaCl concentrations: 50 mM (gray), 100 nM (dark purple), and 150 nM (light purple). Solid lines are fitting curves according to the model introduced in [63].

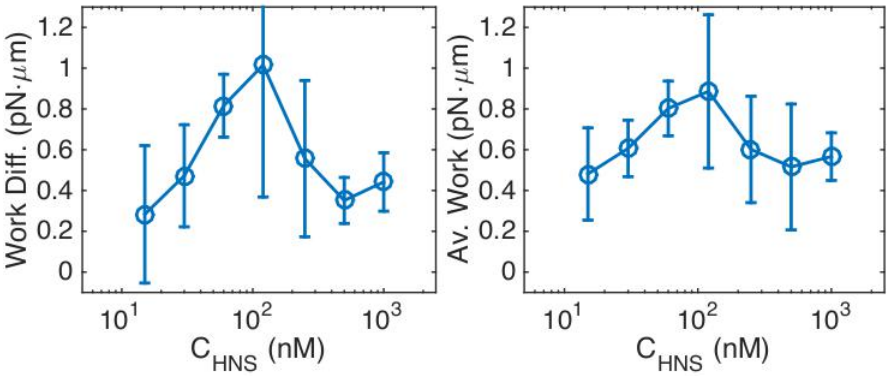

Figure 12.4.: Average values of work difference (W_{diff}) and average work (W_{ave}) as a function of H-NS protein concentration. Data from MT force-extension measurements presented in chapter 9 and performed in H-NS buffer (60 mM KCl, 10 mM $MgCl_2$).

respond to data collected at a different ionic strength, namely 50 mM (gray), 100 nM (dark purple), and 150 nM (light purple) of NaCl. The latter is the condition more similar to my experiments. In the figure 12.4 below the same quantities are plotted as a function of H-NS protein concentrations, from the data collected during MT experiments. These figures suggest that the binding mechanisms of the two proteins are quite different, even if both proteins form multimeric structures and induce DNA condensation. Indeed in Dps the W_{diff} was constant at different protein concentrations and W_{ave} had a logarithmic dependence, while H-NS showed a very similar behavior for W_{diff} and W_{ave}: both quantities exhibited a maximum for intermediate protein concentration.

It should be pointed out that the protein concentration ranges are completely different in the two experiments: Dps concentration varies from 2 to 8 μM, whereas for my experiments I chose a much wider range of concentrations, spanning about two orders of magnitude, and values are lower, from 15 nM to 1 μM.

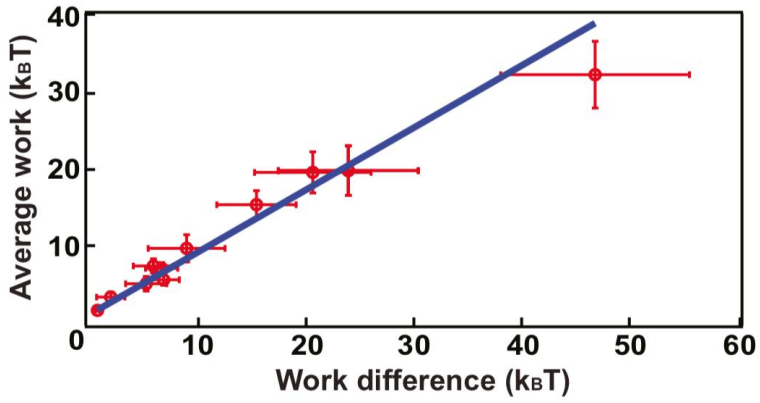

Figure 12.5.: Correlation between average work (W_{ave}) and work difference (W_{diff}) for Dps-DNA complexes. W_{ave} values plotted against W_{diff} values (red points) and linear fit applied to data (blue line). The two quantities exhibit a strong correlation, Pearson's $R = 0.89$. Data from [63].

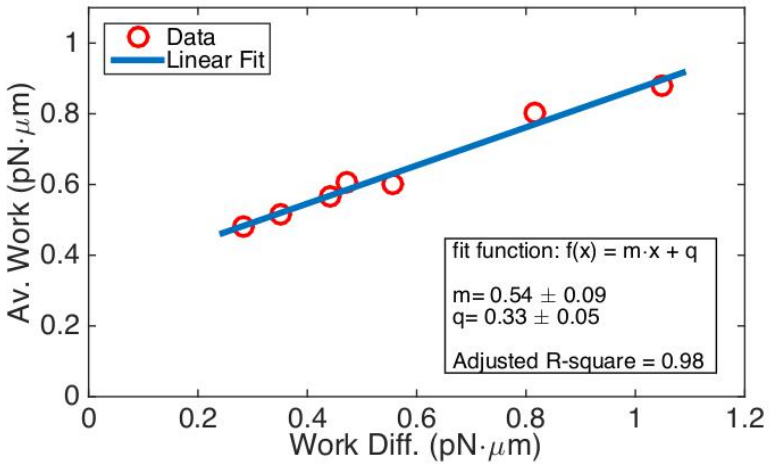

Figure 12.6.: Correlation between average work (W_{ave}) and work difference (W_{diff}) for H-NS-DNA complexes. W_{ave} values plotted against W_{diff} values (red points) and linear fit applied to data (blue line). The two quantities exhibit a strong correlation, the R-squared values computed by Matlab curve fitting tool is ~ 0.98.

Another crucial difference is the presence of divalent ions: as already explained I included 10 mM of $MgCl_2$ in my experiments, necessary to observe the bridging mechanism of H-NS [82, 83], while in [63] authors noticed that Mg^{2+} weakened the stability of Dps-DNA complexes. In general they observed that salt concentration significantly altered the behavior of Dps binding, more precisely higher salt concentrations destabilise Dps-DNA complexes.

The affinity of Dps protein for DNA binding was tested by measuring the correlation between W_{ave}, related to the overall stability of the protein-DNA complex, and W_{diff}, representing the amount of

hysteresis. I verified the same dependence in my data and I observed a strong linear correlation between W_{ave} and W_{diff} for H-NS, similarly to Dps, see figures 12.5 and 12.6.

These results reasonably confirmed a high affinity of H-NS bridging binding mechanism for DNA, but despite this similarity with Dps, the more complicated concentration dependence behavior remains unclear and not explained by current models.

12.2.2 *H-NS binding domains*

Another strategy to understand in more detail the molecular mechanism of DNA-H-NS interactions is the analysis of the temporal traces shown in paragraph 9.1.2. In figures 9.4 and 9.5-9.6 the stepwise kinetics of DNA extension during H-NS binding revealed distinct extension jumps, whose quantitative analysis could provide useful information. I reported two other examples of temporal traces in figures 12.7 and 12.8, emphasizing the extension jumps. I systematically measured the length of these jumps across all the data I collected at different protein concentrations, with the purpose of finding some specific trends providing information about H-NS binding domains. These extension jumps are in fact tightly related to the length of the bridges, i.e. the DNA loops, formed by the protein. For the sake of simplicity, I analysed only the bridging curves in this part, because the data of the unfolding curves are too noisy and complicated to interpret, as clearly shown by figure 9.3 and D.2.

In order to estimate these lengths, I first quantified the residual extension of the DNA molecule after each H-NS binding event, because the bridges formed by the protein reduce of a certain amount the DNA extension. The remaining part of the DNA continues to behave as a polymer following the worm-like chain model (equation 3.7), therefore I used the WLC curve to fit these data and extract the residual contour length of the polymer. It is important to calculate the contour length L_0 and not the end-to-end extension L_e because the latter is strictly related to the force, in this case to the bridging or unfolding forces at which the binding event occurs. However for this analysis I want to study only the length of the loops, separately from any other variable such as the force. We can consider the contour length a sort of normalization of DNA extension relative to the force.

Figures 12.9 and 12.10 represents two examples of the WLC fits (red curves) performed to calculate the residual contour length of DNA after H-NS binding events. FJC fits are also included (blue curves), because this model is analytically much simpler compared to WLC (see sections 3.2-3.3) and this could be useful for the development of a future theoretical model describing the nanomechanics of DNA-H-NS complexes, provided that the discrepancies of FJC curves from the data are acceptable. Assuming that H-NS in bridging binding mode

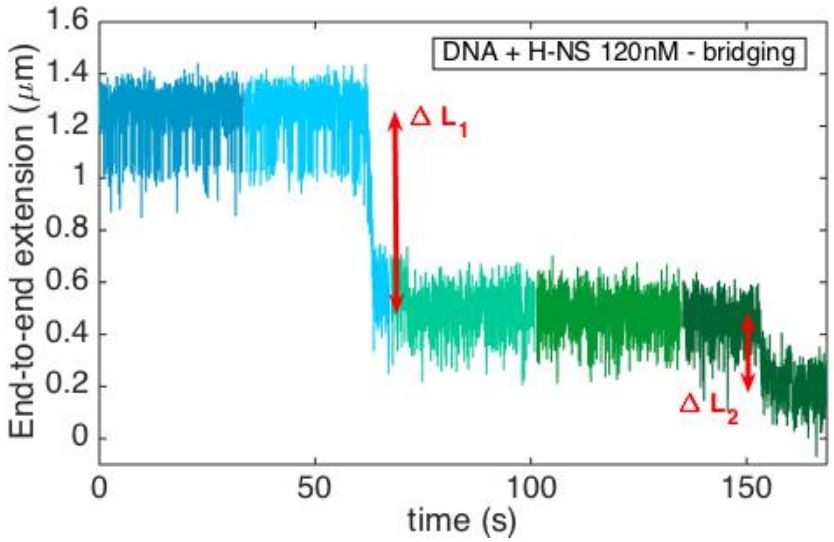

Figure 12.7.: Kinetics during a DNA bridging process in presence of 120 nM H-NS. The colours identify different forces applied to the DNA. Each abrupt extension jump represents an H-NS binding event, namely the formation of a loop, here indicated by the change in DNA extension ΔL.

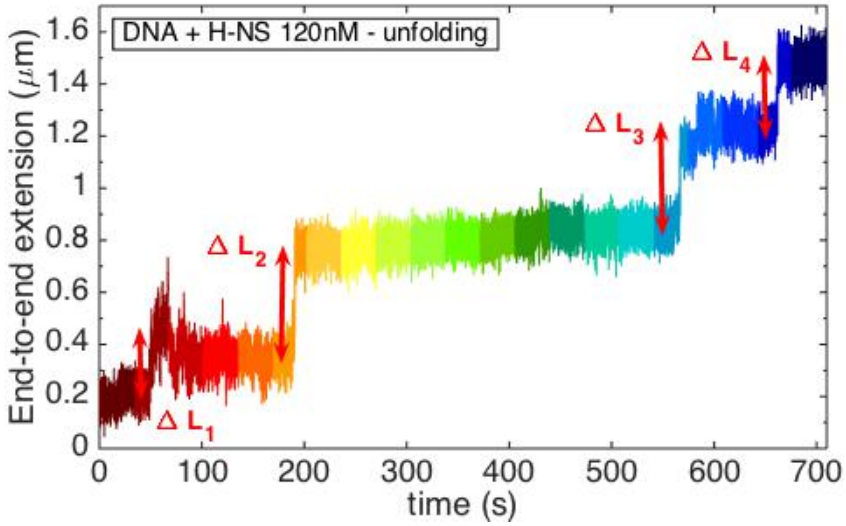

Figure 12.8.: Kinetics during a DNA-H-NS complex unfolding process, in presence of 120 nM H-NS. The colours identify different forces applied to the DNA. Each abrupt extension jump represents an H-NS binding event, namely the disruption of a loop, here indicated by the change in DNA extension ΔL.

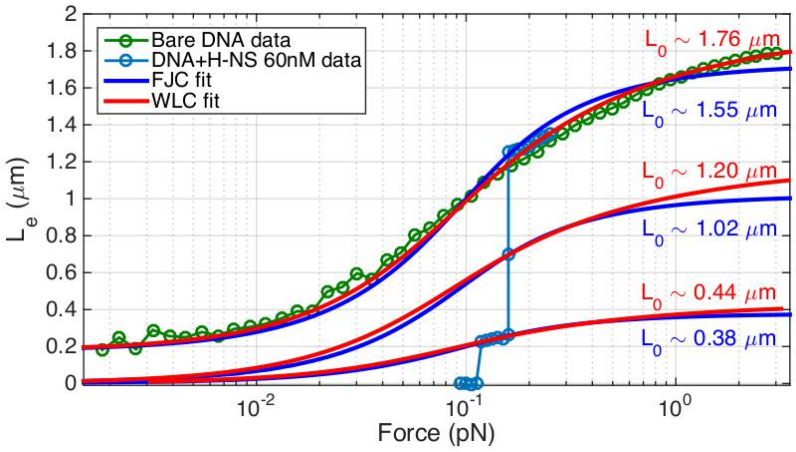

Figure 12.9.: FJC (blue solid lines) and WLC (red solid lines) fit curves performed on force-extension data of bare DNA (green dots) and residual DNA after two binding events with 60 nM H-NS (light blue dots). The contour length values (L_0) resulting from the fits are reported as well.

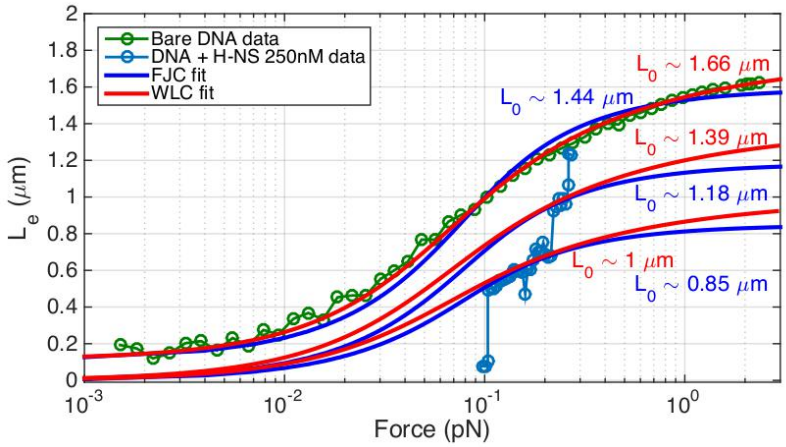

Figure 12.10.: FJC (blue solid lines) and WLC (red solid lines) fit curves performed on force-extension data of bare DNA (green dots) and residual DNA after two binding events with 250 nM H-NS (light blue dots). The contour length values (L_0) resulting from the fits are reported as well.

negligibly alters the persistence length of DNA [82–84], the fitting procedures of residual DNA fragments were performed by fixing L_P at the value obtained from the WLC/FJC fit of the corresponding bare DNA curve.

In this way there was only a fit parameter, the contour length L_0, and the quality of the fit is good even if there were a few data points.

From the L_0 values thus calculated it was straightforward to obtain the values ΔL_0 of the extension jumps, namely the effective length of DNA loops formed by H-NS. The first thing I noticed is a remarkable difference between the length of the first formed loop and the

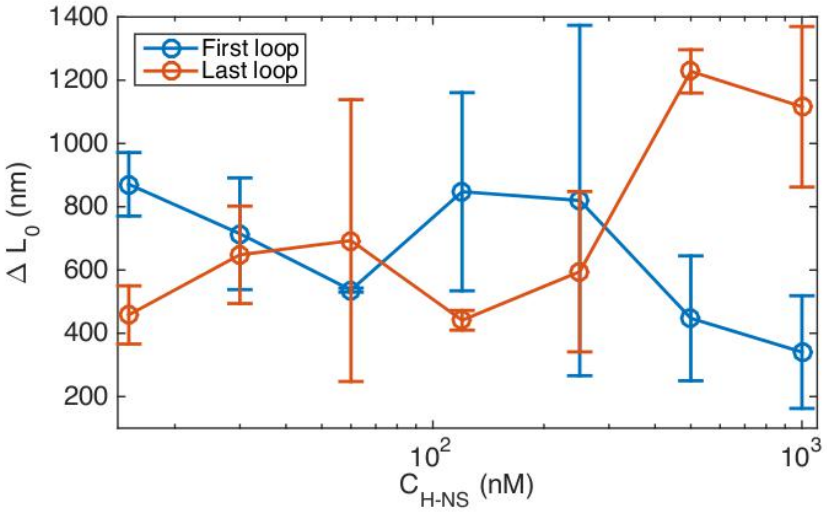

Figure 12.11.: Contour length average values of the extension jumps, namely the length ΔL_0 of the DNA loops. Data are related to the first loop formed by H-NS (blue) and the last loop (orange), after which DNA is completely collapsed. Error bars are standard deviations of the data.

following ones, with particular focus on the differences between the first and the last loop as a function of protein concentration, see figure 12.11. The most striking information is the completely opposite behavior of H-NS at low concentrations or at high concentrations: the length of the first loop reached the maximum value at 15 nM and the minimum value at 1 μM, the last loop had an exactly opposite behavior. Specifically, the comparison between the lowest (15 nM) and the two highest concentrations (500 nM and 1 μM) shows a statistical significance. The difference of forming a DNA loop sooner or later can be associated to the probability for H-NS of binding specific regions of the investigated DNA sequence (section 5.5). As a consequence, we could interpret the first loop as that one presumably related to the most probable DNA binding sites of H-NS. The results presented here seem to suggest, counter-intuitively, that when the protein concentration is low the most probable binding sites are quite far away, whereas at higher concentration the probable sites are closer. A possible explanation could be that the DNA binding sites having the highest affinity for H-NS, that means with a low potential barrier for the formation of the DNA-H-NS bond, are located in pretty far regions, producing the long loops observed at 15 nM H-NS. On the other hand, at the highest concentrations ($\geqslant$ 500 nM), there are a lot of proteins in solution promoting multi-binding processes and a higher level of H-NS oligomerization on DNA, this reduces the potential barriers of many other binding sites and enables the formation of several loops between closer regions, resulting overall in shorter loops.

The next step was to evaluate if the measured extension of the loops was consistent with the expected binding regions of H-NS. H-NS does not have a proper consensus sequence like many other proteins [54], it exhibits only a higher affinity for AT-rich DNA sequences, as mentioned in section 2.2. However, a 10 bp binding motif for H-NS has been identified in literature [85, 260, 261] and by using this sequence as a template a number of possible binding sites were observed in the DNA sequence adopted for my experiments as well. The template binding motif is the following:

tCG(t/a)T(a/t)AATT

and the with the help of SnapGene and ClustalΩ softwares we found nine potential binding sequences very similar to the initial template sequence (table 12.1).

These sequences were approximately clustered in three regions of the DNA, and their distances provided a prediction of the length of the loops that H-NS could form between these binding sites, see schematic in figure 12.12. The distribution of these lengths is shown by the histogram with red bars of figure 12.13, and the histogram related to the experimentally measured values is superimposed with blue bars. There is a general agreement between the main populations of the experimental distribution and the consensus sequence prediction, although data have a wider distribution, especially for low extension values. I considered only the lower protein concentrations ($\leqslant$ 250 nM) because at the highest concentrations, as explained before, the sizeable number of proteins in solutions likely promotes the formation of less probable loops because of an H-NS higher oligomerization on DNA, thus leading to a spreading of the distribution.

Template sequence	tCG(t/a)T(a/t)AATT
Binding sites	ACCAATAAATT
	AGGTAAAATT
	TCGTTCACTT
	TCAATAAATT
	TCGTAAAAGTT
	TCACTAAATT
	ACGGTTAATT
	TCGCTTAATT
	CCGTTAAGTT

Table 12.1.: The nine most probable binding sites identified in our DNA sequence, starting from the template sequence reported in [261].

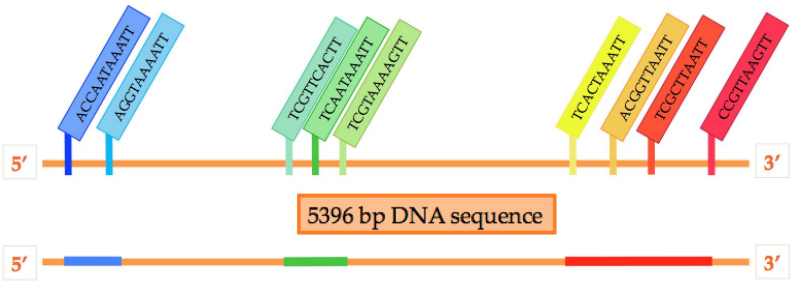

(a)

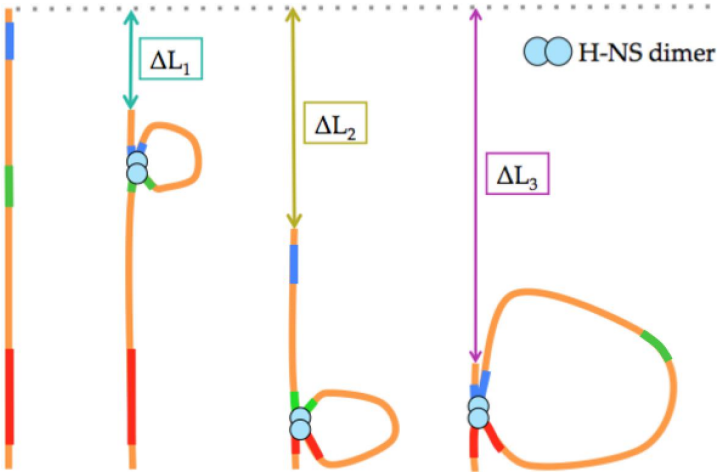

(b)

Figure 12.12.: **(a)** Schematic representation of the DNA sequence studied during the MT experiments of the H-NS role project. The potential H-NS binding sites identified from the template motif are reported as well, these sequences that can be clustered in three main regions.
(b) Schematic sketch, not to scale, of the formation of three illustrative DNA loops of different length.

This preliminary and simple analysis of H-NS binding already confirms, at least qualitatively, the potential and reliability of the MT technique in measuring the H-NS-DNA binding mechanism.

12.2.3 *H-NS and PEG influence on dsDNA stability*

The results presented in paragraph 9.2.3 confirmed the expected results about the H-NS structural effects on the stability of DNA double helix: the presence of the protein stabilised the plectonemic supercoiled structures penalising DNA melting [83]. I quantified this phenomenon by analysing the characteristic force F_{char} introduced in chapter 3 and I observed a significant shift to higher forces, that means higher forces are required to open and extend the DNA double-helical structure. More precisely, the F_{char} values for DNA-H-NS complexes ranged from approximately 0.9 to 1.3 pN, whereas the typical

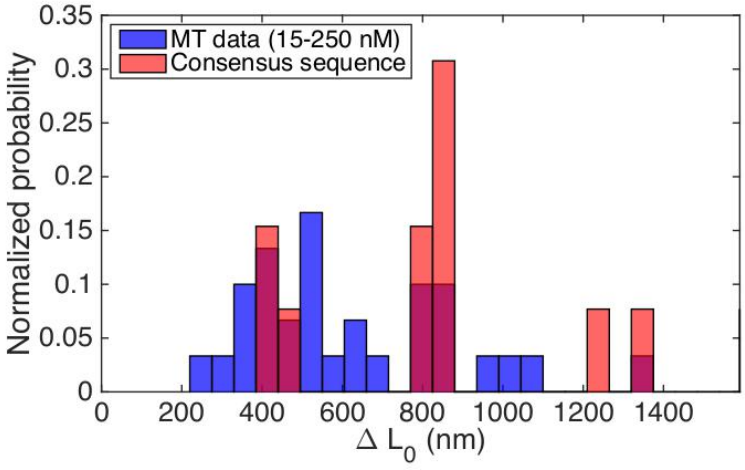

Figure 12.13.: Comparative histograms of the loops length ΔL_0: experimentally measured values at low H-NS concentrations (blue bars) and predicted distribution from the consensus sequence. Concentration range: 15-250 nM.

value for bare is between 0.6 and 0.8 pN, see section 3.5. The wide spreading of F_{char} values for DNA-H-NS complexes does not derive from experimental errors, but it is related to the presence of multiple peaks corresponding to different characteristic forces, as it will be discussed below. Therefore, the H-NS protein can increase the characteristic force of denaturation by as much as two-fold, and F_{char} values were not dependent on the protein concentration. Now, if I recall the quadratic relation between F_{char} and the denaturation energy α (equation 3.16), along with the fact that the bridging binding mechanism does not alter the L_P, I can estimate that the energy necessary to create melting bubbles in a DNA-H-NS complex can be up to ≈ 1.4 times higher than the corresponding value of bare DNA. Since α is usually around $1.1\text{-}1.2 \cdot 10^{-19}$ J [137, 138, 175], the value of the DNA denaturation energy in presence of H-NS should range from ≈ 1.2 to $\approx 1.6 \cdot 10^{-19}$ J.

Very similar denaturation effects were observed for DNA molecules in crowding conditions induced by PEG: the formation of supercoiled structures is favored over melting bubbles. This could be odd because the two interaction mechanisms with DNA are completely different: H-NS involves a real binding with the double helix of DNA, while PEG, when the concentration is high enough, exerts depletion forces inducing DNA collapse. The main difference between H-NS and PEG effect concerns again the concentration dependent behavior: the value of the characteristic force of denaturation changed with PEG concentration, but without a clear trend such as in figure 9.10. For instance, at relatively low concentration (13% v/v) the F_{char} was comparable with typical values for bare DNA, 0.6-0.8 pN (see figure D.14

in supplementary), while at higher concentration (19% v/v) values ranged between 1.1 and 1.6 pN. Overall, the macromolecular crowding effects on DNA structural stability vary widely across different PEG concentrations, but the increase of F_{char} can be significant at sufficiently high concentrations, even more effective than H-NS effects.

I also mentioned that a multistep process has been identified both in H-NS and PEG experiments. This is clearly visible from the multiple peaks of figures 9.8 and 9.16, where each of them represent a F_{char} related to a denaturation event. The explanation of this phenomenon is quite straightforward for H-NS binding mechanism: the protein promotes the stabilisation of intermediate DNA states of a specific extension, similarly to what happens during force extension experiments and shown in temporal traces (figure 12.7-12.8). Considering PEG-induced crowding, the stepwise characteristic could be related to non specific interactions of PEG with DNA but also with the surface of the class coverslip, confirmed by the fact that at high concentrations it was impossible to observe unfolding curves because the surface of the chamber became sticky (page 127).

An interesting feature of this multistep process is that the autocorrelation analysis identified this phenomenon, but the analysis in terms of the variance did not, as shown in figures at pages 179-180. The nanomechanical analysis of the DNA denaturation may indeed be performed in two ways: by simply calculating the variance (σ^2_{Le}) of the fluctuations of DNA extension, or by obtaining the autocorrelation characteristic time (τ), see section 3.4.2. The difference between the two analyses corroborates the particular sensitivity of the parameter τ in studying the details of the nanomechanical denaturation of DNA. The calculation of τ could represent a very useful tool for the analysis of intermediate and metastable states of DNA or DNA-ligand complexes, characterized by a fast kinetics. An additional factor confirming the rapid kinetics of the denaturation process involving DNA-H-NS complexes or DNA molecules under crowding conditions is the height of the peaks of figures 12.15 and 12.17, orders of magnitude higher than the typical values for DNA [137, 138].

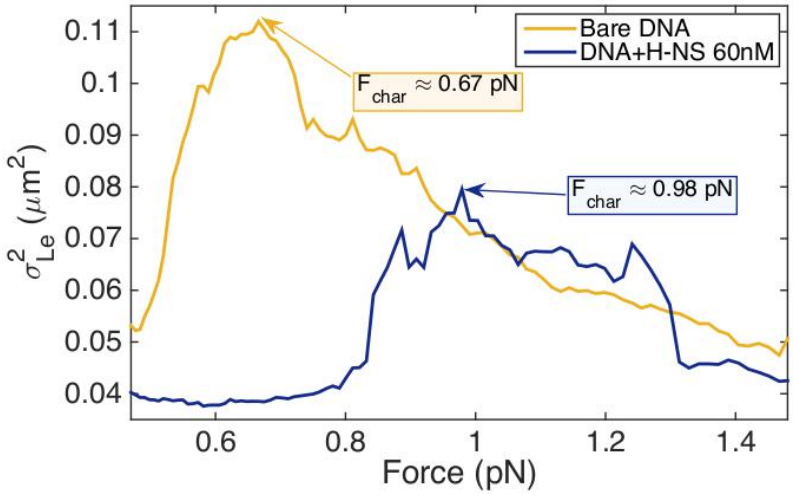

Figure 12.14.: Variance σ^2_{Le} of the DNA extension fluctuations related to a denaturation transition occurring in a bare DNA molecule (yellow) and in a DNA-N-NS complex (dark blue). The force values of the peaks correspond to different characteristic forces. In labels the values of F_{char} are reported.

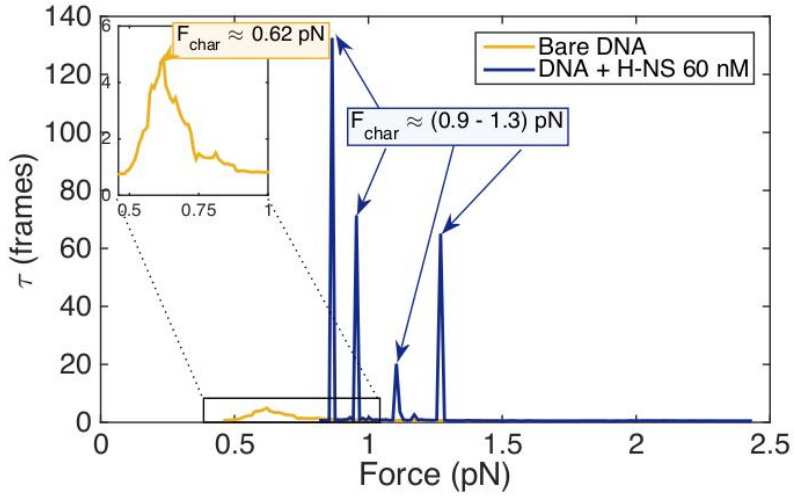

Figure 12.15.: Autocorrelation characteristic time τ of the DNA extension fluctuations related to a denaturation transition occurring in a bare DNA molecule (yellow) and in a DNA-N-NS complex (dark blue). The force values of the peaks correspond to different characteristic forces (F_{char}). In labels the values of F_{char} are reported.

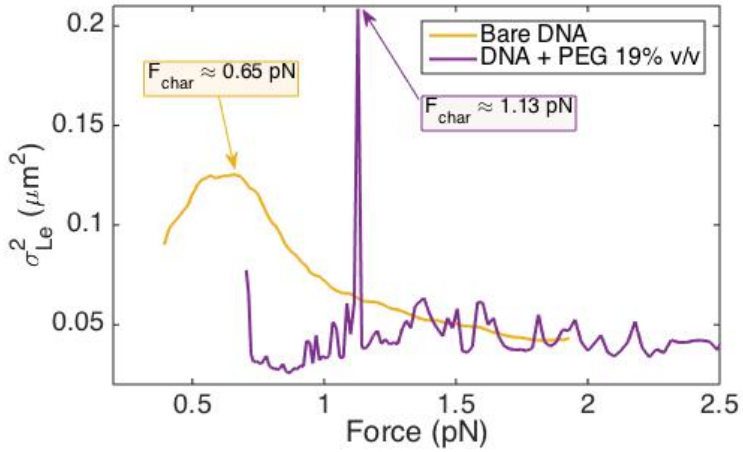

Figure 12.16.: Variance σ^2_{Le} of the DNA extension fluctuations related to a denaturation transition occurring in a bare DNA molecule (yellow) and in a DNA molecule in presence of PEG (purple). The force values of the peaks correspond to different characteristic forces. In labels the values of F_{char} are reported.

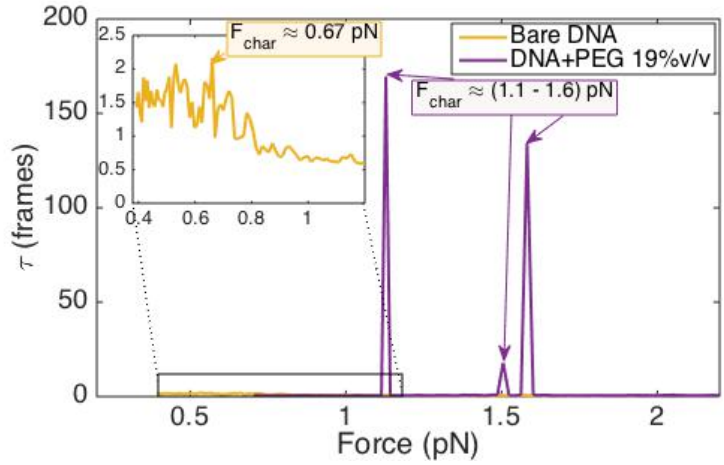

Figure 12.17.: Autocorrelation characteristic time τ of the DNA extension fluctuations related to a denaturation transition occurring in a bare DNA molecule (yellow) and in a DNA molecule in presence of PEG (purple). The force values of the peaks correspond to different characteristic forces (F_{char}). In labels the values of F_{char} are reported.

13

DNA CONDENSATION AND GENE REGULATION: THE H-NS DUAL ROLE

The last chapter of the discussion part deals with an important general topic addressed during this thesis wok: the DNA condensation inside the cell. Particularly, this subject has been investigated in terms of the activity of a specific nucleoid associated protein of *E. coli* cells: the Histone-like Nucleoid Structuring protein (H-NS). Since H-NS does not have this structural function only, complementary experiments were carried out in order to have a more comprehensive study of the biological activity of this protein. A regulatory role of H-NS has been reported in literature [74, 75, 86], more precisely H-NS seems to have an important repression activity [85, 226, 230]. For this reason, additional measurements monitoring the gene expression at the single-cell level were performed.

DNA condensation was tested by a MT single-molecule assay, where the structural binding of H-NS with DNA was studied in combination with macromolecular crowding effects. The aim is to assess a potential higher effectiveness of the protein. Indeed, a possible cooperative effect between the protein and a neutral crowding agent, such as PEG, has been reported in literature [262–264], but the experiments did not achieve conclusive results yet.

In the following, I am going to discuss the results presented in chapter 9 concerning the role of H-NS in the condensation of DNA, after having already discussed the mechanical details of the DNA-H-NS binding mechanism in previous chapter, section 12.2. Finally, the data obtained from the pulling force experiments on DNA molecules in presence of H-NS and PEG (section 9.3) are analysed and interpreted.

The regulatory activity of H-NS was investigated by the gene expression single-cell experiments described in chapter 10. Namely, the fluorescence of individudal *E. Coli* cells was measured during time-lapse microscopy, in a temperature controlled condition (section 4.6). The fluorescence of the cells is associated to the activity of a promoter-gfp construct regulated by H-NS. Specifically, I studied four bacterial strains with a different sensitivity to the activity of the protein: start-

ing from a "control strain" marginally affected by H-NS, I compared the results with two strains where the promoter is inserted within an extended H-NS binding domain. Finally, the regulatory role of H-NS is studied by directly acting on the corresponding gene: the gene expression of an *hns* gene knockout strain was quantified.

13.1 DNA CONDENSATION

13.1.1 *H-NS bridging and unfolding mechanisms*

I start the discussion by recalling the temporal traces reported in paragraph 12.2.2 (figures 12.7-12.8) describing the kinetics of the bridging and unfolding binding events: from these plots it can be easily noticed that the unfolding shows a more gradual stepwise process, which means a higher number of DNA loops formed by H-NS. In figure 13.1 this concept is expressed more clearly: the distributions of the DNA end-to-end extension during the bridging (blue) and the unfolding (orange) are superimposed, so that it is immediate to observe a greater number of extension populations related to the unfolding event. These two distributions share three populations but the extension of the DNA subject to the bridging binding mechanism lacks of two additional populations observed for the unfolding process of the DNA-H-NS complex. The distributions are referred to the experiment shown in figures 12.7-12.8, in supplementary material another example is included.

This is not just an isolated case but a systematic trend, observed for nearly all the the experiments at each protein concentration, as shown in figure 13.2. With the exception of the lowest value (15 nM), in the whole range of concentrations the unfolding process produced a higher number of DNA loops. The error bars are not included here because their large values, especially for the unfolding, make the plot less clear. See supplementary material (figure D.10) for the figure with the errors. This experimental finding strongly suggests that the protein promotes the formation of complex supercoiled DNA structures, in order to compact the chromosome in the tiny space of the cell. Once the first protein dimers bind DNA and form the first bridges, subsequent proteins keep on binding these DNA loops, producing more and more supercoiled and compacted structures. In a MT experiment this means that after the collapse of the DNA during the bridging, additional H-NS proteins start to bind the zero-extension DNA molecule, but these events are not detected by the instrument because they do not induce any variations in DNA extension. These additional H-NS dimers bound to the DNA are revealed during the unfolding curve, when the whole DNA-protein complex is disrupted and the DNA is fully extended.

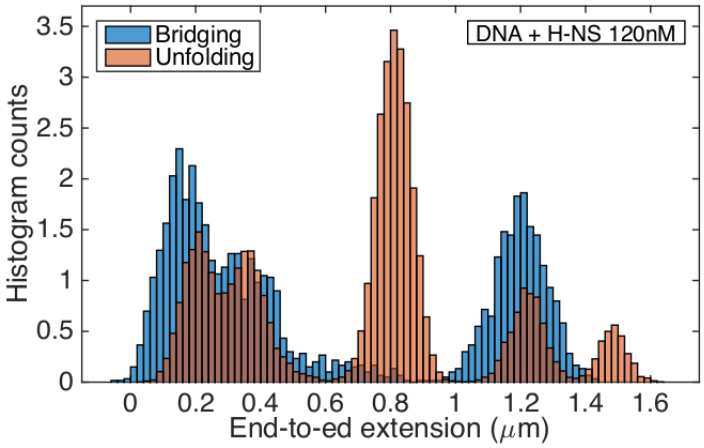

Figure 13.1.: Histograms of the end-to-end extension (L_e) in presence of H-NS 120 nM, measured during bridging (blue bars) and unfolding (orange bars) events. Data are referred to the temporal traces reported on page 172. For the sake of clarity, the plotted distributions considered only the temporal traces involved during the binding mechanism, this is why the bridging histogram seems to have a lower maximum value of L_e, I excluded the data at higher forces before the binding occurred. This choice makes it easier the comparison between these distributions and the related temporal traces, without altering the number of populations.

Figure 13.2 shows that the number of loops formed during the bridging decreases with the concentration, whereas there is not a well-defined trend during the unfolding. This feature could confirm the hypothesis already proposed in section 12.2.2 concerning H-NS binding domains: when the protein concentration is high, the probability of having a higher level of H-NS oligomerization on a DNA molecule is also higher, thus leading to form fewer but larger loops (see also figure 12.11).

As one might expect by looking at figure 9.3, where all the DNA folding curves collapsed approximately at the same point, the critical force of DNA-H-NS bridging does not seem to be affected by protein concentration. The bridging force values (F_{bridg}) calculated for each H-NS concentration are reported in figure 13.3: the average of F_{bridg} is 0.15 ± 0.01 pN, consistent with literature [82, 84]. A similar conclusion holds for the unfolding force F_{unf}, but data are noisier, with higher and more widespread values: the average of F_{unf} is 0.57 ± 0.20 pN (figure 13.4). A larger experimental uncertainty of the unfolding binding mechanism has been observed in figure D.10 as well. This is likely due to the oligomerization of H-NS on the DNA molecule after the first bridging event, which could promote multiple binding processes and lead to the formation of more complex DNA-H-NS structures, revealed only by unfolding curves. These phenomena are probably

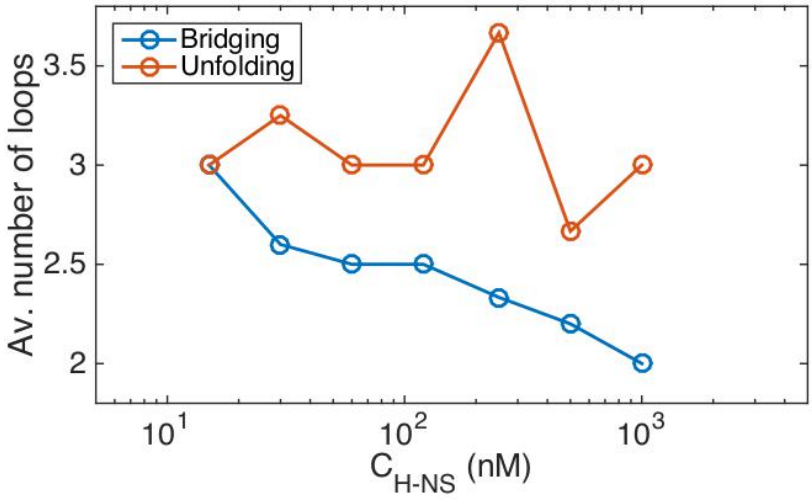

Figure 13.2.: Average number of DNA loops (identified by extension jumps) during the bridging (blue) and unfolding (orange) mechanisms promoted by H-NS protein at different concentrations, ranging from 15 nM to 1 μM. The figure including also the errors (standard deviations) is reported in supplementary material.

characterized by an intrinsic higher variability, as confirmed by larger error bars of unfolding data. Another cause could be related to the interactions between the DNA-protein complexes and the surface of the flow chamber, that sometimes might alter the dynamics of the binding mechanism. For these reasons, the analysis will mostly focus on the bridging, which is less sensitive to this type of issues.

A possible explanation of the results of figure 13.3 is that this single-molecule analysis takes into account a one-to-one interaction. In other words, once the applied force by the magnets is below a certain value around 0.15 pN, the H-NS binding with DNA is energetically permitted and occurs in the same way regardless the number of proteins in solution (provided that protein concentration is above a minimum threshold). This result is confirmed by other force spectroscopy studies focusing on the bridging binding between DNA and H-NS [82, 83]. The protein concentration affects other aspects more related to the dynamics of the binding mechanism, such as the extension or the number of loops, depending on the probability for a DNA molecule to interact with a protein, which in turn is proportional to the number of proteins.

13.1.2 *PEG-induced DNA condensation*

A similar analysis was applied to the DNA condensation observed in presence of the crowding agent PEG. This mechanism is expected to be completely different from that one described in the previous paragraph in presence of H-NS. Indeed the interactions between DNA

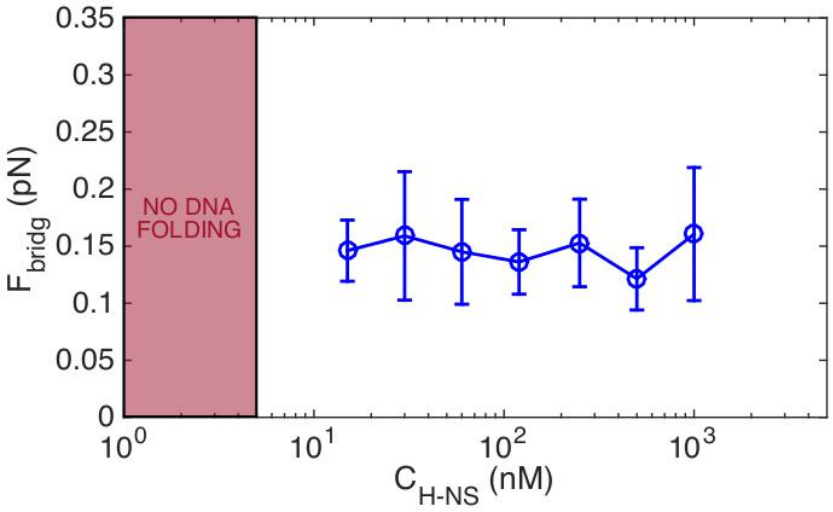

Figure 13.3.: Average values of the bridging force (F_{bridg}) for each H-NS protein concentration, ranging from 15 nM to 1 µM. Error bars indicate the standard deviations. The region below which no clear H-NS binding to DNA was observed is reported in a red shaded area (for $C_{HNS} \leqslant 5$ nM, see figure D.1).

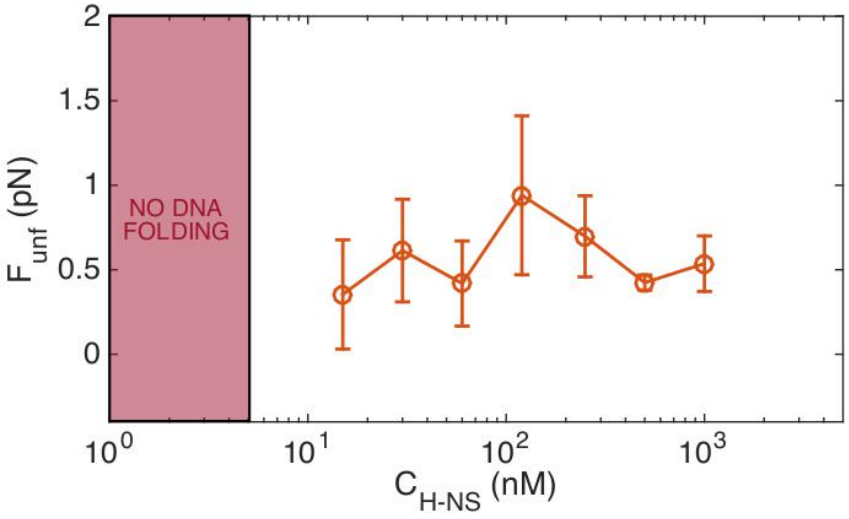

Figure 13.4.: Average values of the unfolding force (F_{unf}) for each H-NS protein concentration, ranging from 15 nM to 1 µM. Error bars indicate the standard deviations. The region below which no clear H-NS binding to DNA was observed is reported in a red shaded area (for $C_{HNS} \leqslant 5$ nM, see figure D.1).

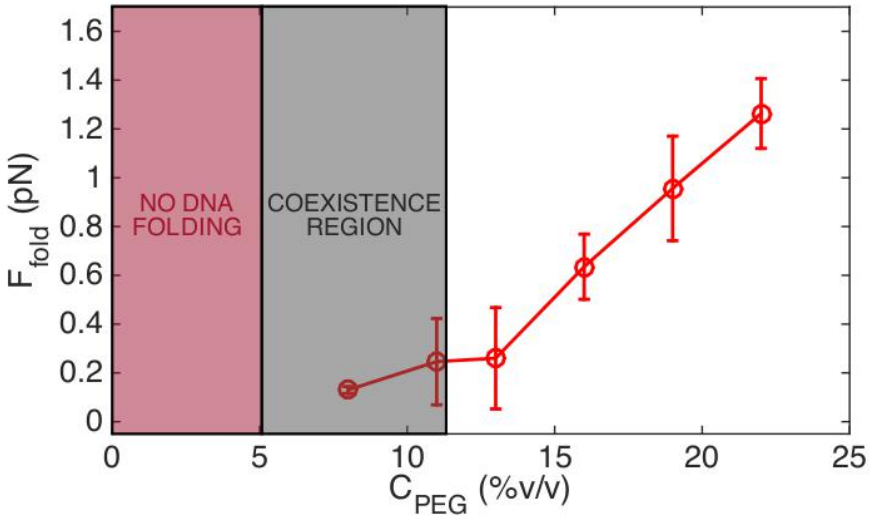

Figure 13.5.: Average values of the DNA folding force (F_{fold}) at different PEG1500 concentrations, with volume fractions ranging from 8% v/v to 22% v/v. Error bars indicate the standard deviations. The region below which no DNA folding was observed is reported in a red shaded area (for $C_{PEG} \leqslant 5\%\, v/v$). The grey shaded area on the right represents a coexistence region where it is possible to find collapsed DNA or extended DNA molecules apparently not affected by PEG interactions.

and PEG do not involve a chemical bond such as in the case of DNA-H-NS complexes. The average values of the critical force of DNA folding in presence of PEG (F_{fold}) confirmed this hypothesis: in figure 13.5 F_{fold} is plotted as a function of PEG concentration, in the range 8%-22% v/v, and a strong dependence has been found.

Similarly to the experiments in presence of H-NS, a red shaded area is reported to indicate the concentration below which DNA folding is no longer observed, in this case for volume fractions $\leqslant 5\%\, v/v$. The Ψ condensation, namely the PEG-induced condensation of DNA (section 2.3), exhibited another peculiar region, indicated in grey in figure 13.5. In this range of concentrations a coexistence region between a collapsed and an extended state was observed, an interesting experimental finding already described in literature [265]. In other words, if $C_{PEG} = 8\%\, v/v$ the probability of DNA folding was quite low, around 17%, while at 11% v/v this probability is increased to $\approx$ 55%, but only for concentrations above 13% v/v the DNA folding occurs with a probability of 100%. Several models have been developed to try to predict this complex phenomenon, explained in detail in [265–267].

For the volume fractions above the coexistence region, the average values of F_{fold} linearly grow from $\approx$ 0.3 pN at 13% v/v to $\approx$ 1.3 at 22% v/v, almost a five-fold increment. This behaviour is completely opposite with respect to the bridging force of H-NS. This result is

reasonable since the depletion forces exerted by PEG are based on excluded-volume interactions: the more neutral polymers are present in solution and the more volume is excluded for DNA, favouring its collapse.

13.1.3 *H-NS and PEG cooperative effect*

After having separately characterized the behavior of DNA during the condensation induced by H-NS or PEG, I could explore the potential cooperative effect of the protein and the crowding agent. The aim is to assess if H-NS activity on DNA condensation is more effective in a condition similar to the crowded cellular environment. I reported a couple of examples of folding and unfolding force-extension curves on page 133, where a significant shift to higher force was observed when the DNA molecule is subject to the combined effect of H-NS and PEG.

I summarised the data collected so far in figure 13.6: the blue and red dots represent the H-NS and PEG data reported in the previous figures 13.3-13.5. The purple dots are the average values of critical folding force of DNA molecules in presence of H-NS and PEG1500 at the same time. Particularly, these three preliminary points considered the following conditions: the first one 15 nM H-NS and 5% v/v PEG, the second 30 nM H-NS and 8% v/v PEG, and the last one at higher concentrations 120 nM H-NS and 13% v/v PEG. It should be pointed out that at 5% of volume fraction PEG alone does not induce any condensation of DNA, while at 8% v/v only in 17% of the cases DNA condensation occurred, therefore the first two purple points are particularly interesting.

One of the possible expected results was that the H-NS and PEG effects simply added up in the protein-crowder mixture. This hypothetical additive effect has been reported with the green dotted line, whose folding force values are roughly the F_{fold} of PEG plus 0.15 pN, the average value of F_{bridg}. Surprisingly, the experimentally measured values of the folding force suggest a quite pronounced cooperative effect, indeed the purple points have a statistically significant higher value compared to the corresponding green point. Note that purple points are not perfectly aligned to both red and blue corresponding points, this superimposition is shown just for a more direct and easier comparison. A purple cooperative curve is reported as a guideline for the hypothetical exponential increase of the folding force, which would be associable to a cooperative effect.

This behaviour can be explained by considering two effects. First, PEG could modify the enthalpic gain of DNA-H-NS bridging by making H-NS more "sticky" to itself and to the DNA as well. In this scenario, the gained binding energy increases in a non-linear way in the presence of the crowder [268], accordingly to the behaviour

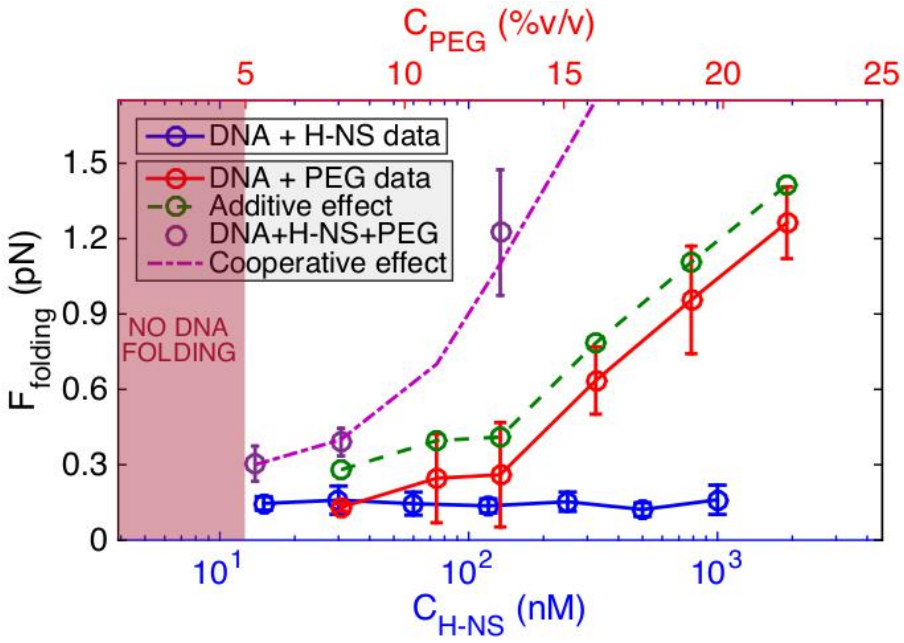

Figure 13.6.: DNA folding force (F_{fold}) resulting from the combined effect of the H-NS protein and the crowding agent PEG1500. F_{fold} values are reported as a function of H-NS concentration (blue, bottom axis) and PEG1500 volume fraction (red, top axis). Blue and red dots correspond to the F_{bridg} of H-NS and to the F_{fold} of PEG reported in figure 13.3 and 13.5 respectively. The green dotted line represent the values of the critical folding force if the combined effect H-NS+PEG was just additive. Purple dots are instead experimental data points of DNA folding in presence of both H-NS and PEG. Error bars indicate the standard deviations. The purple dotted curve is just a guideline for a hypothetical exponential trend typical of a cooperative effect. The red shaded area represents the region below which no DNA folding is observed.

of conventional depletion forces. Secondly, the crowder could make DNA effectively self-attracting with short-ranged interactions [269]. As a consequence, the looping entropy is modified by the presence of the crowder, which may facilitate H-NS-mediated loop formation by partly counteracting DNA electrostatic self-repulsion. The combination of these two effects could justify the synergistic effect of H-NS and PEG leading to that increment of the critical folding force. Other studies in literature suggested a potential synergy in the combined effect of the protein in presence of a crowder. In [264] gel electrophoresis and Fluorescence Correlation Spectroscopy seem to show that the presence of PEG enhanced the effectiveness of H-NS binding to DNA. However, completely reliable conclusions about H-NS-PEG cooperative effect were not drawn in these works. Consequently, there is the need of a sophisticated technique able to quantify more precisely these effects. The MT force spectroscopy experiments presented here

are a very promising tool to study these complex molecular mechanism, indeed the quantity F_{fold} is very sensitive to the presence of macromolecular crowding and, additionally, this type of setup can measure very accurately the applied force.

13.2 GENE REGULATION

13.2.1 *Genomic position and kanamycin protection*

The analysis of the regulatory role of H-NS first considered the genomic position influence on gene expression, because it turned out to be a crucial factor for promoters activity [229, 230, 234]. As previously explained, I investigated the activity of a shortened version of *rrnB*P1 promoter (P1 short), by means of a GFP fluorescent reporter, inserted in two positions: one close to the origin (*ori*3), in order to have a sort of control strain not significantly affected by H-NS, and another one included within a large H-NS binding domain (*nsr*3), therefore strongly regulated by the protein.

The gene expression levels shown in figures 10.3 confirmed that P1*nsr*3 is more repressed and this is most likely due to the activity of the H-NS protein binding DNA in the *nsr*3 chromosomal region. Quantitatively, the upshift increment of cell fluorescence was decreased by approximately 32%, the GFP concentration even more, by 38%, and the statistical significance is greater (see error bars in figure 10.3(b)). On the other hand, the size growth exhibited an opposite behavior: the size of the cells of P1*nsr*3 strain is more sensitive to the upshift stimulus compared to the corresponding P1*ori*3 cells. Differences are slighter and within experimental uncertainties, the cell area in *nsr*3 increases $\approx$ 13% more than in *ori*3 and by considering the cell volume this difference becomes $\approx$ 25% (see E.1). For a deeper study of the size growth is very useful to introduce another quantity: the growth rate, namely the frequency at which the bacterial cell increases its volume. In figure 13.7 I reported the comparison between the two strains: it is very clear that P1*nsr*3 cells grows bigger and faster after the upshift, more precisely the increment factor is $\approx$ 53% for P1*nsr*3 and $\approx$ 24% for P1*ori*3.

This result can be explained in terms of available resources for the cells during the nutrient stimulus. Since the activity of the promoter-gfp construct in *ori*3 position is very high because it is not repressed by H-NS, each cell spends a considerable amount of energy in producing GFP fluorescent proteins. However, the production of GFP does not reflect the normal functions of *rrnB*P1 promoter, this is an additional and "useless" work for the cell, that consequently has less energy to grow in size. Conversely, the P1 short promoter has a lower activity in *nsr*3, thus providing more energy for the cells to grow in size as a response to the upshift stimulus.

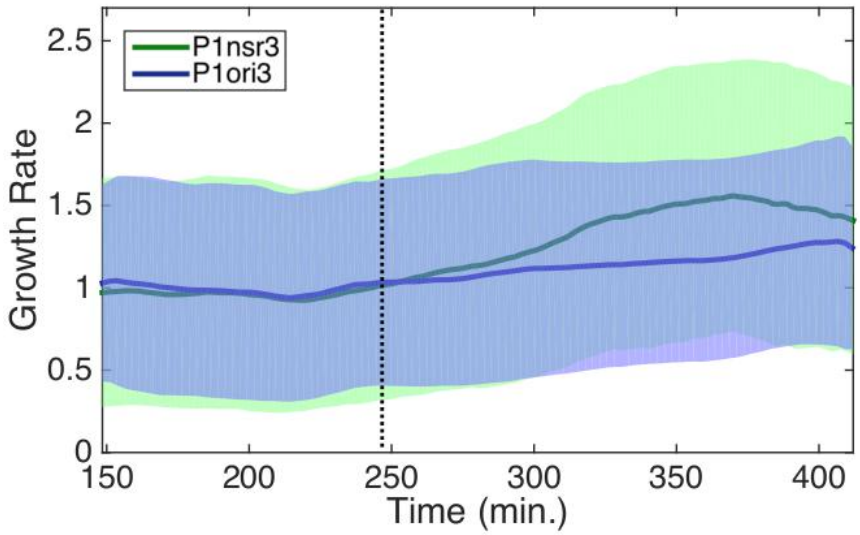

Figure 13.7.: Upshift experiment of the cell average growth rate as a function of time, for P1*ori*3 (blue) and P1*nsr*3 (green) strains. Solid lines and shaded areas represent the average and the standard deviation over 3000-4000 cells. Data are normalized to the average value before the upshift. The dotted line approximately represents the time when the rich medium reached the chamber.

Moreover, the higher repression activity of H-NS in the P1*nsr*3 strain has been observed in terms of another feature of the bacterial cells. Figure 13.8 illustrates two example channels filled up with cells of P1*ori*3 (a) and P1*nsr*3 (b): the overall fluorescence signal is distributed in a completely different manner in the two cases, namely P1*nsr*3 has a much more pronounced heterogeneity. In the particular example of figure 13.8(b) two population are distinguishable. It should be pointed out that this event did not occur in each channel of P1*nsr*3 experiments and sometimes it has been observed for P1*ori*3 as well, but there was a definitely higher tendency to find this heterogeneity in *nsr*3 strain. This is just a preliminary evaluation but it already corroborates the hypothesis of a potential strong influence of H-NS protein on gene regulatory activity: in some cells the H-NS-regulated promoter activity is almost entirely repressed.

A second strategy to analyse the gene regulatory role of H-NS was the measurement of gene expression in a condition in which the protein is expected to be even more effective. The activity of P1 short promoter was studied again in the H-NS-sensitive region, in *nsr*3 position, but the KanR cassette was not included. Indeed, as described in chapter 10, the transcription of *Kan* gene seems to protect the promoter from H-NS activity [236, 237]. The data presented in section 10.3 confirmed this hypothesis and the gene expression level of

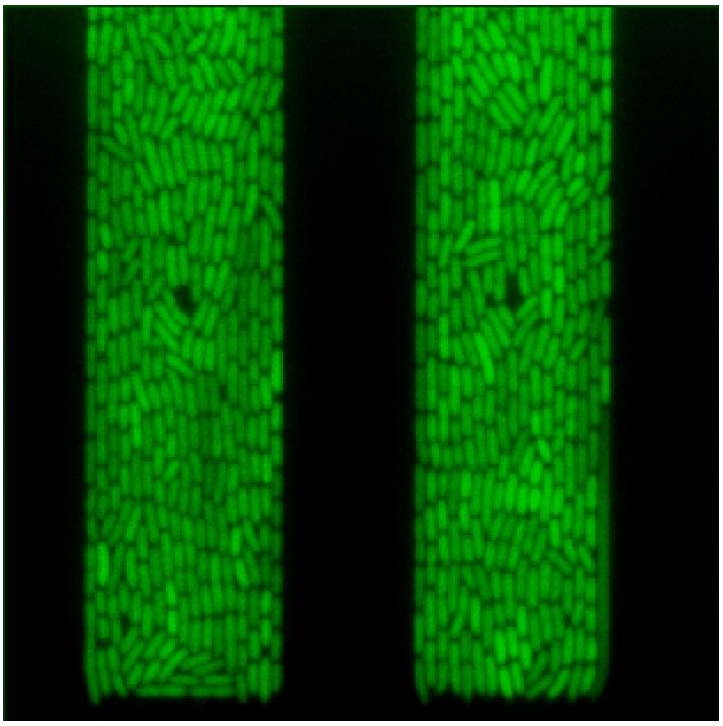

(a)

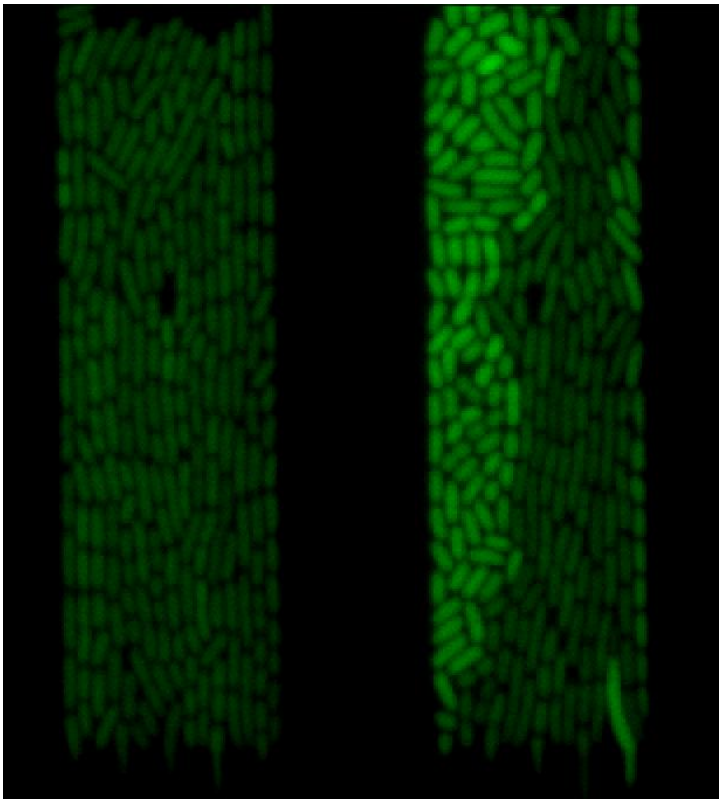

(b)

Figure 13.8.: Representative field of view of a fluorescence image for P1*ori*3**(a)**and P1*nsr*3**(b)** cells. Snapshots taken after the upshift stimulus (0.4% Glu +0.5% CAA). The size of the channels is $60 \times 15\,\mu m$.

P1*nsr*3(NoKan) was slightly lower than the equivalent strain including KanR cassette, which in turn exhibited a lower activity compared to the control strain P1*ori*3. I show the comparison of all the three strains in figure 13.9(a), where the gradual decrease of the fluorescence upshift increment can be noticed in detail, from P1*ori*3 down to P1*nsr*3(NoKan). Since the strain lacking of KanR showed an overshoot right after the upshift (page 143), I preferred to compare the fluorescence values after a longer period, when cells had the time to adapt to the nutrient stimulus and the promoter activity is stable, see figure 13.9(b). In fact, after more than 9 hours the cell fluorescence signal is very stable and the three strains can be distinguished very clearly: the gene expression of P1*nsr*3(NoKan) in response to the upshift was $\approx$ 17% lower than P1*nsr*3 and even $\approx$ 44% lower than P1*ori*3. Similar differences have been observed for the GFP concentration (see figure E.4 in supplementary material). Therefore, the promoter without the "transcriptional protection" of KanR turned out to be, as expected, in the most sensitive condition to H-NS activity. H-NS protein proved to be crucial for gene expression and it almost halved promoter activity.

The overshoot observed in absence of KanR is probably related to cell adaptation. It can be speculated that if H-NS repression activity is strong, such as in P1*nsr*3(NoKan) strain, the cells need more time to adapt to the nutrient upshift and exhibit a high gene expression activity before stabilising definitively.

As regards the size of the cells, I compared the growth rate of the three strains. P1*ori*3 cells are still those ones growing less and slower, for the same reason explained before: a high gene expression activity needs a lot of energy of the cell, that is no longer available to be used for size growth. The lack of KanR did not induce any substantial effect, not comparable with those related to gene expression, there is only a slight delay in responding to the upshift, see figure 13.10.

13.2.2 *The role of hns gene*

In the previous section I quantified the regulatory activity of H-NS by inserting the P1 short promoter in genomic positions differently affected by the protein. In this paragraph H-NS effects are assessed by manipulating the *hns* gene directly involved in the protein transcription. This approach enabled to measure how H-NS affects the global behaviour of the cell, not only the gene expression, because bacteria lacking of such a crucial regulator are expected to have several issues related to cell physiology. I measured the promoter activity in *ori*3 position. The strains compared are P1*ori*3, the control strain, and P1*ori*3-Δ*hns*, the same strain with an *hns* gene knockout.

The gene expression experiments presented in section 10.4 did not show the expected results, namely a higher promoter activity without

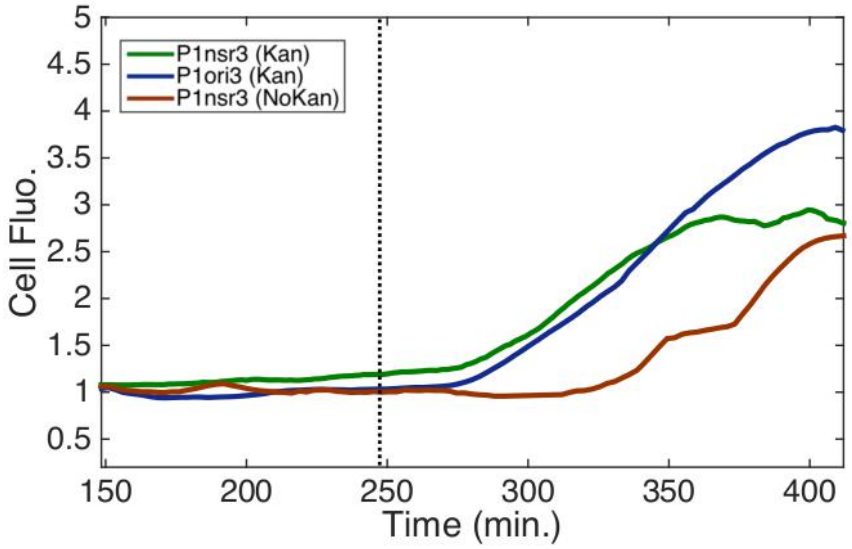

(a)

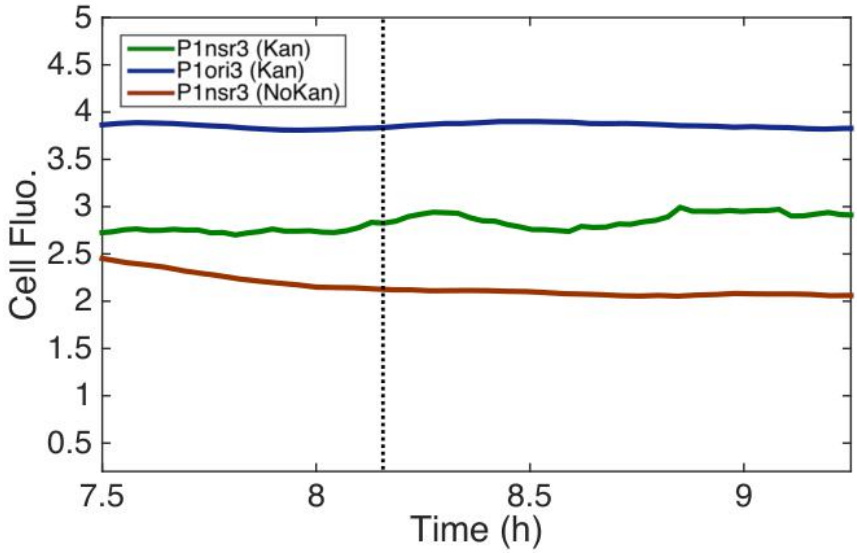

(b)

Figure 13.9.: Comparative upshift experiments between P1*ori*3, P1*nsr*3 and P1*nsr*3(NoKan) **(a)** Cell average fluorescence as a function of time for P1*ori*3 (blue), P1*nsr*3 (green) and P1*nsr*3(NoKan) (red). Data calculated from an average over 3000-4000 cells and normalized to the average value before the upshift. The dotted line approximately represents the time when the rich medium reached the chamber.
(b) Saturation values of cell average fluorescence after the upshift. Data are normalized to the average value before the upshift, shown in (a).

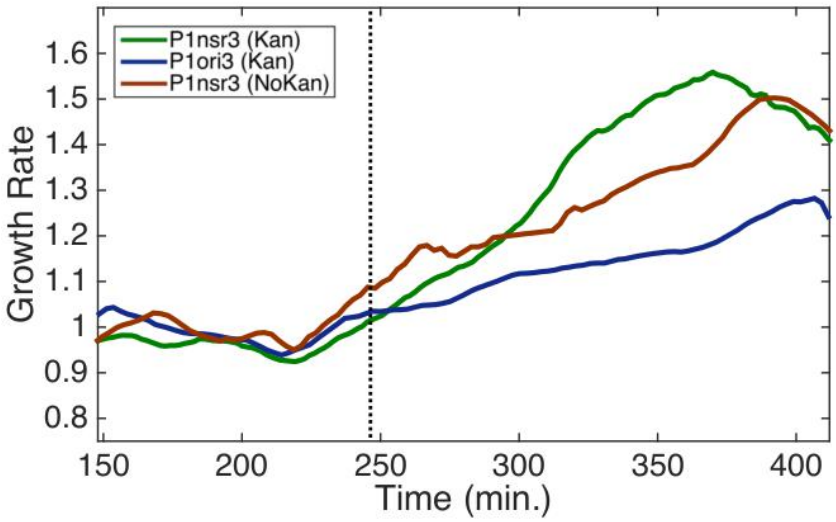

Figure 13.10.: Upshift experiment of the cell average growth rate as a function of time, for P1*ori*3 (blue), P1*nsr*3 (green) and P1*nsr*3(NoKan) (red) strains. Data calculated from an average over 3000-4000 cells and normalized to the average value before the upshift. The dotted line approximately represents the time when the rich medium reached the chamber.

the repression by H-NS proteins. The fluorescence and GFP concentration showed an increment after the upshift very similar in the two strains. It should be also taken into account the experimental error of the exact point at which the upshift of P1*ori*3-Δ*hns* started, previously described. This uncertainty has negatively affected the analysis and prevented a reliable measurement of the growth rate. Nevertheless, it is clear that the difference, if any, is very small and not significant.

An interesting result was however revealed at longer times, because P1*ori*3 showed a stable activity over several hours, as above described, while the *hns* deletion strain exhibited a quick drop of fluorescence 1.5 - 2 hours after the conclusion of the upshift, see figure 13.11. In these plots I reported the last part of the upshift experiments of figure 10.6, thus emphasizing the gene expression drop of P1*ori*3-Δ*hns* at the end: the cell average fluorescence decreased of about 46%, the GFP concentration of $\approx$ 22%. The curious thing is that the average size of cells showed a reduction as well, see figure E.5. Overall, these results suggest that the global physiology of the cell suffers from the lack of H-NS proteins regulating the nucleoid chromosome organisation and the gene expression activity. It can be speculated that these "sick" cells are not able to properly bear a nutrient stimulus and sustain for long periods the activity levels acquired after the upshift, as the healthy cells.

This conclusion is corroborated by a qualitative analysis of figure 13.13, where two examples channels containing P1*ori*3 (a) and

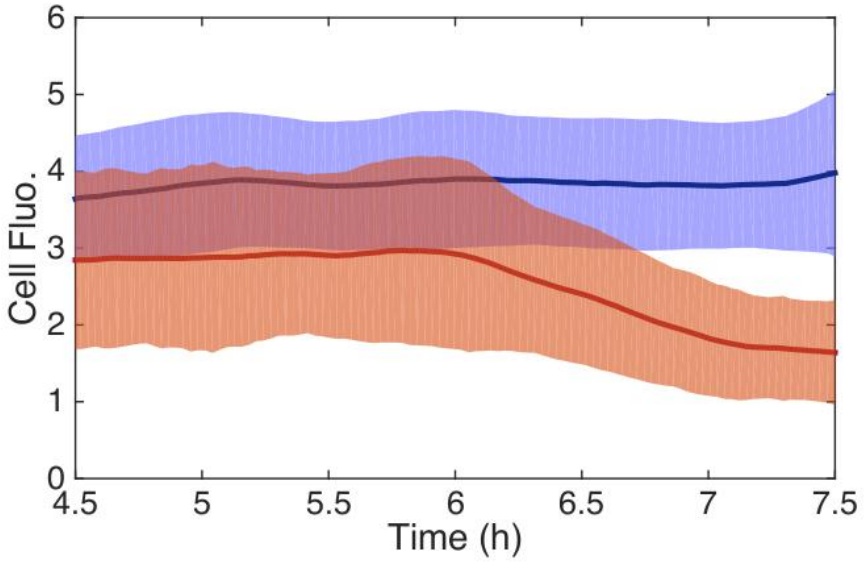

(a)

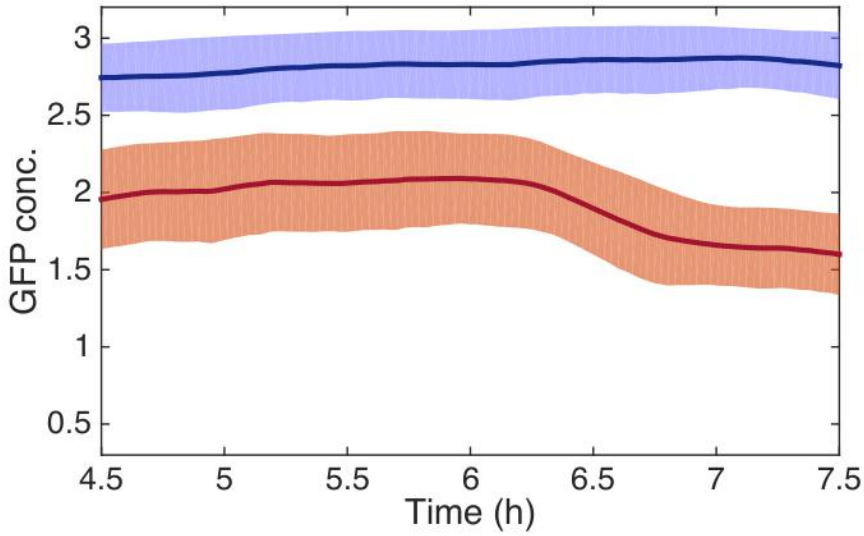

(b)

Figure 13.11.: Average values of cell fluorescence **(a)** and GFP concentration **(b)** after the conclusion of the upshift, for P1*ori*3 (blue) and P1*ori*3-Δ*hns* (red). Data are normalized to the average value before the upshift, shown in figure 10.6. Solid lines and shaded areas represent the average and the standard deviation over 3000-3500 cells.

P1*ori*3-Δ*hns* (b) cells are reported. Many of the bacterial cells of the gene knockout strain have an unusual and circular shape, different from the typical rod-like shape of *E. Coli* bacteria. These cells have likely developed a cell wall synthesis mutation, inducing an overgrowth. These kind of cell mutations were almost never observed in other strains, whereas in the *hns* knockout strain similar events were rare but they occurred in roughly one every fifteen channels.

A possible strategy to separately analyse these mutated cells is to calculate the aspect ratio, indeed the rod-like shape bacteria should be surely more than twice longer than their width, while the aspect ratio of the mutated round bacteria should be closer to 1. The resulting calculation (cut-off= 2) identified two distinct populations, one with an expected aspect ratio between 3.5 and 4 and the other one ≈ 1.5, see figure 13.12. The dotted line in the plot is again representing the upshift time.

It is remarkable that the "round" cells did not change their aspect ratio as a response to the uspshift, because their length did not increase significantly, see figure 13.14(a) (in supplementary material curves related to width and area are also included). Regarding the gene expression, figure 13.14(b), the GFP concentration of the mutated cells was lower as expected, also because these cells are bigger (figure E.6(b)). However, the upshift increment was proportionally similar to that one of normal cells, this means that the overall gene expression activity of the round cells is lower, but the cell adaptation to the nutrient stimulus is likely similar.

In conclusion, I summarised the main results obtained during the single-cell upshift experiments in table 13.1. I reported increment factors as response to the upshift stimulus.

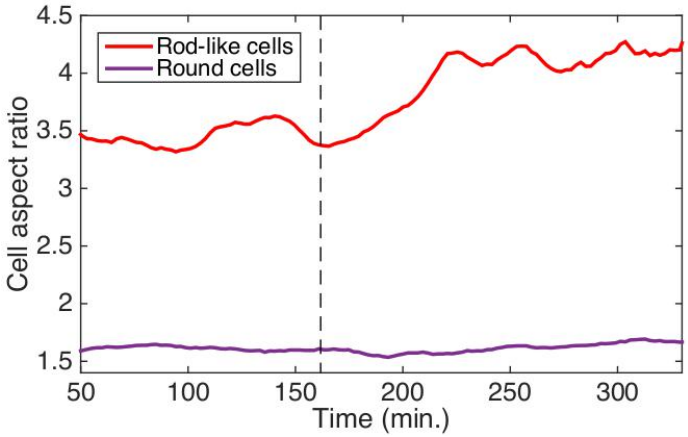

Figure 13.12.: Aspect ratio of the cells during the upshift experiment reported in figure 13.13. Comparison between typical rod-like bacteria of P1*ori*3 strain (red) and mutated round bacteria of P1*ori*3-Δ*hns* (purple). The dotted line represents the time.

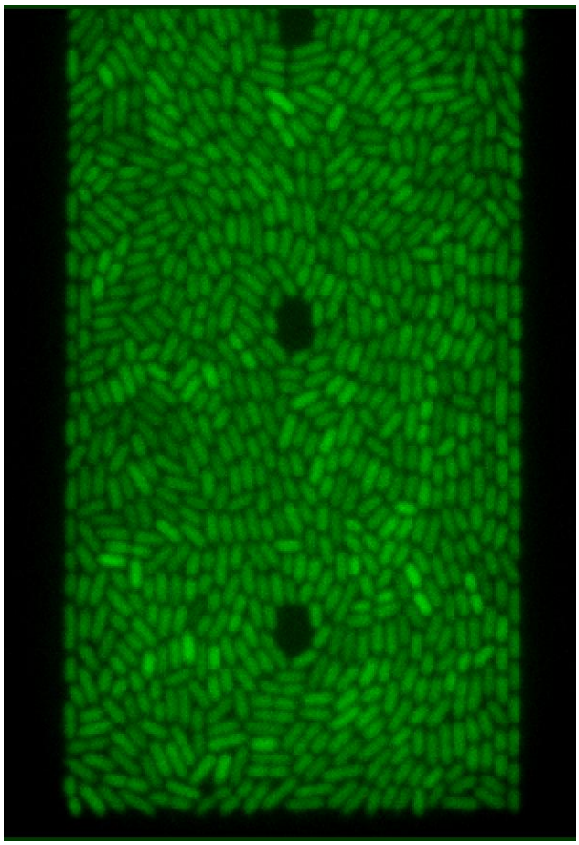

(a)

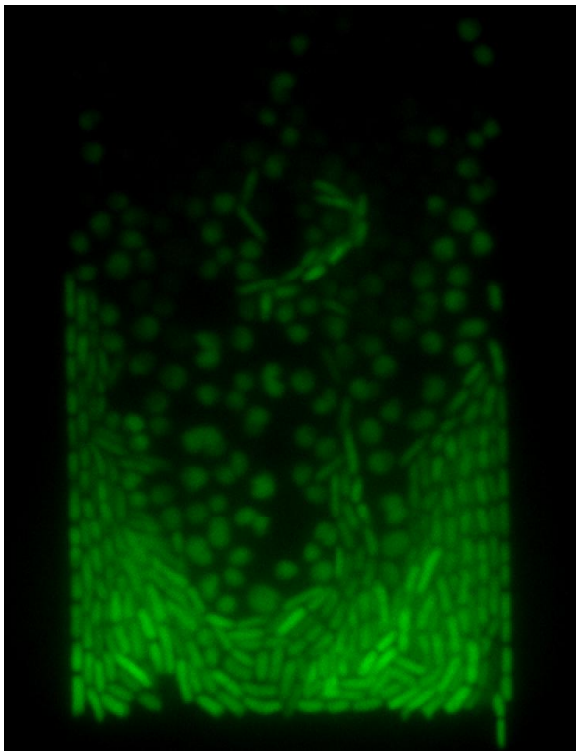

(b)

Figure 13.13.: Representative field of view of a fluorescence image for P1*ori*3**(a)**and P1*ori*3-Δ*hns***(b)** cells. Snapshots taken before the upshift stimulus (0.4% Glu). The size of the channels is $60 \times 30\ \mu m$.

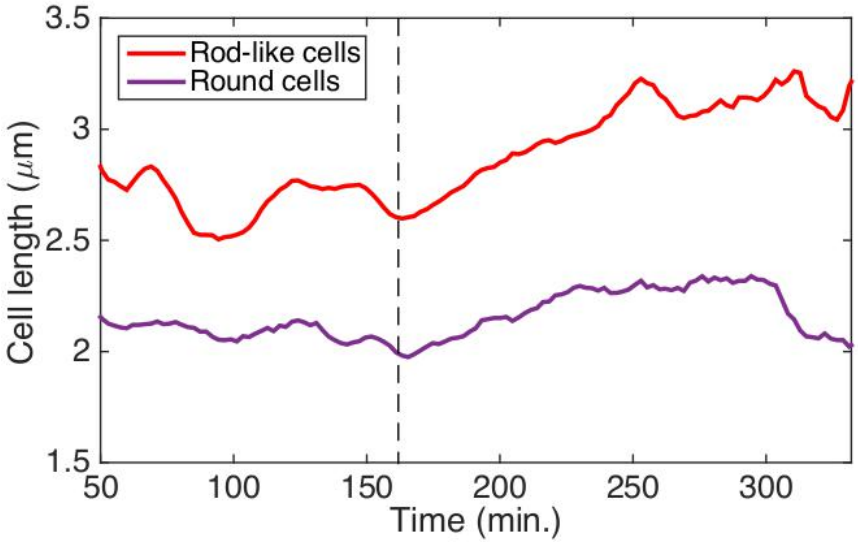

(a)

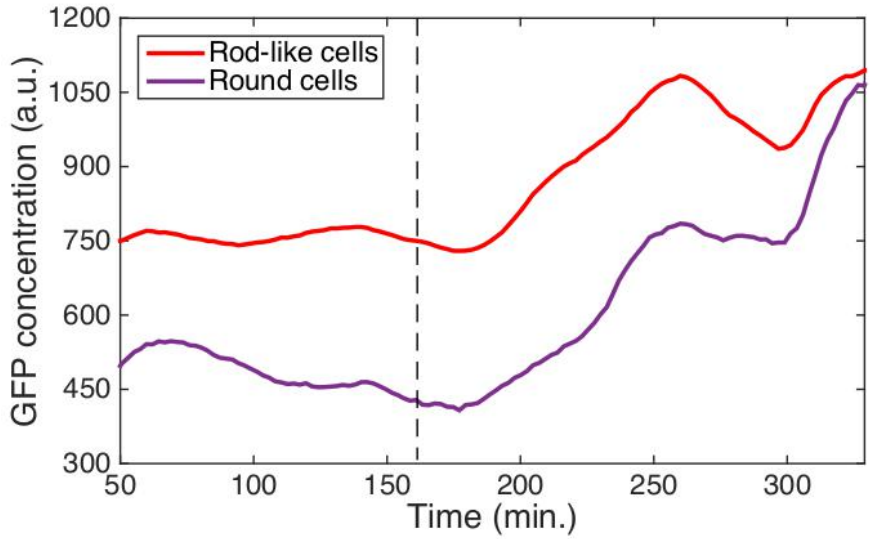

(b)

Figure 13.14.: Size and gene expression activity of the cells during the upshift experiment reported in figure 13.13. Comparison of cell length **(a)** and GFP concentration **(b)** between typical rod-like bacteria of P1*ori*3 strain (red) and mutated round bacteria of P1*ori*3-Δ*hns* (purple). The dotted line approximately represents the time when the rich medium reached the flow chamber.

Strain	Increment factor		
	Fluorescence	**GFP conc.**	**Area**
P1*ori*3 (Kan)	3.7	2.6	1.4
P1*nsr*3 (Kan)	2.5	1.6	1.6
P1*nsr*3 (NoKan)	2.1	1.5	1.4
P1*ori*3-Δ*hns*	~ 2.1	~ 1.9	1.1

Table 13.1.: Summary table of the results achieved from upshift experiments. The increment factor after the upshift related to the cell fluorescence, the GFP concentration, and the cell area are reported for each of the four investigated bacterial strains. These values are taken at saturation points (see text).

CONCLUSION

In this Ph.D. thesis work I used single-molecule and single-cell techniques to quantitatively study peculiar properties of the DNA double-helical structure, as well as to monitor stochastic processes of individual bacteria. As above mentioned, conventional methods cannot explore in depth all the features of DNA molecules or bacterial cells, because bulk experiments measure an ensemble of objects and average the collected information, thus missing crucial details.

Specifically, I investigated three general topics from different perspectives and by means of complementary techniques. The first topic addressed the structural polymorphism of DNA, namely the propensity of DNA to adopt alternative structures under specific conditions. I used two approaches to study the DNA structural polymorphism: a chemical modification of a nucleotide composing the helix, and the application of extreme topological conditions.

The second topic was the nanomechanics of DNA molecules interacting with small ligands, such as drugs or proteins. The studied drugs were anticancer platinum-based compounds with different nanomechanical effects on DNA. On the other hand, I investigated the binding mechanism between DNA and a nucleoid- associated protein, the H-NS protein. I firstly explored the nanomechanical effects of the interactions of the protein with DNA, and then I focused on its role in organising and compacting DNA supercoiled structures.

Indeed, the last theme concerns precisely the analysis of the dual role of H-NS. This protein turned out to have two biological functions: it is involved in a structural role for the nucleoid organisation of prokaryotic cells, similarly to the histones in eukaryotes. Secondly, H-NS is a crucial gene regulator widely reported in literature, and in particular it has a strong repression activity.

Chapters 6-7 and chapter 11 describe the experiments and analyse the related results concerning the structural polymorphism, respectively.

In chapter 6 has been shown that the diaminopurine nucleotide analogue (DAP) not only stabilises DAP-T pairs compared to A-T pairs, but significantly modifies dsDNA mechanics and favors conformational changes as well, particularly towards A-DNA and S-DNA structures. The additional amino group on its 2'-carbon participates in a third hydrogen bond when base paired with thymine and thus raises the melting temperature. On the other hand, the additional amine extends into the minor-groove of the B-DNA helix, decreasing

the compressibility of the groove by steric hindrance and reducing bending flexibility. Through AFM imaging and force spectroscopy using a magnetic tweezer, I showed that DAP substitution biases DNA molecules to adopt an A-like-DNA helix at zero applied tension and resists flexural bending at low-to-moderate tension (< 10 pN), yet also decreases the overstretching force threshold from roughly 62 pN to 54 pN. From an energetics perspective, the steric clashes of DAP's extra amine penalize entropic bends (increasing the persistence length) but, perhaps paradoxically, also raises the conformational free energy of the B-form helix, facilitating axial extension and initiating the B-to-S transition at a lower tension.

Chapter 7 described the behaviour of DNA under extremely high supercoiling regimes. These conditions favoured two specific structural transition: the left-handed DNA helix, named L-DNA, and the lesser-known Pauling-like structure called P-DNA. The analysis was performed in terms of the characteristic force of the transition (equation 3.16). The parameter F_{char} measures the situation where a DNA molecule has an equal probability to be in the zero-extension plectonemic state or in the extended denatured state. The resulting values of F_{char} as a function of the superhelical density σ revealed that the structural transitions for negative or positive supercoiling are very different. The increasing fraction of L-DNA decreased the effective persistence length of the molecule, thus leading to a greater entropic contribution and requiring an higher F_{char} for higher σ. On the contrary, the characteristic force was roughly constant for positive supercoiling. The reason is that in the explored range of forces, below 20 pN, the P-DNA helix is formed only in the plectonemic phase and the extended state is still the conventional B-form with unchanged persistence length. As regards the L-DNA structure, an interesting sequence dependence was observed: the increment of GC content decreased B-DNA stability, despite the additional hydrogen bond. Finally, an extension of the denaturation model presented in section 3.5 was developed to describe the experimental F_{char} values of all three different GC-content sequences: the good agreement between data and model suggests that this simple model describes the crucial ingredients necessary to describe fairly well DNA stability.

The nanomechanics of DNA-ligands interactions is discussed in chapter 12, where the results of chapter 8 and a part of the measurements of chapter 9 are analysed.

Chapter 8 explored the effects of antitumor drugs on DNA nanomechanics and on the structural stability of the double helix. The DNA extension was affected only by the biggest compound, BBR3464, and the bending rigidity reduction confirmed the higher influence of this drug on DNA properties. This is likely due to the ability of the flexible structure of BBR3464 to form long range DNA adducts and, in

addition, to the high positive charge of this drug. The DNA extension and its bending rigidity were quantified in terms of the contour length L_0 and the persistence length L_P respectively, as obtained from the WLC fit equation. The results of the second part of the work, namely the measurement of the mechanical denaturation of DNA-drugs complexes, allowed me to evaluate the resistance of DNA to open initial melting bubbles, complementing the information regarding the thermal melting transition. The single-molecule analysis indicates the presence of destabilized DNA regions, whereas the bulk measurements show an increment of the average stability. Simultaneously, the decrease in the starting points of the melting transitions of the transplatinated drugs agrees with the single-molecule observations. Small values of the denaturation energy α or the relevant T_s decrement are indicators of an action of the drug on DNA. These results suggest that a combination of single-molecule and bulk biophysical methods could represent a starting point for guiding the design and development of more efficient platinum-based drugs.

In section 12.2 I analysed in detail the mechanical interactions between the H-NS protein and DNA described in chapter 12. The force spectroscopy experiments carried out with the magnetic tweezers revealed an important hysteresis of the H-NS binding mechanism: the force necessary to unfold the DNA-protein complex was significantly higher than the force to form this complex. I compared my data with the experimental findings described in a study by Abbondanzieri at al. on Dps, another NAP similarly inducing DNA condensation (page 17). The quantitative analysis of the hysteresis areas confirmed that H-NS has a high affinity for DNA binding, similarly to Dps (figures 12.5-12.6), but the concentration dependence behaviours are dramatically different (figures 12.3-12.4). This difference suggests that an alternative and new model describing the dynamics of the DNA-protein binding mechanism is needed. The reliability of these experiments on DNA-H-NS complexes was verified by evaluating the most probable binding domains of H-NS. I systematically measured the extension of the DNA loops formed by H-NS and compared the results with the general consensus sequence reported in literature: despite experimental data are noisier, there is a reasonable agreement with the main populations predicted by the consensus sequence. As expected, my experiments confirmed that H-NS stabilises the plectonemic supercoiled structures of DNA.

Finally, chapter 13 dealt with the dual role of H-NS. It includes both the analysis of the single-molecule experiments that investigated the structural role of the protein (chapter 9) and the single-cell measurements that verified the regulatory activity of H-NS (chapter 10).

The analysis of the kinetics of H-NS binding mechanism showed a more gradual and step-wise process during the unfolding com-

pared to the bridging (folding). This experimental finding strongly suggested that the protein stabilises highly supercoiled and complex DNA structures, in order to promote the compaction of the chromosome in the cell. The critical forces of bridging and unfolding turned out to be constant with the protein concentration, particularly $F_{bridg} \approx 0.15\,pN$ and F_{unf} was roughly four times higher, $\approx 0.60\,pN$. The explanation is that DNA-H-NS interaction is a one-to-one interaction, an individual H-NS dimer is sufficient to form a DNA loop. After having analysed the condensation of DNA in presence of the crowding agent alone (PEG1500), I analysed the combined effect of H-NS and PEG: preliminary results suggest that a cooperative effect is present and that the macromolecular crowding conditions typical of cellular environment effectively help the protein activity. The hypothesis of this synergistic effect could be that the crowding agent makes H-NS more "sticky" to itself and to the DNA or alternatively it enhance the self-attracting interactions of DNA.

The regulatory role of H-NS protein was explored by time-lapse microscopy experiments that enabled to measure in real time the fluorescence of individual cells related to the activity of an H-NS-regulated promoter. The strategy has been to evaluate the promoter activity in conditions differently affected by H-NS activity. I observed that the gene expression was significantly lower when the promoter was inserted within a large H-NS binding domain. The difference was larger than 40% when a trascriptional protection is removed (KanR cassette), which enhances the potential effect of H-NS and confirms the strong influence of this protein on gene silencing functions. Additionally, a higher heterogeneity was identified (figure 13.8), suggesting that H-NS can almost entirely repress the promoter activity. In the last part of the study an *hns* gene knockout was studied and confirmed that H-NS affects the global physiology of the bacteria. Indeed, the cells lacking of the protein cannot sustain the upshift nutrient stimulus for long periods such as the normal cells. The absence of H-NS promoted cell mutations as well, as reported in figure 13.13.

ACKNOWLEDGEMENTS

First, I wish to thank my thesis reviewers for their comprehensive reports and useful comments. They helped me to improve the general quality of this work.

Ora preferisco passare all'italiano per i ringraziamenti meno formali verso i colleghi, tutti connazionali.
Vorrei innanzitutto ringraziare i miei capi: Cecco e Dome. Li ringrazio per avermi guidato e permesso di crescere in questo percorso di formazione nel mondo della ricerca, coinvolgendomi sempre in tutte le fasi dell'attività e lasciandomi spesso una grande libertà decisionale. La loro pazienza e comprensione nei miei confronti non possono non essere menzionate, soprattutto nell'ultimo periodo! Un dottorando tanto ambizioso quanto testardo come il sottoscritto metterebbe a dura prova chiunque, quindi grazie. Inoltre mi hanno continuamente incentivato e dato la possibilità di fare esperienze all'estero, dalle summer school, alle conferenze, ai periodi di ricerca. Di questo sarò sempre molto grato loro, in quanto hanno costituito un bagaglio di esperienze uniche e indimenticabili, dal punto di vista umano e professionale. Grazie Cecco anche per la tua domanda del giorno, sarà un rito che mi mancherà molto.

Ringrazio anche Vale e Robi, per le misure di AFM che hanno reso più completi diversi progetti di ricerca che ho seguito, permettendo agli esperimenti di magnetic tweezers di essere indirizzati da quelli AFM e viceversa. Grazie a Vale per essersi prestata come biologa in un gruppo di fisici ignoranti in tale materia e aver preparato la maggioranza dei campioni di DNA che ho analizzato, senza il suo aiuto i miei esperimenti non sarebbero stati possibili. E grazie per la sua capacità di esprimere il proprio pensiero direttamente, senza troppi giri di parole (qualcuno doveva pur farlo no?). Grazie mille a Robi, un'ottima collega di dottorato: divertente, spontanea, e sempre sul pezzo in laboratorio, in definitiva una perfetta compagna di disavventure. E grazie per avermi fatto da segretaria per le varie faccende burocratiche nelle quali tendevo a perdermi!

Grazie Eli e Gu, i fidi tesisti dediti agli esperimenti di magnetic tweezers con il sottoscritto, ore e ore passate nello stesso laboratorio, come potevo non citarvi. Un ringraziamento speciale ad Eli, buona parte degli esperimenti single-molecule sull'interazione DNA-H-NS è stata possibile grazie al suo aiuto, un braccio destro indispensabile: rapida nell'apprendere e precisa, la tesista che ogni dottorando dovrebbe avere in dotazione. Grazie a Gu, per le cazzate che ci siamo detti, con freddure e doppi sensi ovunque. Abbiamo condiviso mo-

menti di intense riflessioni per gli esperimenti ad alto superavvolgimento, misure che poi hai ereditato e proseguito egregiamente.

Ringrazio Luca, il miglior confidente che abbia avuto nel laboratorio, con la straordinaria abilità di spaziare le discussioni dai peggiori turpiloqui fino alle coltissime disquisizioni di natura scientifica e/o politica, con tanto di arguti paralleli con l'epoca romana. Grazie Luca perché hai sempre mostrato molto interesse per il mio dottorato: il metterti sul mio stesso piano ti ha permesso di immedesimarti al meglio nella mia posizione e di capirmi al volo, qualità non comune.

Grazie a Cla, la nostra ufficiale e vera biologa del gruppo, che ha ereditato con successo il lavoro di Vale. Ti sono molto grato per i campioni che hai preparato, mestiere verso il quale sono sempre stato reticente, come hai più volte constatato. Grazie anche per il dispendioso, seppur poco fruttuoso per ora, lavoro sulla purificazione dell'H-NS, sappi che l'ho notato e apprezzato, sebbene possa non darne l'idea. Devo ringraziare anche Enrico, il primo degli adepti di Cla e nuovo tassello bio del gruppo. Purtroppo le tempistiche ci sono state sfavorevoli bel biondo, è stato un rapporto breve ma intenso. Ora che hai ereditato il progetto sul G4 che altro dire... good luck!

E infine grazie Natalia, per il suo essenziale supporto informatico. Ti ringrazio anche per le discussioni politiche più o meno accese avute ogni tanto, ma sempre con garbo. La tua capacità di trasmettere pace e serenità sarà per me un utile esempio in futuro.

Passando ai ringraziamenti oltre i confini nazionali...

Ringrazio molto Pietro che mi ha ospitato nel suo laboratorio in una piacevole città come Cambridge. Innanzitutto mi ha colpito la sua onniscienza nel proprio campo, sempre sul pezzo nei più disparati argomenti degli interessanti group meeting. Nonostante i suoi mille impegni accademici lo rendano un'entità quasi evanescente, mostra il suo interesse per il gruppo organizzando cene, barbecue, group retreat ecc ecc.. e questo funziona bene. Il suo gruppo è ricco di persone tanto diverse tra loro quanto speciali, che hanno reso quel periodo di più di sette mesi un ricordo indelebile all'interno del mio percorso accademico, è stato veramente un periodo unico.
Grazie a Mia e Michal per avermi insegnato e inizialmente seguito per gli esperimenti single-cell su batteri.

Ringrazio Marco, il collaboratore teorico, quello che riesce sempre a vedere più lontano, con il suo intuito e i suoi voli pindarici... la bellezza di fare modelli teorici e non esperimenti! Grazie Marco per la tua affabilità e l'ottima indole nel fare networking, prerogativa essenziale se si vuole fare ricerca di buon livello, ma che aiuta anche a crescere dal punto di vista umano, perché ci si confronta con pareri diversi. Eśtato un prezioso insegnamento per me. Ti ringrazio inoltre per le conferenze che mi hai spinto a frequentare, ambienti stimolanti.

Soprattutto a Parigi, con quelle partite di ping pong fino all'una di notte contro quei simpatici e ostinati giapponesi.

Grazie anche a Bianca, l'indispensabile controparte bio del progetto di ricerca inerente l'H-NS. La persona che in ogni confronto via Skype o di persona serviva a riportare la banda di fisici con i piedi per terra, a fare i conti con la realtà, ovverosia la biologia. Ti ringrazio Bianca, sei stata una persona squisita e una maestra paziente, soprattutto mentre ero a Cambridge e brancolavo nel buio tra i batteri. Un sentito grazie anche alla tua discepola, Ilaria, con la quale ho avuto modo di consolarmi condividendo le innumerevoli disavventure degli esperimenti single-cell: prima a Cambridge, poi in Sardegna e infine a Parigi.

In conclusione, i ringraziamenti più ovvi, quelli alla mia famiglia: mamma, papà e Lori. Un grazie perché otto anni di università non sono mica uno scherzo eh.. ci ho passato un terzo della mia vita! E per tutti questi anni ho sempre ricevuto il sostegno e la fiducia necessari per proseguire con (quasi) sufficiente serenità il mio percorso. Nel mio caso, a dire il vero, al fiducia di mia mamma e di mio papà nei miei confronti è stata anche fin troppa, maggiore di quella che io stesso ho nutrito a tratti, il che ha contribuito a rendermi il pallone gonfiato che sono ora, sono pur sempre laureato in fisica, mica in scienze delle merendine!

E the very last grazie è per la mia ragazza, Francesca, la mia paziente ragazza. Lei proprio non può sopportare la fisica, anzi, a breve smetterà di sopportare anche chi studia o ha studiato la fisica. Una cosa però ora è certa: la fine di questo dottorato è una grossa soddisfazione non solo per me, ma anche per lei, perché finalmente ce ne siamo liberati! E ora, freschi di una recente convivenza, siamo pronti a raccogliere tutti i frutti di questi anni, e sono certo che ci attendono sorprese anche più importanti nel prossimo futuro...

Part V

SUPPLEMENTARY MATERIAL

A

MATERIALS & METHODS

A.1 PDMS PREPARATION PROTOCOL

1. Weigh PDMS and 1/10 of the curing agent, required to create cross-links.
2. Mix quickly until you get a cloudy solution.
3. Put the PDMS solution in a desiccator to create vacuum and push air bubbles out.
4. Leave for about 20 minutes until all bubbles are gone.
5. Gently pour the PDMS on the mould wafer avoiding to create bubbles.
6. Put it in the fridge for an hour if there are still some bubbles.
7. Bake at 60°C for a couple of hours

A.2 STRAINS FOR SINGLE-CELL EXPERIMENTS

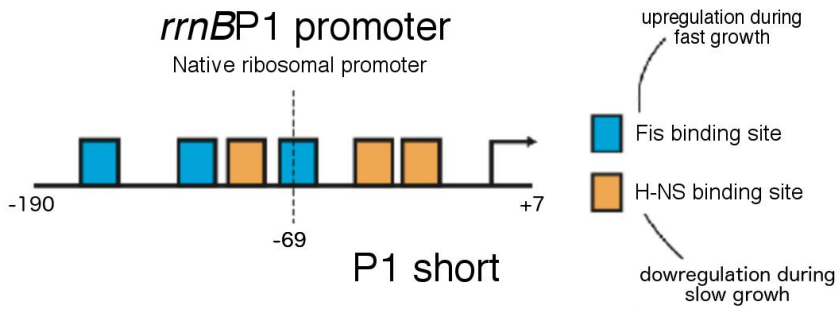

Figure A.1.: Schematic of the *rrnB*P1 promoter in its full-length, including the shortened P1short version (on the right of dotted line). The binding sites of Fis and H-NS proteins are reported: the P1 short promoter contains only two binding sites of H-NS and no one of Fis.

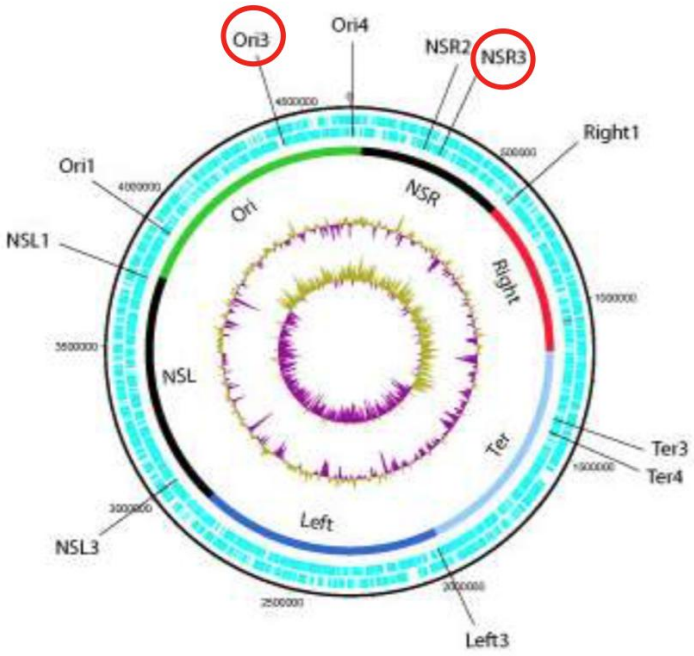

Figure A.2.: Macrodomain organization of the *E. coli* genome as defined in [**?**]. The red circles indicate the two positions of the insertion of P1 short promoter in the strains studied in this thesis. The %GC and the GC skew ($\frac{GC}{G+C}$) are also reported. Figure adapted from [**?**].

A.3 GROWTH MEDIA

Stock reagent solutions:

- 5X M9 salts
- 50X complementary salts
- 20% glucose
- 10 mg/ml BSA
- 10% CAA

Slow growth medium (M9 + 0.4% Glu, volume 50 ml):

- 10 ml 5X M9 salts
- 1 ml 50X complementary salts
- 1 ml 20% glucose
- 0.5 ml 10 mg/ml BSA
- 37.5 ml distilled water

Fast growth medium (M9 + 0.4% Glu +0.5% CAA, volume 50 ml):

- 10 ml 5X M9 salts
- 1 ml 50X complementary salts
- 1 ml 20% glucose
- 2.5 ml 10% CAA
- 0.5 ml 10 mg/ml BSA
- 35 ml distilled water

B

DNA ANALOGUE

B.1 DNA SEQUENCES FOR MELTING

40%GC:
tcttttactttcaccagcgtttctgggtgagcaaaaacaggaaggcaaaat
gccgcaaaaaagggaataagggcgacacggaaatgttgaatactcata
ctcttccttttttcaatattattgaagcatttatcagggttattgtctcatgagcgg

54%GC:
ttccggctggctggtttattgctgataaatctggagccggtgagcgtggg
tctcgcggtatcattgcagcactggggccagatggtaagccctcccgta
tcgtagttatctacacgacggggagtcaggcaactatggatgaacgaa

65%GC:
gtttcggcgagaagcaggccattatcgccggcatggcggccgacgcgct
gggctacgtcttgctggcgttcgcgacgcgaggctggatggccttccccatt
atgattcttctcgcttccggcggcatcgggatgcccgcgttgcaggccatgctgt

B.2 THERMAL MELTING EXPERIMENTS

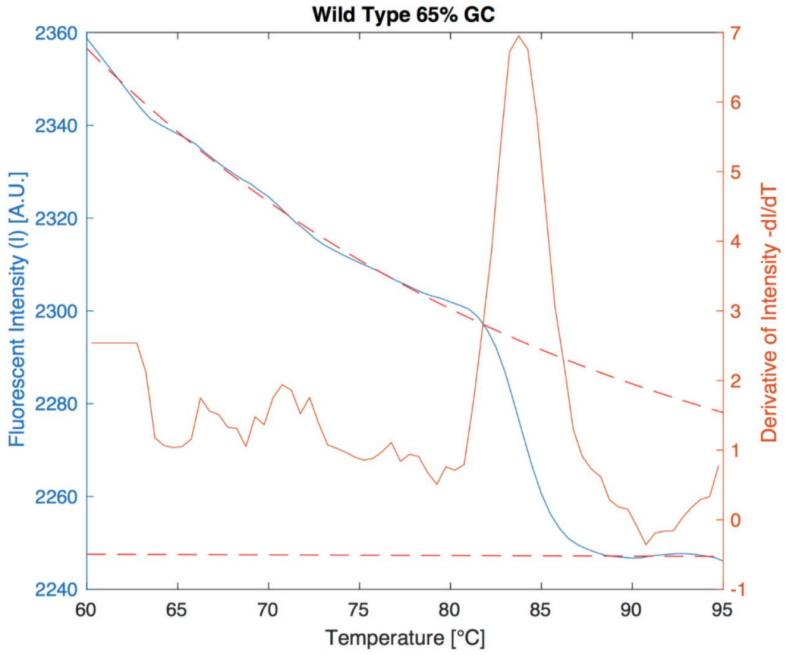

Figure B.1.: Example raw fluorescent melting curve with accompanying background and dye-sensitivity fits (red-dashed).

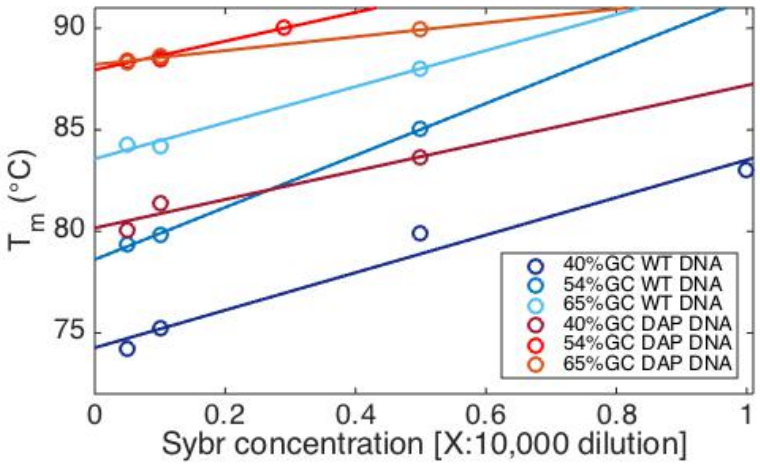

Figure B.2.: Linear projection of melting temperatures. For each molecule, the melting points as a function of Sybr concentration was fit with a line, in order to extrapolate the dye-free melting temperature from the y-intercept of the fit.

C

DNA-DRUGS INTERACTIONS

C.1 L_P TITRATION CURVES OF DNA-DRUG COMPLEXES

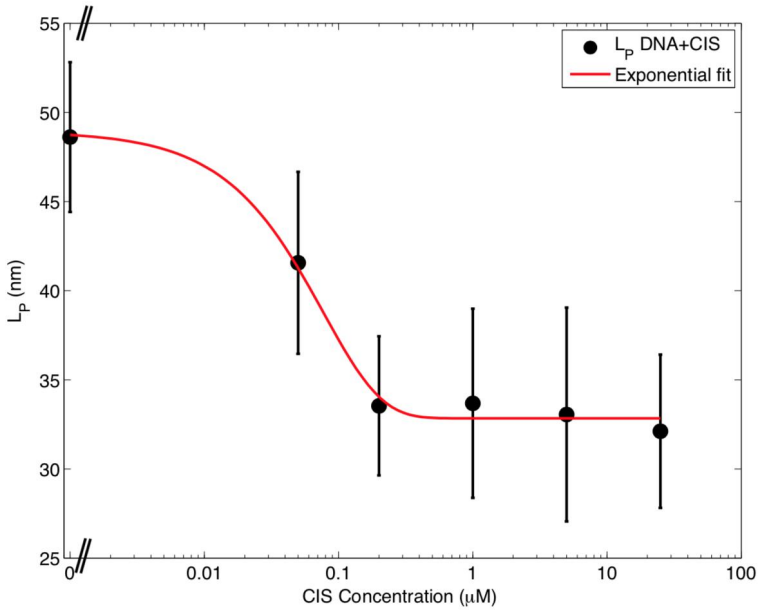

Figure C.1.: Persistence length (L_P) variations with drug concentration for CIS. Black dots are mean values of L_P and error bars are standard deviations, while the red line is the best exponential fit following the equation $a * e^{-b \cdot x} + c$. In this case, c resulted equal to 33 ± 2 nm. Figure from [175].

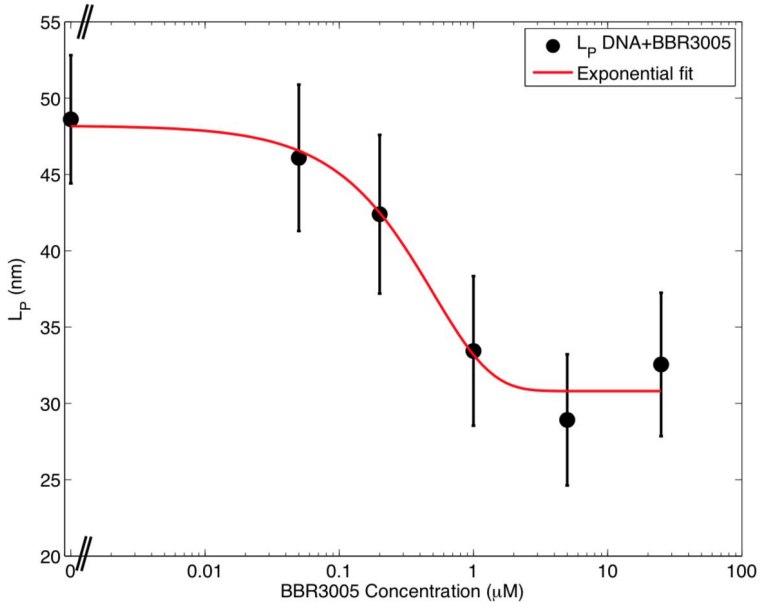

(a)

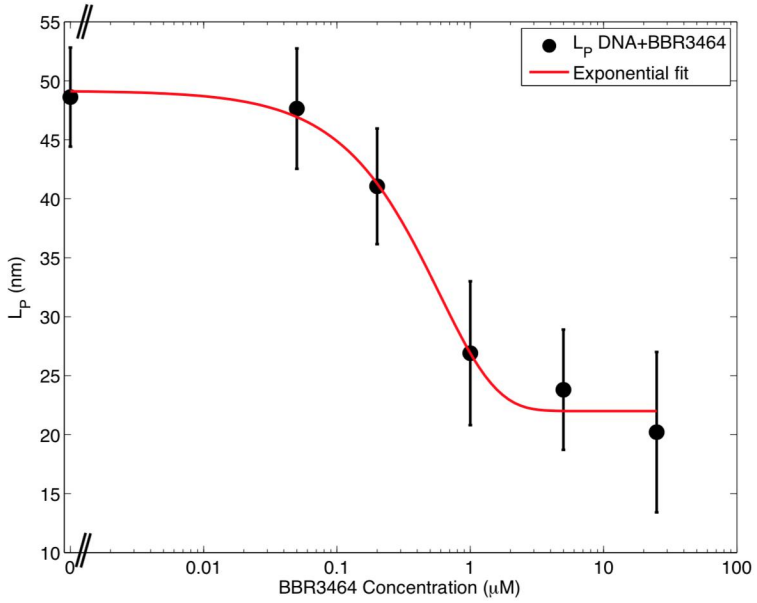

(b)

Figure C.2.: Persistence length (L_P) variations with drug concentration for BBR3005 **(a)** and BBR3464 **(b)**. Black dots are mean values of L_P and error bars are standard deviations, while the red line is the best exponential fit following the equation $a * e^{-b \cdot x} + c$. The values of c are 31 ± 3 and 22 ± 4 nm for BBR3005 and BBR3464 respectively. Figures from [175].

C.2 ADDITIONAL WLC CURVES

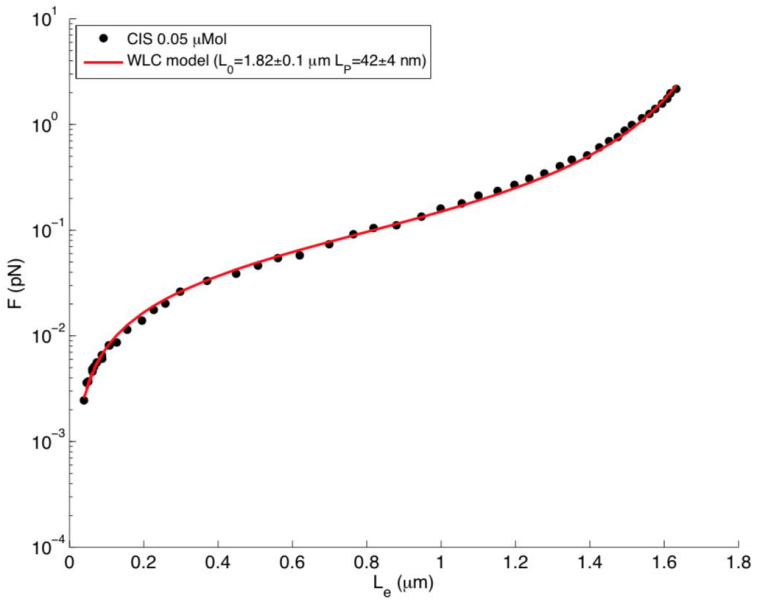

(a)

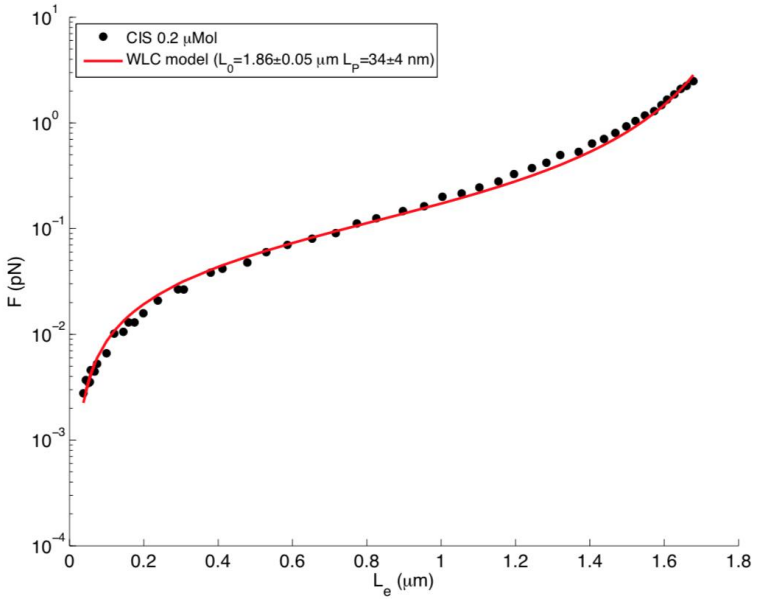

(b)

Figure C.3.: WLC curves of DNA in presence of CIS at 0.05 μM **(a)** and 0.2 μM **(b)**. Black dots are data points, red lines the WLC fits. In the insets concentration of the drug and fitting parameters are reported. Figures from [175].

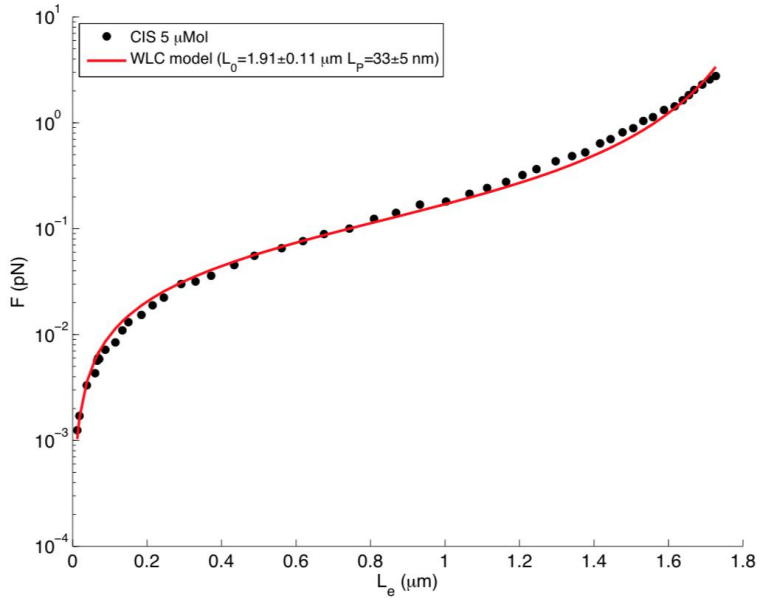

(a)

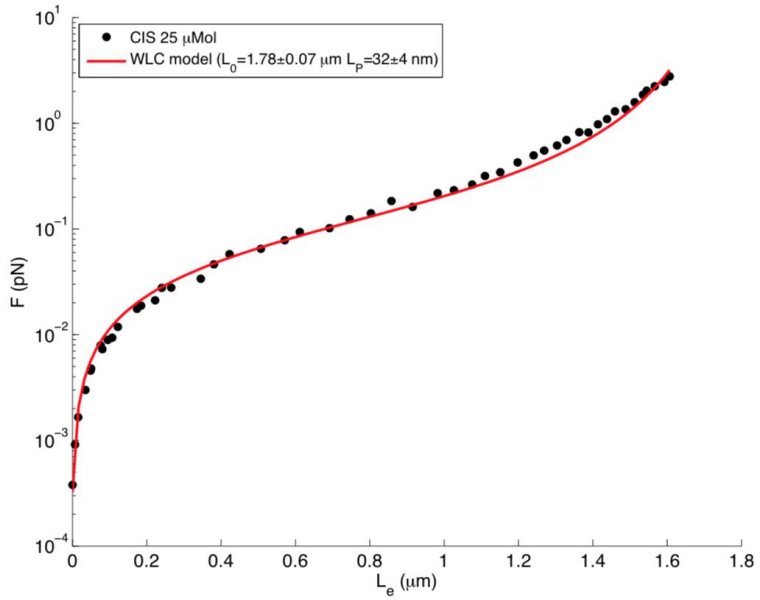

(b)

Figure C.4.: WLC curves of DNA in presence of CIS at 5 μM **(a)** and 25 μM **(b)**. Black dots are data points, red lines the WLC fits. In the insets concentration of the drug and fitting parameters are reported. Figures from [175].

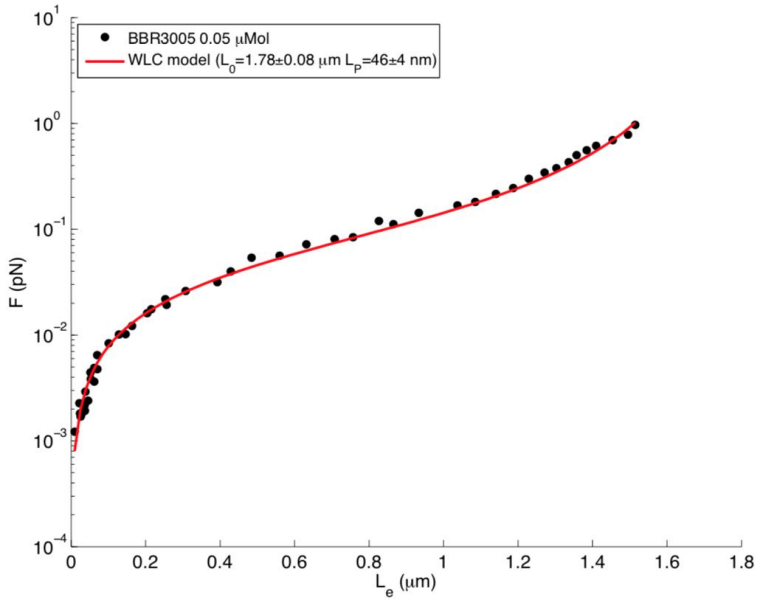

(a)

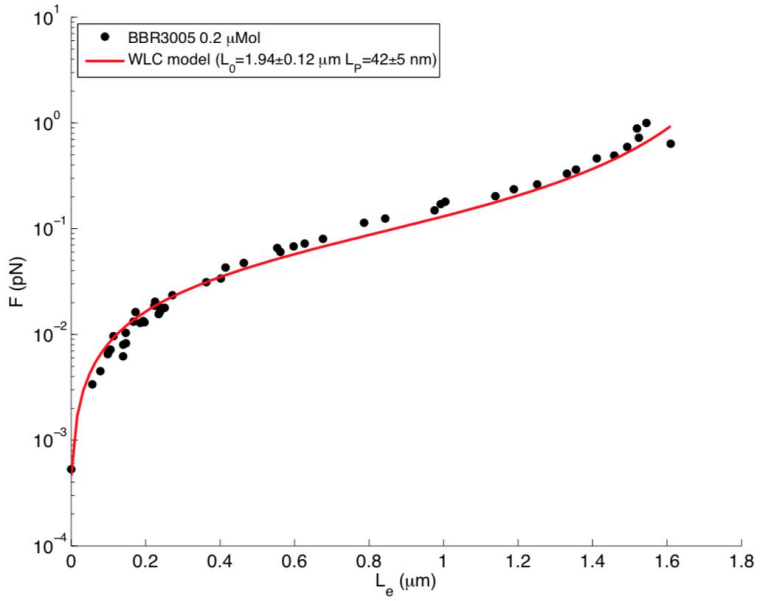

(b)

Figure C.5.: WLC curves of DNA in presence of BBR3005 at 0.05 μM **(a)** and 0.2 μM **(b)**. Black dots are data points, red lines the WLC fits. In the insets concentration of the drug and fitting parameters are reported. Figures from [175].

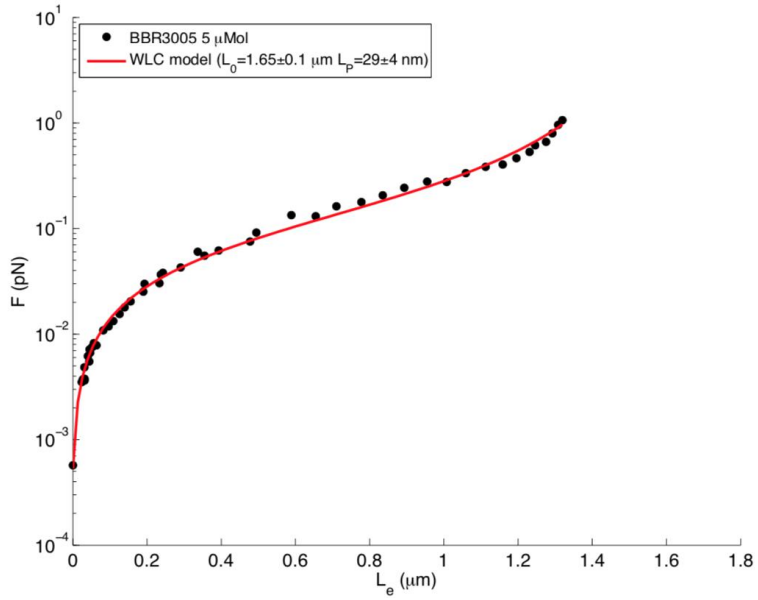

(a)

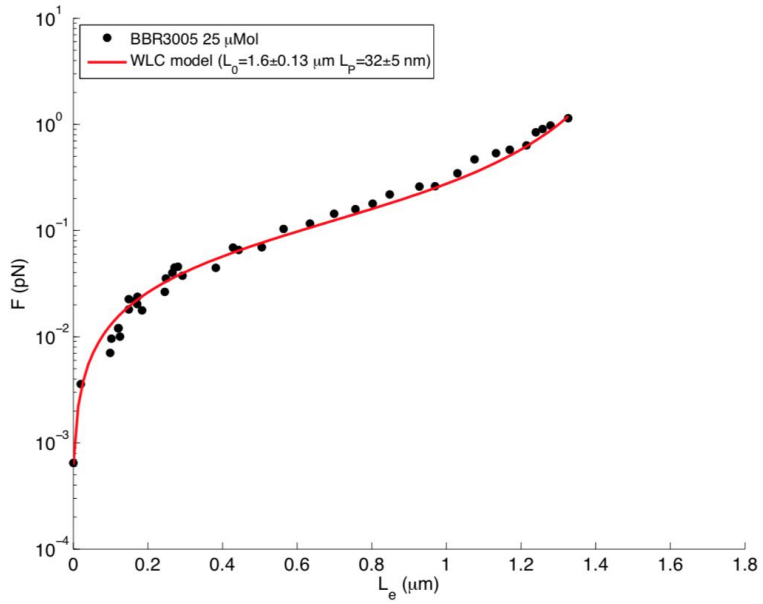

(b)

Figure C.6.: WLC curves of DNA in presence of BBR3005 at 5 μM **(a)** and 25 μM **(b)**. Black dots are data points, red lines the WLC fits. In the insets concentration of the drug and fitting parameters are reported. Figures from [175].

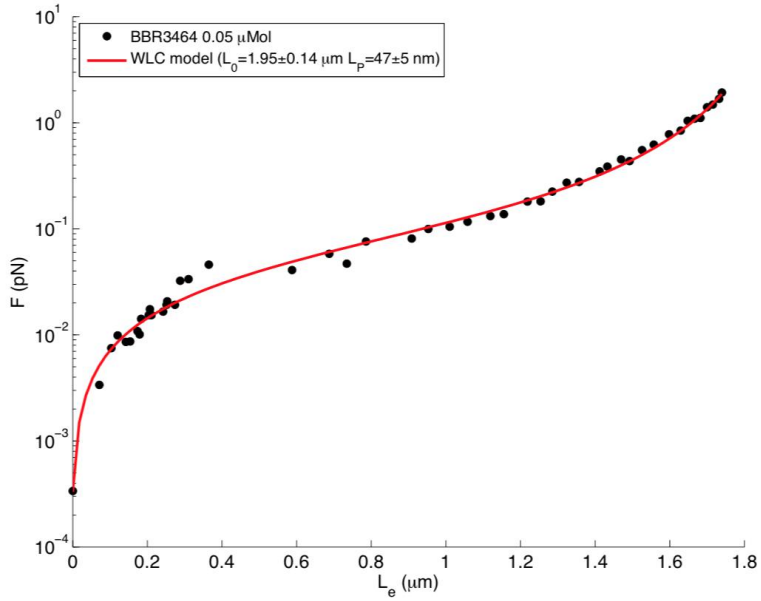

(a)

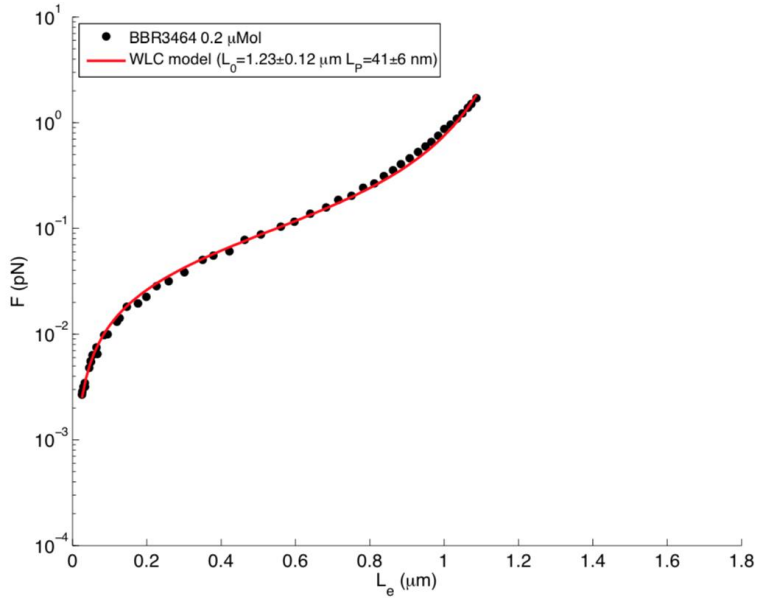

(b)

Figure C.7.: WLC curves of DNA in presence of BBR3464 at 0.05 μM **(a)** and 0.2 μM **(b)**. Black dots are data points, red lines the WLC fits. In the insets concentration of the drug and fitting parameters are reported. Figures from [175].

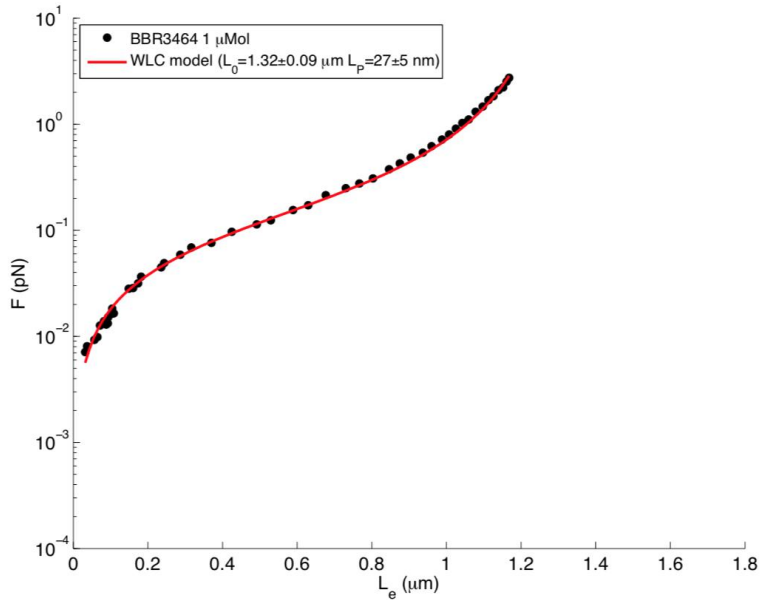

(a)

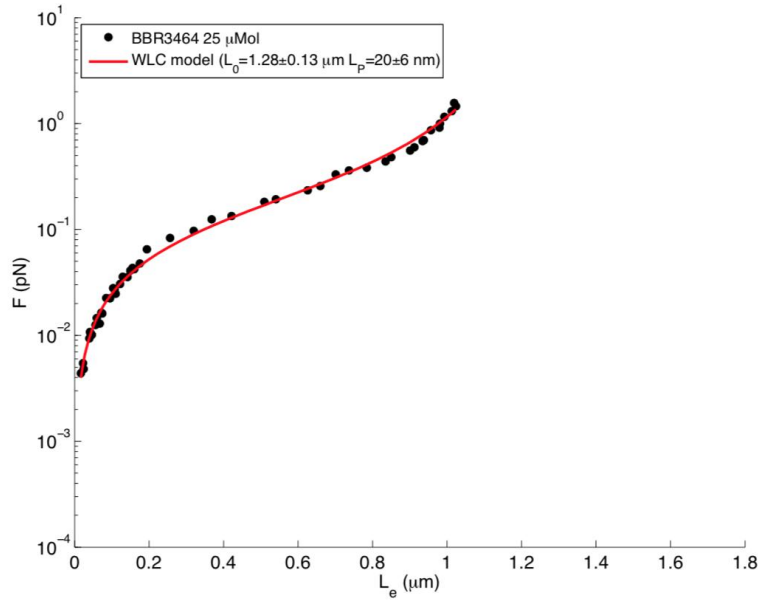

(b)

Figure C.8.: WLC curves of DNA in presence of BBR3464 at 1 μM **(a)** and 25 μM **(b)**. Black dots are data points, red lines the WLC fits. In the insets concentration of the drug and fitting parameters are reported. Figures from [175].

D

H-NS STRUCTURAL ROLE (SINGLE-MOLECULE)

D.1 BUFFER SOLUTIONS

D.1.1 *Buffer solutions for H-NS protein purification*

Stock buffer TN 5X:

- 100 mM Tris-HCl
- 3.75 M NaCl

Lysis buffer:

- buffer TN 1X
- 70 mM Imidazole
- 1 mM EDTA
- 5% glycerol
- 5 mM β-MercaptoEthanol
- 1 mM Pefabloc SC PLUS 4-(2-Aminoethyl)-benzenesulfonyl-flouride, hydrochloride (AEBSF)

Loading buffer:

- buffer TN 1X
- 70 mM Imidazole
- 5% glycerol

Elution buffer:

- buffer TN 1X
- 250 mM Imidazole
- 5% glycerol

D.1.2 *Buffer solution for MT experiments*

H-NS Buffer:

- 10 mM Tris-HCl (pH 7.5)
- 60 mM KCl
- 10 mM $MgCl_2$
- 1 mM EDTA
- 3.5 mM DTT

D.2 ADDITIONAL DNA FOLDING AND UNFOLDING CURVES

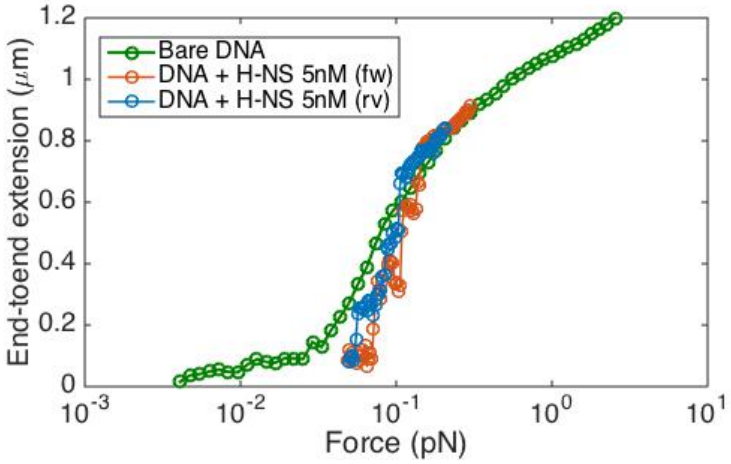

Figure D.1.: DNA folding and unfolding curves resulting from the interaction with 5 nM H-NS protein. The green curve represents bare DNA, while blue and orange DNA in presence of H-NS during the bridging/folding and the unfolding event, respectively. This low concentration of H-NS is not enough to induce a proper DNA folding, but only a slight change in the WLC curve.

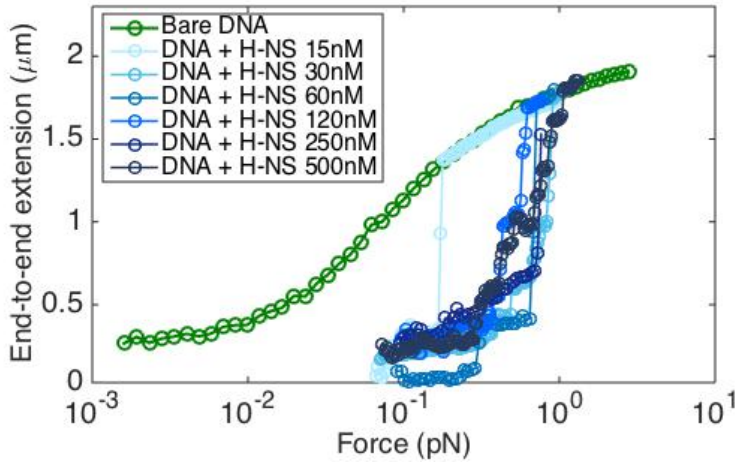

Figure D.2.: Concentration dependence of H-NS-DNA complex unfolding mechanism. Force-extension curve of bare DNA (green), and the blue-ish coloured curves corresponding to DNA in presence of different H-NS concentrations, ranging in a wide range between 15 nM and 500 nM.

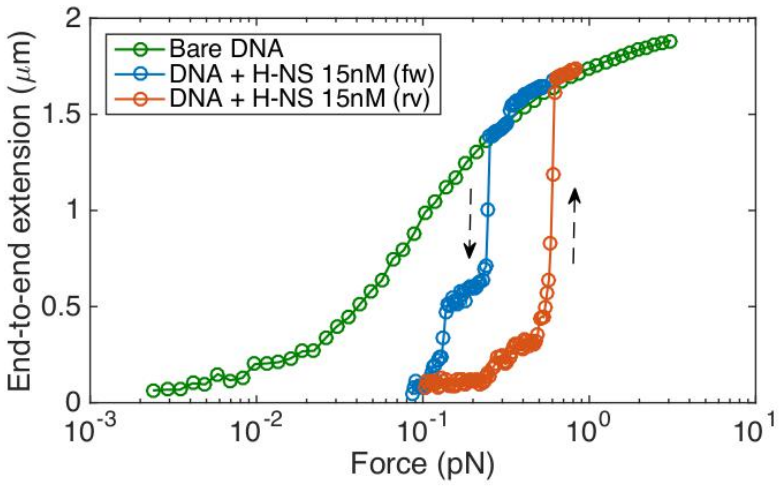

Figure D.3.: DNA folding and unfolding curves resulting from the interaction with 15 nM H-NS protein. The green curve represents bare DNA, while blue and orange DNA in presence of H-NS during the bridging/folding and the unfolding event, respectively. The two black arrows indicate the direction of the measurements.

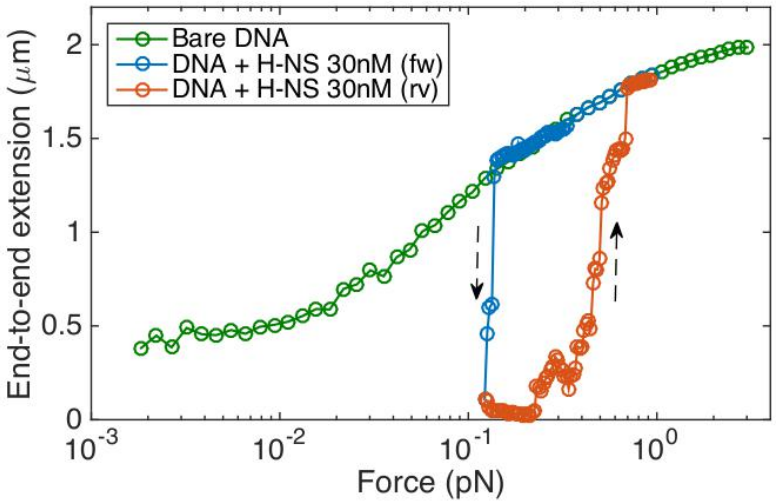

Figure D.4.: DNA folding and unfolding curves resulting from the interaction with 30 nM H-NS protein. The green curve represents bare DNA, while blue and orange DNA in presence of H-NS during the bridging/folding and the unfolding event, respectively. The two black arrows indicate the direction of the measurements.

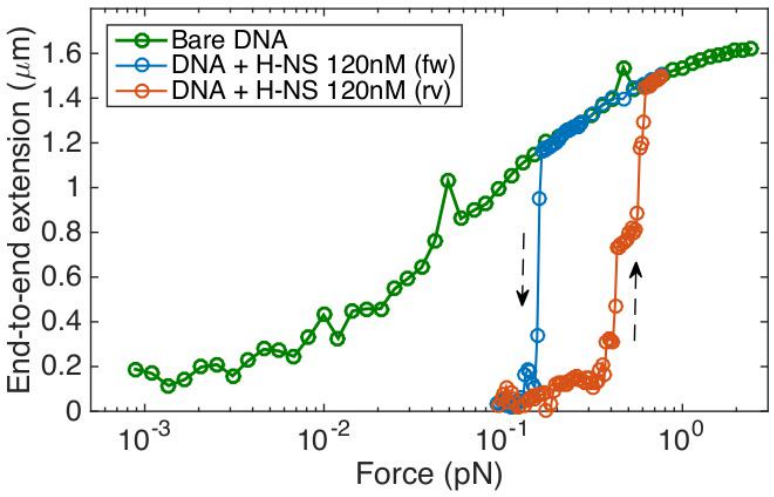

Figure D.5.: DNA folding and unfolding curves resulting from the interaction with 120 nM H-NS protein. The green curve represents bare DNA, while blue and orange DNA in presence of H-NS during the bridging/folding and the unfolding event, respectively. The two black arrows indicate the direction of the measurements.

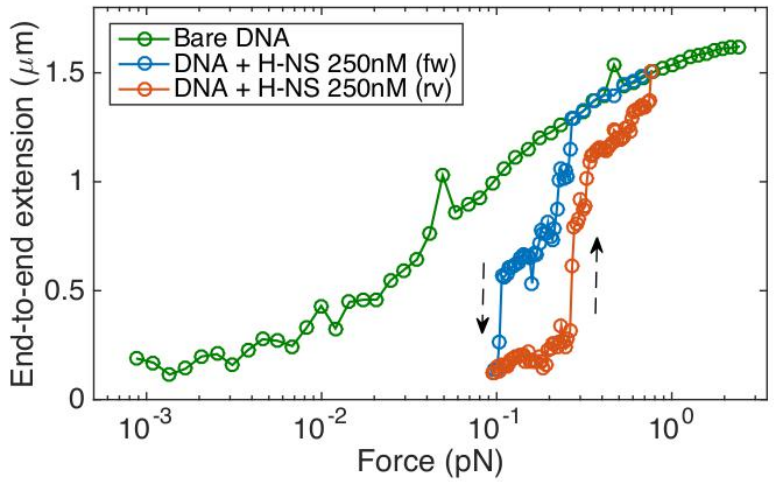

Figure D.6.: DNA folding and unfolding curves resulting from the interaction with 250 nM H-NS protein. The green curve represents bare DNA, while blue and orange DNA in presence of H-NS during the bridging/folding and the unfolding event, respectively. The two black arrows indicate the direction of the measurements.

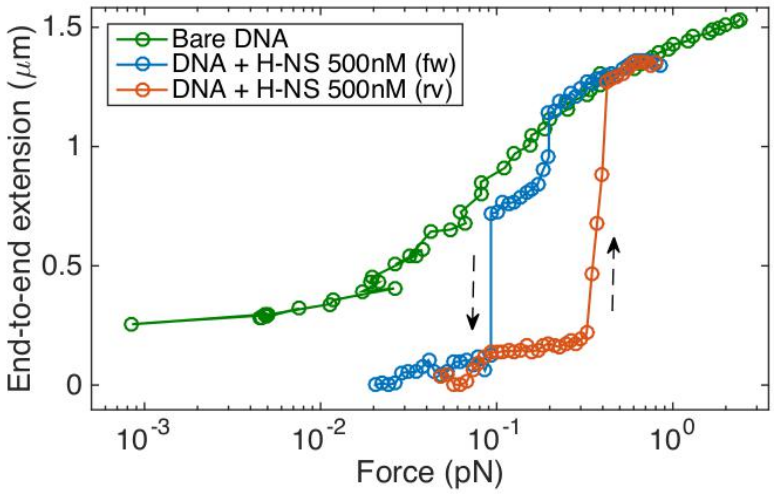

Figure D.7.: DNA folding and unfolding curves resulting from the interaction with 500 nM H-NS protein. The green curve represents bare DNA, while blue and orange DNA in presence of H-NS during the bridging/folding and the unfolding event, respectively. The two black arrows indicate the direction of the measurements.

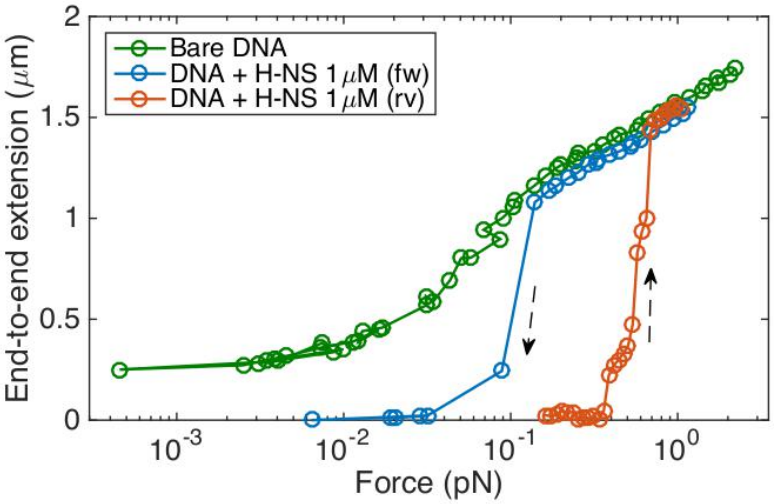

Figure D.8.: DNA folding and unfolding curves resulting from the interaction with 1 μM H-NS protein. The green curve represents bare DNA, while blue and orange DNA in presence of H-NS during the bridging/folding and the unfolding event, respectively. The two black arrows indicate the direction of the measurements.

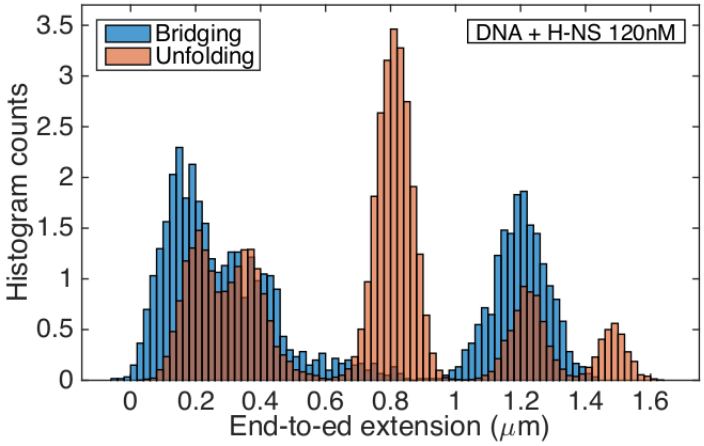

Figure D.9.: Histograms of the end-to-end extension (L_e) in presence of H-NS 30 nM, measured during bridging (blue bars) and unfolding (orange bars) events. For the sake of clarity, the plotted distributions considered only the temporal traces involved during the binding mechanism, this is why the bridging histogram seems to have a lower maximum value of L_e, I excluded the data at higher forces before the binding occurred. This choice makes it easier the comparison between these distributions and the related temporal traces, without altering the number of populations.

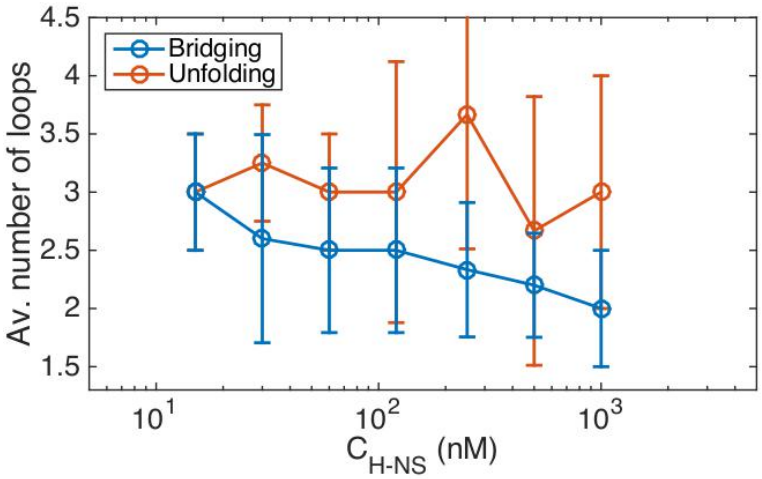

Figure D.10.: Average number of DNA loops during the bridging (blue) and unfolding (orange) mechanisms promoted by H-NS protein at different concentrations, ranging from 15 nM to 1 μM. Error bars are the standard deviation values.

D.3 ADDITIONAL DENATURATION CURVES

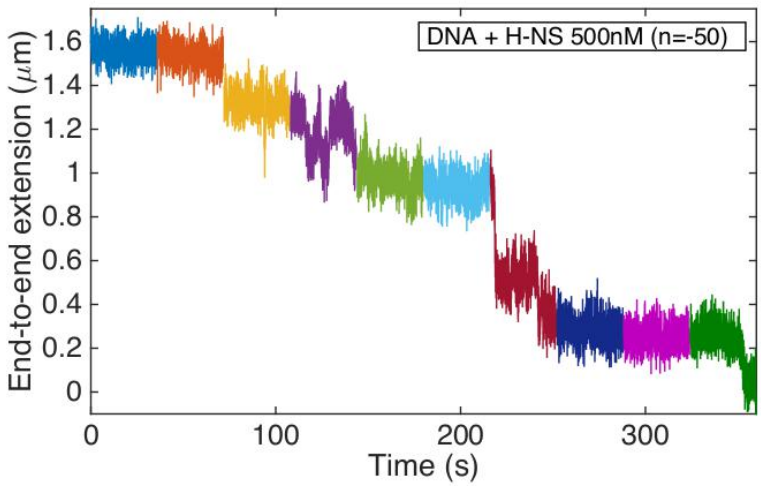

Figure D.11.: Temporal traces of a force-extension experiment during the mechanical denaturation of a H-NS-DNA complex (500 nM H-NS). Each coloured trace is collected at a different force. The mutlistep process can be clearly identified by the extension jumps.

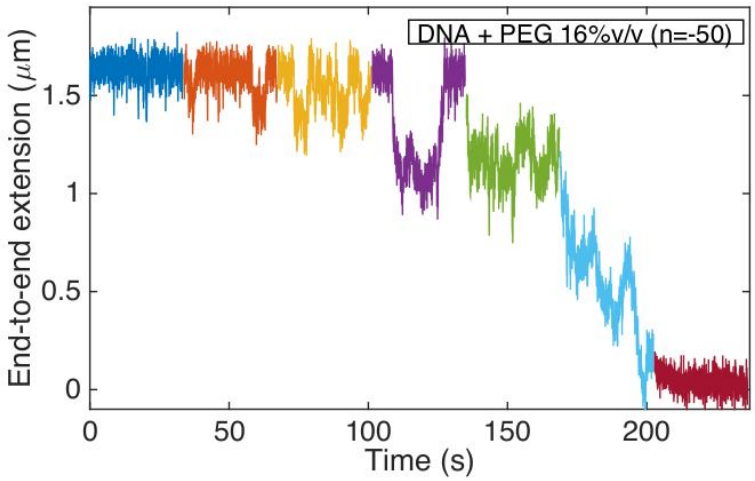

Figure D.12.: Temporal traces of a force-extension experiment during the mechanical denaturation of DNA in presence of 16% v/v PEG1500. Each coloured trace is collected at a different force. The mutlistep process can be clearly identified by the extension jumps.

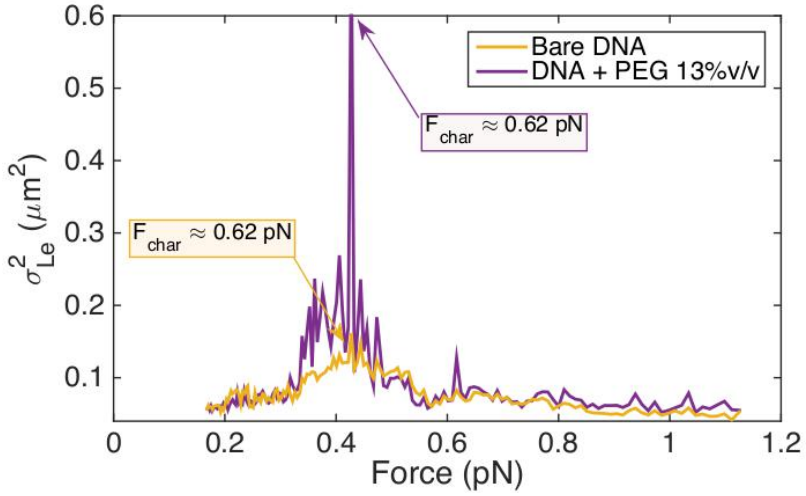

Figure D.13.: Variance σ^2_{Le} related to a denaturation transition occurring in a bare DNA molecule (yellow) and in a DNA molecule in presence of PEG 13% v/v (purple). The force values of the peaks correspond to different characteristic forces. In labels the values of F_{char} are reported.

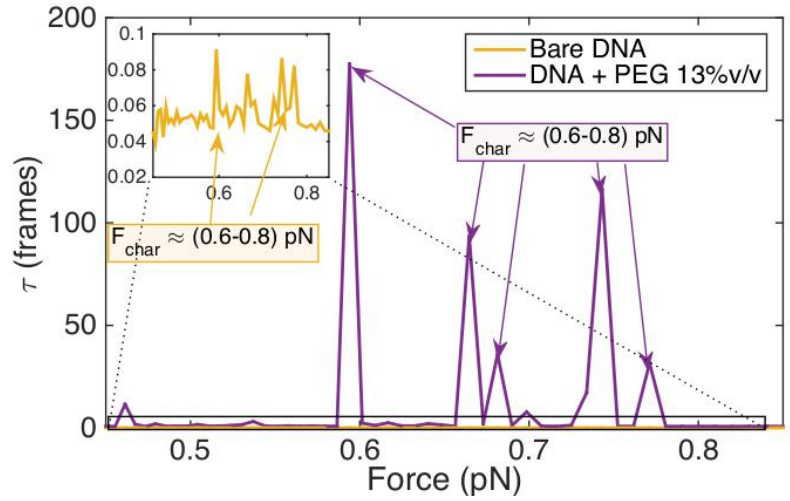

Figure D.14.: Autocorrelation characteristic time τ related to a denaturation transition occurring in a bare DNA molecule (yellow) and in a DNA molecule in presence of PEG 13% v/v (purple). The force values of the peaks correspond to different characteristic forces (F_{char}). In labels the values of F_{char} are reported.

E

H-NS REGULATORY ROLE (SINGLE-CELL)

E.1 ADDITIONAL UPSHIFT CURVES

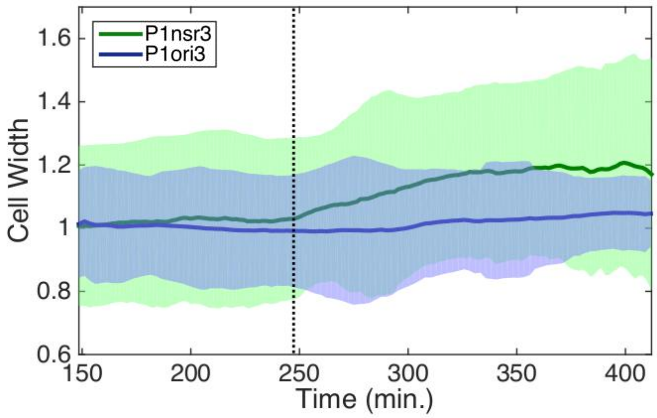

(a)

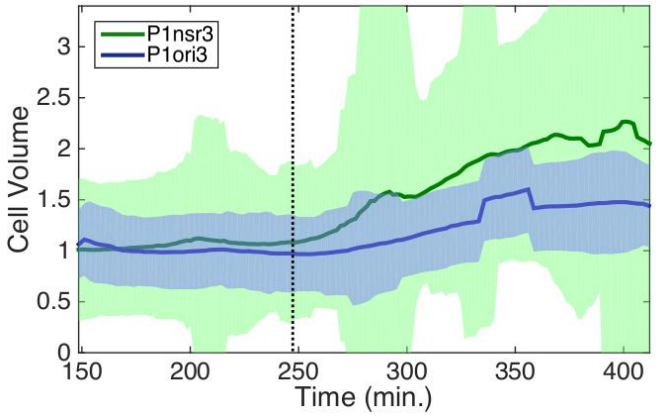

(b)

Figure E.1.: Upshift experiments showing the cell average width **(a)** and the cell average volume **(b)** as a function of time for P1*ori*3 (blue) and P1*nsr*3 (green) strains. Solid lines and shaded areas represent the average and the standard deviation over 3000-4000 cells. Data are normalized to the average value before the upshift. The dotted line approximately represents the time when the rich medium reached the chamber.

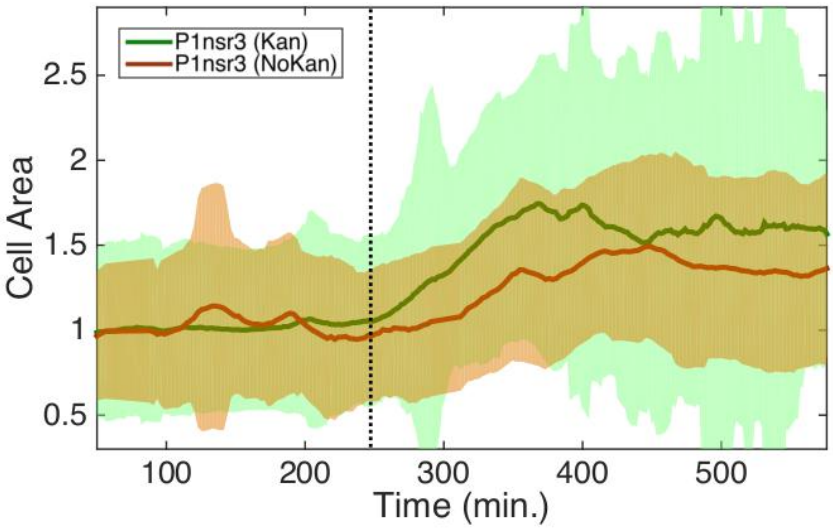

Figure E.2.: Upshift experiments showing the cell average area as a function of time for P1*nsr*3 (NoKan) strain, compared with the same strain including KanR cassette. Solid lines and shaded areas represent the average and the standard deviation over 3500-4000 cells. Data are normalized to the average value before the upshift. The dotted line approximately represents the time when the rich medium reached the chamber.

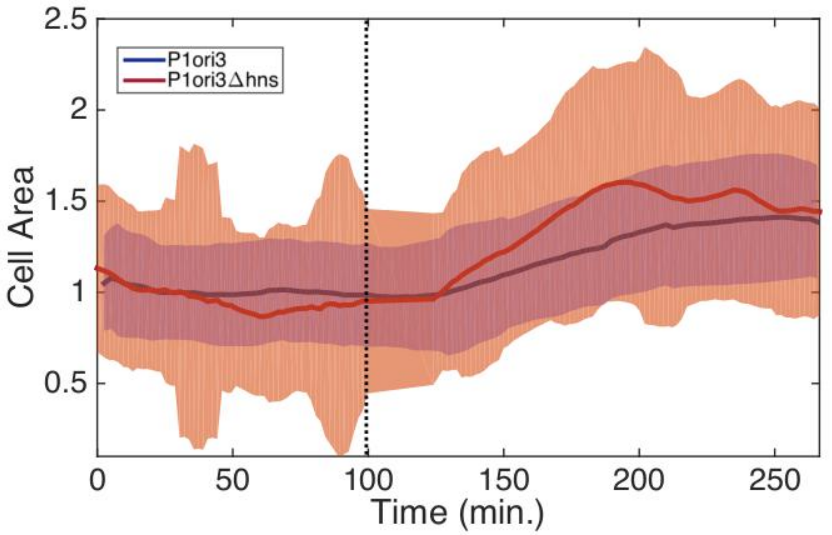

Figure E.3.: Upshift experiments showing the cell average area as a function of time for P1*ori*3-Δ*hns* strain, compared with the control strain P1*ori*3 including *hns* gene. Solid lines and shaded areas represent the average and the standard deviation over 3000-3500 cells. Data are normalized to the average value before the upshift. The dotted line approximately represents the time when the rich medium reached the chamber.

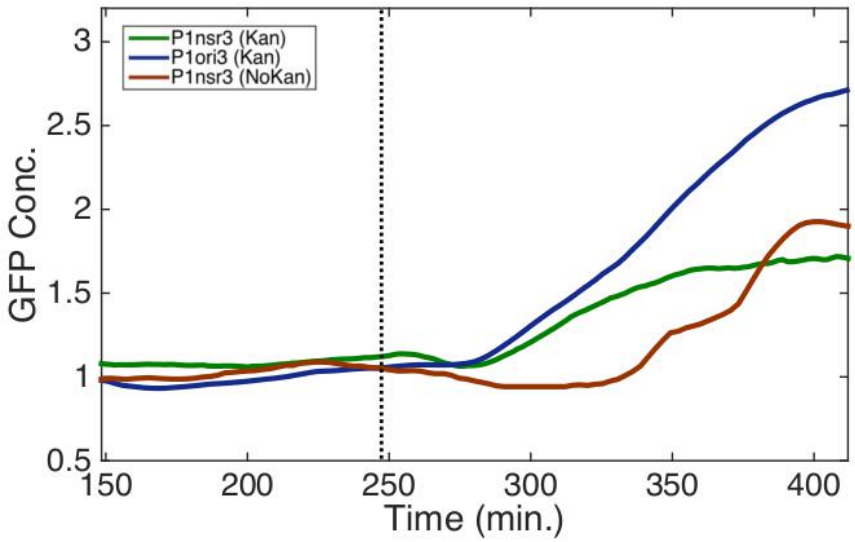

(a)

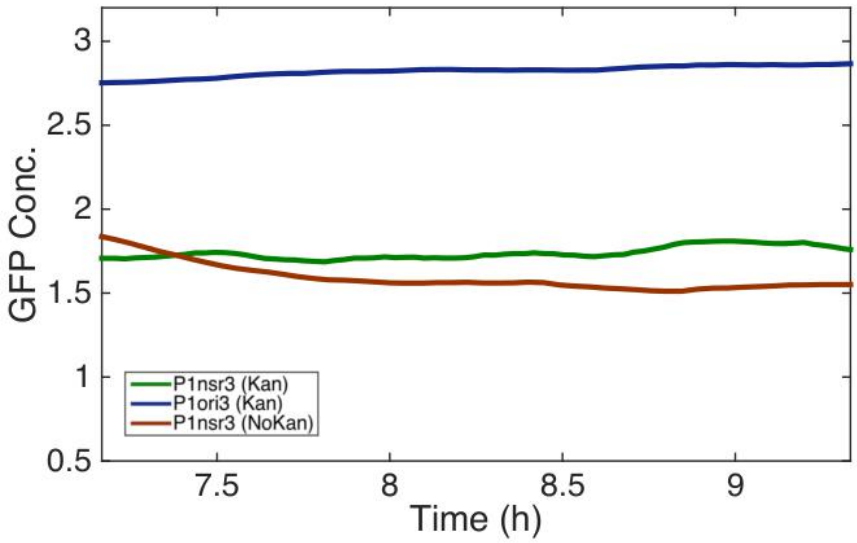

(b)

Figure E.4.: Comparative upshift experiments between P1*ori*3, P1*nsr*3 and P1*nsr*3(NoKan) **(a)** GFP average concentration as a function of time for P1*ori*3 (blue), P1*nsr*3 (green) and P1*nsr*3(NoKan) (red). Data calculated from an average over 3000-4000 cells and normalized to the average value before the upshift. The dotted line approximately represents the time when the rich medium reached the chamber.
(b) Saturation values of GFP average concentration after the upshift. Data are normalized to the average value before the upshift, shown in (a).

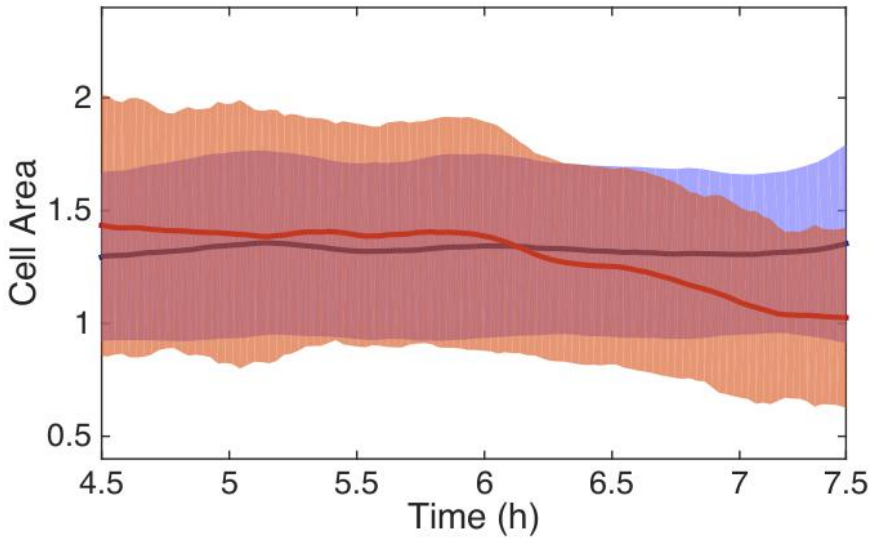

Figure E.5.: Average value of cell area after the conclusion of the upshift for P1*ori3* (blue) and P1*ori3*-Δ*hns* (red). Data are normalized to the average value before the upshift, shown in figure 10.6. Solid lines and shaded areas represent the average and the standard deviation over 3000-3500 cells.

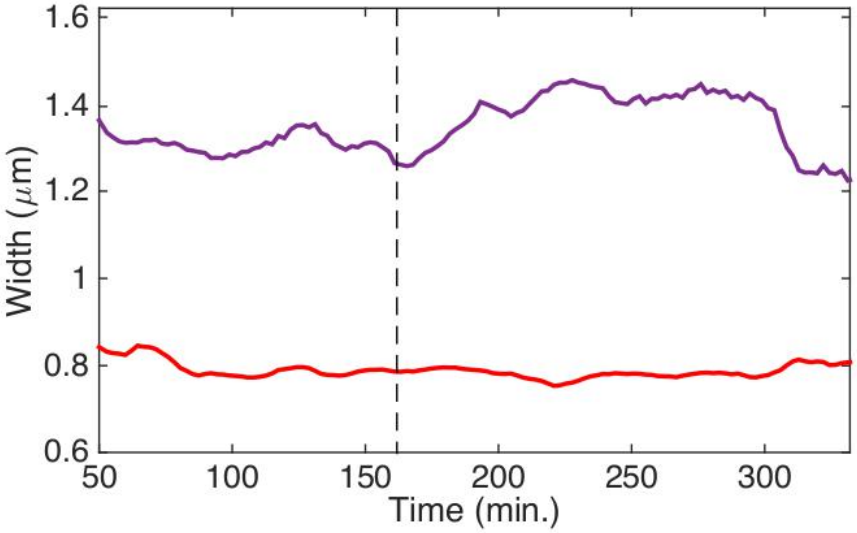

(a)

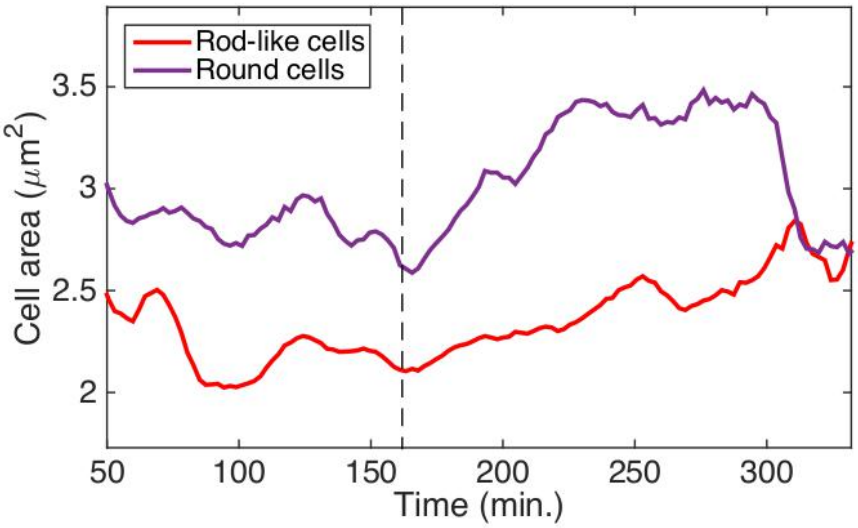

(b)

Figure E.6.: Comparison of cell width **(a)** and cell area **(b)** between typical rod-like bacteria of P1*ori3* strain (red) and mutated round bacteria of P1*ori3*-Δ*hns* (purple). Data from the upshift experiment reported in figure 13.13. The dotted line approximately represents the time when the rich medium reached the flow chamber.

BIBLIOGRAPHY

[1] A. Vologodskii, *Biophysics of DNA*, Cambridge University Press, Cambridge, (2015).

[2] J. C. Garcia-Ramos, R. Galindo-Murillo, F. Cortés-Guzman, and L. Ruiz-Azuara, *Metal-Based Drug-DNA Interactions*, J. Mex. Chem. Soc., **57**, 245-259, (2013).

[3] T. R. Strick, M.-N. Dessinges, G. Charvin, N. H. Dekker, J.-F. Allemand, D. Bensimon, and V. Croquette, *Stretching of macromolecules and proteins*, Rep. Prog. Phys., **66**, 1-45, (2003).

[4] W. Kabsch, C. Sander and E. N. Trifonov, *The ten helical twist angles of B-DNA*, Nucleic Acids Res., **10**, 1097-1104, (1982).

[5] C. R. Calladine, H. R. Drew, B. F. Luisi, and A. A. Travers, *Understanding DNA*, Elsevier Academic Press, San Diego, (2004).

[6] J. C. Wang, *Helical repeat of DNA in solution*, Proc. Natl. Acad. Sci., **76**, 200-203, (1979).

[7] L. J. Peck, and J. C. Wang, *Sequence dependence of the helical repeat of DNA in solution*, Nature, **292**, 375-378, (1981).

[8] R. E. Dickerson, and H.-L. Ng, *DNA structure from A to B*, Proc. Natl. Acad. Sci., **98**, 6986-6988, (2001).

[9] P. L. Privalov, A. I. Dragan, C. Crane-Robinson, K. J. Breslauer, D. P. Remeta, and C. A. S. A. Minetti, *What Drives Proteins into the Major or Minor Grooves of DNA?*, J. Mol. Biol., **365**, 1-9, (2007).

[10] R. E. Dickerson, H. R. Drew, B. N. Conner, R. M. Wing, A. V. Fratini, M. L. Kopka, *The Anatomy of A-, B-, and Z-DNA*, Science, **216**, 475-485, (1982).

[11] W. Saenger, *Principles of Nucleic Acid Structure*, Springer Advanced Texts in Chemistry, Springer New York, New York, NY, (1984).

[12] D. Y. Krylov, V. L. Makarov, and V. I. Ivanov, *The B-A transition in superhelical DNA*, Nucleic Acids Res., **18**, 759-761, (1990).

[13] M. D. Frank-Kamenetskii, *Biophysics of the DNA molecule*, Phys. Rep., **288**, 13-60, (1997).

[14] S. Hormeno, B. Ibarra, J. L. Carrascosa, J. M. Valpuesta, F. Moreno-Herrero, and J. R. Arias-Gonzalez, *Mechanical Properties of High-G,C Content DNA with A-Type Base-Stacking*, Biophys. J., **100**, 1996-2005, (2011).

[15] S. Hormeno, F. Moreno-Herrero, B. Ibarra, J. L. Carrascosa, J. M. Valpuesta, and J. R. Arias-Gonzalez, *Condensation Prevails over B-A Transition in the Structure of DNA at Low Humidity*, Biophys. J., **100**, 2006-2015, (2011).

[16] Y. Nishimura, C. Torigoe, and M. Tsuboi, *An A-form poly (dG).poly(dC) in H_2O solution*, Biopolymers, **24**, 1841-1844, (1985).

[17] R. Stefl, L. Trantirek, M. Vorlickova, J. Koca, V. Sklenar, and J. Kypr, *A-like Guanine-Guanine Stacking in the Aqueous DNA Duplex of d(GGGGCCCC)*, J. Mol. Biol., **307**, 513-524, (2001).

[18] J. Kypr, I. Kejnovska, D. Renciuk and M. Vorlickova, *Circular dichroism and conformational polymorphism of DNA*, Nucleic Acids. Res., **37**, 1713-1725, (2009).

[19] Y. Mitsui, R. Langridge, B. E. Shortle, C. R. Cantor, R. C. Grant, M. Kodama, and R. D. Wells, *Physical and Enzymatic Studies on Poly d(I–C).Poly d(I–C), an Unusual Double-helical DNA*, Nature, **228**, 1166-1169, (1970).

[20] F. M. Pohl, T. M. Jovin, *Salt-induced co-operative conformational change of a synthetic DNA: equilibrium and kinetic studies with poly (dG-dC)*, J. Mol. Biol., **67**, 375-396, (1972).

[21] A. H. Wang, G. J. Quigley, F. J. Kolpak, J. L. Crawford, J. H. van Boom, G. van der Marel, A. Rich, *Molecular structure of a left-handed double helical DNA fragment at atomic resolution* Nature, **282**, 680-686, (1979).

[22] H. Drew, T. Takano, S. Tanaka, K. Itakura and R.E. Dickerson, Nature, *High-salt d(CpGpCpG), a left-handed Z' DNA double helix*, Nature, **286**, 567-573, (1980).

[23] A. Rich, A. Nordheim, and A. H.-J. Wang, (*The chemistry and biology of left-handed Z-DNA*, Annu. Rev. Biochem., **53**, 791-846, (1984).

[24] Z. Bryant, M. D Stone, J. Gore, S. B. Smith, N. R. Cozzarelli, and C. Bustamante, *Structural transitions and elasticity from torque measurements on DNA*, Nature, **424**, 338-341, (2003).

[25] F. C. Oberstrass, L. E. Fernandes, and Z. Bryant, *Torque measurements reveal sequence-specific cooperative transitions in supercoiled DNA*, Proc. Natl. Acad. Sci., **109**, 6106-6111, (2012).

[26] L. J. Peck, and J. C. Wang, *Energetics of B-to-Z transition in DNA*, Proc. Natl. Acad. Sci., **80** 6206-6210, (1983).

[27] A. T. Phan, *Human telomeric G-quadruplex: structures of DNA and RNA sequences*, FEBS J., **277**, 1107-1117, (2009).

[28] S. Burge, G. N. Parkinson, P. Hazel, A. K. Todd, and S. Neidle, *Quadruplex DNA: sequence, topology and structure*, Nucleic Acids Res., **34**, 5402-5415, (2006).

[29] H. You, X. Zeng, Y. Xu, C. J. Lim, A. K. Efremov, A. T. Phan, and J. Yan, *Dynamics and stability of polymorphic human telomeric G-quadruplex under tension*, Nucleic Acids Res., **42**, 8789-8795, (2014).

[30] H. You, J. Wu, F. Shao, and J. Yan, *Stability and Kinetics of c-MYC Promoter G-Quadruplexes Studied by Single-Molecule Manipulation*, J. Am. Chem. Soc., **137**, 2424-2427, (2015).

[31] S. Selvam, Z. Yu and H. Mao, *Exploded view of higher order G-quadruplex structures through click-chemistry assisted single-molecule mechanical unfolding*, Nucleic Acids Res., **44**, 45-55, (2015).

[32] S. L. Noer, S. Preus, D. Gudnason, M. Aznauryan, J.-L. Mergny and V. Birkedal, *Folding dynamics and conformational heterogeneity of human telomeric G-quadruplex structures in Na^+ solutions by single molecule FRET microscopy*, Nucleic Acids Res., **44**, 464-471, (2015).

[33] R. Dulbecco and M. Vogt, *Evidence for a ring structure of polyoma virus dna*, Proc. Natl. Acad. Sci., **50**, 236-243, (1963).

[34] R. Weil and J. Vinograd, *The cyclic helix and cyclic coil forms of polyoma viral DNA*, Proc. Nat. Acad. Sci., **50**, 730-738, (1963).

[35] J. Vinograd, J. Lebowitz and R. Watson, *Early and Late Helix-Coil Transitions in Closed Circular DNA The Number of Superhelical Turns in Polyoma DNA*, J. Mol. Biol., **33**, 173-197, (1968).

[36] S. M. Mirkin, *DNA topology: fundamentals*, Encyclopedia of Life Sciences (ELS), John Wiley & Sons, Ltd, Chichester, West Sussex, UK, (2001).

[37] J. H. White, *Self-linking and the Gauss integral in higher dimensions*, Am. J. Math., **91**, 693-728, (1969).

[38] F. B. Fuller, *The Writhing Number of a Space Curve*, Proc. Nat. Acad. Sci., **68**, 815-819, (1971).

[39] G. Charvin, J.-F. Allemand, T. R. Strick, D. Bensimon, and V. Croquette, *Twisting DNA: single molecule studies*, Contemp. Phys., **45**, 383-403, (2004).

[40] K. C. Neuman and A. Nagy, *Single-molecule force spectroscopy: optical tweezers, magnetic tweezers and atomic force microscopy*, Nat. Methods, **5**, 491-505, (2008).

[41] T. E. Ouldridge A. A. Louis, and J. P. K. Doyle, *DNA Nanotweezers Studied with a Coarse-Grained Model of DNA*, Phys. Rev. Lett., **104**, 178101, (2010).

[42] Structural, mechanical, and thermodynamic properties of a coarse-grained DNA model, J. Chem., Phys., **134**, 085101, (2011).

[43] T. R. Strick, V, Croquette, and D. Bensimon, *Single-molecule analysis of DNA uncoiling by a type II topoisomerase*, Nature, **404**, 901-904, (2000).

[44] G. Charvin, D. Bensimon, and V. Croquette, *Single-molecule study of DNA unlinking by eukaryotic and prokaryotic type-II topoisomerases*, Proc. Nat. Acad. Sci., **100**, 9820-9825, (2003).

[45] J. Lipfert, D. A. Koster, I. D. Vilfan, S. Hage, and N. H. Dekker *Single-Molecule Magnetic Tweezers Studies of Type IB Topoisomerases*, in D. Clarke (eds) DNA Topoisomerases. Methods in Molecular Biology (Methods and Protocols), Humana Press, **582**, 71-89, (2009).

[46] Y. Seol, K.C. Neuman, *Single-Molecule Measurements of Topoisomerase Activity with Magnetic Tweezers*, in G. Mashanov, C. Batters (eds) Single Molecule Enzymology. Methods in Molecular Biology (Methods and Protocols), Humana Press, **778**, 229-241, (2011).

[47] Y. Seol, K.C. Neuman, *The dynamic interplay between DNA topoisomerases and DNA topology*, Biophys. Rev., **8**, 101-111, (2016).

[48] D. A. Koster, V. Croquette, C. Dekker, S. Shuman, and N. H. Dekker, *Friction and torque govern the relaxation of DNA supercoils by eukaryotic topoisomerase IB*, **434**, 671-674, (2005).

[49] D. A. Koster, K. Palle, E. S. M. Bot, M.-A. Bjornsti, and N. H. Dekker, *Antitumour drugs impede DNA uncoiling by topoisomerase I*, **448**, 213-217, (2007).

[50] B. Gollnick, C. Carrasco, F. Zuttion, N. S. Gilhooly, M. S. Dillingham, F. Moreno-Herrero, *Probing DNA helicase kinetics with temperature-controlled magnetic tweezers*, Small, **11**, 1273-1284, (2015).

[51] S. Hodeib, S. Raj, M. Manosas, W. Zhang, D. Bagchi, B. Ducos, J.-F. Allemand, D. Bensimon, and V. Croquette, *Single molecule studies of helicases with magnetic tweezers*, Methods, **105**, 3-15, (2016).

[52] R. Vlijm, A. Mashaghi, S. Bernard, M. Modestib, and C. Dekker, *Experimental phase diagram of negatively supercoiled DNA measured by magnetic tweezers and fluorescence*, Nanoscale, **7**, 3205-3216, (2015).

[53] J. F. Allemand, D. Bensimon, R. Lavery, and V. Croquette, *Stretched and overwound DNA forms a Pauling-like structure with exposed bases*, Proc. Natl. Acad. Sci., **95**, 14152-14157, (1998).

[54] S. C. Dillon and C. J. Dorman, *Bacterial nucleoid-associated proteins, nucleoid structure and gene expression*, Nat. Rev. Microbiol., **8**, 185-195, (2010).

[55] N. Laurens, R. P.C. Driessen, I. Heller, D. Vorselen, M. C. Noom, F. J. H. Hol, M. F. White, R. T. Dame, and G. J.L. Wuite, *Alba shapes the archaeal genome using a delicate balance of bridging and stiffening the DNA*, Nat. Comm., **3**, 1328, (2012).

[56] R. P. C. Driessen, S.-N. Lin, W.-J. Waterreus, A. L. H. van der Meulen, R. A. van der Valk, N. Laurens, G. F. Moolenaar, N. S. Pannu, G. J. L. Wuite, N. Goosen, and R. T. Dame, *Diverse architectural properties of Sso*10*a proteins: Evidence for a role in chromatin compaction and organization*, Sci. Rep., **6**, 29422, (2016).

[57] A. Japaridze, G. Muskhelishvili, F. Benedetti, A. F. M. Gavriilidou, R. Zenobi, P. De Los Rios, G. Longo, and G. Dietler, *Hyperplectonemes: A Higher Order Compact and Dynamic DNA Self-Organization*, Nano Lett., **17**, 1938-1948, (2017).

[58] G. Lia, D. Bensimon, V. Croquette, J.-F. Allemand, D. Dunlap, D. E. A. Lewis, S. Adhya, and L. Finzi,*Supercoiling and denaturation in Gal repressor heat unstable nucleoid protein (HU)-mediated DNA looping*, **100**, 11373-11377, (2003).

[59] F. Guo and S. Adhya, *Spiral structure of Escherichia coli HU*$\alpha\beta$ *provides foundation for DNA supercoiling*, Proc. Natl. Acad. Sci., **104**, 4309-4314, (2007).

[60] K. K. Swinger and P. A. Rice, *IHF and HU: flexible architects of bent DNA*, Curr. Opin. Microbiol.,**14**, 28-35, (2004).

[61] P. A. Rice, S.-W. Yang, K. Mizuuchi, and H. A. Nash, *Crystal Structure of an IHF-DNA Complex: A Protein-Induced DNA U-Turn*, Cell, **87**, 1295-1306, (1996).

[62] S. Nair, S. E. Finkel, *Dps protects cells against multiple stresses during stationary phase*, J. Bacteriol., **186**, 4192-4198, (2004).

[63] N. N. Vtyurina, D. Dulin, M. W. Docter, A. S. Meyer, N. H. Dekker, and E. A. Abbondanzieri, *Hysteresis in DNA compaction by Dps is described by an Ising model*, **113**, Proc. Natl. Acad. Sci., 4982-4987, (2016).

[64] B. Xiao, H. Zhang, R. C. Johnson, and J. F. Marko, *Force-driven unbinding of proteins HU and Fis from DNA quantified using a thermodynamic Maxwell relation*, Nucleic Acids Res., **39**, 5568-5577, (2011).

[65] R. D. Giuntoli, N. B. Linzer, E. J. Banigan, C. E. Sing, M. Olvera de la Cruz, J. S. Graham, R. C. Johnson, and J. F. Marko, *DNA-segment-facilitated dissociation of Fis and NHP6A from DNA detected via single-molecule mechanical response*, J. Mol. Biol., **427**, 3123-3136, (2015).

[66] S. Stella, D. Cascio, R. C. Johnson, *The shape of the DNA minor groove directs binding by the DNA-bending protein Fis*, Genes Dev., **24**, 814-826, (2010).

[67] S. T. Arold, P. G. Leonard, G. N. Parkinson, and J. E. Ladbury, *H-NS forms a superhelical protein scaffold for DNA condensation*, Proc. Natl. Acad. Sci., **107**, 15728-15732, (2010).

[68] R. S. Winardhi, J. Yan, and L. J. Kenney, *H-NS Regulates Gene Expression and Compacts the Nucleoid: Insights from Single-Molecule Experiments*, Biophys. J., **109**, 1321-1329, (2015).

[69] D. C. Grainger, *Structure and function of bacterial H-NS protein*, Biochem Soc Trans., **44**, 1561-1569, (2016).

[70] Y. Gao, Y. H. Foo, R. S. Winardhi, Q. Tang, Jie Yan, and L. J. Kenney, *Charged residues in the H-NS linker drive DNA binding and gene silencing in single cells*, Proc. Natl. Acad. Sci., **114**, 12560-12565, (2017).

[71] W. W. Navarre, S. Porwollik, Y. Wang, M. McClelland, H. Rosen, S. J. Libby, F. C. Fang, *Selective Silencing of Foreign DNA with Low GC Content by the H-NS Protein in Salmonella*, Science, **313**, 236-238, (2006).

[72] B. R. Gordon, Y. Li, A. Cote, M. T. Weirauch, P. Ding, T. R. Hughes, W. W. Navarre, B. Xia, J. Liu, *Structural basis for recognition of AT-rich DNA by unrelated xenogeneic silencing proteins*, Proc. Natl. Acad. Sci., **108**, 10690-10695, (2011).

[73] R.A. van der Valk, J. Vreede, F. Crémazy, R. T. Dame, *Genomic Looping: A Key Principle of Chromatin Organization*, J. Mol. Microbiol. Biotechnol., **24**, 344-359, (2014).

[74] C. J. Dorman, *H-NS: a universal regulator for a dynamic genome*, Nat. Rev. Microbiol., **2**, 391-400, (2004).

[75] E. Bouffartigues, M. Buckle, C. Badaut, A. Travers, and S. Rimsky, *H-NS cooperative binding to high-affinity sites in a regulatory element results in transcriptional silencing*, Nat. Struct. Mol.Biol., **14**, 441-448, (2007).

[76] R. T. Dame, C. Wyman, and N. Goosen, *H-NS mediated compaction of DNA visualised by atomic force microscopy*, Nucleic Acids Res., **28**, 3504-3510, (2000).

[77] R. T. Dame, C. Wyman, R. Wurm, R. Wagner, and N. Goosen, *Structural Basis for H-NS-mediated Trapping of RNA Polymerase in the Open Initiation Complex at the rrnB P*1, J. Biol. Chem., **277**, 2146-2150, (2002).

[78] R. T. Dame and G. J. L. Wuite, *On the Role of H-NS in the Organization of Bacterial Chromatin: From Bulk to Single Molecules and Back...*, Biophys. J., **85**, 4146-4148, (2003).

[79] R. T. Dame, M. C. Noom, and G. J. L. Wuite, *Bacterial chromatin organization by H-NS protein unravelled using dual DNA manipulation*, Nature, **444**, 387-390, (2006).

[80] I. Heller, N. Laurens, D. Vorselen, O. D. Broekmans, A. S. Biebricher, G. A. King, I. Brouwer, G. J. L. Wuite, and E. J. G. Peterman, *Versatile Quadruple-Trap Optical Tweezers for Dual DNA Experiments*, in A. Gennerich (eds) Optical Tweezers. Methods in Molecular Biology, Humana Press, **1486**, 257-272, (2017).

[81] R. Amit, A. B. Oppenheim, and J. Stavans, *Increased Bending Rigidity of Single DNA Molecules by H-NS, a Temperature and Osmolarity Sensor*, Biophys. J., **84**, 2467-2473, (2003).

[82] Y. Liu, H. Chen, L. J. Kenney, and J. Yan, *A divalent switch drives H-NS/DNA-binding conformations between stiffening and bridging modes*, Genes Dev., **24**, 339-344, (2010).

[83] C. J. Lim, L. J. Kenney, and J. Yan, *Single-molecule studies on the mechanical interplay between DNA supercoiling and H-NS DNA architectural properties*, Nucleic Acids Res., **42**, 8369-8378, (2014).

[84] R. S. Winardhi, S. Castang, S. L. Dove, J. Yan, *Single-Molecule Study on Histone-Like Nucleoid- Structuring Protein (H-NS) Paralogue in Pseudomonas aeruginosa: MvaU Bears DNA Organization Mode Similarities to MvaT*, PLoS One, **9**, e112246, (2014).

[85] F. C. Fang and S. Rimsky *New insights into transcriptional regulation by H-NS*, Curr. Opin. Microbiol., **11**, 113-120, (2008).

[86] C. J. Dorman, *H-NS, the genome sentinel*, Nat. Rev. Microbiol., **5**, 157-161, (2007).

[87] S. Lucchini, G. Rowley, M. D. Goldberg, D. Hurd, M. Harrison, and J. C. D. Hinton, *H-NS mediates the silencing of laterally acquired genes in bacteria*, PLoS Pathog., **2**, e81, (2006).

[88] T. Oshima, S. Ishikawa, K. Kurokawa, H. Aiba, and N. Ogasawara, *Escherichia coli histone-like protein H-NS preferentially binds to horizontally acquired DNA in association with RNA polymerase*, DNA Res., **13**, 141-153, (2006).

[89] C. Buchrieser, P. Glaser, C. Rusniok, H. Nedjari, H. D'Hauteville, F. Kunst, P. Sansonetti, and C. Parsot, *The virulence plasmid pWR*100 *and the repertoire of proteins secreted by the type III secretion apparatus of Shigella flexneri*, Mol. Microbiol., **38**, 760-771. (2000).

[90] J. Brussow, C. Canchaya, and W. D. Hardt, *Phages and the evolution of bacterial pathogens: from genomic rearrangements to lysogenic conversion*, Microbiol. Mol. Biol. Rev., **68**, 560-602, (2004).

[91] D. C. Grainger, D. Hurd, M. D. Goldberg, and S. J. W. Busby, *Association of nucleoid proteins with coding and non-coding segments of the Escherichia coli genome*, Nucleic Acids Res., **34**, 4642-4652, (2006).

[92] G. Prosseda, M. Falconi, M. Giangrossi, C. O. Gualerzi, G. Micheli, B. Colonna, *The virF promoter in Shigella: more than just a curved DNA stretch*, Mol. Microbiol., **51**, 523-537, (2004).

[93] M. D. Wang, M. J. Schnitzer, S. M. Block, *Force and velocity measured for single molecules of RNA polymerase*, Science, **282**, 902-907, (1998).

[94] D. Song and J. J. Loparo, *Building bridges within the bacterial chromosome*, Trends Genet., **31**, 164-173, (2015).

[95] D. Pastré, L. Hamon, A. Mechulam, I. Sorel, S. Baconnais, P. A. Curmi, E. Le Cam, and O. Piétrement, *Atomic Force Microscopy Imaging of DNA under Macromolecular Crowding Conditions*, Biomacromol., **8**, 3712-3717, (2007).

[96] H.-X. Zhou, G. Rivas, and A. P. Minton, *Macromolecular Crowding and Confinement: Biochemical, Biophysical, and Potential Physiological Consequences*, Annu. Rev. Biophys., **37**, 375-97, (2008).

[97] K. A. Sharp, *Unpacking the origins of in-cell crowding*, Proc. Natl. Acad. Sci., **113**, 1684-1685, (2016).

[98] L. S. Lerman, *A Transition to a Compact Form of DNA in Polymer Solutions*, Proc. Natl. Acad. Sci., **68**, 1886-1890, (1971).

[99] H. Kawakita, T. Uneyama, M. Kojima, K. Morishima, Y. Masubuchi, H. Watanabe, *Formation of globules and aggregates of DNA chains in DNA/polyethylene glycol/monovalent salt aqueous solutions*, J. Chem. Phys., **131**, 094901, (2009).

[100] R. de Vries, *Flexible polymer-induced condensation and bundle formation of DNA and F-actin filaments*, Biophys J., **80**, 1186-1194, (2001).

[101] J. E. B. Ramos Jr., R. de Vries, and J. Ruggiero Neto, *DNA Ψ-Condensation and Reentrant Decondensation: Effect of the PEG Degree of Polymerization*, J. Phys. Chem. B, **109**, 23661-2366, (2005).

[102] H. Kang, N. M. Toan, C. Hyeon, and D. Thirumalai, *Unexpected Swelling of Stiff DNA in a Polydisperse Crowded Environment*, J. Am. Chem. Soc., **137**, 10970-10978, (2015).

[103] V. V. Vasilevskaya, A. R. Khokhlov, Y. Matsuzawa, and K. Yoshikawa, *Collapse of single DNA molecule in poly(ethylene glycol) solutions*, J. Chem. Phys., **102**, 6595, (1995).

[104] K. Hirano, M. Ichikawa, T. Ishido, M. Ishikawa, Y. Baba, and K. Yoshikawa, *How environmental solution conditions determine the compaction velocity of single DNA molecules*, Nucleic Acids Res., **40**, 284-289, (2012).

[105] H. Ojala, G. Ziedaite, A. E. Wallin, D. H. Bamford, E. Hæggstrom, *Optical tweezers reveal force plateau and internal friction in PEG-induced DNA condensation*, Eur. Biophys. J., **43**, 71-79, (2014).

[106] M. S. Rocha, A. G. Cavalcante, R. Silva, and E. B. Ramos, *On the Effects of Intercalators in DNA Condensation: A Force Spectroscopy and Gel Electrophoresis Study*, J. Phys. Chem. B, **118**, 4832-4839, (2014).

[107] F. A. P. Crisafuli, L. H. M. da Silva, G. M. D. Ferreira, E. B. Ramos, M. S. Rocha, *Depletion Interactions and Modulation of DNA-Intercalators Binding: Opposite Behavior of the "Neutral" Polymer Poly(Ethylene-Glycol)*, Biopolymers, **105**, 227-233, (2015).

[108] C. Cheng, J.-L. Jia, and S.-Y. Ran, *Polyethylene glycol and divalent salt-induced DNA reentrant condensation revealed by single molecule measurements*, Soft Matter, **11**, 3927-3935, (2015).

[109] A. Vologodskii, *DNA Extension under the Action of an External Force*, Macromolecules, **27**, 5623-5625, (1994).

[110] R. Phillips, J. Kondev, J. Theriot and H. G. Garcia, *Physical Biology of the Cell*, Garland Science (Second Edition), (2013).

[111] S. B. Smith, L. Finzi, C. Bustamante, *Direct Mechanical Measurements of the Elasticity of Single DNA Molecules by Using Magnetic Beads*, Science, **258**, 1122-1126, (1992).

[112] P. Nelson, *Biological Physics: Energy, Information, Life*, W. H. Freeman & Co Ltd, (2001).

[113] C. Bustamante, Z. Bryant, and S. B. Smith, *Ten years of tension: single-molecule DNA mechanics*, Nature, **421**, 423-427, (2003).

[114] C. Bustamante, S. B. Smith, J. Liphardt, and D. Smith, *Single-molecule studies of DNA mechanics*, Curr. Opin. Struct. Biol., **10**, 279-285, (2000).

[115] S. B. Smith, Y. Cui, and C. Bustamante, *Overstretching B-DNA: The Elastic Response of Individual Double-Stranded and Single-Stranded DNA Molecules*, Science, **271**, 795-799, (1996).

[116] M. C. Williams, I. Rouzina, and M. J. McCauley, *Peeling back the mystery of DNA overstretching*, Proc. Natl. Acad. Sci., **106**, 18047-18048, (2009).

[117] X. Zhang, H. Chen, H. Fu, P. S. Doyle, and J. Yan, *Two distinct overstretched DNA structures revealed by single-molecule thermodynamics measurements*, Proc. Natl. Acad. Sci., **109**, 8103-8108, (2012).

[118] X. Zhang, H. Chen, S. Le, I. Rouzina, P. S. Doyle, and J. Yan, *Revealing the competition between peeled ssDNA, melting bubbles, and S-DNA during DNA overstretching by single-molecule calorimetry*, Proc. Natl. Acad. Sci., **110**, 3865-3870, (2013).

[119] A. Ahsan, J. Rudnick, and R. Bruinsma, *Elasticity Theory of the B-DNA to S-DNA Transition*, Biophys. J., **74**, 132-137, (1998).

[120] J. F. Marko, *DNA under high tension: Overstretching, undertwisting, and relaxation dynamics*, Phys. Rev. E, **57**, 2134, (1998).

[121] S. Cocco, J. Yan, J. F. Léger, D. Chatenay, and J. F. Marko, *Overstretching and force-driven strand separation of double-helix DNA*, Phys. Rev. E, **70**, 18, (2004).

[122] I. Rouzina, and V. A. Bloomfield, *Force-induced melting of the DNA double helix 1. Thermodynamic analysis*, Biophys. J., **80**, 882-893, (2001).

[123] M. C. Williams, J. R. Wenner, I. Rouzina, and V. A. Bloomfield, *Entropy and heat capacity of DNA melting from temperature dependence of single molecule stretching*, Biophys. J., **80**, 1932-1939, (2001).

[124] M. Rief, H. Clausen-Schaumann, and H. E. Gaub, *Sequence-dependent mechanics of single DNA molecules*, Nat. Struct. Biol., **6**, 346-349, (1999).

[125] C.-H. Guo, N. C. Harris, S. S. Wijeratne, E. W. Frey, and C.-H. Kiang, *Multiscale mechanobiology: mechanics at the molecular, cellular, and tissue levels*, **3**, 25, (2013).

[126] C. Bustamante, J. F. Marko, E. D. Siggia, S. Smith, *Entropic Elasticity of λ-Phage DNA*, Science, **265**, 1599-1600, (1994).

[127] J. F. Marko and E. D. Siggia, *Statistical mechanics of supercoiled DNA*, Phys. Rev. E, **52**, 2912, (1995).

[128] J. F. Marko and E. D. Siggia, *Stretching DNA*, **28**, Macromolecules, 8759-8770, (1995).

[129] M. Fixman and J. Kovac, *Polymer conformational statistics. III. Modified Gaussian models of stiff chains*, J. Chem. Phys., **58**, 1564-1568, (1973).

[130] J. D. Moroz and P. Nelson, *Torsional directed walks, entropic elasticity, and DNA twist stiffness*, Proc. Natl. Acad. Sci., **94**, 14418-14422, (1997).

[131] C. Bouchiat and M. Mézard, *Elasticity theory of supercoiled DNA molecules*, Phys. Rev. Lett., **80**, 1556-1559, (1998).

[132] C. Maffeo, R. Schopflin, H. Brutzer, R. Stehr, A. Aksimentiev, G. Wedemann, and R. Seidel, *DNA–DNA Interactions in Tight Supercoils Are Described by a Small Effective Charge Density*, Phys. Rev Lett., **105**, 158101, (2010).

[133] S. Neukrich and J. F. Marko, *Analytical Description of Extension, Torque, and Supercoiling Radius of a Stretched Twisted DNA*, Phys. Rev. Lett., **106**, 138104, (2011).

[134] J. F. Marko and S. Neukrich, *Competition between curls and plectonemes near the buckling transition of stretched supercoiled DNA*, Phys. Rev. E, **85**, 011908, (2012).

[135] P.-M. Lam and Y. Zhen, *Extension, torque, and supercoiling in single, stretched, and twisted DNA molecules*, J. Chem. Phys., **143**, 174901, (2015).

[136] F. Mosconi, J.-F. Allemand, D. Bensimon, and V. Croquette, *Measurement of the Torque on a Single Stretched and Twisted DNA Using Magnetic Tweezers*, Phys. Rev. Lett., **102**, 078301, (2009).

[137] D. Salerno, A. Tempestini, I. Mai, D. Brogioli, R. Ziano, V. Cassina, and F. Mantegazza, *Single-Molecule Study of the DNA Denaturation Phase Transition in the Force-Torsion Space*, Phys. Rev. Lett., **109**, 118303, (2012).

[138] A. Tempestini, V. Cassina, D. Brogioli, R. Ziano, S. Erba, R. Giovannoni, M. G. Cerrito, D. Salerno, and F. Mantegazza, *Magnetic tweezers measurements of the nanomechanical stability of DNA against denaturation at various conditions of pH and ionic strength*, Nucleic Acids Res., **43**, 2009-2012, (2013).

[139] C. Gosse and V. Croquette, *Magnetic Tweezers: Micromanipulation and Force Measurement at the Molecular Level*, Biophys. J., **82**, 3314-3329, (2002).

[140] I. De Vlaminck and C. Dekker, *Recent Advances in Magnetic Tweezers*, Annu. Rev. Biophys., **41**, 453-472, (2012).

[141] J. van Mameren, G.J.L. Wuite, and I. Heller, *Introduction to Optical Tweezers: Background, System Designs, and Commercial Solutions*, in E. Peterman (eds) Single Molecule Analysis. Methods in Molecular Biology, Humana Press, **1665**, 3-23, (2018).

[142] N. Jalili and K. Laxminarayana, *A review of atomic force microscopy imaging systems: application to molecular metrology and biological sciences*, Mechatronics, **14**, 907-945, (2004).

[143] F. Amblard, B. Yurke, A. Pargellis, and S. Leibler, *A magnetic manipulator for studying local rheology and micromechanical properties of biological systems*, Rev. Sci. Instrum., **67**, 818, (1996).

[144] T. R. Strick, J.-F. Allemand, D. Bensimon, and V. Croquette, *The Elasticity of a Single Supercoiled DNA Molecule*, Science, **271**, 1835-1837, (1996).

[145] I. D. Vilfan, J. Lipfert., D. A. Koster, S. G. Lemay, and N. H. Dekker, *Magnetic Tweezers for Single-Molecule Experiments*, in P. Hinterdorfer, A. Oijen (eds) Handbook of Single-Molecule Biophysics, Springer, 371-395, (2009).

[146] D. Salerno, D. Brogioli, V. Cassina, D. Turchi, G. L. Beretta, D. Seruggia, R. Ziano, F. Zunino, and F. Mantegazza, *Magnetic tweezers measurements of the nanomechanical properties of DNA in the presence of drugs*, Nucleic Acids Res., **38**, 7089-7099, (2010).

[147] J. Lipfert, X. Hao, and N. H. Dekker, *Quantitative Modeling and Optimization of Magnetic Tweezers*, Biophys. J., **96**, 5040-5049, (2010).

[148] A. J. W. te Velthuis, J. W. J. Kerssemakers, J. Lipfert, N. H. Dekker, *Quantitative Guidelines for Force Calibration through Spectral Analysis of Magnetic Tweezers Data*, Biophys. J., **99**, 1292-1302, (2010).

[149] G. Binnig, C. F. Quate, and C. Gerber, *Atomic force microscope*, Phys. Rev. Lett., **56**, 930-936, (1986).

[150] M. Rief, M. Gautel, F. Oesterhelt, J. M. Fernandez, H. E. Gaub, *Reversible unfolding of individual titin immunoglobulin domains by AFM*, Science, **276**, 1109-1112, (1997).

[151] P. C. Braga and D. Ricci, *Atomic Force Microscopy - Biomedical Methods and Application*, Methods in Molecular Biology, **242**, Humana Press, (2004).

[152] A. Ikai, *The World of Nano-Biomechanics*, Elsevier, (2008).

[153] V. Cassina, M. Manghi, D. Salerno, A. Tempestini, V. Iadarola, L. Nardo, S. Brioschi, and F. Mantegazza, *Effects of cytosine methylation on DNA morphology: An atomic force microscopy study*, Biochim. Biophys. Acta - Gen. Subj., **1860**, 1-7, (2016).

[154] V. Cassina, D. Seruggia, G. L. Beretta, D. Salerno, D. Brogioli, S. Manzini, F. Zunino, and F. Mantegazza, *Atomic force microscopy study of DNA conformation in the presence of drugs*, Eur. Biophys. J., **40**, 59-68, (2011).

[155] C. Rivetti, M. Guthold, and C. Bustamante, *Scanning force microscopy of DNA deposited onto mica: Equilibration versus kinetic trapping studied by statistical polymer chain analysis*, J. Mol. Biol., **264**, 919-932, (1996).

[156] A. Podestà, M. Indrieri, D. Brogioli, G. S. Manning, P. Milani, R. Guerra, L. Finzi, and D. Dunlap, *Positively charged surfaces increase the flexibility of DNA*, Biophys. J., **89**, 2558-2563, (2005).

[157] P. Wiggins, T. V. Der Heijden, F. Moreno-Herrero, A. Spakowitz, R. Phillips, J. Widom, C. Dekker, and P. C. Nelson, *High flexibility of dna on short length scales probed by atomic force microscopy*, Nat. Nanotechnol., **1**, 137-141, (2009).

[158] L. Potvin-Trottier, S. Luro and J. Paulsson, *Microfluidics and single-cell microscopy to study stochastic processes in bacteria*, Curr. Opin. Microbiol., **43**, 186-192, (2018).

[159] M. Thanbichler and L. Shapiro, *MipZ, a spatial regulator coordinating chromosome segregation with cell division in Caulobacter*, Cell, **126**,147-62, (2006).

[160] A. Fiebig, K. Keren, and J. A. Theriot, *Fine-scale time-lapse analysis of the biphasic, dynamic behaviour of the two Vibrio cholerae chromosomes*, Mol. Microbiol., **60**, 1164-1178, (2006).

[161] G. Joyce,1 B. D. Robertson, and K. J. Williams, *A modified agar pad method for mycobacterial live-cell imaging*, BMC Res. Notes, **4**, 73, (2011).

[162] A. Javer, Z. Long, E. Nugent, M. Grisi, K. Siriwatwetchakul, K. D. Dorfman, P. Cicuta, and M. Cosentino Lagomarsino, *Short-time movement of E. coli chromosomal loci depends on coordinate and subcellular localization*, **4**, 3003, (2013).

[163] A. Javer, N. J. Kuwada, Z. Long, V. G. Benza, K. D. Dorfman, P. A. Wiggins, P. Cicuta, and M. Cosentino Lagomarsino, *Persistent super-diffusive motion of Escherichia coli chromosomal loci*, Nat. Comm., **5**, 3854 , (2014).

[164] N. Q. Balaban, J. Merrin, R. Chait, L. Kowalik, and S. Leibler, *Bacterial persistence as a phenotypic switch*, Science, **305**, 1622-1625, (2004).

[165] S. Cookson, N. Ostroff, W. L. Pang, D. Volfson, and J. Hasty, *Monitoring dynamics of single-cell gene expression over multiple cell cycles*, Mol. Syst. Biol., **22**, (2005).

[166] P. Hammar, M. Wallden, D. Fange, F. Persson, O. Baltekin, G. Ullman, P. Leroy, and J. Elf, *Direct measurement of transcription factor dissociation excludes a simple operator occupancy model for gene regulation*, Nat. Genet., **46**, 405-408, (2014).

[167] T. Danino, O. Mondragon-Palomino, L. Tsimring, J. Hasty, *A synchronized quorum of genetic clocks*, Nature, **463**, 326-330, (2010).

[168] P. Wang, L. Robert, J. Pelletier, W. L. Dang, F. Taddei, A. Wright, and S. Jun, *Robust Growth of Escherichia coli*, Curr. Opin. Microbiol., **20**, 1099-1103, (2010).

[169] T. M. Norman, N. D. Lord, J. Paulsson, and R. Losick, *Memory and modularity in cell-fate decision making*, Nature, **503**, 481-486, (2013).

[170] J. R. Moffitt, J. B. Lee, and P. Cluzel, *The single-cell chemostat: an agarose-based, microfluidic device for high-throughput, single-cell studies of bacteria and bacterial communities*, Lab Chip, **12**, 1487-1494, (2012).

[171] Z. Long, E. Nugent, A. Javer, P. Cicuta, B. Sclavi, M. Cosentino Lagomarsino and K. D. Dorfman, *Microfluidic chemostat for measuring single cell dynamics in bacteria*, Lab Chip, **13**, 947-954, (2013).

[172] J. Sheats, B. Sclavi, M. Cosentino Lagomarsino, P. Cicuta and K. D. Dorfman, *Role of growth rate on the orientational alignment of Escherichia coli in a slit*, R. Soc. open sci., **4**, 170463, (2017).

[173] S. Stylianidou, C. Brennan, S. B. Nissen, N. J. Kuwada, and P. A. Wiggins, *SuperSegger: robust image segmentation, analysis and*

lineage tracking of bacterial cells, Mol. Microbiol., **102**, 690-700, (2016).

[174] J. A. Cass, S. Stylianidou, N. J. Kuwada, B. Traxler, and P. A. Wiggins, *Probing bacterial cell biology using image cytometry*, Mol. Microbiol., **103**, 818-828, (2017).

[175] D. Salerno, G. L. Beretta, G. Zanchetta, S. Brioschi, M. Cristofalo, N. Missana, L. Nardo, V. Cassina, A. Tempestini, R. Giovannoni, M. G. Cerrito, N. Zaffaroni, T. Bellini, and F. Mantegazza, *Platinum-Based Drugs and DNA Interactions Studied by Single-Molecule and Bulk Measurements*, Biophys. J., **110**, 2151-2161, (2016).

[176] B. Laine, P. Sautiere, A. Spassky, S. Rimsky, *A DNA-binding protein fromE. coliisolation, characterization and its relationship with proteins H1 and B1*, **119**, Biochem. Biophys. Res. Comm., 1147-1153, (1984).

[177] A. Spassky, S. Rimsky, H. Garreau, H. Buc, *Hla, an E. coli DNA-binding protein which accumulates in stationary phase, strongly compacts DNA in vitro*, Nucleic Acids Res.,**12**, 5321-5340, (1984).

[178] C. Bailly and M. J. Wairing, *The use of diaminopurine to investigate structural properties of nucleic acids and molecular recognition between ligands and DNA*, Nucleic Acids Res., **26**, 4309-4314, (1998).

[179] J . P. Schrum, A. Ricardo, M. Krishnamurthy, J. C. Blain, and J. W. Szostak, *Efficient and rapid template-directed nucleic acid copying using 2′-amino-2′,3′-dideoxyribonucleoside-5′- phosphorimidazolide monomers*, J. Am. Chem. Soc., **131**, 14560-14570, (2009).

[180] M. D. Kirnos, I. Y. Khudyakov, N. I. Alexandrushkina, and B. F. Vanyushin, *2-Aminoadenine is an adenine substituting for a base in S-2L cyanophage DNA*, Nature, **270**, 369-370, (1977).

[181] I. Y. Khudyakov, M. D. Kirnos, N. I. Alexandrushkina, and B. F. Vanyushin, *Cyanophage S-2L contains DNA with 2,6-diaminopurine substituted for adenine*, Virology, **88**, 8-18, (1978).

[182] A. Cerami, E. Reich, D. C. Ward, and I. H. Goldberg, *The interaction of actinomycin with DNA: requirement for the 2-amino group of purines*, Proc. Natl. Acad. Sci., **57**, 1036-42, (1967).

[183] M. Fernández-Sierra, Q. Shao, C. Fountain, L. Finzi, and D. Dunlap, *E. coli gyrase fails to negatively supercoil diaminopurine-substituted DNA*. J. Mol. Biol., **427**, 2305-2318, (2015).

[184] C. Bailly, D. Payet, A. A. Travers, and M. J. Waring, *PCR-based development of DNA substrates containing modified bases: An efficient system for investigating the role of the exocyclic groups in chemical and structural recognition by minor groove binding drugs and proteins*, Proc. Natl. Acad. Sci., **93**, 13623-13628, (1996).

[185] M. Tomasz, A. Das, K. S. Tang, M. G. Ford, A. Minnock, S. M. Musser, and M. J. Waring, *The purine 2-amino group as the critical recognition element for sequence-specific alkylation and cross-linking of DNA by mitomycin C*, J. Am. Chem. Soc., **120**, 11581-11593, (1998).

[186] E. Marco, A. Negri, F. J. Luque, and F. Gago, *Role of stacking interactions in the binding sequence preferences of DNA bisintercalators: Insight from thermodynamic integration free energy simulations*, Nucleic Acids Res., **33**, 6214-6224, (2005).

[187] Y. D. Tseng, H. Ge, X. Wang, J. M. Edwardson, M. J. Waring, W. J. Fitzgerald, and R. M. Henderson, *Atomic force microscopy study of the structural effects induced by echinomycin binding to DNA*, J. Mol. Biol., **345**, 745-758, (2005).

[188] E. A. Véliz, L. M. Easterwood, and P. A. Beal, *Substrate analogues for an RNA-editing adenosine deaminase: Mechanistic investigation and inhibitor design*, J. Am. Chem. Soc., **125**, 10867-10876, (2003).

[189] S. D. Gilbert, S. J. Mediatore, and R. T. Batey, *Modified pyrimidines specifically bind the purine riboswitch*. J. Am. Chem. Soc., **128**, 14214-14215, (2006).

[190] K. Kawai, H. Kodera, and T. Majima, *Long-range charge transfer through DNA by replacing adenine with diaminopurine*, J. Am. Chem. Soc., **132**, 627-630, (2010).

[191] D. T. Kovari, M. Cristofalo, D. Dunlap, and L. Finzi, *The Overstretching Transition of Diaminopurine Substituted Triply Hydrogen-Bonded DNA*, Biophys. J., **110 (3)**, 183A-184A, (2016).

[192] D. T. Kovari, M. Cristofalo, R. Corti, D. Salerno, V. Cassina, Y. Lee, G. Malla, L. Finzi, F. Mantegazza, and D. Dunlap, *Experimentally Motivated Sequence-Dependent Models of Melting and Overstretching for Diaminopurine-Substituted DNA*, Biophys. J., **114 (3)**, 88A, (2018).

[193] M. Cristofalo, D. T. Kovari, R. Corti, D. Salerno, V. Cassina, D. Dunlap, and F. Mantegazza, *Nanomechanics of diaminopurine-substituted DNA*, under review.

[194] P. Sulc, F. Romano, T. E. Ouldridge, L. Rovigatti, J. P. Doye, and A. A. Louis, *Sequence-dependent thermodynamics of a coarse-grained DNA model*. J. Chem. Phys., **137**, 135101, (2012).

[195] A. Sen, and P. E. Nielsen, *Hydrogen bonding versus stacking stabilization by modified nucleobases incorporated in PNA·DNA duplexes*, Biophys. Chem., **141**, 29-33, (2009).

[196] J. P. Peters, S. P. Yelgaonkar, S. G. Srivatsan, Y. Tor, and L. James Maher, *Mechanical properties of DNA-like polymers*, Nucleic Acids Res., **41**, 10593-10604, (2013).

[197] E. Smith, M. E. Jones, and P. A. Drew,*Quantitation of DNA methylation by melt curve analysis*, BMC Cancer, **9**, 123, (2009).

[198] L. N. Sanford, J. O. Kent, and C. T. Wittwer, *Quantum Method for Fluorescence Background Removal in DNA Melting Analysis*, Anal. Chem., **85**, 9907-9915, (2013).

[199] J. SantaLucia, *A unified view of polymer, dumbbell, and oligonucleotide DNA nearest-neighbor thermodynamics*, Proc. Natl. Acad. Sci., **95**, 1460-1465, (1998).

[200] J. SantaLucia, and D. Hicks, *The Thermodynamics of DNA Structural Motifs*, Annu. Rev. Biophys. Biomol. Struct., **33**, 415-440. (2004).

[201] J. F. Léger, G. Romano, A. Sarkar, J. Robert, L. Bourdieu, D. Chatenay, and J. F. Marko, *Structural transitions of a twisted and stretched DNA molecule*, Phys. Rev. Lett., **83**, 1066-1069, (1999).

[202] G. A. King, E. J. G. Peterman, and G. J. L. Wuite, *Unravelling the structural plasticity of stretched DNA under torsional constraint*, Nat. Comm., **7**, 11810, (2016).

[203] J. Singh, and P. K. Purohit, *Structural transitions in torsionally constrained DNA and their dependence on solution electro- statics*, Acta Biomater., **55**, 214-225, (2017).

[204] N. Bosaeus, A. H. El-Sagheer, T. Brown, S. B. Smith, B. Akerman, C. Bustamante, and B. Nordén, *Tension induces a base-paired overstretched DNA conformation*, Proc. Natl. Acad. Sci., **109** 15179-15184, (2012).

[205] H. Fu, H. Chen, X. Zhang, Y. Qu, J. F. Marko, and J. Yan, *Transition dynamics and selection of the distinct S-DNA and strand unpeeling modes of double helix overstretching*, Nucleic Acids Res., **39**, 3473-3481, (2011).

[206] X. Zhang, Y. Qu, H. Chen, I. Rouzina, S. Zhang, P. S. Doyle, and J. Yan, *Interconversion between three overstretched DNA structures*, J. Am. Chem. Soc., **136**, 16073-16080, (2014).

[207] R. Vlijm, J. v. d.Torre, C. Dekker, *Counterintuitive DNA Sequence Dependence in Supercoiling-Induced DNA Melting*, Plose One, **10**, e0141576, (2015).

[208] M. Y. Sheinin, S. Forth, J. F. Marko, and M. D. Wang, *Underwound DNA under Tension: Structure, Elasticity, and Sequence-Dependent Behaviors*, Phys. Rev. Lett, **107**, 108102, (2011).

[209] A-Y. Kwon, G-M. Nam, A. Johner, S. Kim, S-C. Hong, N-K. Lee, *Competition between B-Z and B-L transitions in a single DNA molecule: Computational studies*, Phys. Rev. E, **93**, 022411, (2016).

[210] D. Salerno, M. Cristofalo, C. Marrano, E. Chiodi, N. Missana, R. Corti, L. Nardo, V. Cassina, F. Mantegazza, *Single molecule study of DNA phase transitions under forces. A focus on the mixed phase condition*, Eur. Biophys. J., **46**, S192-S192, (2017).

[211] J. Lipfert, S. Klijnhout and N. H. Dekker, *Torsional sensing of small-molecule binding using magnetic tweezers*, Nucleic Acids Res., **38**, 7122-7132, (2010).

[212] J. R. Moffitt, Y. R. Chemla, S. B. Smith, and C. Bustamante, *Recent advances in optical tweezers*, Annu. Rev. Biochem., **77**, 205-228, (2008).

[213] A. Crut, D. A. Koster, R. Seidel, C. H. Wiggins, and N. H. Dekker, *Fast dynamics of supercoiled DNA revealed by single-molecule experiments*, Proc. Natl. Acad. Sci., **104**, 11957-11962, (2007).

[214] J. F. Marko, and S. Neukrich, *Global force-torque phase diagram for the DNA double helix: Structural transitions, triple points, and collapsed plectonemes*, **88**, 062722, (2013).

[215] V. Brabec, J. Kasparkova, O. Vrana, O. Novakova, J. W. Cox, Y. Qu, and N. Farrell, *DNA modifications by a novel bifunctional trinuclear platinum phase I anticancer agent*, Biochemistry, **38**, 6781-6790, (1999).

[216] K. Chvalova, V. Brabec, and J. Kasparkova. *Mechanism of the formation of DNA-protein cross-links by antitumor cisplatin*, Nucleic Acids Res., **35**, 1812-1821, (2007).

[217] P. M. Takahara, A. C. Rosenzweig, C. A. Frederick, and S. J. Lippard *Crystal structure of double-stranded DNA containing the major adduct of the anticancer drug cisplatin*, Nature, **377**, 649-652, (1995).

[218] V. Cepeda, M. A. Fuertes, J. Castilla, C. Alonso, C. Quevedo, and J. M. Perez, *Biochemical mechanisms of cisplatin cytotoxicity*, Anticancer. Agents Med. Chem., **7**, 3-18, (2007).

[219] N. J. Wheate and G. Collins, *Multi-nuclearplatinumcomplexes as anti-cancer drugs*, Coord. Chem. Rev., **241**, 133-145, (2003).

[220] I. Heller, T. P. Hoekstra, G. A. King, E. J. G. Peterman, and G. J. L. Wuite, *Optical Tweezers Analysis of DNA-Protein Complexes*, Chem. Rev., **114**, 3087-3119, (2014).

[221] A. A. Almaqwashi, T. Paramanathan, I. Rouzina, and M. C. Williams, *Mechanisms of small molecule–DNA interactions probed by single-molecule force spectroscopy*, Nucleic Acids Res., **44**, 3971-3988, (2016).

[222] A. S. Biebricher, I. Heller, R. F. H. Roijmans, T. P. Hoekstra, E. J.G. Peterman, and G. J.L. Wuite, *The impact of DNA intercalators on DNA and DNA-processing enzymes elucidated through force-dependent binding kinetics*, Nat. Comm., **6**, 7304, (2015).

[223] M. Ritzefeld, V. Walhorn, D. Anselmetti, and N. Sewald, *Analysis of DNA interactions using single-molecule force spectroscopy*, Amino Acids, **44**, 1457-1475, (2013).

[224] S. J. Koch and M. D. Wang, *Dynamic Force Spectroscopy of Protein-DNA Interactions by Unzipping DNA*, Phys. Rev. Lett., **91**, 028103, (2003).

[225] J. L Syrjanen, I. Heller, A. Candelli, O. R. Davies, E. J. G. Peterman, G. J. L. Wuite, and L. Pellegrini, *Single-molecule observation of DNA compaction by meiotic protein SYCP3*, eLife, **6**, e22582, (2017).

[226] R. S. Winardhi, W. Fu, S. Castang, Y. Li, S. L. Dove, J. Yan, *Higher order oligomerization is required for H-NS family member MvaT to form gene-silencing nucleoprotein filament*, Nucleic Acids Res., **40**, 8942-8952, (2012).

[227] B. J. Paul, W. Ross, T. Gaal, and R. L. Gourse, *rRNA transcription in Escherichia coli*, Annu. Rev. Genet., **38**, 749-770, (2004).

[228] P. P. Dennis, M. Ehrenberg, and H. Bremer, *Control of rRNA synthesis in Escherichia coli: a systems biology approach*, Microbiol. Mol. Biol. Rev., **68**, 639-668, (2004).

[229] J. A. Bryant, L. E. Sellars, S. J. W. Busby, and D. J. Lee *Chromosome position effects on gene expression in Escherichia coli K*-12, Nucleic Acids Res., **42**, 11383-11392, (2015).

[230] E. Brambilla, and B. Sclavi, *Gene Regulation by H-NS as a Function of Growth Conditions Depends on Chromosomal Position in Escherichia coli*, **5**, 605-614, (2015).

[231] B. Sendy, D. J. Lee, S. J. W. Busby, and J. A. Bryant, *RNA polymerase supply and flux through the lac operon in Escherichia coli*, Philos. Trans. R. Soc. Lond. B. Biol. Sci., **371**, 20160080, (2016).

[232] D. H. S. Block, R. Hussein, L. W. Liang, and H. N. Lim, *Regulatory consequences of gene translocation in bacteria*, Nucleic Acids Res., **40**, 8979-8992, (2012).

[233] M. Berger, V. Gerganova, P. Berger, R. Rapiteanu, V. Lisicovas, and U. Dobrindt, *Genes on a Wire: The Nucleoid-Associated Protein HU Insulates Transcription Units in Escherichia coli*, Sci. Rep., **6**, 31512, (2016).

[234] V. Gerganova, M. Berger, E. Zaldastanishvili, P. Sobetzko, C. Lafon, M. Mourez, A. Travers, and G. Muskhelishvili, *Chromosomal position shift of a regulatory gene alters the bacterial phenotype*, Nucleic Acids Res., **43**, 8215-8226, (2015).

[235] T. Vora, A. K. Hottes, and S. Tavazoie, *Protein occupancy landscape of a bacterial genome*, Mol. Cell, **35**, 247-253, (2009).

[236] K. L. Ohlsen and J. D. Gralla, *Interrelated effects of DNA supercoiling, ppGpp, and low salt on melting within the Escherichia coli ribosomal RNA rrnB P1 promoter*, Mol. Microbiol., **6**, 2243-2251, (1992).

[237] K. Sneppen, I. B. Dodd, K. E. Shearwin, A. C. Palmer, R. A. Schubert, B. P. Callen, and J. B. Egan, *A mathematical model for transcriptional interference by RNA polymerase traffic in Escherichia coli*, J. Mol. Biol., **346**, 399-409, (2005).

[238] P. Yakovchuk, E. Protozanova, and M. D. Frank-Kamenetskii, *Base-stacking and base-pairing contributions into thermal stability of the DNA double helix*, Nucleic Acids Res., **34**, 564-574, (2006).

[239] L. Bongini, V. Lombardi, and P. Bianco, *The transition mechanism of DNA overstretching: a microscopic view using molecular dynamics*, J. R. Soc. Interface, **11**, 20140399, (2014).

[240] L. Bongini, C. Pongor, G. Falorsi, I. Pertici, M. Kellermayer, V. Lombardi, and P. Bianco, *An AT-barrier mechanically controls DNA reannealing under tension*, Nucleic Acids Res., **44**, 7954-7962, (2016).

[241] N. Bosaeus, A. H. El-Sagheer, T. Brown, B. Åkerman, and B. Nordén, *Force-induced melting of DNA - Evidence for peeling and internal melting from force spectra on short synthetic duplex sequences*, Nucleic Acids Res., **42**, 8083-8091, (2014).

[242] H. Fu, H. Chen, J. F. Marko, and J. Yan, *Two distinct overstretched DNA states*, Nucleic Acids Res., **38**, 5594-5600, (2010).

[243] S. Whitelam, S. Pronk, and P. L. Geissler, *There and (slowly) back again: Entropy-driven hysteresis in a model of DNA overstretching*, Biophys. J., **94**, 2452-2469, (2008).

[244] F. Romano, D. Chakraborty, J. P. Doye, T. E. Ouldridge, and A. A. Louis, *Coarse-grained simulations of DNA overstretching*, J. Chem. Phys., **138**, 085101, (2013).

[245] Clausen-Schaumann, H., M. Rief, C. Tolksdorf, and H. E. Gaub, *Mechanical stability of single DNA molecules*, Biophys. J., **13**, **78**, 1997-2007, (2000).

[246] J. Virstedt, T. Berge, R. M. Henderson, M. J. Waring, and A. A. Travers, *The influence of DNA stiffness upon nucleosome formation*, J. Struct. Biol., **148**, 66-85, (2004).

[247] J. P. Peters, L. S. Mogil, M. J. McCauley, M. C. Williams, and L. J. Maher, *Mechanical properties of base-modified DNA are not strictly determined by base stacking or electrostatic interactions*, Biophys. J., **107**, 448-459, (2014).

[248] A. A. Travers, *The structural basis of DNA flexibility*, Philos. Trans. R. Soc. A Math. Phys. Eng. Sci., **362**, 1423-1438, (2004).

[249] C. R. Calladine, *Mechanics of sequence-dependent stacking of bases in B-DNA*, J. Mol. Biol., **161**, 343-352, (1982).

[250] J. D. Kahn, E. Yun, and D. M. Crothers, *Detection of localized DNA flexibility*, Nature, **368**, 163-166, (1994).

[251] T. Strick, J.-F. Allemand, V. Croquette, D. Bensimon, *Twisting and stretching single DNA molecules*, Prog. Biophys. Mol. Biol., **74**, 115-140, (2000).

[252] A. Sarkar, J. F. Leger, D. Chatenay, J. F. Marko, *Structural transitions in DNA driven by external force and torque*, Phys. Rev. E, **63**, 051903, (2001).

[253] S. Goyal, N. C. Perkins, and C. L. Lee, *Nonlinear dynamics and loop formation in Kirchhoff rods with implications to the mechanics of DNA and cables*, J. Comput. Phys., **209**, 371-389, (2005).

[254] P. K. Purohit, *Plectoneme formation in twisted fluctuating rods*, J. Mech. Phys. Solids., **56**, 1715-1729, (2008).

[255] F. A. Crisafuli, E. C. Cesconetto, E. B. Ramos, M. S. Rocha. *DNA-cisplatin interaction studied with single molecule stretching experiments*, Integr. Biol. (Camb.), **4**, 568-574, (2012).

[256] N.-K. Lee, J.-S. Park, A. Johner, S. Obukhov, J.-Y. Hyon, K. J. Lee, and S.-C. Hong, *Investigation of the elasticity of a cisplatin-DNA adduct via single-molecule measurements and bimodal modeling*, Phys. Rev. E, **79**, 041921, (2009).

[257] P. Di Blasi, A. Bernareggi, G. Beggiolin, L. Piazzoni, E. Menta, M. L. Formento, *Cytotoxicity, cellular uptake and DNA binding of the novel trinuclear platinun complex BBR 3464 in sensitive and cisplatin resistant murine leukemia cells*, Anticancer Res., **18**, 3113-3117, (1998).

[258] J. D Roberts., J. Peroutka, and N. Farrell.*Cellularpharmacology of polynuclear platinum anti-cancer agents*, J. Inorg. Biochem., **77**, 51-57, (1999).

[259] P. Perego, L. Gatti, C. Caserini, R. Supino, D. Colangelo, R. Leone, S. Spinelli, N. Farrell, and F. Zunino, *The cellular basis of the efficacy of the trinuclear platinum complex BBR 3464 against cisplatin- resistant cells*, J. Inorg. Biochem., **77**, 59-64, (1999).

[260] B. Lang, N. Blot, E. Bouffartigues, M. Buckle, M. Geertz, C. O. Gualerzi, R. Mavathur, G. Muskhelishvili, C. L. Pon, S. Rimsky, S. Stella, M. M. Babu, and A. Travers, *High-affinity DNA binding sites for H-NS provide a molecular basis for selective silencing within proteobacterial genomes*, Nucleic Acids Res., **35**, 6330-6337, (2007).

[261] M. Sette, R,Spurio, E. Trotta, C. Brandizi, A. Brandi, C. L. Pon, G. Barbato, R. Boelens, C. O. Gualerzi, *Sequence-specific recognition of DNA by the C-terminal domain of nucleoid-associated protein H-NS*, J. Biol. Chem., **284**, 30453-30462, (2009).

[262] A. S. Wegner, K. Wintraecken, R. Spurio, C. L. Woldringh, R. de Vries, T. Odijk, *Compaction of isolated Escherichia coli nucleoids: Polymer and H-NS protein synergetics*, J. Struct. Biol., **194**, 129-137, (2016).

[263] S. K. Ramisetty and R. S. Dias, *Synergistic role of DNA-binding protein and macromolecular crowding on DNA condensation. An experimental and theoretical approach*, J. Mol. Liq., **210**, 64-73, (2015).

[264] S. K. Ramisetty, P. Langlete, R. Lale, R. S. Dias, *In vitro studies of DNA condensation by bridging protein in a crowding environment*, Int. J. Biol. Macromol., **103**, 845-853, (2017).

[265] J. Pelletier, K. Halvorsen, B.-Y. Ha, R. Paparcone, S. J. Sandler, C. L. Woldringh, W. P. Wong, and S. Jun, *Physical manipulation of the Escherichia coli chromosome reveals its soft nature*, **109**, E2649-E2656, (2012).

[266] S. Cunha, C. L. Woldringh, and T. Odijk, *Polymer-mediated compaction and internal dynamics of isolated Escherichia coli nucleoids*, J. Struct. Biol., **136**, 53-66, (2001).

[267] S. Jun, D. Thirumalai, B. Y. Ha, *Compression and stretching of a self-avoiding chain in cylindrical nanopores*, Phys Rev Lett, **101**, 138101, (2008).

[268] R. Hancock and K.W. Jeon, *New Models of the Cell Nucleus: Crowding, Entropic Forces, Phase Separation, and Fractals*, International Review Of Cell And Molecular Biology, **307**, (2014).

[269] V. F. Scolari and M. Cosentino Lagomarsino, *Combined collapse by bridging and self-adhesion in a prototypical polymer model inspired by the bacterial nucleoid*, Soft Matter, **11**, 1677-1687, (2015).